Finite element modelling, construction and experimental characterization of piezoelectric transducers for gas

Håvard Råheim Økland

Thesis for the degree
Master of science in Ocean technology
Marine Measurement systems and Acoustics

Department of Physics and Technology
University of Bergen

June 2023

Acknowledgements

With these words, I want to express my deepest gratitude to all the individuals who have contributed to the completion of my Master's thesis in Ocean Technology. First and foremost, I would like to thank my supervisor, Prof. Per Lunde, and co-supervisors, Assoc Prof Emer. Magne Vestrheim and Dr. Mathias Sæter for their guidance, knowledge, and experience throughout this work. I am grateful for your passion and dedication to the field of acoustics, which I have also learned to cherish. This work would not have been possible without our fruitful conversations and your endless ideas and proposals.

I would also like to thank the other members of the acoustics group at the University of Bergen, especially Eivind Nag Mosland and Audun Opedal Pedersen, who have provided invaluable help and time with the acoustic measurement system and laboratory instruments.

I am grateful to the staff in the mechanical workshop at the Department of Physics and Technology at UiB, particularly Roald Langøen, who has been helpful with his crafting skills and ability to deliver the required parts on short notice. I also want to thank senior engineer Bilal Hasan Qureshi and Master Student Ola Wiik for their assistance with soldering the piezoelectric disks.

Furthermore, I thank my friends and fellow students in the Ocean Technology program for the wonderful memories we have created throughout our studies. A special thanks go out to the group in room 209 for the great times we have shared; the two years as master students would not have been the same without you.

Lastly, I would like to express my gratitude to Mie and the rest of my family for their unconditional support and belief in my abilities throughout this project. Your love and understanding have given me the strength I need to overcome any challenge, no matter how difficult.

Håvard Råheim Økland
Bergen, 01.06.2023

Contents

Chapter 1

Introduction

1.1 Background and motivation

Ultrasonic meters (USMs) for fiscal gas flow measurement have penetrated the market for meters rapidly since 2000, and have become one of the prime flowmeter concepts for custody transfer and allocation measurement [1]. The Norwegian oil and gas industry is moving towards subsea fiscal allocation measurements of gas, where traditional methods such as gas chromatography to measure the gas composition and gross calorific value (GCV) cannot be used [2].

The Gas Analyzer developed by CMR (now, NORCE) [3] is an alternative method to gas chromatography, where the GCV and density can be calculated using the velocity of sound (VOS) from an ultrasonic flowmeter. However, the Gas Analyzer method is currently not applicable in fiscal measurements due to a lack of calibration and traceability to national and international standards and regulations for the VOS measurement [4]. Therefore a sound velocity measurement cell for gas that can be used to calibrate the VOS measurement from the ultrasonic flowmeters to within a specified uncertainty level is required. The uncertainty of the sound velocity measurements should tentatively be in the 100 to 200 ppm range, a value that is estimated from the required uncertainty for the GCV [5–7].

The resonance frequency of ultrasonic transducers used in ultrasonic gas flow meters is typically in the range of 100 kHz to 500 kHz [8]. This frequency range is used, as ultrasonic waves with higher frequencies tend to attenuate more rapidly in gas [9, 10]. Furthermore, the sound velocity in gas exhibits frequency dependence due to ultrasonic dispersion [11], making it necessary for the transducers within the VOS cell to operate in the same frequency range as the ultrasonic flowmeter. This rules out the use of VOS-cells that operate in the audible frequency range [5], where a precision of 1 ppm has been achieved for VOS measurements in argon [12, 13].

The fundamental thickness extensional mode (TE1) is commonly employed in transducer applications of piezoelectric ceramic disks due to its favorable characteristics. The TE1 mode exhibits a vibration pattern that closely resembles plane piston vibration, thus providing a good approximation when utilizing models under this assumption [14]. The relatively low ultrasonic frequencies of USM's makes the use of thickness-extensional (TE1) mode piezoelectric transducers impractical. For instance, by using the resonance frequency spectra for the symmetric modes of a circular piezoelectric disks made out of the material PZT-5A [14], a disk with the

TE1 mode at 100 kHz would require a thickness of around 20 mm and a diameter of 200 mm, when using a diameter-to-thickness-ratio, $D/T = 10$. These dimensions are deemed too large for use in a VOS cell. As a result, the work in this thesis is focused on exploring the use of radial modes (RM) of piezoelectric ceramic disks. The resonance frequencies of radial modes are significantly lower in frequency compared to thickness extensional modes. Consequently, smaller disk dimensions can be employed in the transducers.

This master thesis is part of the research project "Subsea gas energy and quality measurement using ultrasonic flow meters" [2], where the aim is to develop a measurement method and a laboratory high-pressure VOS measurement cell for gas. The project will serve as as a scientific basis to achieve a high-precision calibration of the USM [2].

1.2 Prior work

The first widespread practical use of ultrasonic transducers dates back to the First world war. In 1917 Paul Langevin created a piezoelectric quartz transducer to detect German U-boats. The transducer remains to this day as a foundation of all modern ultrasonic techniques [15].

Throughout the years, a wide variety of models used to describe piezoelectric transducers have been developed. This includes several analytical one-dimensional models [16–18], where the transducer can be interpreted as an equivalent circuit describing the electromechanical relationships of it. One-dimensional models include among others, the Mason thickness extensional (TE) mode model [16] and the Mason-Meitzler-O'Bryan-Tiersten (MMOT) model [17], which is used to describe radial modes. Both have been found to yield a reasonable agreement with experimental results in their expected ranges of validity, (D/T » 10), for the Mason Te-mode model and, (D/T » η_n), for the MMOT model, where D/T is the diameter to thickness ratio of the disk, η_n is root No. n of Eq. (118) in [19], and n is radial mode number, n [18].

The Mason TE-mode model can describe the thickness vibration in a thin piezoceramic disk with added front and backing layers using transmission lines [20, 21]. The propagation of acoustic waves from the transducer to a fluid medium and vice versa can then be modeled using a uniformly vibrating surface, e.g., the baffled piston model [22]. However, the MMOT model used to describe radial modes in piezoelectric disks does not possess these capabilities and does not account for coupling to the medium, coupling to the thickness vibration component, or other finite disk thickness effects [18]. The one-dimensional analytical approach is generally limited to describing one-dimensional plane wave propagation in the piezoelectric transducer [23], but can be a good approximation in many instances, as for, e.g., a thin piezoelectric discs vibrating in the TE-mode, as shown in [24]. For piezoelectric disks where the conditions of the one-dimensional models can not be met, the models fail to describe the vibration of the disk [14]. Alternative, two or three dimensional models like e.g. the Finite element (FE) method or the Finite difference method can then be used [14].

The finite element method saw its first use on piezoelectric media in the late 1960's and early 1970's. Allik and Hughes [25] formulated the FE method for a three dimensional piezoelectric medium in 1970 using a principle developed by EerNisse in 1967 [26]. The FE-method was further developed to include an acoustic medium in 1973 [27]. By the introduction of the

first commercial finite element program ANSYS in 1986 the method started to see widespread use [14].

A finite element software solely dedicated to the modeling of axis-symmetric piezoelectric disks and transducers, "FEMP," was developed by Kocbach in the late 1990's [14]. FEMP is a finite element software for a numerical description of piezoelectric, mechanical, and fluid media. Finite element models where a fluid medium is included, also allow for an accurate study of the acoustic propagation from the transducer surface. Near-field effects and contributions from the side and back surfaces of the transducer can then be studied. These effects are typically not available using one-dimensional analytical models [6]. In 2006 the finite element software FEMP was extended to 3D [28]. It has been employed in numerous projects at UiB and CMR (now NORCE), specifically investigating the behavior of piezoelectric disks and transducers in the transmission and reception of ultrasound.

In 2007 Norli investigated the electrical and acoustical properties of commercial transducer, as a part of the development of a high-precision VOS measurement cell for gas [6]. However, a sufficiently precise agreement between FEMP and measurement results could not be made as the construction details, material data, and dimensions of commercial transducers are usually strictly kept secrets by the manufacturer [6].

In 2013 Øyerhamn and Mosland developed an ultrasonic transmit-receive measurement system model based on FE-modeling of a piezoelectric disk and sound propagation in the fluid medium [29, 30]. The receiver was described using spherical reciprocity [30] [29]. A good agreement between simulations and measurements was achieved for a Pz27 piezoelectric disk acting as the transmitting and receiving transducers [31]. Three transducers were also constructed and modeled using the same approach, but the same quality of agreement could not be achieved.

In 2015 Storheim [4] investigated diffraction correction of non-uniformly vibrating sources, as this was uncovered to be one of the largest sources of uncertainty in the VOS measurement works conducted by Norli in 2007 [6]. Storheim investigated the behaviour of uniformly vibrating sources, and both baffled and unbaffled piezoceramic disks using FE-software. The numerical simulation results was compared to both measurements and traditional analytical models for diffraction correction such as the baffled piston diffraction correction model [32, 33].

1.3 Objectives

The master thesis aims to design, construct, and characterize an ultrasonic piezoelectric transducer as a scientific foundation in transducer development for a future VOS measurement cell. During the construction of the piezoelectric transducers, step-by-step experimental measurements will be conducted and compared with finite element simulations. The purpose of this is to further investigate the level of accuracy finite element simulations can provide during and after the transducer construction.

Ultrasonic piezoelectric transducers are usually an essential part of any ultrasonic measurement system, and may significantly influence the precision or applicability of the system [14]. As a result, the transducer design plays a crucial role in the measurement system. In this

work, the transducers will be designed to hold a set of key transducer characteristics that are considered beneficial when measuring the speed of sound in gas [34]. The characteristics include a high voltage source sensitivity, a large frequency bandwidth, and a beam pattern with a narrow main lobe, and small side lobe levels.

Construction of piezoelectric transducers with a high voltage source sensitivity and large bandwidth in air is challenging due to an impedance mismatch between the air and the piezoelectric disk inside the transducer [35]. A large transducer bandwidth is needed to shorten the length of the transmitted pulses without distorting the signal, and a high voltage source sensitivity is desirable to increase the measurement system's signal-to-noise ratio and to reduce the required transducer driving voltage.

For a pair of transmitting and receiving transducers with a finite size, the generated sound pressure field becomes diffracted due to effects from both the transmitting and receiving transducer [32, 33]. The diffraction effects have to be corrected for and are shown to be the most significant uncertainty contributor in the measurement of the VOS [6]. Models, such as, E.g., the baffled piston diffraction correction model (BPDC) [32, 36], are commonly employed when correcting for the transducer diffraction effects. The model makes an assumption that the transmitting transducer is a baffled uniform piston, thereby generalizing the problem. Due to this, the model neglects the acoustic radiation effects originating from the non-uniformly vibrating front surface and sides of the transducer [4]. Additionally, the model does not incorporate diffraction effects arising from the receiving transducer. When using finite element modeling, the diffraction effects can be more accurately corrected for by creating a numerical model of the sound pressure field surrounding the two transducers. To utilize a finite element diffraction correction model, the accuracy of the transducer simulation is essential [4, 37–39]. Therefore, this project serves as a basis to investigate what accuracy level can be achieved by using the finite element method.

1.4 Thesis outline

The master thesis consists of 9 chapters and 2 included appendices. In **Chapter1**, the motivation and background of the project is given. A brief overview of previous work related to the subject of the thesis is given, before the objective of the work is presented. **Chapter 2** presents the theoretical foundation upon which the thesis is built. **Chapter 3** describes the simulation setup and settings used in the various finite element simulations. In addition, the material parameters and the FEMP structures used to simulate each step of the transducer construction are described. In **Chapter 4**, the experimental setup and various measurement methods used during the thesis will be presented. In addition a complete equipment list and a detailed description of the acoustical and electrical measurement setups are provided. The methods used in the post-processing of recorded measurement data will also be provided here. In **Chapter 5**, the results from an initial simulation study are presented. The simulation results presented in the three different articles [40], [41], and [42] are compared to results obtained using the numerical simulation tool "FEMP." The results are further investigated to study the applicability of similar principles in an ultrasonic gas transducer. **Chapter 6** offers a series of simulation results related to the design of the ultrasonic gas transducer. The transducer design is gradu-

ally built from a single piezoelectric element to a full transducer with a casing, backing, and matching layer. In **Chapter 7**, the construction of the final transducer design developed in Chapter 6 is described step by step. The methods used, and challenges encountered along the way are covered and discussed. **Chapter 8** presents experimental results from the electrical measurements conducted for each step in the construction process. The measured electrical results are compared to simulation results from the finite element simulation structures presented in Chapter 3. The acoustical measurement results from the completed transducers are then compared to simulations of the final transducer structure. Finally, **Chapter 9** concludes the thesis by summarizing the findings from the study. The study's contributions and possible limitations of the approaches used are discussed. During the chapter, possible directions going forward are introduced

Chapter 2

Theory

Chapter 2 presents the theoretical foundation upon which the thesis is built. In Sec. 2.1 the characteristics used in the description of the transducers electrical and acoustical properties are defined. Sec. 2.2 provides an analytical plane wave propagation model used to estimate the ideal thickness of a matching layer, in order to transfer as much acoustics energy as possible into the fluid medium. In Sec. 2.3 the system model describing the acoustical measurement setup in Chapter 4 will be provided. Sec. 2.4 presents the ANSI standard used to calculate the absorption of sound in the atmosphere. In Sec. 2.5 a short summary of the theoretical background used in the finite element software FEMP 6.1 is presented.

2.1 Transducer characteristics

Transducer characteristics are used to describe the essential capabilities of a transducer shortly and concisely. These characteristics are often highly frequency dependent and can be shown as a function of frequency or only at a specific operating frequency. The transducer characteristics will be studied when comparing simulations to the acoustical and electrical measurements in Chapter 5

2.1.1 Electric admittance

Electrical measurements can provide useful information about an ultrasonic transducer. During this work, the transducer conductance, G_T, and susceptance B_T are measured at different frequencies and later compared to simulated values of the same parameters. This comparison indicates the compliance between the simulation model and the physical transducer. Some fundamental relations between different electrical quantities and the definition of the different transducer resonant frequencies will be given here.

The transducer admittance Y_T is defined as [43]

$$Y_T = G_T + iB_T = \frac{1}{Z_T}, \tag{2.1}$$

where G_T and B_T are the transducer electrical conductance and susceptance, respectively. The transducers electrical impedance Z_T is inversely proportional to the electrical admittance Y_T [43]. During this work, the conductance, G_T, and susceptance, B_T, are the parameters of

choice when displaying electrical measurements. The conductance, G_T, will be plotted as a function of frequency, in decibels relative to a reference value G_{ref} as follows:

$$20 \log_{10} \left(\frac{G_T}{G_{ref}} \right) [\text{dB re 1 S}]. \tag{2.2}$$

The reference value, G_{ref} = 1 S. The transducer susceptance, B_T, will be plotted directly as a function of frequency without any logarithmic conversion.

Based on electrical measurements a series of different transducer "resonance frequencies" can be found. The different resonance frequencies used during this work are defined as follows[19]:

f_s Frequency of maximum conductance, G_T

f_p Frequency of maximum resistance, R_T,

where f_s is the series resonance frequency, and f_p is the parallel resonance frequency. The transducer resistance, R_T, and transducer reactance, X_T, is related to the conductance G_T and susceptance B_T, through the following relation:

$$R_T = \frac{G_T}{|Y|^2} \qquad\qquad X_T = -\frac{B_T}{|Y_T|^2}. \tag{2.3}$$

2.1.2 Voltage source sensitivity, S_V

The voltage source sensitivity of a transducer quantifies the quality of the electro-acoustic conversion. It expresses the relation between the input (voltage) and output (pressure) values of the transducer [44]. The voltage source sensitivity of a transducer can be expressed in terms of voltage as [22],

$$S_V = \frac{P(r = 1\text{m}, \theta = 0, \phi = 0)}{V_{in}}, \tag{2.4}$$

where $P(r = 1\text{m}, \theta = 0, \phi = 0)$ is the acoustic pressure amplitude on the acoustic axis in the far field, extrapolated spherically back to a distance, r = 1 m away from the center of the source front surface. V_{in} is the amplitude of the driving voltage, ϕ is the angle around the z-axis, and θ is the angle around the y-axis of the coordinate system in Fig.2.1. Amplitudes in equation 2.4 are typically expressed in RMS.

The voltage source sensitivity can also be expressed in decibels relative to a reference value, $S_{V_{ref}}$. In this work, $S_{V_{ref}}$ = 1 Pa/V at r = 1 m, giving [43]

$$20\log_{10} \left(\frac{|S_V|}{S_{V_{ref}}} \right) \left[\text{dB re } 1 \tfrac{Pa}{V}\right]. \tag{2.5}$$

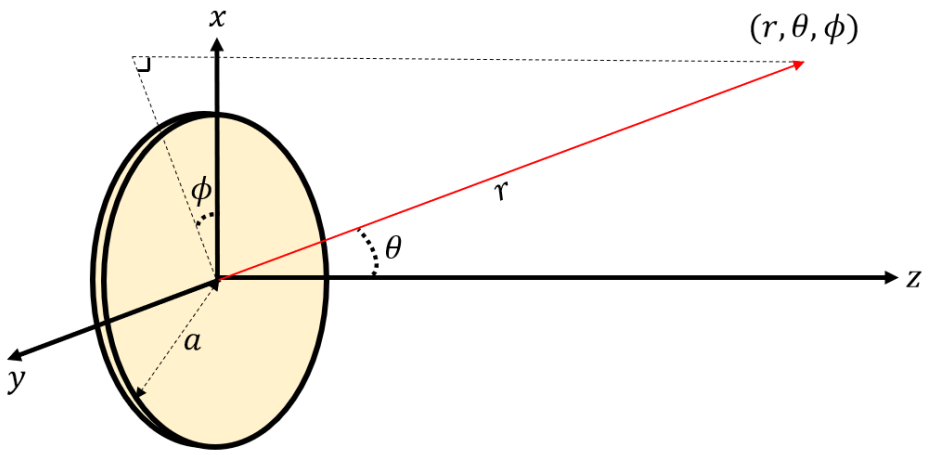

Figure 2.1: A piezoelectric disk with radius, a, in a spherical coordinate system

2.1.3 Far field distance

The far field of an ideal plane piston radiator is considered to start at a distance greater than the Rayleigh distance z_r, defined as [22]

$$z_r \equiv \frac{\pi a^2}{\lambda}, \tag{2.6}$$

where a is the radius of the transducer, and λ is the acoustic wavelength in the fluid medium. It is important that the pressure measurements performed during transducer characterization is performed at a distance $z > z_r$ to avoid interference effects associated with the near field of a piston source [22].

2.1.4 Receiver sensitivity, M_V

The free-field open-circuit receiving sensitivity, of an acoustic transducer or microphone can generally be defined as [45]

$$M_V(f) = \frac{V_{open}(f)}{P_{ff}(f)} = |M_V(f)|e^{i\phi_{M_V}}, \tag{2.7}$$

where V_{open} is the open-circuit voltage, in response to, $P_{ff}(f)$, the average acoustic pressure amplitude across the transducer face measured in the free field, i.e without the transducer present, at a given distance from a source [45]. The phase term ϕ_{M_V} is the phase difference between the open circuit voltage, V_{open} and the free field pressure, P_{ff}

2.1.5 Beam pattern

The beam pattern of a transducer,

$$D(\theta,\phi) = 20\log_{10}\left(\frac{P(r,\theta,\phi)}{P_{ax}(r)}\right), \tag{2.8}$$

expresses the angular energy response of a transducer in the far field for a given frequency as a function of angles and normalized respective to its maximum [44]. In Eq. 2.8, $P(r,\theta,\phi)$ is the acoustic pressure amplitude at a given point, (r,θ,ϕ) in the spherical coordinate system displayed in Fig.2.1. $P_{ax}(r)$ is the acoustic pressure amplitude on the acoustic axis a distance, r from the front surface of the transducer, which is usually located in the angular direction ($\theta = 0, \phi = 0$). In this work, all transducers are assumed to show an axial symmetry around the z-axis. Equation 2.8 can therefore be simplified to

$$D(\theta) = 20\log_{10}\left(\frac{P(r,\theta)}{P_{ax}(r)}\right), \tag{2.9}$$

where P_{ax} is the acoustic pressure amplitude on the acoustic axis, usually located in the angular direction ($\theta = 0$).

2.1.6 Bandwidth

A ultrasonic transducer is generally designed to operate at a particular frequency, referred to as the operating frequency, f_0. In this work the operating frequency, f_0 is defined as the frequency of maximum voltage source sensitivity magnitude, $|S_V|$. The transducers bandwidth is the frequency span that the transducer can transmit efficiently around its operating frequency [44]. The -3 dB quality factor, Q_{3dB} quantifies the relative bandwidth at the operating frequency f_0, and is defined as [44]

$$Q_{3dB} = \frac{f_0}{f_{3dB}^{+} - f_{3dB}^{-}}, \tag{2.10}$$

where f_{3dB}^{-} and f_{3dB}^{+} are the respective frequencies above and below f_0, where a 3 dB decrease in the voltage source sensitivity magnitude, $|S_V|$ is achieved.

2.2 Impedance matching layer

One or multiple matching layers can be used to increase the coupling of acoustic impedance between the piezoelectric element and transmission medium, so that the ultrasonic wave from the piezoelectric element can propagate more efficiently. Matching layers can provide better acoustic impedance matching between the piezoelectric element and the radiation medium, thus improving transducer performance in terms of both bandwidth and pulse duration time [46].

A plane wave propagation model is used to study the transmission of an acoustic wave from the piezoelectric disk through the matching layer and into the air, as shown in Fig. 2.2.

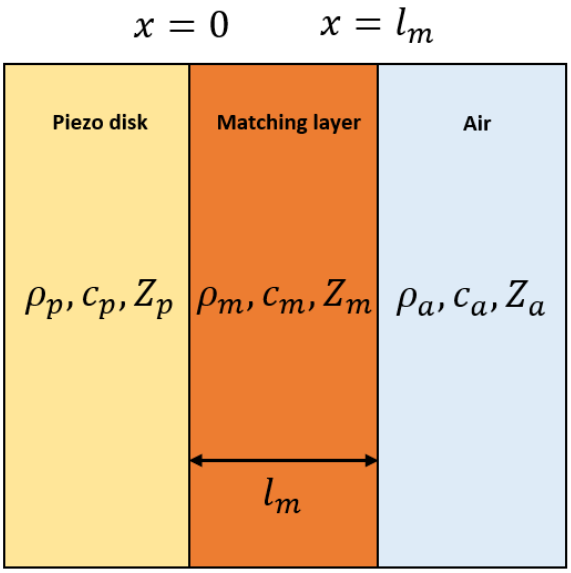

Figure 2.2: Acoustic matching layer [43]

In Fig.2.2, ρ is the material density, c is the longitudinal sound velocity, and $Z = \rho c$ is the materials characteristic acoustic impedance. The subscripts p, m, and a indicate the three materials in a layer within the figure. Specifically, these materials are a piezoelectric disk (p), a matching layer (m), and air (a). The parameter l_m is the thickness of the matching layer.

When assuming a plane wave propagating from the disk to the matching layer the specific input impedance Z_{in}, seen by the wave in the piezoelectric disk, is given by [43]

$$Z_{in} = \frac{\left(\frac{Z_a}{Z_m}\right) + i\tan(k_m l_m)}{1 + i\left(\frac{Z_a}{Z_m}\right) tan(k_m l_m)} Z_m, \tag{2.11}$$

where $k_m = \frac{2\pi f}{c_m}$ is the acoustic wave number of the matching layer. By choosing a matching layer thickness, $l_m = \frac{\lambda}{4}$, the expression in equation 2.11 can be simplified to

$$Z_{in} = \frac{Z_m^2}{Z_a}. \tag{2.12}$$

If the matching layer characteristic acoustic impedance equals the geometric mean of the air's characteristic acoustic impedance, Z_a, and the piezo disk impedance, Z_p,

$$Z_m = \sqrt{Z_p Z_a}. \tag{2.13}$$

The piezoelectric disk will then experience an characteristic acoustic impedance input impedance,

$$Z_{in} = Z_p. \tag{2.14}$$

This should lead to a total transmission of the acoustic wave from the piezo disk to the fluid medium at the quarter wavelength frequency, as the propagating wave does not experience an impedance change through the layers.

2.3 System model

In the present work, the signal propagation within the acoustic measurement system is described through the utilization of a system model. The system model and theory behind it is based on the model presented in [29, 31], and only a summary of its theory will be provided here. A full theoretical description of the model can be found in [29, 31].

The system model has previously been implemented by Øyerhamn et al. in [4, 29–31], and describes a measurement system very similar to the one employed in the current thesis. The model comprises a collection of distinct nodes and modules labeled 0-6 and A-G, respectively. The nodes and modules constitute the system, as shown in Figure 2.3. Each module represents a component of the acoustic measurement system which is described in Sec. 4.3

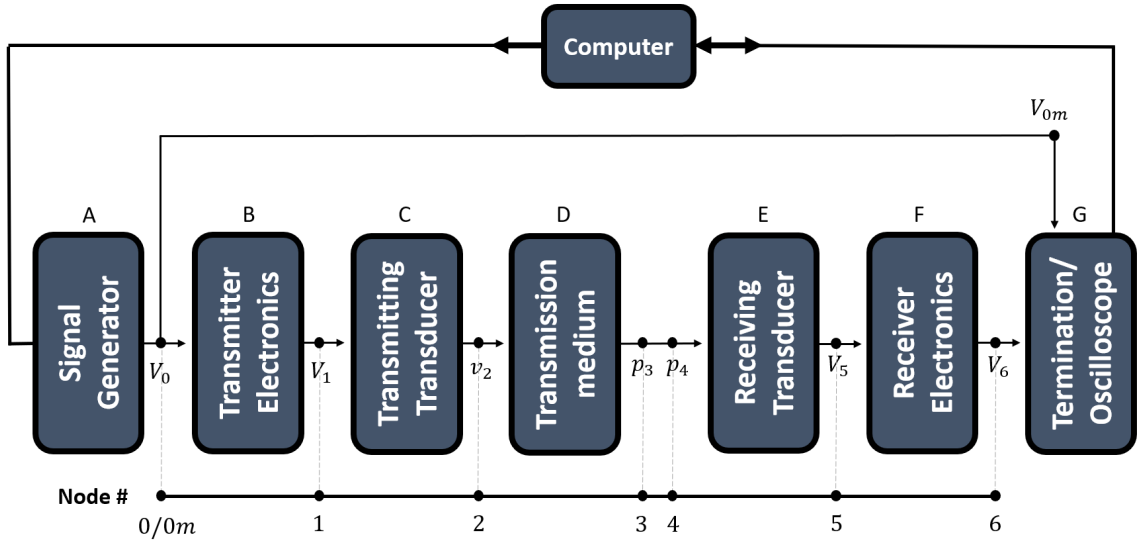

Figure 2.3: Block diagram representing the system model with modules A-G, based on Fig. 2.1 in [29]

A short description of the content in each module and the nodes in between them is given below. No time dependent variables are used in this chapter, and a time dependency of $e^{i\omega t}$ is assumed for all variables[29]. The notation showing the frequency dependence of the variables e.g ("f") has therefore been omitted [29].

Module A represents the signal generator, with the electrical voltage V_0 at node 0 as output [31]. The signal generator creates a monochromatic voltage signal with a constant amplitude and a finite number of periods, hereby referred to as a "burst."

Module B represents the transmitting electronics consisting of coaxial cable # 1, which converts the voltage in node 0, V_0, to electrical voltage, V_1, across the input terminals of the transmitting transducer in node 1 [31].

Module C represents the transmitting piezoelectric transducer. The module converts the voltage in node 1, V_1, to the particle velocity at the center of the transmitting transducers front surface, v_2 in node 2 [31].

Module D represents the fluid sound propagation medium in the system [31]. In this work, the fluid medium is air at 1 atm and 20 C° [22]. The output from module D is the axial free-field sound pressure, p_3 at a reference distance $d_0 = 1$ m from the transmitters front

surface[29]. The sound pressure p_4 in node 4 is the axial free-field sound pressure at the center of the receiving transducers front surface [29].

Module E represents the receiving transducer, converting the pressure, p_4, to the electrical voltage, V_5 over the output terminals of the receiving transducer, in node 5 [31].

Module F represents the receiving electronics, converting the voltage signal V_5 to the electrical voltage at the input terminal of the oscilloscope V_6 in node 6 [31]. The receiving electronics consists of a measurement amplifier, a frequency filter, and two coaxial cables numbered 3 and 4. Cable # 3 connects the receiving transducer to the measurement amplifier, and cable # 4 connects the amplifier/filter output to the oscilloscope [31].

Module G represents the termination of the measurement system, in this work consisting of a high impedance digital oscilloscope [31]. The oscilloscope has two input terminals, where the voltage signals V_6 and V_{0m} are recorded. V_{0m} is the voltage transferred through cable # 2 from the signal generator to the input terminals on the oscilloscope, and V_6 is the recorded voltage signal from the measurement amplifier through cable # 4. The voltage V_0 is different from the recorded voltage V_{0m} because of the difference in cable length and termination impedance of the transmitting transducer, Z_T^{Tx}, and the oscilloscope, Z_S (Cf. Sec. 2.3.2).

When calculating the system model, each system module in Fig. 2.3 is represented by a linear transfer function, relating the output value in the node after the module to the input in the node before [20]. The transfer function can be derived using an analytical model, as later shown for the transmitter and receiver electronics in Sec. 2.3.2 and 2.3.4, or as for the signal propagation from module C-E using the finite element method (FEM).

After specifying the transfer function representing the different modules in the system, a transfer function, H_{ij} from node i to j can be calculated by multiplying the transfer functions given by the modules in between [31]. An example of this is shown for the transfer function, H_{0m6}^{VV} in equation 2.15, giving the relation between the recorded output voltage from the receiver electronics, V_6 and the recorded output voltage from the signal generator, V_{0m} [29], as

$$H_{0m6}^{VV} \equiv \frac{V_6}{V_{0m}} = \frac{V_0}{V_{0m}} \cdot \frac{V_1}{V_0} \cdot \frac{v_2}{V_1} \cdot \frac{p_3}{v_2} \cdot \frac{\langle p_4 \rangle}{p_3} \cdot \frac{V_5}{\langle p_4 \rangle} \cdot \frac{V_5^{open}}{V_5} \cdot \frac{V_6}{V_5^{open}}. \tag{2.15}$$

In Eq. 2.15, $\langle p_4 \rangle$ denotes that the axial free-field sound pressure at the center of the receiving transducers front surface, p_4 is averaged across the acoustically sensitive area of the receiving transducer [29]. In this work the acoustically sensitive area of the transducer is given by the radius of the piezoelectric disk, a. V_5^{open} is the open-circuit voltage, across the receiving transducer output terminals when under open circuit conditions.

2.3.1 Cables

Coaxial cables used in the measurement setup will affect signal propagation through the system and must therefore be taken into account. An uniform transmission line model is used, and any losses related to dissipation effects in the cables are omitted. A cable of any length terminated by an impedance Z_L has a characteristic impedance[47],

$$Z_0 = \sqrt{\frac{L}{C}}, \tag{2.16}$$

where C and L are the capacitance and inductance per meter for the cable, respectively. The electromagnetic wavenumber for the signal in the cable, k_{em} is given by[31],

$$k_{em} = \omega\sqrt{LC}. \tag{2.17}$$

When the coaxial cable is terminated in an impedance, Z_L, it can be represented by the equivalent circuit shown in Fig. 2.4[43].

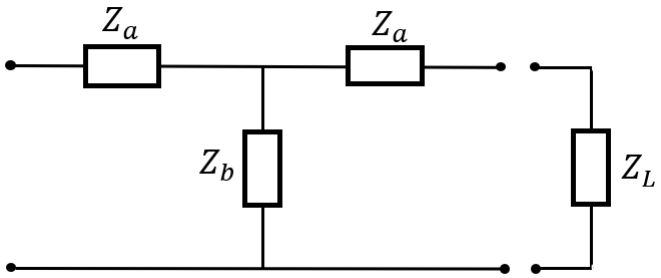

Figure 2.4: Equivalent circuit representing a coaxial cable terminated in an impedance Z_L

The two impedance's Z_a and Z_b is given by,

$$Z_a = iZ_0 tan\left(k_{em}\frac{l}{2}\right) \quad , \tag{2.18}$$

and

$$Z_b = \frac{Z_0}{i\sin(k_{em}l)}, \tag{2.19}$$

where l is the length of the cable. This gives an input impedance Z_{in} for the coaxial cable terminated in the impedance Z_L[43, 47],

$$Z_{in} = Z_0\frac{Z_L + iZ_0 tan(k_{em}l)}{Z_0 + iZ_L tan(k_{em}l)}. \tag{2.20}$$

2.3.2 Transmitter Electronics

The transmitter electronics in module B is made up by coaxial cables transferring the output signal from the signal generator, V_0, to the input signal at the transmitting transducer, V_1, and the measured input signal at the oscilloscope V_{0m} [31]. The cables can be represented by equivalent circuits as shown in Fig. 2.5 [29, 31]. The subscript numbering of the cable impedances denotes the cable number as listed in Tab. 4.2.

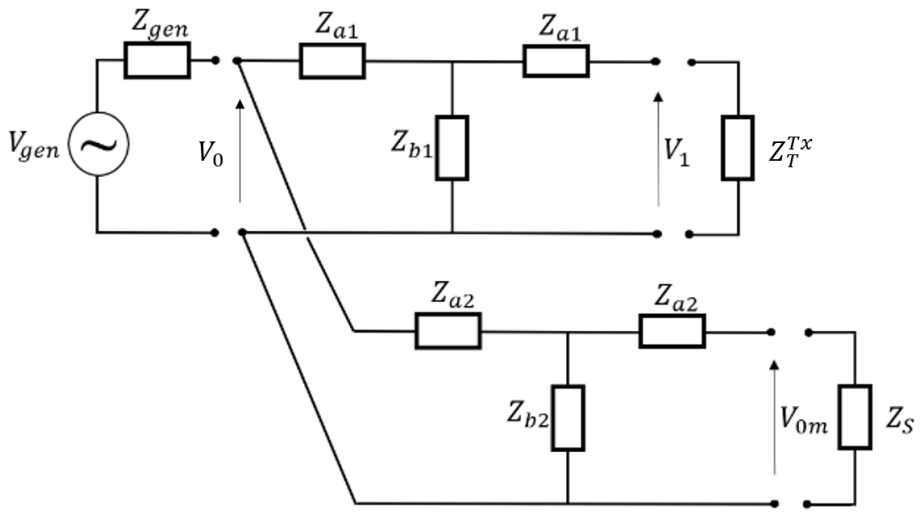

Figure 2.5: Equivalent circuit representing the signal generator and the cables connecting it to the transmitting transducer and oscilloscope. Based on Fig. 2.5 in [29]

The impedances, Z_{a1}, Z_{b1} and Z_{a2}, Z_{b2} in Fig. 2.5 is the impedances of the cables numbered 1 and 2 respectively, calculated using Eqs. 2.18 and 2.19 by inserting the length of the respective cable, l. Z_T^{Tx} is the electrical input impedance of the transmitting transducer, and Z_S is the oscilloscope input impedance, as listed in Tab. 4.3.

By applying Kirchhoff's second law to the circuit in Fig. 2.5 it can be shown that the transfer function, H_{01}^{VV}, relating the driving voltage of the transmitting transducer, V_1 to the output voltage, V_0 from the signal generator is given by [29, 31]:

$$H_{01}^{VV} \equiv \frac{V_1}{V_0} = \frac{Z_T^{Tx} Z_{b1}}{Z_{a1}^2 Z_T^{Tx} Z_{a1} + 2Z_{a1} Z_{b1} + Z_T^{Tx} Z_{b1}} \tag{2.21}$$

By using the same methods applied to derive Eq. 2.21, the transfer function H_{00m}^{VV}, which relates the recorded output voltage from the signal generator, V_{0m} to the actual output voltage from the signal generator, V_0 is given by [29, 31]:

$$H_{00m}^{VV} \equiv \frac{V_{0m}}{V_0} = \frac{Z_S Z_{b2}}{Z_{a2}^2 Z_s Z_{a2} + 2Z_{a2} Z_{b2} + Z_S Z_{b1}} \tag{2.22}$$

The transfer function H_{0m1}^{VV}, relates the driving voltage on the transmitting transducer, V_1, to the recorded output voltage from the signal generator, V_{0m}. The transfer function is obtained by combing Eqs. 2.21 and 2.22 [29, 31]:

$$H_{0m1}^{VV} \equiv \frac{V_1}{V_{0m}} = \frac{H_{01}^{VV}}{H_{00m}^{VV}} \tag{2.23}$$

2.3.3 Calculation of $H_{15}^{VV,open}$

The transfer function, $H_{15}^{VV,open}$ relates the open circuit voltage at the output terminals of the receiving transducer or microphone V_5^{open}, to the input voltage, V_1 at the input terminals of the transmitting transducer [29, 31]:

$$H_{15}^{VV,open} \equiv \frac{V_5^{open}}{V_1} = \frac{v_2}{V_1} \cdot \frac{p_3}{v_2} \cdot \frac{\langle p_4 \rangle}{p_3} \cdot \frac{V_5^{open}}{\langle p_4 \rangle}. \tag{2.24}$$

$H_{15}^{VV,open}$ represents modules (C-E) in the system model shown in Fig. 2.3. The modules contain the transmitting transducer, the sound propagation fluid medium and the receiving transducer as shown in Fig. 2.6.

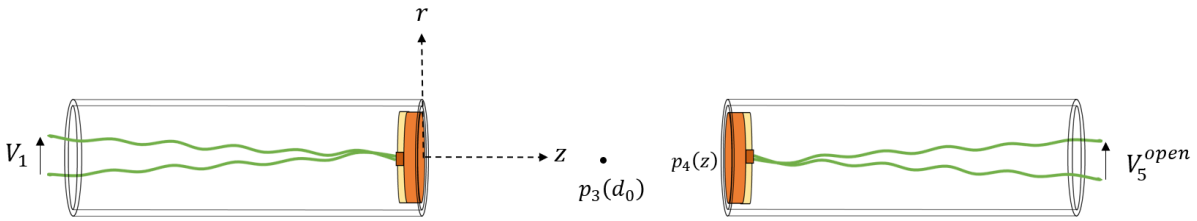

Figure 2.6: Transmitting and receiving transducers separated by a sound propagation fluid medium. The transducers and the fluid medium are represented by the transfer function $H_{15}^{VV,open}$

In Fig. 2.6, the origin of the cylindrical coordinate system is at the center of the transmitting transducers front surface. r is the radial distance, and z is the axial distance from the origin to the front surface of the receiving transducer.

In [29] two different models are introduced when calculating, $H_{15}^{VV,open}$, and model 1 will be used during this work. The model was developed in [48], and has later been applied in [4, 29–31].

In model 1 the voltage V_5^{open} is expressed using both a general sound propagation model, V_5^{open}, and a plane wave propagation model $V_{5,plane}^{open}$ which is used as a normalization for the diffraction correction, H^{dif} [29]. The baffled piston diffraction correction model (BPDC) is used here, as defined by Khimunin in [32]. The expression H_{dif} is defined as in Eq. 23 from [31]

The derived transfer function $H_{15}^{VV,open}$ from [29] is given by

$$H_{15}^{VV,open} = \frac{z_{ff}c}{i\pi a^2 f V_1} p_4(z_{ff}) M_V^{Rx} H^{dif}(z) e^{(ik(z_{ff}-z))}, \tag{2.25}$$

where c is the speed of sound in the fluid medium and $p_4(z_{ff})$ is the axial free-field sound pressure in the medium at the far field distance z_{ff}. The sound pressure $p_4(z_{ff})$ is calculated using the finite element method (Cf. Sec. 2.5) at a far field distance z_{ff}, and than extrapolated back to the distance d_0 under the assumption that the waves are spherical in the far-field. The open-circuit free-field receiving voltage sensitivity of the receiving transducer, M_V^{Rx} is calculated by the use of spherical wave reciprocity as presented in [29, 31].

Eq. 2.25 does not account for a lossy fluid medium, as is the case for the experimental setup described in Sec. 4.3. The absorption in air is therefore included in the model by defining a

complex wavenumber κ [29], defined as,

$$\kappa \equiv k - i\alpha, \tag{2.26}$$

where α is the absorption coefficient in air. The absorption coefficient in air is calculated using the MATLAB script **absorpsjonluft.m** listed in appendix B.3, which is based on the standard presented in [10]. The standard will be summarized in Sec. 2.4. When the absorption in air is taken into account Eq. 2.25 can be expressed as [29]:

$$H_{15,\alpha}^{VV,open} = \frac{z_{ff}c}{i\pi a^2 f V_1} p_4(z_{ff}) M_V H^{dif}(z) e^{(ik(z_{ff}-z))} \cdot e^{-\alpha z}, \tag{2.27}$$

The lossy transfer function in Eq. 2.27 can then be inserted into Eq. 2.15 giving $H_{0m6,\alpha}^{VV}$ with a lossy fluid medium in module D [29].

$$H_{0m6,\alpha}^{VV} \equiv \frac{V_6}{V_{0m}} = \frac{V_0}{V_{0m}} \cdot \frac{V_1}{V_0} \cdot H_{15,\alpha}^{VV,open} \cdot \frac{V_5'}{V_5^{open}} \cdot \frac{V_6}{V_5'} \tag{2.28}$$

2.3.4 Receiver Electronics

In the present work two types of receivers are used in Module E. This includes the developed transducers constructed during the work, and a Type 4138 pressure condenser microphone from Brüel & Kjær [49]. The microphone is connected to a measurement amplifier using a preamplifier and proprietary cables supplied by the manufacturer. The characterization of this receiver system has not been prioritized during this work. Therefore, when utilizing the microphone as a receiver, the receiver electronics have not been compensated for, and it is assumed that V_5^{open} is equal to the recorded electrical voltage at input terminal on the oscilloscope V_6. The 60 dB amplification from the measurement amplifier is subtracted from the measurements during the signal processing (cf. Sec. 4.6)

When the traducers are used as both transmitter and receiver the transfer function of the receiving electronics $H_{5open6}^{VV} = V_6/V_5^{open}$ relates the voltage, V_6, to the open-circuit voltage, V_5^{open}, across the transducer output terminals under open circuit conditions. H_{5open6}^{VV} is calculated in two steps by expressing it as [29]:

$$H_{5open6}^{VV} \equiv \frac{V_6}{V_5^{open}} = \frac{V_5'}{V_{5^{open}}} \cdot \frac{V_6}{V_5'}, \tag{2.29}$$

where V_5' is defined as the voltage over both the input and output terminals of the amplifier [29]. The receiving transducer is connected to the signal amplifier through coaxial cable # 3, as represented by the equivalent circuit in Fig. 2.7.

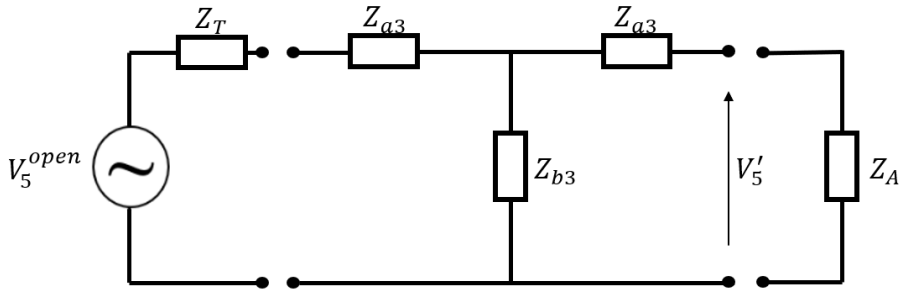

Figure 2.7: Equivalent circuit representing the receiving transducer terminated in the measurement amplifier through coaxial cable # 3. Based on Fig. 2.9 in [29]

V_5^{open} in Fig. 2.7 is the open-circuit output voltage from the receiving transducer and Z_T^{Rx} is the output impedance of the receiving transducer [29]. Z_A is the input impedance of the amplifier, as listed in Tab. 4.3, and the impedances Z_{a3} and Z_{b3} is calculated by inserting the length of cable # 3, l_3 from Tab. 4.2 into Eqs. 2.18 and 2.19 respectively.

By applying Kirchhoffs second law to the equivalent circuit in Fig. 2.7 it can be shown that the transfer function relating V_5^{open} to V_5' is given by [29, 31]:

$$H_{5open5'}^{VV} \equiv \frac{V_5'}{V_5^{open}} = \frac{Z_A Z_{b3}}{Z_T^{Rx} Z_{b3} + Z_T^{Rx} Z_A + Z_T^{Rx} Z_{a3} + Z_A Z_{a3} + Z_{a3}^2 + 2Z_{a3} Z_{b3} + Z_A Z_{b3}} \tag{2.30}$$

In the system model the measurement amplifier is connected directly to the oscilloscope through cable # 4 as represented by the equivalent circuit in Fig. 2.8. Modeling of the frequency filter in the measurement setup is not included, and the filter is assumed to not affect the magnitude of the signal at the measured frequency [29].

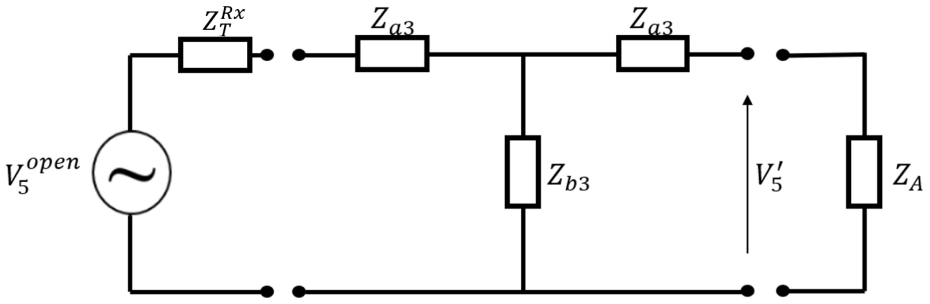

Figure 2.8: Equivalent circuit representing the measurement amplifier terminated in the oscilloscope through coaxial cable # 4. Based on Fig. 2.10 in [29]

In Fig. 2.8, $Z_{A,out}$ is the output impedance of the measurement amplifier, as listed in Tab. 4.3. By applying Kirchhoffs second law to the equivalent circuit in Fig. 2.8 it can be shown that the transfer function, $H_{5'6}^{VV}$, relating the voltage recorded by the oscilloscope, V_6 to the output voltage from the measurement amplifier V_5' is given by [29]:

$$H_{5'6}^{VV} \equiv \frac{V_6}{V_5'} = \frac{Z_{A,out} Z_{b4}}{Z_{A,out} Z_{b4} + Z_{A,out} Z_S + Z_{A,out} Z_{a4} + Z_S Z_{a4} + Z_{a4}^2 + 2Z_{a4} Z_{b4} + Z_S Z_{b4}}. \tag{2.31}$$

By inserting Eqs. 2.30 and 2.31 into Eq. 2.29, the transfer function relating the voltage recorded by the oscilloscope, V_6 to open circuit voltage on the receiver, V_5^{open} can be expressed as [29]:

$$H_{5open6}^{VV} \equiv \frac{V_6}{V_5^{open}} = \frac{V_5'}{V_{5^{open}}} \cdot \frac{V_6}{V_5'} = H_{5open5'}^{VV} \cdot H_{5'6}^{VV}. \tag{2.32}$$

The transfer function, H_{0m1}^{VV} from Eq. 2.23 and the transfer function, H_{5open6}^{VV} is then inserted into Eq. 2.28, giving the transfer function $H_{0m6,\alpha}^{VV}$, which relates the recorded output voltage from the receiver electronics, V_6 to the recorded output voltage from the signal generator, V_{0m} [29]:

$$H_{0m6,\alpha}^{VV} = H_{0m1}^{VV} \cdot H_{15,\alpha}^{VV,open} \cdot H_{5open6}^{VV}. \tag{2.33}$$

In Chapter 8 the transfer function $H_{0m6,\alpha}^{VV}$ will be used when comparing the simulated results to measurements conducted using the experimental setup, as presented in Sec. 4.3 .

2.4 Attenuation of sound in Air

When sound waves propagate through air, the amplitude of the sound wave decreases as some of the energy carried by the wave is converted into random thermal energy[22]. There are four mechanisms that cause sound energy to be absorbed and sound waves to be attenuated as they propagate in a homogeneous fluid [50]. The four effects include Viscous (shear) effects, Thermal conduction, molecular absorption, and thermoviscous boundary layer losses [50]. The latter effect will not be included in the absorption model used during this work as boundary effects from, e.g., walls and laboratory equipment, are neglected in the simulation models.

The Finite element simulations performed in this work consider a lossless fluid medium. The decrease in pressure amplitude of the propagating wave caused by attenuation must therefore be added to the simulation results before comparisons with experimental results can be made.

By solving the lossy wave equation, with respect to the acoustic sound pressure, p, a plane wave traveling in the z-direction as a function of time, t, can be described by [22].

$$p(z,t) = Ae^{i(\omega t - kz)}e^{-\alpha_{Np/m} \cdot z} \tag{2.34}$$

where A is a complex constant decided by the initial and boundary conditions of the wave, ω is the angular frequency of the wave, k is the acoustic wave number in air, and $\alpha_{Np/m}$ is the absorption coefficient in air neper per meter. The atmospheric absorption coefficient is commonly referred to in dB per meter, with the following relationship between them:

$$\alpha_{dB/m} = 20\log_{10}(e) \cdot \alpha_{Np/m} \approx 8.686 \cdot \alpha_{Np/m}. \tag{2.35}$$

An absorption model based on ANSI standard S1.26-2014 [10], will be used when absorption losses are taken into account. A summary of the necessary formulas used to calculate the atmospheric absorption coefficient $\alpha_{Np/m}$ by the ANSI standard will be given here.

The atmospheric absorption coefficient $\alpha_{Np/m}$ is calculated from [10]

$$\begin{aligned}\alpha_{Np/m} = f^2\Bigg(\left[1.84\times10^{-11}\left(\frac{p_r}{p_a}\right)\left(\frac{T}{T_r}\right)^{\frac{1}{2}}\right]+\left(\frac{T_r}{T}\right)^{\frac{5}{2}}\\ \times\left\{0.01275\left[e^{\left(\frac{-2239.1}{T}\right)}\right]\left[\frac{f_{rO}}{f_{rO}^2+f^2}\right]+0.1068\left[e^{\left(\frac{-3352.0}{T}\right)}\right]\left[\frac{f_{rN}}{f_{rN}^2+f^2}\right]\right\}\Bigg)\end{aligned} \tag{2.36}$$

where f is the frequency of the sound, T is the measured ambient temperature in kelvins, p_a is the measured ambient pressure in kPa. The value p_r = 101.325 kPa, is a reference pressure value, and the reference temperature value T_r = 293.15 K. The values, f_{rO} and f_{rN}, are the relaxation frequency of oxygen and nitrogen, respectively. The relaxation frequency of oxygen is calculated using [10]

$$f_{rO} = \frac{p_a}{p_r}\left\{24+\left[\frac{(4.04\times10^4 h)(0.02+h)}{0.391+h}\right]\right\}, \tag{2.37}$$

where, h is the molar concentration of water vapor in percent that can be calculated from the measured relative humidity, h_{rel}, using [10]

$$h = h_{rel}\left(\frac{p_{sat}}{p_r}\right)\left(\frac{p_r}{p_a}\right). \tag{2.38}$$

p_{sat} is the saturated pressure which is calculated by the formula [10]

$$p_{sat} = p_r 10^V. \tag{2.39}$$

with the exponent V given by [10],

$$\begin{aligned}V = 10.79586\left(1-\frac{T_0}{T}\right)-5.02808\log_{10}\left(\frac{T}{T_0}\right)\\ +1.50474\times10^{-4}\left(1-10^{-8.29692\left(\frac{T}{T_0}-1\right)}\right)\\ +0.42873\times10^{-3}\left(10^{\left(4.76955\left(1-\frac{T_0}{T}\right)\right)}-1\right)-2.2195983,\end{aligned} \tag{2.40}$$

where T_0 is the triple-point isotherm temperature of 273.16 K [10]. The relaxation frequency of nitrogen is calculated using [10]

$$f_{rN} = \frac{p_a}{p_r}\left(\frac{T_r}{T}\right)^{\frac{1}{2}}\left(9+280h\cdot e^{-4.170\left(\left(\frac{T_r}{T}\right)^{\frac{1}{3}}-1\right)}\right). \tag{2.41}$$

The accuracy of the attenuation coefficients is estimated to be ±10% for the frequency area 50-300 kHz, with temperatures between -20 °C and 50 °C with a atmospheric pressure less than 200 kPa [10].

2.5 The Finite Element method

Describing a transducer construction or piezoelectric disk radiating in a vacuum or fluid medium is a complex physical problem. In a FE process, the region of analysis, i.e., the transducer and fluid medium, is approximated by a finite number of smaller volumes [14]. These volumes are the elements in the FE method [14]. Within each element, specific points referred to as nodes are defined. These nodes serve as locations where the unknown quantities, namely mechanical displacement and electrical potential are determined [14]. In this work, a numerical simulation tool, "Finite Element Modeling of Piezoelectric structures 6.1" (FEMP 6.1), will be used [14]. The tool can simulate the transducer characteristics (cf. sect 2.1) by solving the equations governing the problem numerically [23].

A short summary of the theoretical foundation used in FEMP will be given here. A complete description of the theoretical background can be found in [14], including the formulation for a disc vibrating in a fluid medium. During the summary, Einsteins summation convention subscripts is used. The convention is that any lower-case alphabetic subscript that appears exactly twice in any term of an expression is understood to be summed over all the values that a subscript in that position can take [51].
For computational reasons, the finite element simulations in FEMP are simplified by assuming axial symmetry around the z-axis of the simulated structure[14]. The assumption implies

$$\frac{\partial}{\partial \theta} = 0, \tag{2.42}$$

where θ is the angle around the Z-axis in Fig. 2.9.

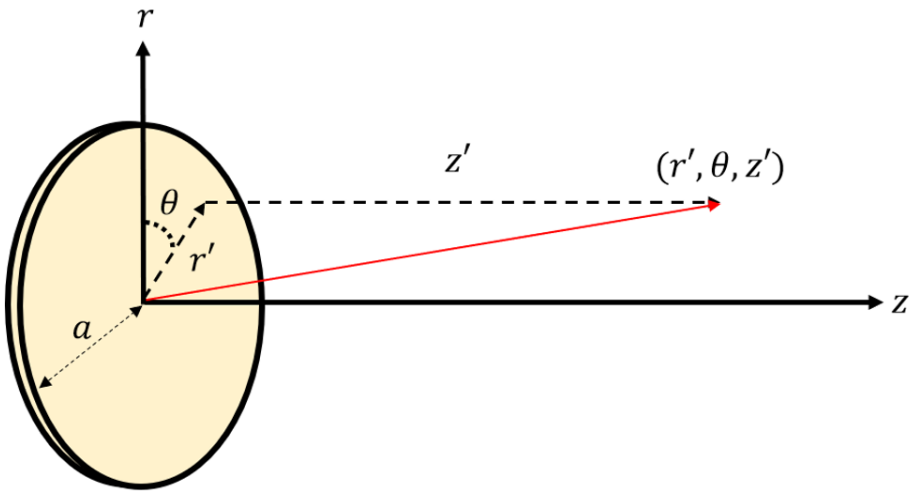

Figure 2.9: A piezoelectric disk in the cylindrical coordinate system

The equations of motion for a piezoelectric body are given by [19].

$$\rho_p \ddot{u}_i = T_{ij,j}, \tag{2.43}$$

where ρ_p is the density of the piezoelectric material, $\ddot{u}_i$ is the particle acceleration vector, and T_{ij} is the stress tensor.

By assuming a harmonic state with angular frequency ω on the form $e^{i\omega t}$, equation 2.43 can be rewritten as,

$$-\omega^2 \rho_p u_i = T_{ij,j}, \tag{2.44}$$

where u_i is the particle displacement vector. The electric displacement vector D_i in the piezoelectric material satisfies the electrostatic equation of an insulator [19], which implies:

$$D_{i,i} = 0. \tag{2.45}$$

The constitutive relations for a piezoelectric media give the coupling between the system's mechanical and electrical parts [14]. They are given by [19],

$$T_{ij} = c^E_{ijkl} S_{kl} - e_{kij} E_k, \tag{2.46}$$

and

$$D_i = e_{ikl} S_{kl} + \varepsilon^S_{ik} E_k, \tag{2.47}$$

where a description of the variables used in Eq. 2.46 and 2.47 are given in Tab. 2.1.

Table 2.1: Definition of the different variables used in Eq. 2.46 and 2.47[14].

Variable	Description[14]	Unit
T_{ij}	The mechanical stress tensor	[N/m]
S_{kl}	The mechanical strain tensor	
D_i	The electric displacement vector	[C/m^2]
E_k	The electric field vector	[V/m]
c^E_{ijkl}	The elastic stiffness constant tensor evaluated at constant electric field	[N/m^2]
e_{ikl}	The piezoelectric constant tensor	[C/m^2]
ε^S_{ik}	The dielectric constant tensor evaluated at constant strain	[F/m]

Eq. 2.44-2.47 are the equations governing the problem, when a time harmonic solution is sought along with the appropriate boundary conditions[14]. The boundary conditions for the particle displacement, u_i, surface traction, t_i, electric potential, ϕ, and charge density σ, are given on the surface of the piezoelectric body, Γ_p [14].

After imposing the boundary conditions, Eq. 2.44-2.47 are used to set up a weak formulation of the problem[14]. The weak formulation of a boundary-value problem with added boundary conditions, can be derived by multiplying the governing differential equations of the problem with appropriate weight functions and integrating over the solution domain [52]., i.e., the volume of the piezoelectric body, Ω_p. This leads to the weak formulations

$$-\omega^2 \int_{\Omega_p} \rho_p v_i u_i d\Omega = \int_{\Omega_p} v_i T_{ij,j} d\Omega, \tag{2.48}$$

and

$$\int_{\Omega_p} w D_{i,i} d\Omega = 0, \tag{2.49}$$

where v_i is a weight function corresponding to the displacement vector and w, is a weight function corresponding to the electric potential [14]. By using Green's formula, test functions,

and the specified boundary conditions from [14], each part of the weak formulation can be solved by splitting the volume, Ω_p into a sum of, M_p smaller volumes, $\Omega_p^{(m)}$, $m = 1...M_P$, and solving the integral for each volume using a Gauss Legendre quadrature [14]. The solved FE formulation for an unloaded piezoelectric disk is given as follows [14]:

$$-\omega^2 \begin{bmatrix} M_{uu} & 0 \\ 0 & 0 \end{bmatrix} \begin{Bmatrix} \hat{u} \\ \hat{\phi} \end{Bmatrix} + \begin{bmatrix} K_{uu} & K_{u\phi} \\ K_{\phi u} & K_{\phi\phi} \end{bmatrix} \begin{Bmatrix} \hat{u} \\ \hat{\phi} \end{Bmatrix} = \begin{Bmatrix} F \\ -Q \end{Bmatrix} \tag{2.50}$$

Where the variables in Eq 2.50 are defined in Tab. 2.2.

In order to make the calculation of resonance frequencies and response functions for the transducer structure easier, the FE equations are transformed to H-form, where the potential in the nodes of the elements are condensed out of the FE equations, and instead, the voltage V and the current $I = \frac{\partial Q}{\partial t} = i\omega Q$ is introduced [14].

$$-\omega^2 \begin{bmatrix} M_{uu} & 0 \\ 0 & 0 \end{bmatrix} \begin{Bmatrix} \hat{u} \\ V \end{Bmatrix} + \begin{bmatrix} H_{uu} & H_{u\phi} \\ H_{\phi u} & H_{\phi\phi} \end{bmatrix} \begin{Bmatrix} \hat{u} \\ V \end{Bmatrix} = \begin{Bmatrix} F \\ -I/(i\omega) \end{Bmatrix} \tag{2.51}$$

When the direct method is applied to calculate the response functions of a piezoelectric transducer, which is the case throughout this work, the solution is calculated directly from the FE equations using matrix manipulation[14].

When considering the case of a structure vibrating without any fluid loading i.e. there are no forces acting on the surface of the piezoelectric medium (F=0), Eq. 2.51 can be rewritten as [14]

$$\left[D\right] \left\{\hat{u}\right\} = -\left\{H_{u\phi}\right\} V, \tag{2.52}$$

where $[D] = [H_{uu}] - \omega^2 [M_{uu}]$. The expression for the mechanical harmonic response of the structure when excited by a harmonically varying voltage with frequency ω is then [14].

$$\left\{\hat{u}\right\} = -\left[D\right]^{-1} \left\{H_{u\phi}\right\} V \tag{2.53}$$

Inserting the expression for the displacement, $\hat{u}$ given in Eq. 2.53 into the second part of Eq. 2.51, results in the following expression for the electrical input admittance [14]:

$$Y_T = i\omega \left[\left\{H_{u\phi}\right\}^T [D]^{-1} \left\{H_{u\phi}\right\} - H_{\phi\phi} \right] \tag{2.54}$$

Table 2.2: Definition of the variable used in Eq. 2.50

Variable	Description[14]
$[M_{uu}]$	Global mass matrix
$[K_{uu}]$	Global stiffness matrix
$[K_{u\phi}]$	Global piezoelectric stiffness matrix
$[K_{\phi u}]$	Global piezoelectric stiffness matrix
$[K_{\phi\phi}]$	Global dielectric stiffness matrix
$\{Q\}$	Global charge vector
$\{\hat{u}\}$	Global displacemet vector
$\{\hat{\phi}\}$	Global charge vector
ω	Angular frequency

For the unloaded case that is presented here, the only simulated volume is that of the piezoelectric structure, Ω_p. When simulating a structure vibrating in a fluid medium the fluid region, Ω^f, is also considered. The theory related to this can be found in [14], and will not be provided here.

Chapter 3

Finite element simulation setup

In this chapter, a description of the different setups and settings used for the finite element simulations are provided. Sec. 3.1 gives a brief description of the finite element software FEMP 6.1, and the files necessary to run a simulation. In Sec. 3.2, the simulation parameters used in this work and values associated with them is presented. The material parameters used for the modeling of different materials in the work are given in Sec. 3.3. The various FEMP simulation structures used during the study are described in Sec. 3.4. In Sec. 3.5, challenges related to the build up (meshing) of the elements in the fluid volume of the simulation are discussed. A proposed solution to these challenges is presented along with the methods employed in their implementation.

3.1 FEMP 6.1

The Finite element tool FEMP plays a vital role in a vast majority of the work presented in this work. The program is used when performing the initial simulation study in Chapter 5, during the transducer design process in Chapter 6, and for comparison between simulated and measured results, during and after construction of the piezoelectric transducers in Chapter 7 and 8.

All FE modeling in this work is performed using version 6.1 of the simulation tool "Finite element modeling of piezoelectric transducers," FEMP 6.1. The tool is written in MATLAB and was developed by Kocbach et al. [14, 53] in a cooperation between the University of Bergen and Christian Michelsen Research (CMR).

The FEMP simulations performed during this work are built up by four separate files. An input file, a material file, a project file, and a constant_init file [4, 54]. The simulation input file contains the input parameters for each simulation, as specified by the user. This includes the frequencies of the simulation, elements per wavelength, N_λ, structure dimensions, material choices, etc. In addition, which output parameters to store from the solved finite element problem are specified here. The material file stores all material constants for the different materials used in a simulation; (Cf. Sect 3.3.)

The geometry of the transducer structure, fluid regions, and the boundary conditions are specified in the project file. A set of pre-defined structures are included in FEMP 6.1. Some of the simulations are performed using these structures, while other structures have been manually constructed by the author. The essential simulation structures will be covered in Sec. 3.4, and the project files can be found in appendix A.

3.2 Simulation parameters

A FEMP simulation requires a set of input parameters that are specified by the user in the input file. These parameters include the size of each transducer component and the number of elements per shear wavelength, N_λ used in the radial and axial directions of the transducer. When simulating a fluid medium, the longitudinal wavelength is used to calculate N_λ. The dimensions used in the various finite element simulations performed during and after the transducer construction process can be found in Chapter 7. The dimensions used for the simulations in the initial simulation study and the transducer design process can be found along with the results in their respective chapters 5 and 6.

The accuracy of the simulations are dependant upon several factors. The factors include the number of elements per wavelength, N_λ, the order of the finite and infinite elements, and the radial distance, R_{inf} between the origin of the mesh and the interface separating the finite and infinite fluid elements [14]. For the second-order finite elements that have been used during this work, each element has a total 8 nodes. The order of the infinite fluid elements is 12.

The distance R_{inf} is based on the critical distance, where the simulation error is at it's minimum as estimated by Kocbach in [14]. When using 12th order infinite elements the distance R_{inf} used in the simulations is calculated by [14]

$$R_{inf} = 0.25a^2/\lambda, \tag{3.1}$$

where a is the radius of the piezoelectric disk and λ is the longitudinal wavelength in the fluid medium at the highest frequency of the simulation. The formula in equation 3.1 is based on a plane piston radiator, which is not the case for any of the structures modeled during this work. The effects this has on the simulation accuracy have not been investigated further and might be a source of inaccuracy. An increase of the distance, R_{inf}, larger than what is calculated by using Eq. 3.1, can lead to a small decrease in the simulation accuracy [14]. However, the error is small compared to using a value smaller than what is calculated using Eq. 3.1 [14]. As a result of this, the distance R_{inf}= 0.025 m when simulating structures with nominal disk dimensions (20mm x 2 mm). By using Eq. 3.1, the distance R_{inf} = 0.0219 m, i.e a slightly larger value of R_{inf} is used during the simulations, to ensure that R_{inf} is not to small. In simulations with other disk dimensions, the distance R_{inf} will be provided with the relevant results. This is also the case when simulating the constructed transducers as the length of the transducer exceeds that of R_{inf} calculated by using Eq. 3.1

3.3 Material parameters

FEMP categorizes materials into three different groups. Piezoelectric materials, isotropic (non-piezoelectric) materials, and fluids. Piezoelectric materials are described using the stiffness matrix at a constant electric field [14],

$$[c^E] = \begin{bmatrix} c_{11}^E & c_{12}^E & c_{13}^E & 0 & 0 & 0 \\ c_{12}^E & c_{11}^E & c_{13}^E & 0 & 0 & 0 \\ c_{13}^E & c_{13}^E & c_{33}^E & 0 & 0 & 0 \\ 0 & 0 & 0 & c_{44}^E & 0 & 0 \\ 0 & 0 & 0 & 0 & c_{44}^E & 0 \\ 0 & 0 & 0 & 0 & 0 & \frac{1}{2}(c_{11}^E - c_{12}^E) \end{bmatrix}, \tag{3.2}$$

the dielectric constant matrix at constant strain [14],

$$[\varepsilon^S] = \begin{bmatrix} \varepsilon_{11}^S & 0 & 0 \\ 0 & \varepsilon_{11}^S & 0 \\ 0 & 0 & \varepsilon_{33}^S \end{bmatrix}, \tag{3.3}$$

and the piezoelectric constant matrix [14]

$$[e] = \begin{bmatrix} 0 & 0 & 0 & 0 & e_{15} & 0 \\ 0 & 0 & 0 & e_{15} & 0 & 0 \\ e_{31} & e_{31} & e_{33} & 0 & 0 & 0 \end{bmatrix}. \tag{3.4}$$

Losses in the piezoelectric materials are included using complex material constants [14]. This can be done either by providing a full anisotropic and frequency-dependent set of Q-factors for all of the elastic, piezoelectric, and dielectric constants, or by using a simplified approach where only a single mechanical quality factor Q_m is provided for the stiffness constant and a dielectric loss tangent δ_ε is given for the dielectric constants [14].

The Q-factors introduces an imaginary part to the elastic stiffness constants at constant electric field c_{pq}^E, the piezoelectric constants e_{ip}, and the dielectric constants at constant strain ε_{ij}^S [14]. This results in

$$\mathbf{c_{pq}^E} = c_{pq}^E(1 + i\frac{1}{Q^{c_{pq}^E}}) \tag{3.5}$$

$$\mathbf{e_{ip}} = e_{ip}(1 - i\frac{1}{Q^{e_{ip}}}) \tag{3.6}$$

$$\boldsymbol{\varepsilon_{ij}^S} = \varepsilon_{ij}^S(1 - i\frac{1}{Q^{\varepsilon_{ij}^S}}) \tag{3.7}$$

where i,j take the values 1,2,3 and p,q take the values 1, 2, 3, 4, 5, 6 [14]. The bold font denotes that the value is a complex quantity, and $Q^{c_{pq}^E}$, $Q^{e_{ip}}$ $Q^{\varepsilon_{ij}^S}$ are Q-factors for the stiffness constants, the piezoelectric constants, and the dielectric constants respectively [14].

When using the simplified approach, the mechanical Q-factor, Q_m is used as a replacement for $Q^{c_{pq}^E}$ for all p and q. The inverse of the dielectric dissipation factor $1/\tan(\delta_e^T)$ is used instead of $Q^{\varepsilon_{ij}^S}$ for all i and j [14].

In order to describe an isotropic material with no piezoelectric properties, the density, ρ, the mechanical quality factor, Q_m, the speed of sound for longitudinal waves, c_l and the speed of sound for shear waves, c_s must be given. Based on these values the software calculates the stiffness matrix for the respective material. The mechanical losses are modeled using the simplified approach. Fluids are described by providing the density, ρ and the fluid sound velocity c_l [14]. No losses have been modeled in any of the fluid materials. The effects from attenuation in air is added to the system model simulations and the simulated voltage source sensitivity, S_V, as described in Sec. 2.3.

3.3.1 Piezoelectric ceramics

The piezoelectric material Pz 27 delivered by Ferroperm [55] is the primary piezoelectric material used during this work. There will also be simulations performed using the piezoelectric material PZT-5A as described in [40, 41].

The material parameter accuracy in a finite-element simulation is essential for a match between simulation and experimental results. The material parameters provided by Ferroperm for the Pz 27 material have an uncertainty of $\pm 10\%$ for the dielectric constants, $\pm 5\%$ for the piezoelectric constants, and $\pm 2.5\%$ for the stiffness constants [55].

The material parameters provided by Ferroperm covers piezoelectric elements with a range of different sizes and geometries. They are also set to cover the differences in multiple batches of ceramics, spanning several years of production. Among others these two factors increases the tolerances required when specifying the material data in the Pz27 data sheet. Previous work conducted at UiB by master students Lohne [56] and Knappskog [57] aimed to estimate an adjusted set of material parameters for Pz27 disks that would improve the correspondence between measurements and simulations [57]. The adjusted material parameters for Pz27 will be used during this work, as shown in Tab. 3.1.

Table 3.1: Material data for the Pz27 piezoelectric material.

Parameter	Supplier data [55]	Adjusted data set [57]	Unit
c_{11}^E	14.7	$11.875(1 + i\frac{1}{95.75})$	$[10^{10}$ N/m$^2]$
c_{12}^E	10.5	$7.430(1 + i\frac{1}{71.24})$	$[10^{10}$ N/m$^2]$
c_{13}^E	9.37	$7.425(1 + i\frac{1}{120.19})$	$[10^{10}$ N/m$^2]$
c_{33}^E	11.3	$11.205(1 + i\frac{1}{177.99})$	$[10^{10}$ N/m$^2]$
c_{44}^E	2.3	$2.110(1 + i\frac{1}{75})$	$[10^{10}$ N/m$^2]$
e_{31}	-3.09	$-5.4(1 - i\frac{1}{166})$	[C/m^2]
e_{33}	16.0	$16.0389(1 - i\frac{1}{323.177})$	[C/m^2]
e_{15}	11.64	$11.20(1 - i\frac{1}{200})$	[C/m^2]
ε_{11}^S	10.005	$8.1104(1 - i\frac{1}{50})$	$[10^{-9}$ F/m]
ε_{33}^S	8.0927	$8.14585(1 - i\frac{1}{86.26})$	$[10^{-9}$ F/m]
ρ	7700	7700	[kg/m^3]
Q_m	74	-	
$tan\delta_\varepsilon$	0.017	-	

Tab. 3.2 contains the material parameters for the PZT-5A piezoelectric material presented in [42]. The material parameters in Tab. 3.2 are only used to compare simulation results in FEMP to simulated results presented in [40–42].

Table 3.2: Material data for the PZT-5A piezoelectric material.

Parameter	Supplier data [42]	Unit
c_{11}^E	12.03	[10^{10} N/m^2]
c_{12}^E	7.517	[10^{10} N/m^2]
c_{13}^E	7.509	[10^{10} N/m^2]
c_{33}^E	11.086	[10^{10} N/m^2]
c_{44}^E	2.105	[10^{10} N/m^2]
e_{31}	-5.35	[C/m^2]
e_{33}	15.78	[C/m^2]
e_{15}	12.947	[C/m^2]
ε_{11}^S	8.1370	[10^{-9} F/m]
ε_{33}^S	7.318	[10^{-9} F/m]
ρ	7750	[kg/m^3]
Q_m	75	-
$tan\delta_\varepsilon$	0.02	-

3.3.2 Matching layer

The material Aplex R3 [58] by Precision Acoustics is used as a matching layer. Aplex R3 is a non-conductive synthetic foam with a low specific gravity, and high hydrostatic compressive strength [58]. The material is supplied in sheet form and can then be machined into detailed components [58]; as shown in Fig. 3.1.

Figure 3.1: Aplex R3 matching layer with nominal dimensions 20.14 mm × 4.9 mm

The manufacturer has provided a set of material data that has been adjusted by the former UoB master students Hauge and Mosland [29, 30]. In [29, 30] the adjusted data set shows an improved agreement between simulation and experimental results. Therefore the adjusted data set is used in all simulations where the matching layer is included. The material data supplied by the manufacturer [58] and the adjusted data from [29, 30] are shown i Tab. 3.3

Table 3.3: Material data for Aplex R3 matching layer

Parameter	Supplier data [58]	Adjusted data [29, 30]	Unit
c_l	2034	2100	[m/s]
c_s	909.6	1008.8	[m/s]
ρ	570	598	[kg/m^3]
Q_m	55	40	

3.3.3 Steel

The material parameters used to model steel are shown in Tab. 3.4. The steel material is used in Chapter 5 and 6, during the initial simulation study and the transducer design process, respectively. In the initial simulation study, the density of the steel material is increased to $\rho = 1\times10^8 \frac{kg}{m^3}$ to study the effects radial clamping has on the transducer characteristics. During the transducer design process in Chapter 6, the density of steel is altered between $\rho = 1\times10^3 \frac{kg}{m^3}$ and $\rho = 20\times10^3 \frac{kg}{m^3}$. All the other material parameters for steel remain the same during both chapters. The mechanical quality factor, Q_m is assumed to be the same as for the steel used in [6]

Table 3.4: Material data for steel [59] used in the finite element simulations

Parameter	Value	Unit	Ref
c_l	5780	[m/s]	[59]
c_s	3050	[m/s]	[59]
ρ	8000	[kg/m^3]	[59]
Q_m	100		[6]

3.3.4 Nylon

The transducer casings of the constructed piezoelectric transducers are made out of Nylon. The material parameters c_l, c_s and ρ for Nylon were measured in [60], but a value for the mechanical quality factor Q_m is not provided there. The value $Q_m = 20$ in Tab. 3.5 is based on comparisons between simulations and measurements of the electric conductance, G_T, and susceptance, B_T when the transducer casing has been attached to the disk and front layer. (C.f Sec. 7.5). The value Q_m was altered incrementally to find a value where the best agreement between simulation and measurement result could be achieved. This method is not expected to yield accurate results, but provides a rough estimate without the need for additional experimental measurements. The simplification is likely to be a source of discrepancy between the simulation and measurement results presented in Chapter 8.

Table 3.5: Material data for Nylon used in the finite element simulations

Parameter	Value [60]	Unit	Ref
c_l	2710	[m/s]	[60]
c_s	1120	[m/s]	[60]
ρ	1147	[kg/m^3]	[60]
Q_m	20		

3.3.5 Backing layer

In this work a Tungsten-epoxy mix [61] is used as the transducer backing layer. The content and construction procedure of the backing layer is based on a backing layer constructed by Sæther in [61]. This backing material is chosen because of accessibility to the materials needed during the construction of the transducer. The material parameters have also been measured in [61], which hopefully will provide accurate simulation results.

The material parameters c_l, ρ and Q_m presented in Tab. 3.6 are measured values from [61], and the shear sound velocity c_s is approximated as half the value of c_l [61].

Table 3.6: Material data for the Tungsten-epoxy backing layer [61] used in the finite element simulations

Parameter	Value [61]	Unit
c_l	1600	[m/s]
c_s	800	[m/s]
ρ	7470	[kg/m^3]
Q_m	13.5	

3.3.6 Glue

Ethyl-2-cyanoacrylate [62] is a fast-curing, low-viscosity glue which is used as an adhesive between the piezoelectric disks and the matching layer in the constructed transducers. The meshing structures used in comparison with experimental results in chapter 8 have a glue layer included. To simplify the simulations, the simulations in the transducer design chapter does not include such a layer. The material parameters in Tab. 3.7 are based on measurements performed on a similar glue in [63]. The mechanical quality factor value Q_m =100 is an arbitrary value set by the author, as the absorption effects in the thin glue layer are expected to be unimportant.

Table 3.7: Material data for Ethyl-2-cyanoacrylate glue used in the finite element simulations

Parameter	Value	Unit	Ref
c_l	2030	[m/s]	[63]
c_s	1043	[m/s]	[63]
ρ	1215	[kg/m^3]	[63]
Q_m	100		

3.3.7 Air

Air is modeled using the parameter values specified in Tab. 3.8. The values correspond to a temperature of 20 °C and a pressure of 1 atm [22]. The finite element simulations neglect any dissipation effects in the fluid medium. The absorption in air will be added to simulation results as described in Sec. 2.4.

Table 3.8: Material data for air used in the finite element simulations.

Parameter	Value [22]	Unit
ρ	1.21	[kg/m^3]
c_l	343	[m/s]

3.3.8 Water

In Chapter 5, the simulated sound pressure fields in Figs. 5.3 and 5.6 include water. These simulation results are compared to simulations presented in [40]. The material data used in these simulations has not been found, and a set of general material parameters for water provided in Tab. 3.9 are therefore used. The finite element simulations does not include any dissipation effects in the water, and will not be adjusted later.

Table 3.9: Material data for water used in the finite element simulations

Parameter	Value	Unit
ρ	1000	[kg/m^3]
c_l	1500	[m/s]

3.4 Transducer meshing structures

Every FEMP simulation used during this work includes a two-dimensional mesh. The mesh is created by defining a set of points $(r,\ z)$ in the axis-symmetric coordinate system shown in Fig. 2.9. Based on these points, a number of areas make up the simulated structure. The points, areas and material that each area comprises of is specified in the project file. Based on these parameters, the FEMP software creates the meshed structures that will be covered in this section.

In total, 11 different meshing structures have been used during the work; this includes the built-in FEMP 6.1 structures **`Piezodisk_Vacuum`** and **`Piezodisk_Fluid`**. In addition, several other meshing structures have been constructed by the current author. Each structure represents a step in the transducer construction process in Chapter 7, and allows for a step-by-step comparison of the simulated and measured transducer characteristics. During the transducer design process in chapter 6, the different meshing structures have also been used to study how changes in the characteristic acoustic impedance of transducer materials affect the transducer characteristics.

By doing simulations and measurements for each step in the transducer construction process presented in chapter 7, the cause of deviations between simulations and measurements can be mapped. Suppose a step in a transducer assembly causes a large discrepancy between measurement and simulation. In that case, this assembly will be discarded and not carried along further in the construction process. By discarding the assemblies with the larges discrepancies, both time and materials needed in the construction are saved. It also ensures the best possible agreement between simulation and measurement results for the transducers that make it through all the construction steps.

Most of the meshing structures that are used exist in two different configurations. One configuration simulates the transducer or piezoelectric disk while vibrating in a vacuum. The

other configuration simulates the same structure while vibrating in a fluid medium. When referring to these configurations later in the work they can be separated by their ending, **`Vacuum`** or **`Fluid`**. The fluid configuration demands a lot more computational power and can be quite time-demanding because of the number of fluid elements. The vacuum simulations are therefore preferred when only electrical characteristics are required. A brief description of the transducer meshing structures and their purpose will be provided.

3.4.1 Piezodisk

`Piezodisk_Vacuum` and **`Piezodisk_Fluid`** are built-in simulation structures in FEMP 6.1. The structures simulates a piezoelectric ceramic disk vibrating in a vacuum and fluid medium respectively. The radius of the disk, r_p, and thickness, T_p, is set by the user. Fig. 3.7 shows a mesh constructed using the structure **`Piezodisk_Fluid`**.

3.4.2 PiezodiskClamped

In this thesis, the term "clamp" refers to a circular ring that is placed around the outer edge of a piezoelectric disk, and thus restricting or partially restricting radial motion. The simulation structure **`Piezodisk_Clamped`** is created by the author in FEMP 6.1 to model a piezoelectric disk with a clamp around its circumference. The inner radius of the clamp, r_i, is equal to the radius of the piezoelectric disk, r_p. The user specifies the outer radius of the clamp, r_c, while the thickness of the clamp, T_c, is equal to that of the piezoelectric disk, T_p. The project file for the vacuum configuration of the structure, **`Piezodisk_Clamped_Vacuum`** is listed in appendix A.1, while the fluid configuration, **`Piezodisk_Clamped_Fluid`** is listed in appendix A.2. Figs. 3.2a and 3.2b shows a mesh for a clamped piezoelectric disk with dimensions r_p=10 mm, T_p = 2 mm and r_c= 12 mm, created with the vacuum and fluid configuration, respectively. In Fig. 3.2b the mesh is decimated to a lower frequency thus showing less elements than what is used in the actual simulation. If all the elements were to be displayed when simulating in air at a maximum frequency of 300 kHz, the figure would be totally black because of the black edges surrounding each finite element in the plot.

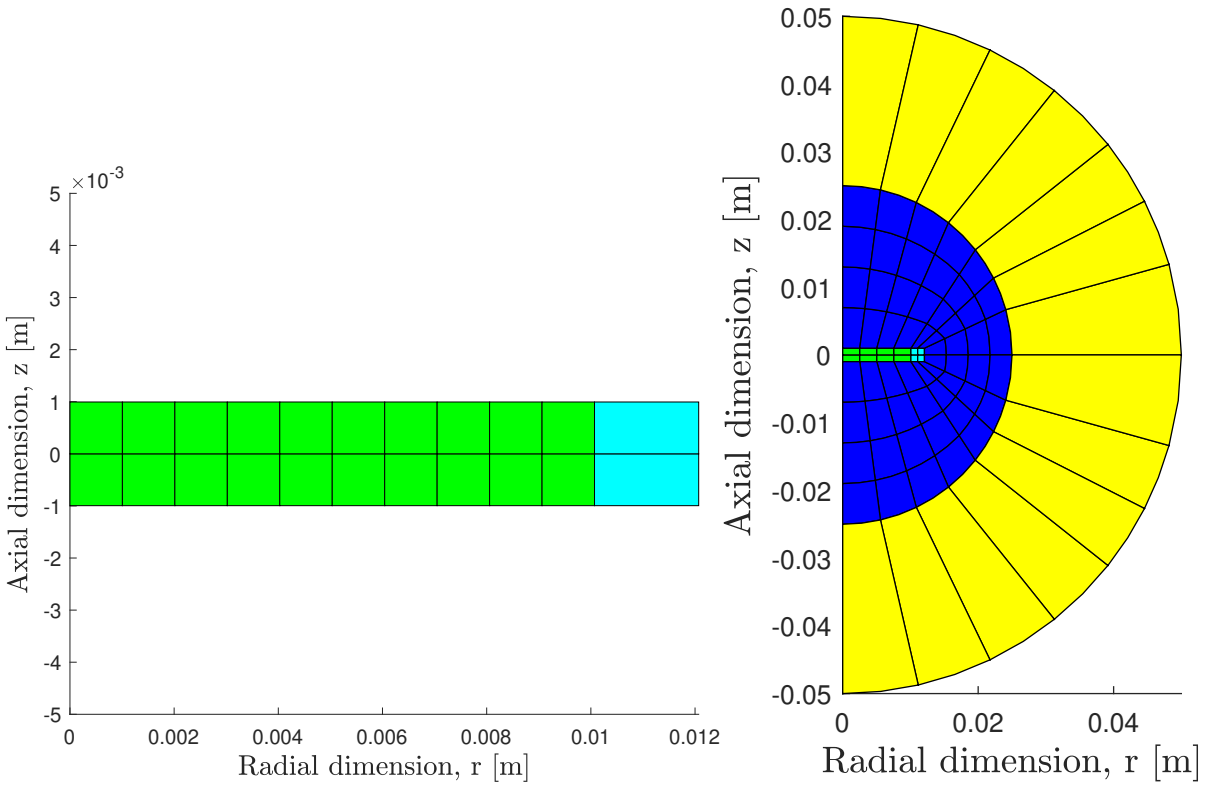

(a) *(b)*

Figure 3.2: (a) Mesh of the FEMP 6.1 Structure **`Piezodisk_Clamped_Vacuum`** *at 300 kHz. The piezoelectric disk and clamp is colored green, and cyan respectively. (b) Decimated mesh of the FEMP 6.1 structure* **`Piezodisk_Clamped_Fluid`** *at 10 kHz. The piezoelectric disk is colored in green, and the clamp in cyan. The finite and infinite fluid elements are colored in dark blue and yellow respectively*

The front surface of the disk and clamp in Fig. 3.2a and 3.2b is not placed at $z = 0$. When FEMP calculates the voltage source sensitivity, S_V this offset from $z = 0$ is automatically corrected for. This adjustment is included in all the following simulation structures.

3.4.3 PiezodiskCasing

`Pizodisk_Casing` is a simulation structure created by the author in FEMP 6.1. The structure models a piezoelectric ceramic disk placed in a transducer casing, while vibrating in a vacuum or fluid medium. The inner radius of the casing r_i is equal to the radius of the piezoelectric disk, r_p. The outer radius of the casing, r_c and length, T_c is specified by the user. The length T_c is set as the length of casing extending behind the piezoelectric disk. The project file for the vacuum configuration of the structure **`Piezodisk_Casing_Vacuum`** is listed in appendix A.3, and the fluid configuration **`Piezodisk_Casing_Fluid`** is listed in appendix A.4. Figs. 3.3a and 3.3b shows the mesh for a piezoelectric disk inside a casing with dimensions r_p=10 mm, T_p = 2 mm, T_c = 8 mm and r_c= 12 mm. $T_p + T_c$ gives a total casing length of 10 mm

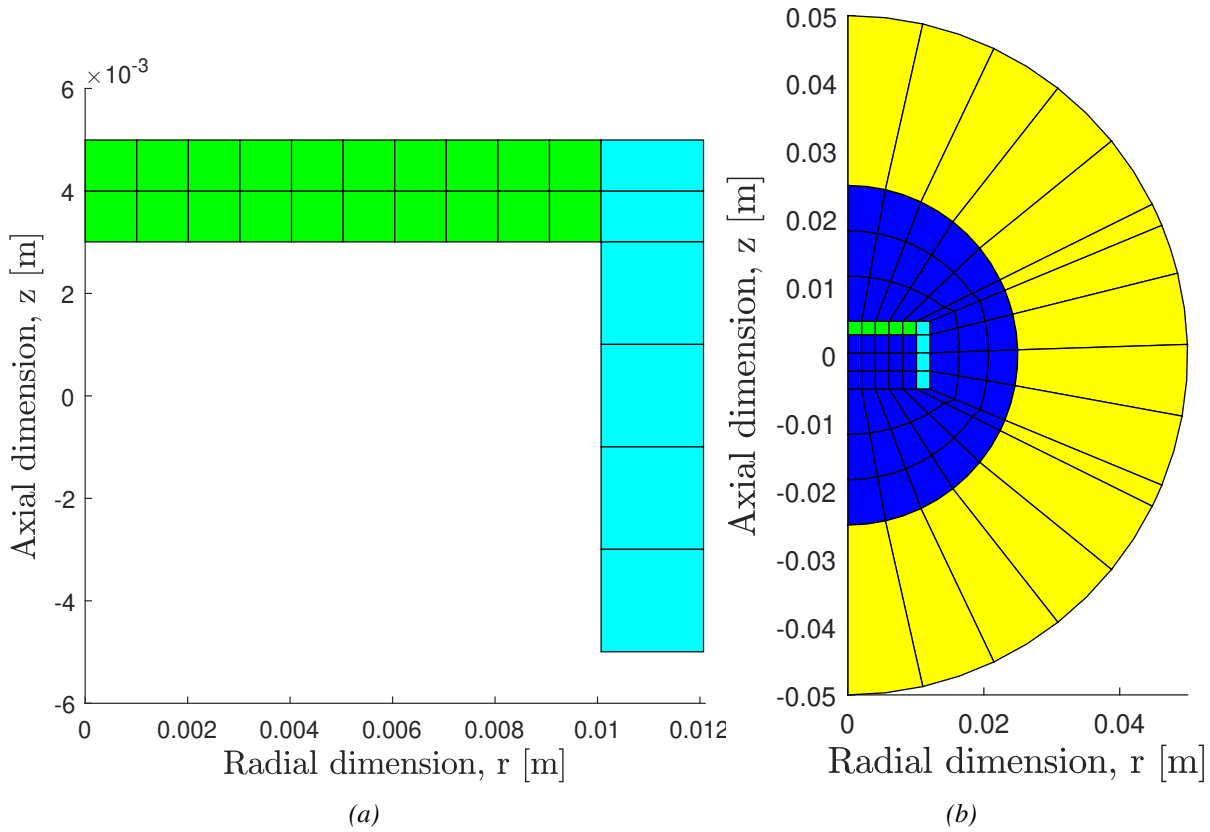

(a) *(b)*

Figure 3.3: (a) Mesh of the FEMP 6.1 Structure **`Piezodisk_Casing_Vacuum`** *at 300 kHz. The piezoelectric disk and casing is colored in green, and cyan respectively. (b) Decimated mesh of the FEMP 6.1 structure* **`Piezodisk_Casing_Fluid`** *at 10 kHz. The piezoelectric disk is colored in green, and the casing is colored in cyan. The finite and infinite fluid elements are colored in dark blue and yellow respectively.*

3.4.4 PiezodiskFrontVacuum

`Piezodisk_Front_Vacuum` is a simulation structure crated by the author in FEMP 6.1. The structure is designed to model a piezoelectric disk with a matching layer vibrating in a vacuum. The radius of the matching layer, r_m equals the radius of the piezoelectric disk, r_p. Between the disk and matching layer there is a glue layer with thickness T_g. Both the thickness of the matching layer, T_m, and glue layer, T_g is set by the user. The project file for the structure is listed in appendix A.5. Fig. 3.4 displays a mesh generated using the structure with the following specifications: T_p = 2 mm, r_p = 10 mm, T_m = 4.9 mm and T_g = 0.09 mm. There is no fluid configuration for this structure.

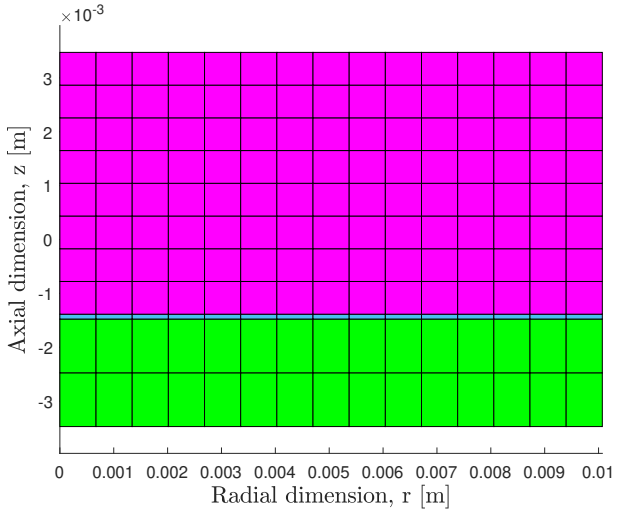

Figure 3.4: Mesh of the FEMP 6.1 Structure ***Piezodisk_Front_Vacuum*** *at 300 kHz. The piezoelectric disk and matching layer is colored green and magenta respectively. A thin glue layer colored blue is placed between the disk and matching layer*

3.4.5 PiezodiskCasingFront

Piezodisk_Casing_Front is a simulation structure created by the author in FEMP 6.1. The structure is designed to model a piezoelectric disk with a matching layer and transducer casing vibrating in a vacuum or a fluid medium.

The radius of the matching layer is equal to that of the piezoelectric disk, r_p. The user specifies the outer radius of the casing, r_c, the thickness of the casing extending behind the piezoelectric disk, T_c, and the thickness of the matching layer, T_m.

In the vacuum configuration, two glue layers are present, one between the piezoelectric disk and the matching layer with thickness, T_g, and another between the transducer casing and both disk and matching layer with width, w_g. The fluid configuration does not include the glue layers as it is intended only for use during the transducer design process in Chapter 6, and not for comparison with experimental measurements, where higher accuracy of the model is demanded. The project files **Piezodisk_Casing_Front_Vacuum** and **Piezodisk_Casing_Front_Fluid** is listed in appendix A.6 and A.7 respectively.

Figs. 3.5a and 3.5b shows a mesh created by the vacuum and fluid configuration of the structures. In Fig. 3.5a The following parameters have been specified: T_p = 2 mm, r_p = 10 mm, r_c = 12 mm, T_m = 4.9 mm, T_c = 133 mm, T_g = 0.09 mm and w_g = 0.1 mm. The transducer casing in Fig. 3.5a extends back to z = -0.07 m but is not displayed in the figure.

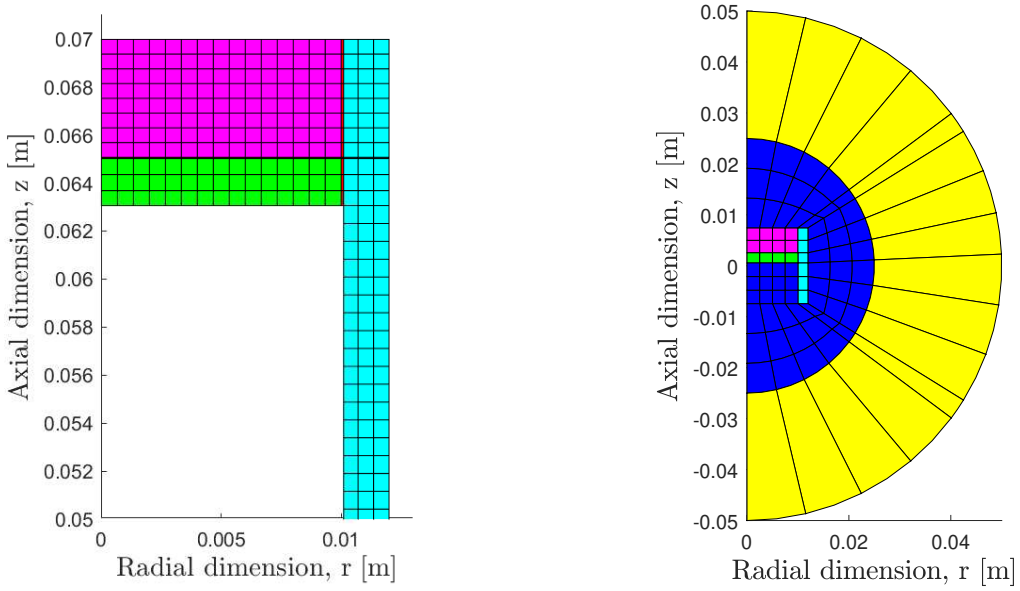

Figure 3.5: (a) Mesh of the FEMP 6.1 Structure ***Piezodisk_Casing_Front_Vacuum*** *at 300 kHz. The piezoelectric disk and matching layer is colored green and magenta, respectively. The transducer casing is colored cyan, and a thin red glue layer red is placed around the matching layer where it makes contact with the disk and transducer casing. (b) A decimated mesh of the FEMP 6.1 Structure* ***Piezodisk_Casing_Front*** *at* $10kHz$. *The same colors as in* (a) *are used, except for the finite and infinite element scolo*

3.4.6 Transducer

Transducer is a simulation structure created by the author in FEMP 6.1. The structure is designed to model the complete piezoelectric transducer constructed during the work, radiating in a vacuum or fluid medium (Cf. Chapter 7). The structure is almost identical to **Piezodisk_Casing_Front**, but a backing layer has replaced the air/vacuum inside the casing. Instead of specifying the length of the casing extending behind the piezoelectric disk, T_c, the length of the backing layer T_b must be specified. Both **Transducer_Vacuum** and **Transducer_Fluid** include the two glue layers, as the simulations performed using **Transducer_Fluid** will be compared to acoustical measurements in Chapter 8. The simulation structure does not include the BNC connector and the portion of the casing exceeding behind the backing layer in Fig. 6.11. Figs. 3.6a and 3.6b show a mesh created by the vacuum and fluid configuration of the structure respectively. In Fig.

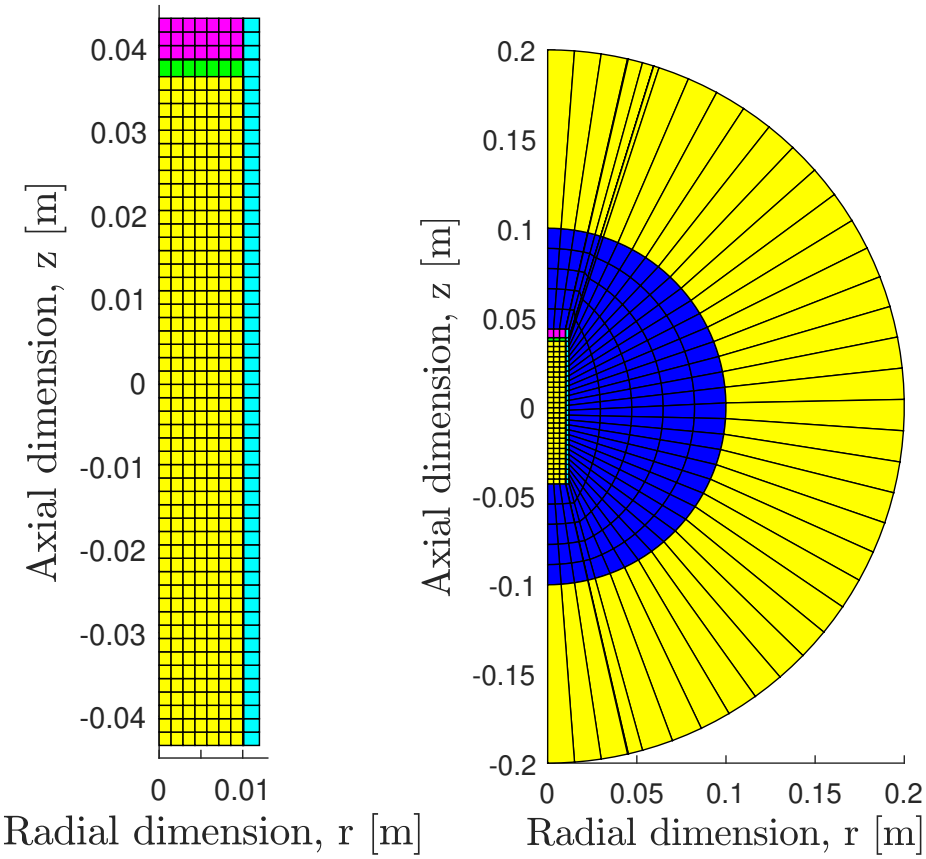

(a) *(b)*

Figure 3.6: (a) Decimated mesh of the FEMP 6.1 Structure ***Transducer_Vacuum*** *at 100 kHz. The colors are the same as in Fig. 3.5a, except for the backing layer displayed in yellow. (b) Decimated mesh of the FEMP 6.1 Structure* ***Transducer_Fluid*** *at 5 kHz. Colors are the same as in Fig. 3.5b, with the backing layer in yellow*

3.5 Meshing challenges

Due to software changes implemented to FEMP in 2016 [23], the elements per wavelength N_λ in the meshing structures has been calculated manually for all structures using finite fluid elements [23]. In this section a superscript notation of f for the fluid variables, and T for the transducer variables will be used.

In previous versions of FEMP (FEMP 4.1) [23], the elements per wavelength in the radial direction of the piezoelectric disks, $N^T_{\lambda,r}$, and axial direction, $N^T_{\lambda,z}$, have been adjusted and calculated automatically, based on the required element size in the fluid, if necessary. If this automatic calculation was implemented for more complex transducer structures, with matching layers, casings etc. is unknown to the author.

In the current version of FEMP (FEMP 6.1) this automatic adjustment of the elements per wavelength in the axial direction of the piezoelectric disks $N^T_{\lambda,z}$ is no longer observed. An example of this is shown in Fig. 3.7(a), where the mesh resolution in the fluid at the side of the disk is clearly deviating from what is used at the front and back of the disk. In Fig. 3.7(b) the value $N^T_{\lambda,z}$ used in the simulation has been computed manually using MATLAB and inserted to the input file. An example of the methods used when calculating the value $N^T_{\lambda,z}$ will be given in this section.

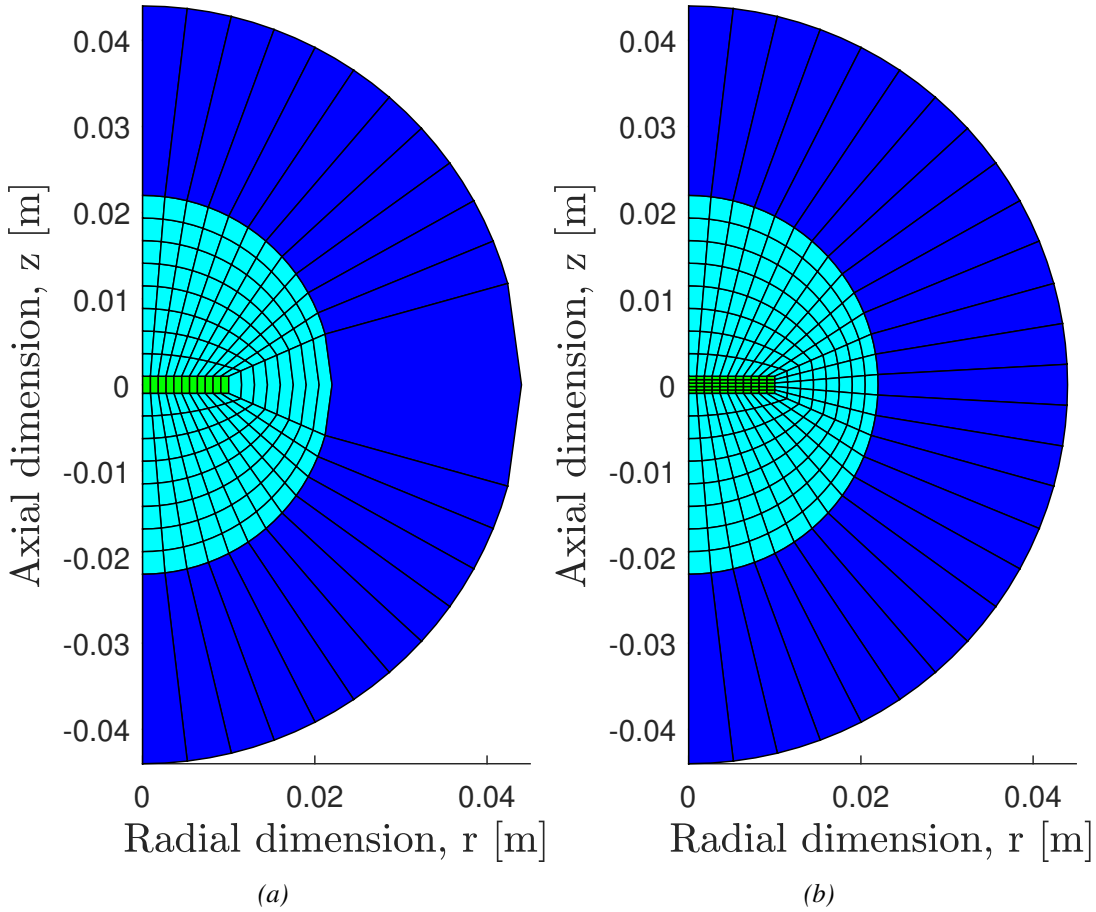

Figure 3.7: (a) Decimated mesh of the FEMP 6.1 Structure **`Piezodisk_Fluid`** *at 25 kHz without calculation of $N^T_{\lambda,r/z}$. (b) Decimated mesh of the FEMP 6.1 Structure* **`Piezodisk_Fluid`** *at 25 kHz with calculation of $N^T_{\lambda,r/z}$ using* **`Elem_calc_piezo`**.

When doing simulations in air, the elements per wavelength in the transducer, N^T_λ, is as-

sumed to be decided by the fluid elements. This assumption is based on the short wavelengths in the air ($\lambda^f \approx 1.1$ mm @ 300 kHz) relative to the shear wavelength of the solid materials used in the transducer, λ_s^T.

In this example of calculating $N_{\lambda,z}^T$, a transducer structure shown in Fig. 3.8, with a piezoelectric disk (yellow), matching layer (green), transducer casing (orange), and transducer backing layer (red) , is surrounded by a fluid medium. The fluid medium is split into separate fluid areas numbered $(i = 1-7)$. Each fluid area has an inner boundary towards the transducer, and an outer boundary at the distance R_{inf}, as shown in Fig. 3.8. The infinite fluid areas extending behind R_{inf} has not been included in Fig. 3.8, but can bee seen as the dark blue region Fig. 3.7.

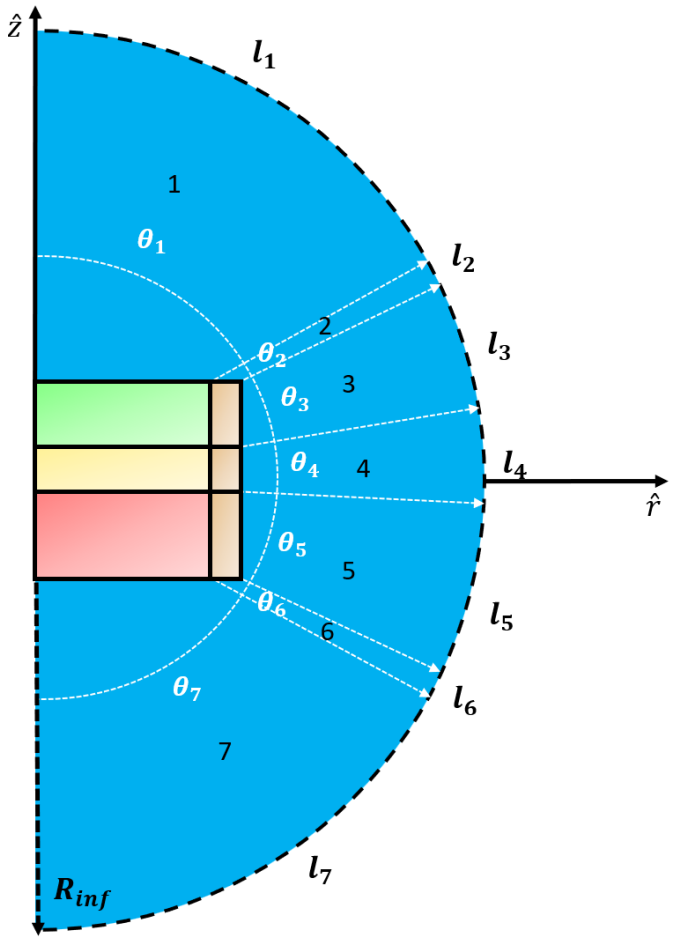

Figure 3.8: Schematic of the FEMP structure ***Transducer_Fluid****. The dimensions of the matching layer (Green), piezoelectric disk (Yellow), backing layer (red) and transducer casing (brown) are purely illustrative. The Finite fluid elements are represented by the blue region.*

The length of the outer boundary for each fluid area, l_i, is calculated using:

$$l_i = R_{inf}\theta_i \qquad i = 1,2,...7 \tag{3.8}$$

Where θ_i is the mesh angle for each fluid section.

In order to achieve $N_\lambda \geq 5$ all over the mesh, the number of elements over the circumference at R_{inf} in fluid region i, $N_{EL,i}^f$ must satisfy

$$N_{EL,i}^f \geq 5\frac{l_i}{\lambda^f}, \tag{3.9}$$

where λ^f is the wavelength in the fluid at the maximum frequency of the simulation. In a proper mesh, the number of elements at the inner boundary equals the number of elements at the outer boundary of an area. Hence, when assuming that the wavelength in the fluid, λ^f is shorter than the shear wavelength in the transducer, λ_s^T , i.e. $(\lambda^f < \lambda_s^T)$, the number of elements in the axial direction at the transducer, $N_{EL,z}^T$, is decided by the number of fluid elements on the side of the transducer.

Suppose an area in the transducer structure does not share a common boundary with a fluid area. In that case, the number of elements is automatically corrected by FEMP so that N_{EL}^T corresponds to the highest value of the two areas shearing the boundary. This means that for the air case, it is only necessary to calculate N_λ^T in the areas that share a boundary with a fluid area, when assuming $\lambda^f < \lambda_s^T$.

FEMP 6.1 receives N_λ^T as input for the different areas in the structure. Therefore the value, N_{EL} calculated by using equation 3.9, has to be converted into the corresponding value for N_λ^T in the area of interest. This is done using a conversion factor, k, giving the ratio between the shear wavelength in the transducer area and the length of the area in the axial direction.

$$k_z = \frac{\lambda_s^T}{l_z^T} \tag{3.10}$$

The number for elements per wavelength in the axial direction at the transducer, $N_{\lambda,z}^T$ needed to satisfy 3.9, can then be calculated using:

$$N_{\lambda,z}^T = k \cdot N_{EL,z}^T \tag{3.11}$$

$N_{\lambda,z}^T$ is calculated using a separate Matlab script **`Elem_calc`**. The calculated value for $N_{\lambda,z}^T$ is always rounded up to the closest integer.

Chapter 4

Experimental setup and measurement methods

This chapter presents the experimental setup, the instruments used during the work, measurement methods, and the signal processing used to analyze the experimental results. The experiments include electric, acoustic, and dimension measurements.

A list of the equipment used during the work will be provided in Sec. 4.1. The setup and methods used in the various electrical measurements are provided in Sec. 4.2. Sec. 4.3 covers the methods and setup used during the acoustic measurements. In Sec. 4.4 the calibration procedure for a Brüel & Kjær type 4138 condenser microphone is presented. Sec. 4.5 covers the equipment and methods used to measure the transducer dimensions. Finally Sec. 4.6, covers the digital signal processing used on the recorded measurement data.

4.1 Equipment

A list of the equipment used during measurements is provided in Tab. 4.1.

Table 4.1: Instruments and motion controllers used in the acoustical and electrical measurement setups

Model/Brand	Equipment	Serial number	Manual
Hewlett Packard 4192A LF	Impedance analyzer	2150J01344	[64]
Agilent 33220A	Signal generator	MY44023589	[65]
Tektronix DPO3012	Oscilloscope	C010246	[66]
Ferroperm/Meggitt PZ27	Piezoelectric disc	N/A	[55]
Brüel & Kjær 4138	1/8-inch pressure-field microphone	1832479	[49]
Brüel & Kjær UA-160	Adaptor - microphone to preamplifier	N/A	[49]
Brüel & Kjær 2633	Preamplifier	N/A	[67]
Brüel & Kjær 2636	Measurement amplifier	1815638	[68]
Brüel & Kjær 4228	Pistonphone	1918465	[69]
Krohn-Hite 3940	Filter	AM2626	[70]
Vaisala HMT313	Humidity and temperature meter	F4850018	[71]
ASL F250 MkII	Thermometer	1365026993	[72]
Paroscientific 740	Barometer	67325	[73]
KEYENCE LK-G32	Laser sensor	2041141/2041143	[74]
KEYENCE LK-G3001PV	Controller with display	1741187	[74]
SMC Hydra TT	Motion Controller	1404-0153	[75]
PI C-843.41	Motion Controller	0095103296	[76]
PI C-852.12	Signal processor/Encoder	1460497	[77]
PI M-535.22	Linear stage (X axis)	1460497	[78]
PI M-531.DG	Linear stage (Y axis)		[79]
PI LS270	Linear stage (Z axis)	414000926	[80]

4.2 Electrical measurement setup

The electrical measurements of the conductance, G_T, and susceptance, B_T are performed using a Hewlett Packard 4192A LF impedance analyzer [64] as illustrated in Fig. 4.1. Measurements are carried out in the frequency range 50 kHz to 300 kHz with a 100 Hz resolution, except for the measurements performed on single piezoelectric disks. For these specific measurements, a resolution of 10 Hz is employed around the resonance peaks of the first and second radial modes, RM1 and RM2. By measuring the conductance and susceptance, the admittance, Y_T, and impedance, Z_T, can be calculated using Eq. 2.1.

Before measurements are performed, a zero adjustment of the impedance analyzer is carried out to compensate for the different wires and the adaptor used in the measurement setup. The adaptor, visible in the lower left corner of Fig. 4.1, facilitates the transfer of wire input from the disks and transducer into a coaxial input for the impedance analyzer. The zero adjustment process is described in [64] and is always performed at the maximum frequency of the measurement series, which is 300 kHz in this work.

Measurement data from the impedance analyzer is transferred to a computer using a GPIB cable and saved using the MATLAB script **`impanal.m`**, as listed in appendix B.1. The measurement frequencies and driving voltage, V_{rms} = 0.3 V, are specified in the script before each measurement. The driving voltage is chosen to avoid nonlinear distortions caused by higher voltages, as observed in [29, 30], while still avoiding problems with the instrument resolution at lower voltages.

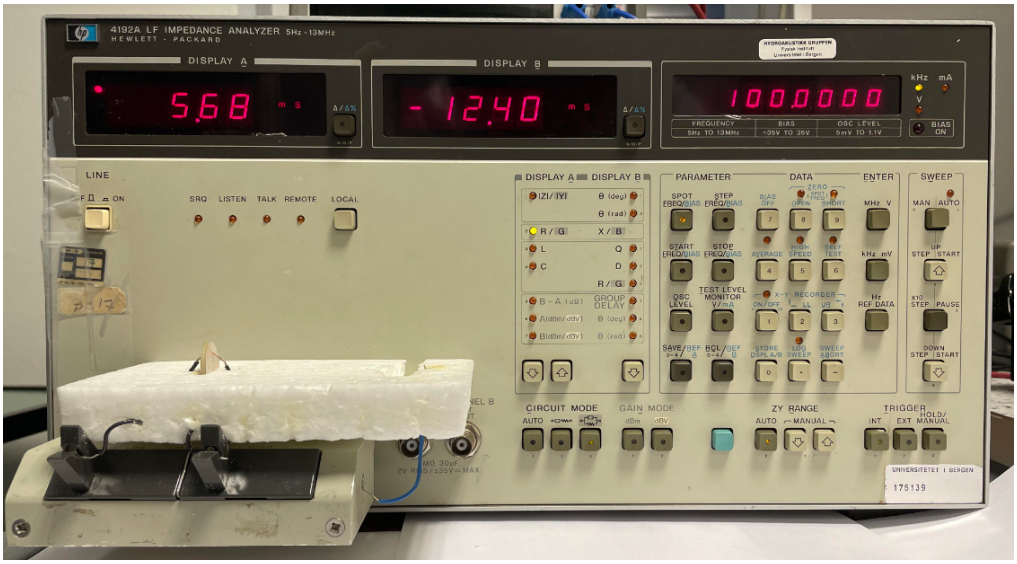

Figure 4.1: Hewlett Packard 4192A LF impedance analyser

When performing measurements on a single piezoelectric disk, the disk is placed in a small grove carved out of a Styrofoam block. Two wires connect the impedance analyzer to each disk electrode, as shown in Fig. 4.1. The wires are kept in contact with the disk using wire tension only, to infer as little mechanical load on the disk as possible.

During the transducer construction presented in Chapter 7 electrical measurements are performed for each step in the construction process. The transducer assembly is then placed resting on a Styrofoam block, as shown in Figs.4.2b - 4.2d.

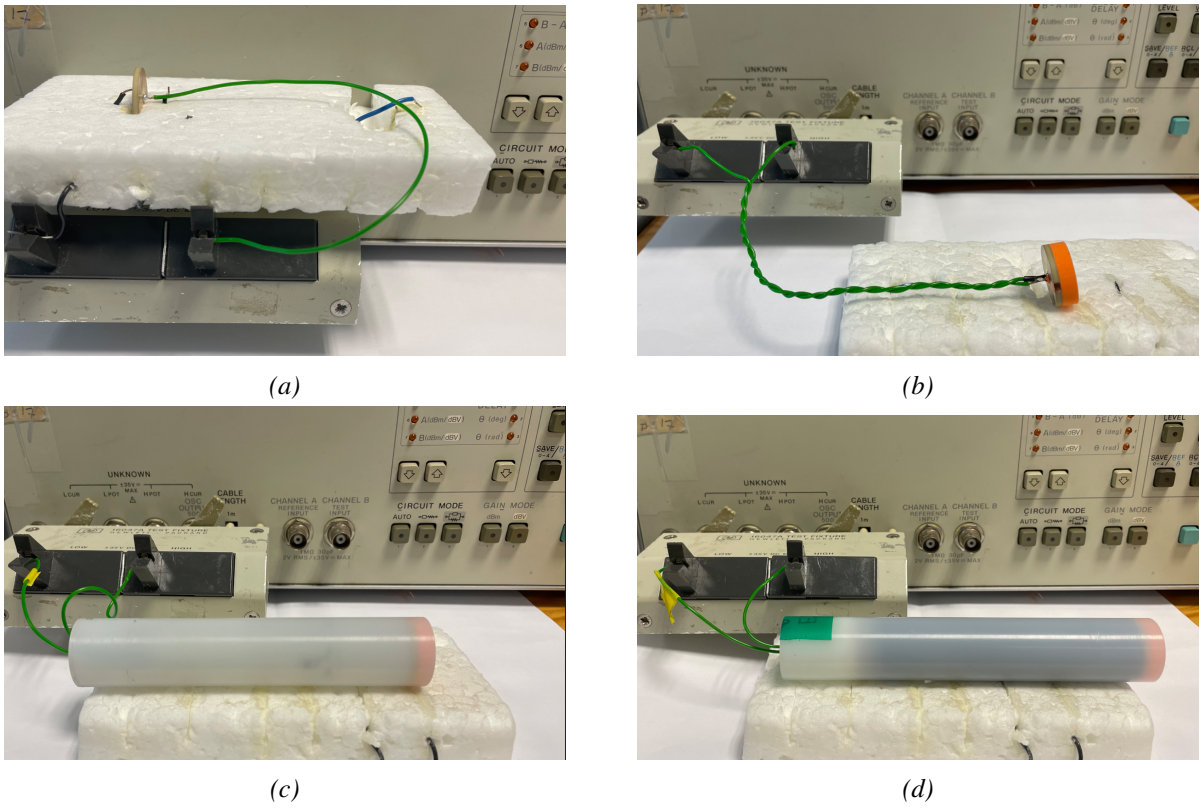

(a) *(b)*

(c) *(d)*

Figure 4.2: (a) Electrical measurement setup after soldering a wire to the electrode facing the backing layer in Sec. 7.2. (b) Electrical measurement setup after attachment of the matching layer in Sec. 7.4. (c) Electrical measurement setup after attachment of the transducer casing in Sec. 7.5. (d) Electrical measurement setup for the final transducer without the coaxial connector in Sec. 7.6.

4.3 Acoustical measurement setup

The acoustical measurement setup used during the work is shown in Figs. 4.3a - 4.3c. The setup is based on work by Amundsen in [81] and was originally developed in [29–31]. The setup has later been further developed in [82–86].

The signal path in the measurement setup starts at the signal generator, denoted (1) in Fig. 4.3. The signal generator produces a sinusoidal electric burst with amplitude, length, and frequency set by the user in the MATLAB script **`add_to_job_list.m`**, as listed in appendix B.2. At the output of the signal generator, the burst is split in two by a T-connector. One side of the T-connector is connected to the transmitting transducer (2) through a coaxial cable, and the other is connected to an oscilloscope (6). In the transmitting transducer, the electrical burst is converted to an acoustic burst which travels through the fluid medium to either a receiving microphone (3) or receiving transducer (3), as shown in Figs.4.3b-4.3c, respectively. In the microphone and receiving transducer, the acoustic burst is converted back to an electric burst which is then transferred to an amplifier (4). The amplified signal is passed through a band-pass filter (5) before it is terminated and measured by the oscilloscope (6).

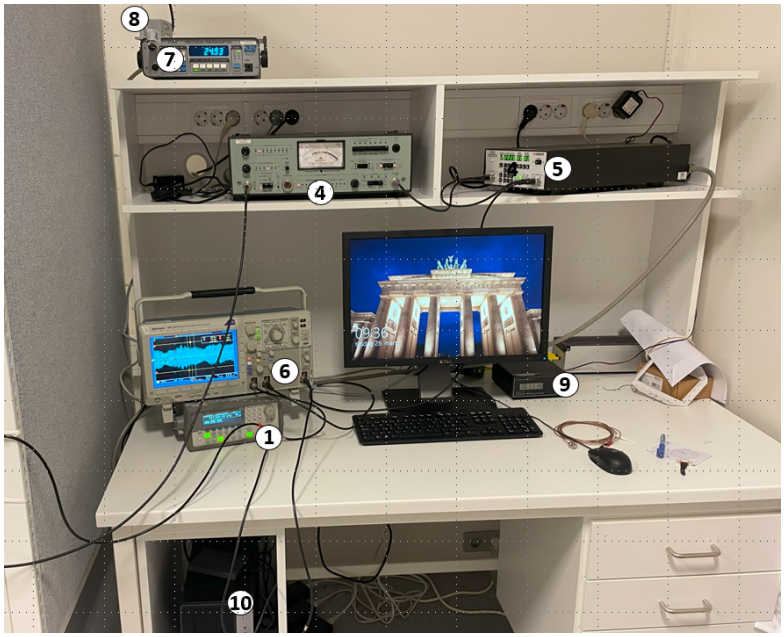

(a)

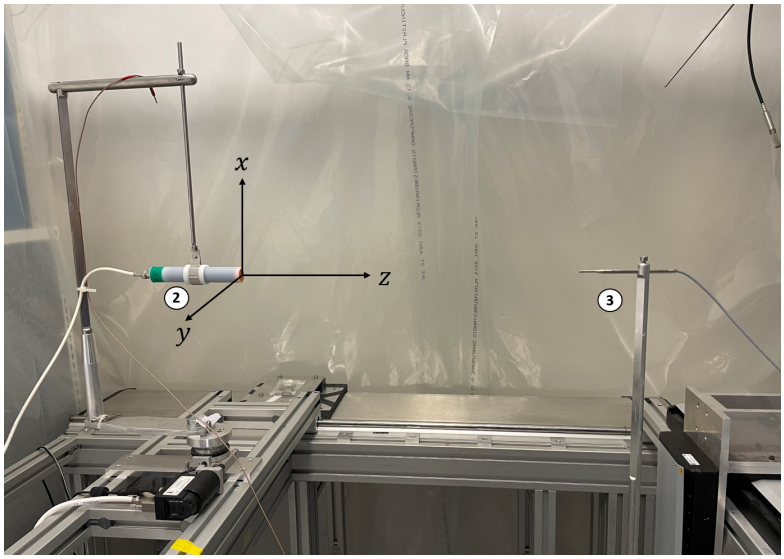

(b)

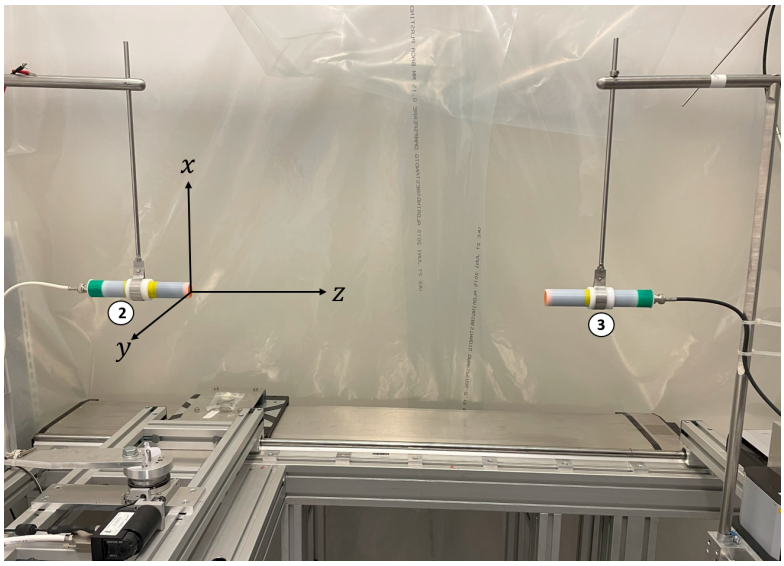

(c)

Figure 4.3: (a) Instruments used in the acoustical measurements. (b) The transmitting transducer (2) and a Brüel & Kjær Type 4138 condenser microphone (3). (c) The transmitting transducer (2) and receiving transducer (3).

The setup also measures the temperature, relative humidity (RH%), and ambient pressure through external hardware. The thermometer (7), hygrometer (8) and barometer (9) are all connected to the computer (10) using serial communication. The signal to and from the computer to the signal generator and receiver electronics goes through a GPIB connection. The oscilloscope is connected to the computer using USB. A schematic overview of measurement setup is displayed in Fig. 4.4.

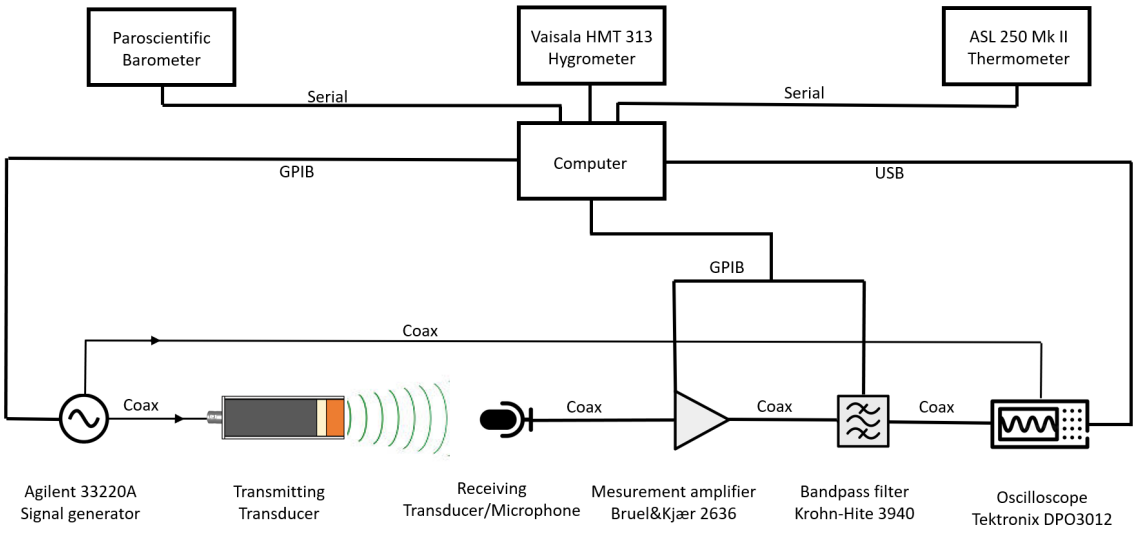

Figure 4.4: Schematic of the measurement setup used in the acoustical measurements

4.3.1 Signal generator

The signal generator used in this work is an Agilent 33220A waveform generator [65]. The signal generator produces a sinusoidal electric burst with amplitude, length, burst period, and frequency set by the user.

The voltage set on the signal generator display is equivalent to the voltage across a theoretical 50 Ω resistance connected in series with the instrument. Because of this, the voltage across the transducer is measured by an oscilloscope in parallel with the transducer during measurements. If the actual load impedance differs from the specified value (50 Ω), the displayed voltage on the signal generator will be incorrect [65]. If the signal generator operates under open circuit conditions, i.e., an infinite impedance is applied across the generator output, the voltage across the load is doubled to 20 V. The constructed transducers are seen to operate at close to open circuit conditions for all frequencies of interest, meaning a voltage, $V_{0m} \approx 20$ V is measured across the transducer. Therefore, all measurements with a specified nominal voltage of 10 V at the signal generator display will be referred to as as a $V_{pp} = 20$ V measurement.

The conducted measurements use a voltage $V_{pp} = 20$V, and a burst rate of 25 Hz. A burst length of 1.3 ms is used in the transducer to microphone measurements, and a 1.2 ms burst length is used in the transducer to transducer measurements. The difference in burst length is unintended, but the measurements have not been repeated, as only a small portion of the recorded burst will be used to measure the signal amplitude. This is further discussed in Sec. 4.6.

A burst length of 1.3 ms corresponds to a signal length of approximately 0.46 m in air, well

below the separation distance between the transmitter and receiver, d = 0.5 m. The separation distance and signal length is chosen to decrease electric cross-talk and avoid reflections from the microphone, transducer holders and other parts of the measurement setup.

4.3.2 Cables

A number of coaxial cables of type RG58 is used to connect the instruments in the acoustical measurement setup. When coaxial cables are modeled in the system model (Cf. Sec.2.3) the cables characteristic impedance, Z_0 is calculated using Eq. 2.16. A set of typical values for the cable inductance per meter, L = 250 nH/m, and capacitance per meter C = 100 pF/m are used during this work [43]. The coaxial cables that are simulated in the system model are listed in Tab. 4.2, together with their number and respective length.

Table 4.2: The RG58 coaxial cables used in acoustical measurement system

Cable #	From	To	Length
1	Signal generator	Transmitting transducer	4.5 m
2	Signal generator	Oscilloscope	2.5 m
3	Receiving Transducer	Measurement amplifier	2.5 m
4	Measurement amplifier	Oscilloscope	0.5 m

4.3.3 Transmitter and Receiver Positioning

Two linear stages are mounted on the receiver side of the setup, and enable movement of the receiver in the xy-plane in Figs. 4.3b and 4.3c. The two stages controlling the xy-movement of the receiver are both controlled by a PI C-843.41 motion controller [76]. The linear stage on the z-axis [80] is mounted on the transmitter side, and allows the transmitter to be moved back and forth along the z-axis. The z-axis stage is controlled via a SMC Hydra TT [75] motion controller. Both the SMC Hydra TT and PI C-843.41 motion controller receives input commands from the computer via a USB connection. The input commands for the two motion controllers are sent via MATLAB, and the various commands used during the work are listed in the controllers respective manuals [75] [76].

In [82] a pair of Keyence LK-G32 laser sensors [74] were installed in the measurement setup to accurately determine the distance, d, between the transmitter and receiver. The laser sensors are applied when measuring the distance between the constructed transducers and the Brüel & Kjær condenser microphone. When the transducers are used as both transmitter and receiver, the lasers can not be applied because of an insufficient distance between the receiving transducer and the laser sensor. Therefore a different method is used during this setup; This will be covered later.

The front of the two sensors are separated by a distance d_x = 182.569 mm [82], as shown in Fig. 4.5.

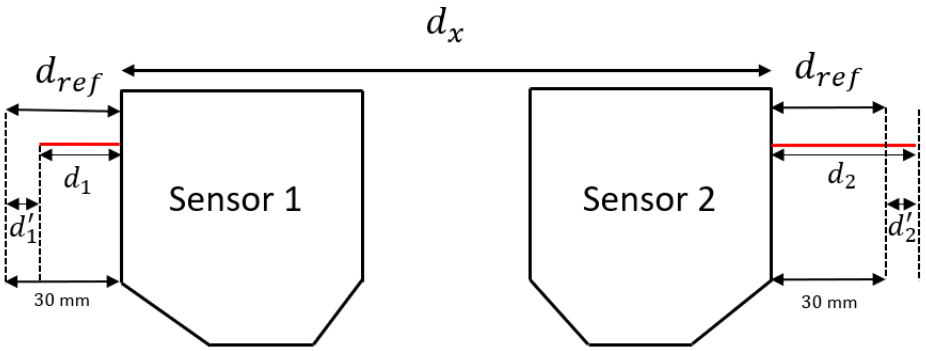

Figure 4.5: Schematic of the Keyence LK-G32 laser sensors. Based on Fig. 3.8 in [82]

Sensor 1 measures the distance, d_1', at which the transmitter is positioned in front of the sensor, with respect to a reference distance d_{ref} = 30 mm. The distance from the transmitter to the front of the sensor, d_1 in Fig. 4.5 can then be found by.

$$d_1 = d_{ref} - d_1'. \tag{4.1}$$

The same relationship holds for sensor 2 but the distance, d_2 between the sensor and the receiver is measured

$$d_2 = d_{ref} - d_2'. \tag{4.2}$$

The total distance between the transmitter and receiver can then be found by

$$d = d_x + d_1 + d_2. \tag{4.3}$$

Because of a limited measuring range for the two sensors the distance, d between the transmitter and receiver is not measured directly. Instead the internal coordinate system of the z-axis motion controller is calibrated using the laser sensors and the MATLAB script **`CalibratePositionAndAlignment.m`** listed in Appendix B.4. After calibration of the motion controllers coordinate system at a measured distance, d_{cal}, the controller keeps track of any change in the distance between transmitter and receiver.

As mentioned previously the laser sensors can not be used when the constructed transducers are used as both transmitter and receiver. The distance, d is then measured by placing the front of the transmitting and receiving transducer together. The z-coordinate, z_0 of the motion controller, when the front of the transducers are placed together is noted, and a distance d = 0 is assumed. To achieve a desired distance, d between the two transducers, the motion controller moves the transmitting transducer to a z-coordinate $z_d = z_0 + d$. This method is obviously not as accurate as the method where the laser sensors are used, and an uncertainty of $\pm$ 1 mm is estimated.

4.3.4 Receiver Electronics

The receiving microphone or transducer is connected to a Brüel & Kjær 2636 measurement amplifier [68]. From the measurement amplifier, the signal is passed through an external Krohn-Hite 3940A digital filter [70], before it is recorded on the Oscilloscope. The measurement amplifier is set to amplify the input signal by 60 dB. Based on the amplifier frequency response presented in [68], the amplifier's frequency response is assumed to be flat from 2 to 200 kHz. The Input and output impedance of the measurement amplifier is listed in Tab. 4.3.

The Receiver electronics also contain a Krohn-Hite 3940A digital filter. The Filter has two channels that are utilized as a bandpass filter. One channel is adjusted to have a cutoff frequency at half the recorded frequency, and the other is adjusted to have a cutoff frequency at double the measurement frequency. The Input and output impedance of the Filter is listed in Tab. 4.3.

Table 4.3: Specified Input and output impedance of the instruments used in the measurement setup

Model	Type of equipment	Input impedance	Output impedance
Brüel & Kjær 2636	Measurement amplifier	1 MΩ || 90 pF	100 Ω
Tektronix DPO3012	Digital oscilloscope	1 MΩ || 11.5 pF	-
Agilent 33220 A	Waveform generator	-	50 Ω
Krohn-Hite 3940A	Digital filer	1 MΩ || 100 pF	50 Ω

4.3.5 Oscilloscope

A Tektronix DPO3012 digital oscilloscope records the input voltage across the transmitting transducer and the output voltage from the receiving microphone. The signal acquisition is triggered by a trigger signal sent from the waveform generator to the oscilloscope through a coaxial cable. The oscilloscope has an input resistance of 1 MΩ in parallel with a capacitance of 11.5 pF [66].

To reduce the effects of random noise in the system, several signal bursts are averaged before being recorded by the computer. A total of 512 bursts are averaged in all the presented measurements. Before averaging, the measurement window on the oscilloscope is adjusted to the input and output signal. The measurement window on the oscilloscope is divided into 8 divisions, and the voltage spanning each division is adjusted, so that the 8-bit resolution of the oscilloscope is utilized as much as possible. 100 000 samples are used in the horizontal direction, giving a sample rate off 25 MHz when using 400 μs per division.

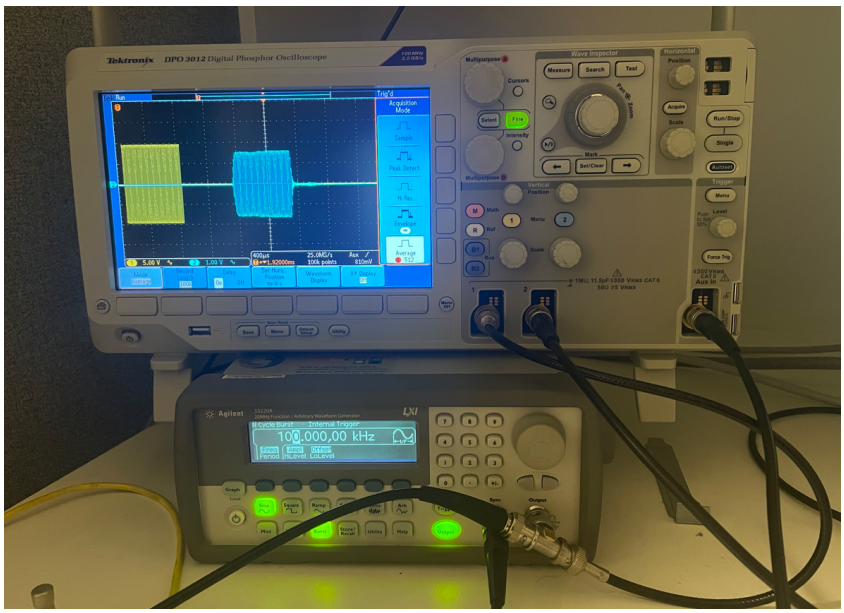

Figure 4.6: The Tektronix DPO3012 digital oscilloscope (top) and Agilent 33220A waveform generator (bottom) used during the measurements

4.4 Bruel & Kjær 4138 Microphone

A Brüel & Kjær microphone system is used in the acoustical measurements. The system includes a B&K 4138 1/8-inch microphone [49] and a B&K 2633 preamplifier [67]. A Type 4138 microphone requires an external polarization voltage of 200 V; therefore, a preamplifier is needed[49]. The manufacturer states that the preamplifier frequency response is flat from 3 Hz to 200 kHz [67], and no corrections will be made to adjust for eventual discrepancies during microphone calibration. The preamplifier is connected to the microphone using a 1/8-inch to 1/4-inch adaptor with a 2 m proprietary cable at the other end.

The manufacturer states that the Brüel & Kjær 4138 microphone is designed to operate in a frequency range spanning from 6.5 kHz to 140 kHz [49]. However, the microphone calibration chart supplied by the manufacturer covers a 20 Hz to 200 kHz range, as shown in Fig. 4.7. The calibration chart shows the open circuit pressure response relative to the response at 250 Hz. The calibration measurements were done using an electrostatic actuator and were performed by the manufacturer upon delivery. The calibration chart of the Brüel & Kjær 4138 microphone with serial no. 1832479, is shown in Fig. 4.7.

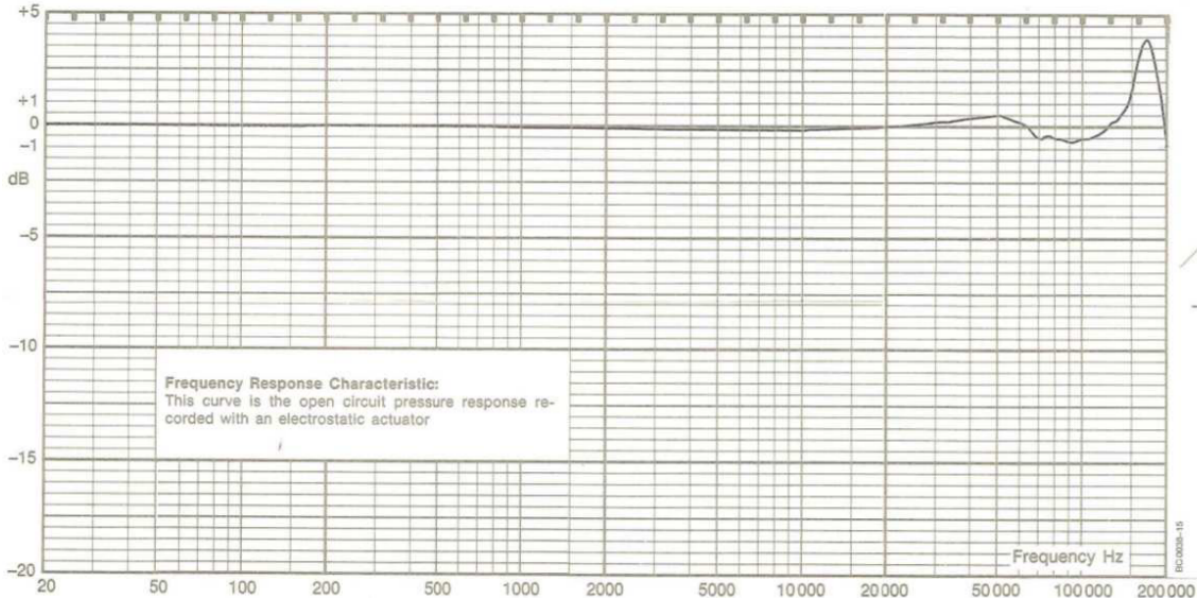

Figure 4.7: Calibration chart of the Brüel & Kjær 4138 microphone with serial no. 1832479

The content of the calibration chart in Fig. 4.7 has been digitized by the author using online software [87]. The software automatically inserts a number of points along the plotted graph, which is then converted into a set of coordinates in the x-y plane. The coordinate points have been extracted and imported to MATLAB as a 2-D array. The result of this digitization process can be seen in Fig. 4.8. Similar digitization processes have been performed in [86] and [85], where the error related to the placement of individual points and other factors, such as skewing of the coordinate system occurring during scanning of the calibration sheet is estimated to be ± 0.1 dB.

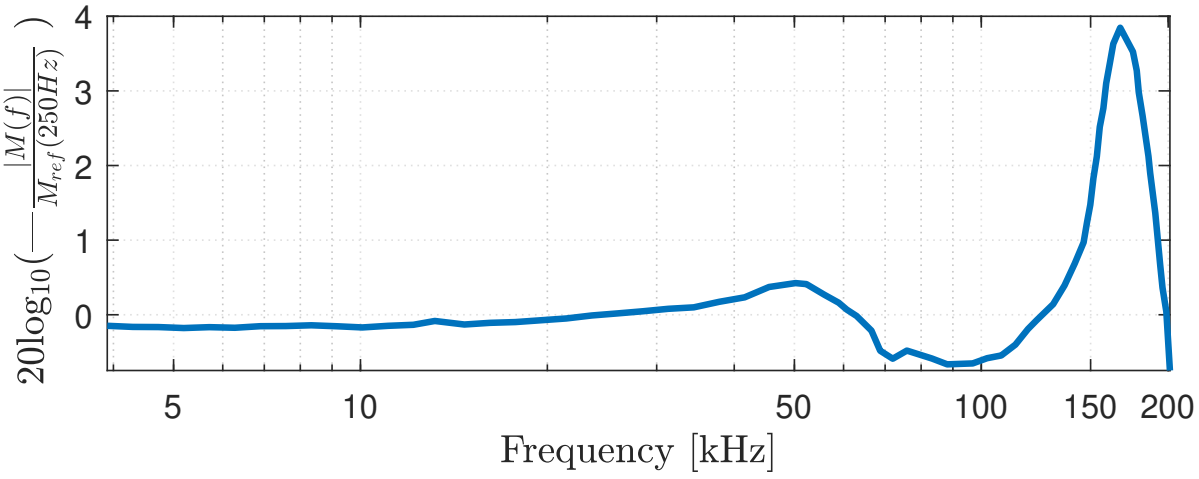

Figure 4.8: Digitized version of the calibration chart in Fig. 4.7

Fig. 4.8 shows the digitized open circuit pressure response relative to the response at 250 Hz from 4 kHz to 200 kHz. The response is relatively flat up to 140 kHz, conforming with the recommended upper frequency of 140 kHz, as specified by the manufacturer [49]. The diaphragm in the microphone has a resonance frequency of 160 kHz, which causes the sharp peak around this frequency[49].

To obtain the free-field response at a specific angle of incidence, it is necessary to incorporate free-field corrections to the open circuit pressure response relative to the response at 250 Hz [49]. The free-field correction accounts for the phenomenon of sound wave diffraction around the microphone, resulting in an increase in sound pressure. This correction becomes significant at high frequencies when the wavelength is comparable to the external dimensions of the microphone [49]. The manufacturer has supplied a set of free field correction curves for various angles of incidence for a B&K Type 4138 microphone with a protection grid [49]. As only normal incidence is used during this work, only the curve denoted "0" in Fig. 4.9 has been digitized by similar means as previously.

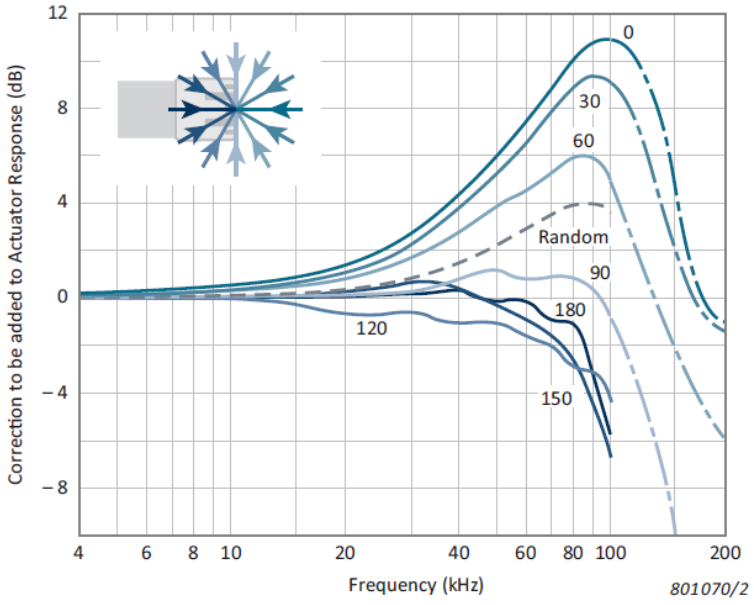

Figure 4.9: Free-field correction curves for various angles of incidence for B&K Type 4138 microphone [49]

Fig. 4.10 shows the digitized free field correction curve for normal incidence from 4 to 200 kHz.

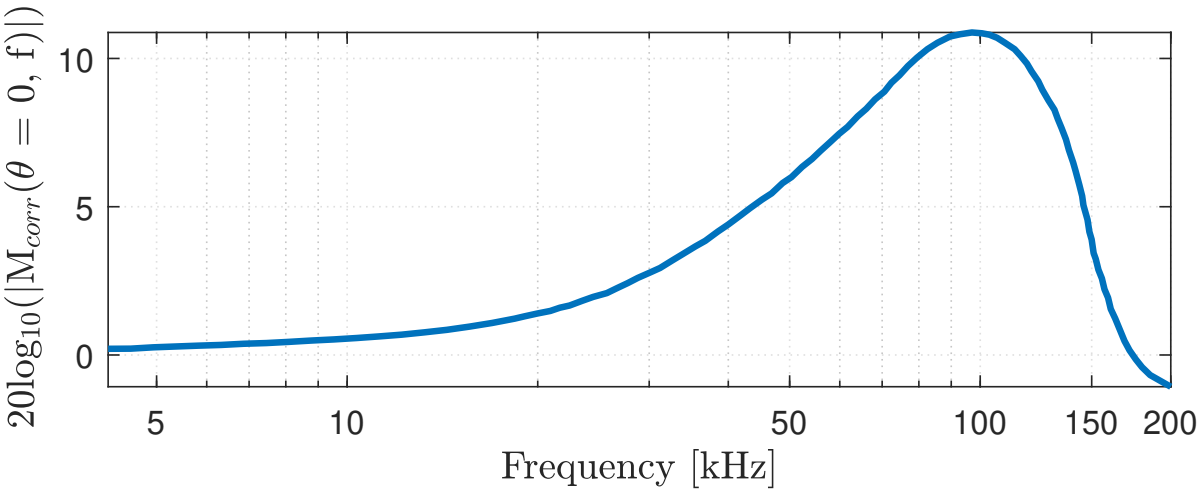

Figure 4.10: Digitized free-field correction curve for normal incidence for a type 4138 B&K

By combining the open circuit pressure response, relative to 250 Hz in Fig. 4.8, and the free field correction curve for normal incidence in Fig. 4.10 the free-field open circuit receiving voltage response of the microphone $|M_V|$ relative to 250 Hz can be determined.

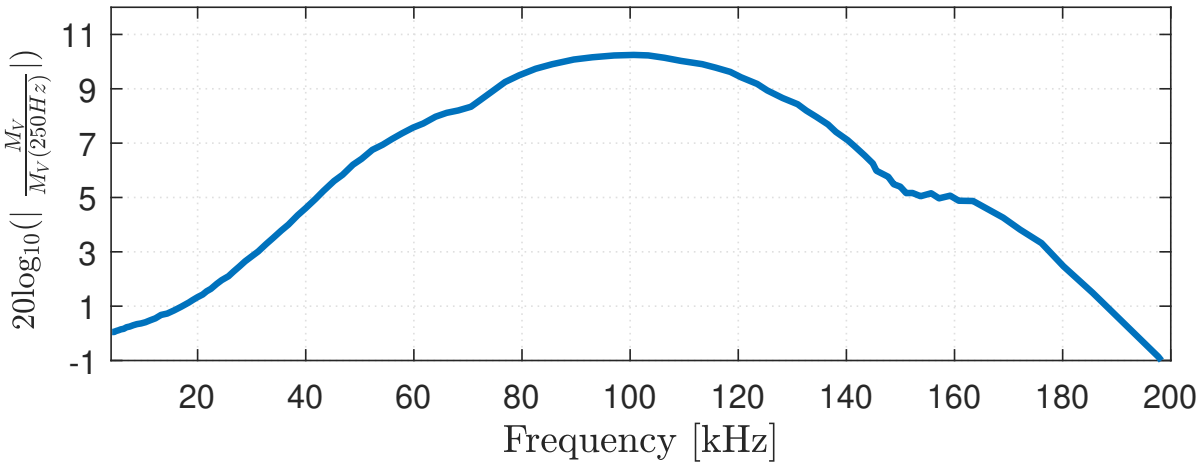

Figure 4.11: The free-field open circuit receiving voltage response of the microphone $|M_V|$ relative to 250 Hz for a typ 4138 B&K condenser microphone

4.4.1 Microphone calibration using a pistonphone

To obtain the free-field open circuit receiving voltage response of the microphone system, the receiving voltage response relative to 250 Hz in Fig. 4.11 is combined with a calibration measurement of the free-field open-circuit receiving voltage response at 250 Hz, $M_V(250Hz)$. The calibration is performed using a Brüel & Kjær 4228 pistonphone[69] with a DP-0774 adaptor connected to the pistonphone. The pistonphone produces an acoustic signal at a nominal frequency of 250 Hz. No free-field correction is needed at 250 Hz as the wavelength of the acoustic wave is much larger than the microphone dimensions [67].

Before the calibration can be started, the tip of the microphone with the preamplifier connected is inserted into the DP-0774 adaptor. The adaptor is then placed in the pistonphone

opening. The microphone and preamplifier are connected to the B&K 2636 measurement amplifier with a 20 dB input gain. The output from the measurement amplifier is recorded by the Tektronix DPO3012 oscilloscope.

After inserting the microphone and adapter in the pistonphone, the pistonphone is turned on. A total of 49 periods from the recorded voltage signal, V^{rec}, is used to calculate the peak-to-peak amplitude, V_{pp}^{rec}, using a fast Fourier transform. The recorded waveform can be seen in Fig. 4.12.

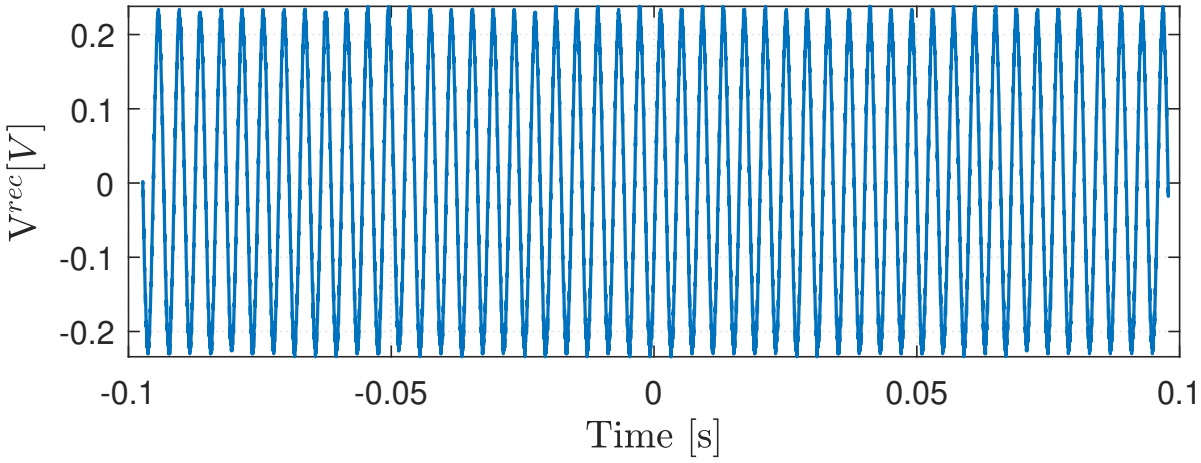

Figure 4.12: Recorded waveform on the Tektronix DPO3012 oscilloscope, of the signal, V^{rec}, with a 20 dB amplifier gain.

The fast Fourier transform returns a peak-to-peak amplitude

$$V_{pp}^{rec}(250Hz) = 0.4428 \text{ V}. \tag{4.4}$$

The effective open-circuit output voltage, V_{rms}^{open}, from the microphone is then calculated, which gives

$$V_{rms}^{open}(250Hz) = \frac{V_{pp}^{rec}(250Hz)}{10 \cdot 2 \cdot \sqrt{2}} = 15.655 \text{ mV}, \tag{4.5}$$

where the recorded signal, V_{pp}^{rec} has been divided by a factor, $10^{20/20} = 10$, to account for the 20 dB amplification in the measurement amplifier.

The Brüel & Kjær 4228 pistonphone produces a nominal sound pressure level SPL_{Stated} of 124.11 $\pm$0.09 dB re 20 μPa at a frequency of 251.2 Hz $\pm$0.2 %[88]. The stated SPL is valid at 20 °C, with an ambient pressure of 1013 hPa and a 65% relative humidity. If calibration is performed under conditions differing from this, the actual SPL can be found by [88]

$$SPL_{actual} = SPL_{stated} + \Delta L_p + \Delta L_V \tag{4.6}$$

,where ΔL_p is the correction for ambient pressure, and ΔL_V is the correction for load volume [88]. The correction value ΔL_V = 0 for a Brüel & Kjær 1/8-inch Type 4138 microphone when a DP0704 adaptor is connected to the pistonphone[69]. The correction value ΔL_p can be read off the UZ0004 barometer that comes with the pistonphone [88]. The calibration used during this work was performed at an ambient pressure of 1030 hPa, giving a correction value ΔL_p = 0.15. The actual SPL under the calibration conditions can then be calculated to

$$SPL_{actual} = 124.11 \text{ dB} + 0.15 \text{ dB} + 0 \text{ dB} = 124.26 \text{ dB}. \tag{4.7}$$

The free-field effective pressure, p_{ff}, produced by the pistonphone at 250 Hz can then be calculated

$$p_{ff}(250Hz) = p_{ref} \cdot 10^{\left(\frac{SPL_{actual}}{20}\right)} = 20\mu\text{Pa} \cdot 10^{\left(\frac{124.26}{20}\right)} = 32.661 \text{ Pa} \tag{4.8}$$

The free-field open-circuit receiving sensitivity M_V, at 250 Hz, can then be calculated using Eq.2.7.

$$M_V(250Hz) = \frac{V_{rms}^{open}(250Hz)}{p_{ff}(250Hz)} = \frac{15.655 \text{ mV}}{31.661 \text{ Pa}} = 0.494 \text{ mV/Pa} \tag{4.9}$$

By combining the measured free-field open-circuit receiving sensitivity at 250 Hz and the free-field open circuit receiving voltage response relative to 250 Hz in Fig. 4.11, the calibrated free-field open circuit receiving voltage response, $M_{V,cal}$, can be calculated. The calibrated free-field open circuit receiving voltage response from 4 to 200 kHz is shown in Fig. 4.13

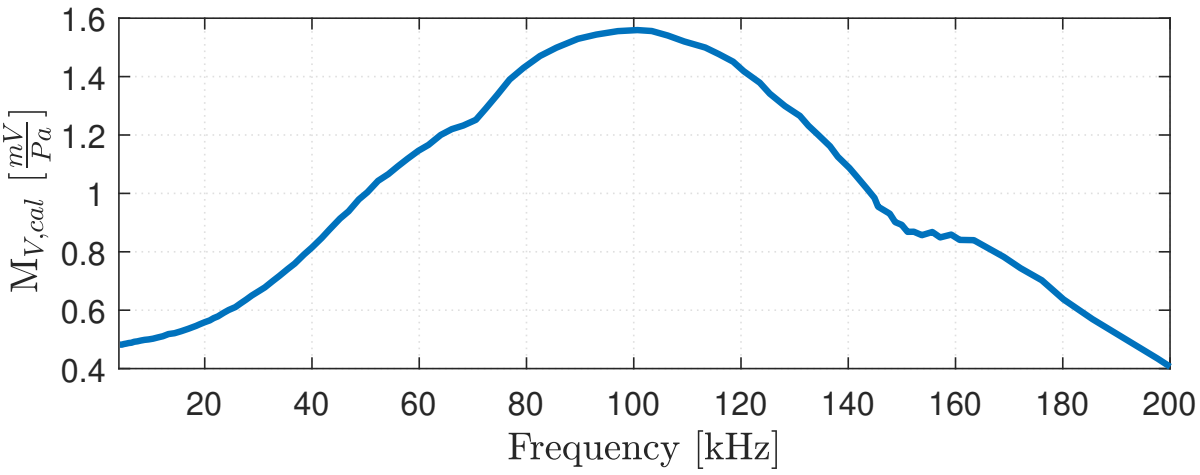

Figure 4.13: The calibrated free-field open circuit receiving voltage response M_V from 4 to 200 kHz.

4.5 Dimension measurements

Accurate determination of the physical dimensions of piezoelectric disks and transducer components is crucial for ensuring the precision of finite element simulations. The primary device used during the dimension measurements is a Mitutoyo MDH-25 digimatic micrometer [89]. The micrometer has a measurement range of 0 to 25 mm, a 1 μm resolution, and a accuracy $\pm$ 0.5 μm.

When doing measurements on parts larger than 25 mm a Mitutoyo 530 series caliper [90] is used. The caliper has a measurement range of 0 to 150 mm, a resolution of 0.01 mm, and a accuracy of $\pm$ 0.03 mm.

A total of of 10 measurements are performed spread evenly across the measured surface. The mean value $\bar{x}$ and, the standard deviation of the measurements, σ_x are then calculated. The total measurement uncertainty is then calculated by combining the standard deviation of the measurements, σ_x and the accuracy of the measurement instrument, σ_{instr}

$$\sigma_{tot} = \sqrt{\sigma_x^2 + (\sigma_{instr}^2)}. \tag{4.10}$$

4.6 Signal processing

The peak to peak amplitude, V_{pp}^{rec}, of the recorded electric waveforms, V_{0m} and V_6 at node 0m, and 6, respectively, is extracted through signal processing. Specifically V_{pp}^{rec} is extracted in the portion of the burst referred to as steady state, using a Fourier transform. The steady state interval of the burst is surrounded by two transient periods; one in the start and one at the end. For V_{0m} the transient period is very short compared to V_6, as the signal does not experience any distortion caused by acoustic transmission through the transducer and fluid medium. The latter is happening for the waveform, V_6, where the length of the transient periods vary with the frequency of the signal. The transient periods of an example waveform can be seen between the red dotted lines in Fig. 4.14. The steady state interval is the portion of the signal between the two transient regions, where the amplitude of the sinusoidal peaks remain constant.

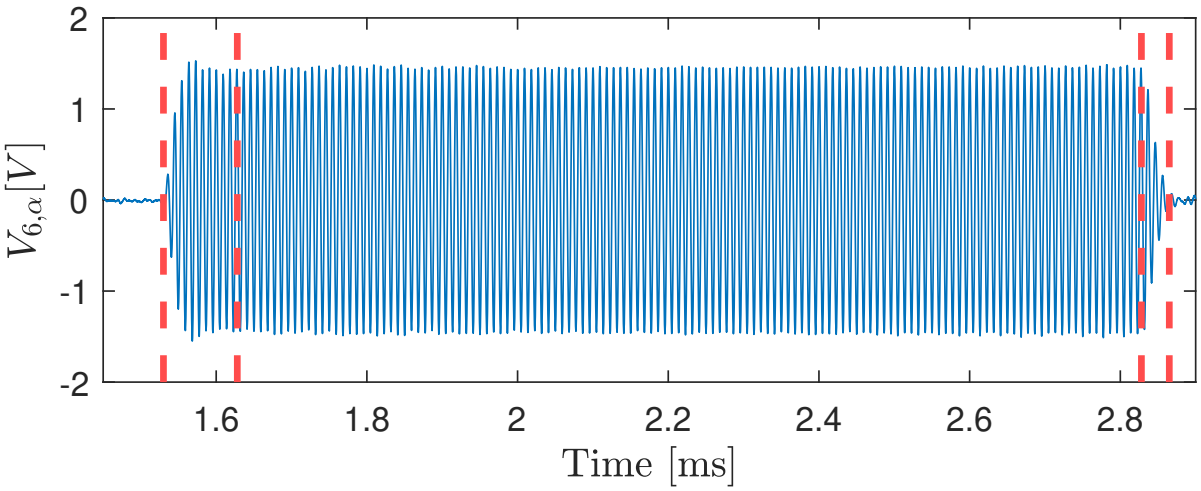

Figure 4.14: Example waveform of the recorded signal V_6 with transient periods in the start and end of the signal

During this work the steady state is assumed to be reached halfway through the burst for all frequencies. This assumption is observed to be reasonable, except for at a few selected frequencies where the transducer has a low transmitting sensitivity, S_V. At these frequencies the steady state can not be reached, as random noise disturbs the recorded signal. This could possibly be avoided by increasing the output voltage from the signal generator, but the signal generator used during this work can not generate voltages higher than $V_{pp} = 20$ V . An example of a burst where the steady state is not reached can be seen in Fig. 4.15.

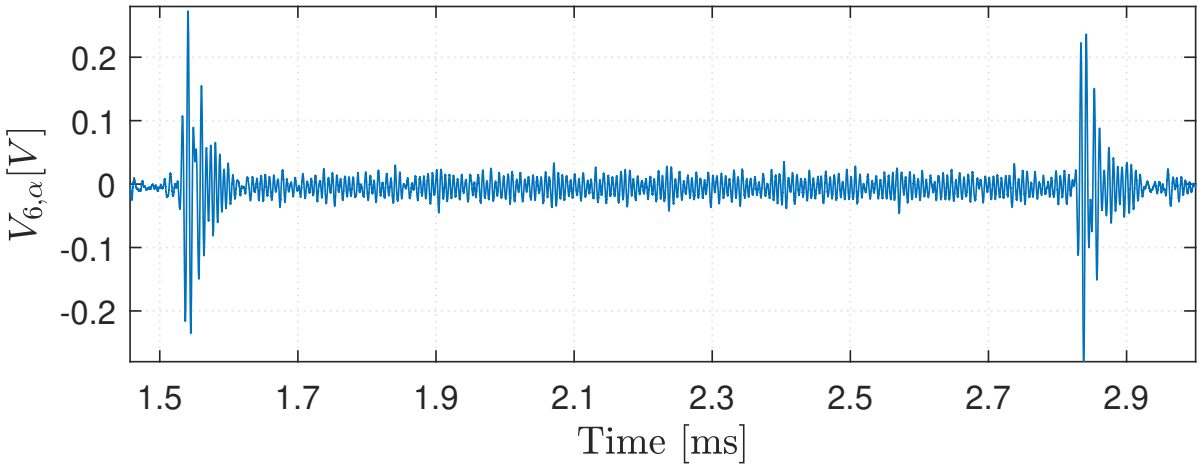

Figure 4.15: Example waveform of the recorded signal V_6 without a clear steady state portion

In order to extract the second half of the burst, the arrival time, t_0 of the electric burst, V_0, is recorded. The samples of V_0 recorded at $t > t_0 + 0.75$ ms is assumed to contain the second half of the burst. To acquire the second half of the acoustic burst, V_6, the transmission time, t_t, through the fluid medium is calculated. The speed of sound in air is calculated using the MATLAB script **`Speedofsoundandre`**. The V_6 samples recorded at $t > t_0 + t_t + 0.75$ ms is assumed to contain the second half of the burst, V_6.

The 25 first periods in the second half of both the electric and acoustic burst is than extracted using a zero crossing detection method. The zero crossing detection used during this work is described in Sec. 5.3.1 in [29]. Before this can be done the DC component of the burst is removed by subtracting the mean value of the recorded waveform.

After extracting 25 periods of the recorded signal a Fourier transform is performed to get the recorded amplitude V_{pp}^{rec}. The signals are sero padded to a total of 200 000 samples.

Chapter 5

Results - Initial simulation study

In this chapter, the results from an initial simulation study are presented. The simulations are performed to further investigate and reproduce a series of results presented by a group of scientists at Los Alamos National Laboratories in the three following papers: [40–42].

The three papers are all related to a numerical investigation of the resonance and vibration characteristics of radial modes of laterally stiffened piezoelectric disks. Lateral stiffening is modeled using a spring with spring stiffness, k, and vibration characteristics of the piezoelectric disk are investigated with increasing lateral stiffness [40]. The numerical simulations in [40–42] are preformed in the finite element software COMSOL. The presented results are of special interest because an increasing lateral stiffness is claimed to significantly reduce the side-lobes in the beam pattern [40]. Therefore, a further investigation of the presented results is needed to see if the results can be reproduced, and to see if this approach can be used when constructing an ultrasonic gas transducer.

In this work, the lateral stiffening is modeled using the FEMP structure **`Piezodisk_Clamped_Fluid`**. The term "clamp" refers to a circular ring that is placed around the outer edge of a piezoelectric disk, and thus restricting (rigid) or partially restricting radial motion. In [40] a rigid clamping effect where the disk is not allowed to move in the radial direction is achieved by increasing the spring stiffness to $k = \infty$. During this work a similar effect is achieved by increasing the density of the clamp material to $\rho = 1 \times 10^8 \ \frac{\text{kg}}{\text{m}^3}$. The value 1×10^8 is based on a convergence test, where the density was gradually increased to the point where a change in the conductance could no longer be detected.

In Sec. 5.1, the simulation results presented in [40] for a single piezoelectric disk without a clamp, are compared to simulation results obtained using the FEMP structure **`Piezodisk_Fluid`**. The comparison is made to confirm that the utilized material data and FEMP can provide similar results to what was presented in [40].

In Sec. 5.2, the simulation results presented in [40] for a laterally stiffened piezoelectric disk with infinite spring stiffness, k, are compared to the results obtained using the FEMP structure **`Piezodisk_Clamped_Fluid`**.

In Sec. 5.3 a further investigation of the voltage source sensitivity, S_V for the disk and clamped disk vibrating in air is presented. The beam pattern of the sound pressure fields shown in [40] for a disk and clamped disk vibrating in water will also be presented.

5.1 Free disk

A free PZT-5A disk with radius, $r_p = 25$ mm and thickness, $T_p = 2.1$ mm is simulated vibrating in both air and water using the FEMP structure **`Piezodisk_Fluid`**. The radius and thickness of the disk comply with the values given in [40]. The PZT-5A, water, and air material parameters are provided in Tabs. 3.2, 3.9 and 3.8 respectively. The simulations are performed in the frequency range 20 to 200 kHz with a 100 Hz resolution.

5.1.1 Electrical admittance

Fig. 5.1 shows the simulated electrical conductance, G_T and susceptance, B_T for the disk vibrating in air, as a function of frequency, from 20 to 200 kHz. The three peaks in the conductance represent the three first radial modes of the disk, RM1, RM2 and RM3.

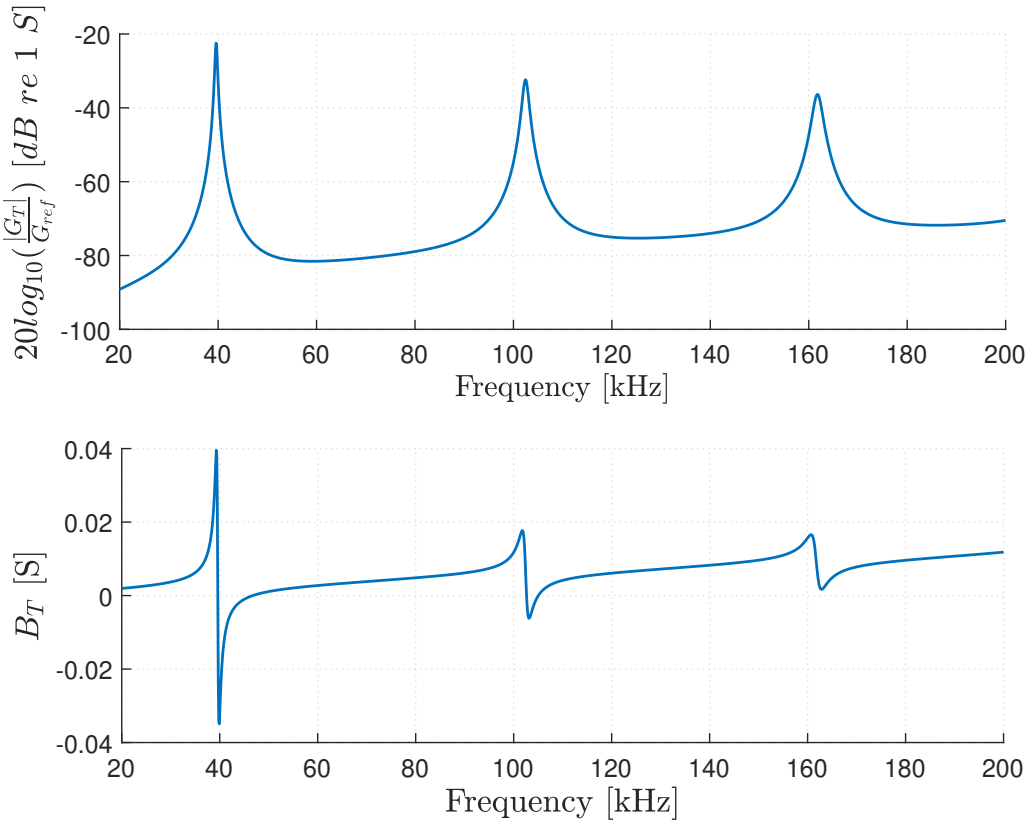

Figure 5.1: Simulated electrical conductance and suceptance of a (25x2.1) mm PZT-5A disk vibrating in air, using FEMP.

In Tab. 5.1, the series resonant frequencies of the three modes shown in Fig. 5.1 are compared to the series resonant frequencies simulated by Chilara et al. in [40].

Table 5.1: Comparison of the simulated series resonant frequencies for a free (25x2.1) mm PZT 5A disk vibrating in air using FEMP, and the simulated series resonant frequencies presented in [40].

Mode	Free disk, FEMP [kHz]	Free disk [40] [kHz]
RM1	39.6	39.6
RM2	102.5	102.5
RM3	161.8	161.8

Tab. 5.1 shows that the series resonance frequencies, f_s, agree with the simulation results presented in [40]. This is a confirmation that the FEMP structure **`Piezodisk_Fluid`** provides similar results to that of the simulation software used in [40].

5.1.2 Front surface displacement

Fig. 5.2a shows the z-component of the simulated out-of-plane displacement pattern on the front surface of the free PZT-5A disk. The disk is simulated vibrating in air using FEMP at the third radial mode RM3. The blue line is the simulated result without any material damping, contrary to the orange dotted line, where dielectric and mechanical damping is included for the material using the simplified approach described in Sec. 3.3 ($Q_m = 75$, $\tan(\delta) = 0.02$). Only a minor difference between the lossless and lossy simulation can be spotted at the disk's outer edge.

Fig. 5.2b shows the z-component of the simulated out-of-plane displacement pattern on the front surface of the free PZT-5A disk as presented in [40]. The disk is simulated vibrating in air at the third radial mode RM3. The red dotted line is a Bessel function fit $|J_0(\alpha r)|$ [40] and has nothing to do with dampening in Fig. 5.2a.

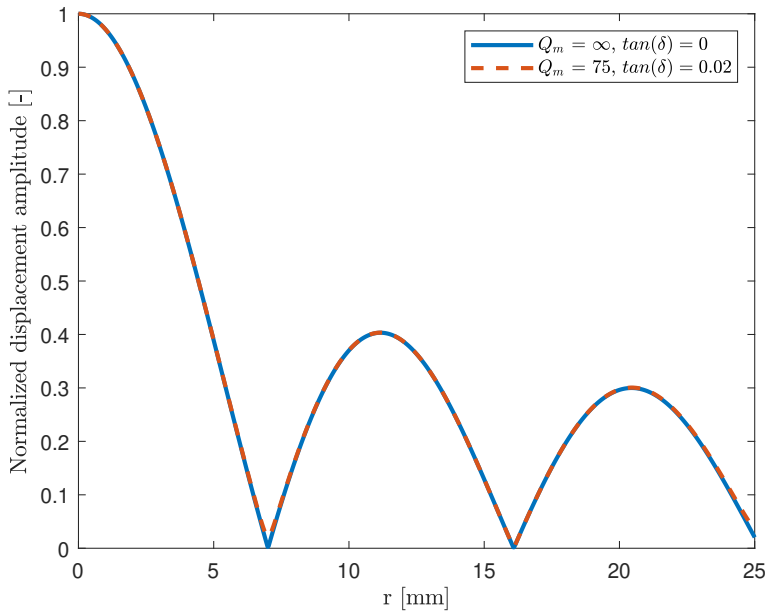

(a)

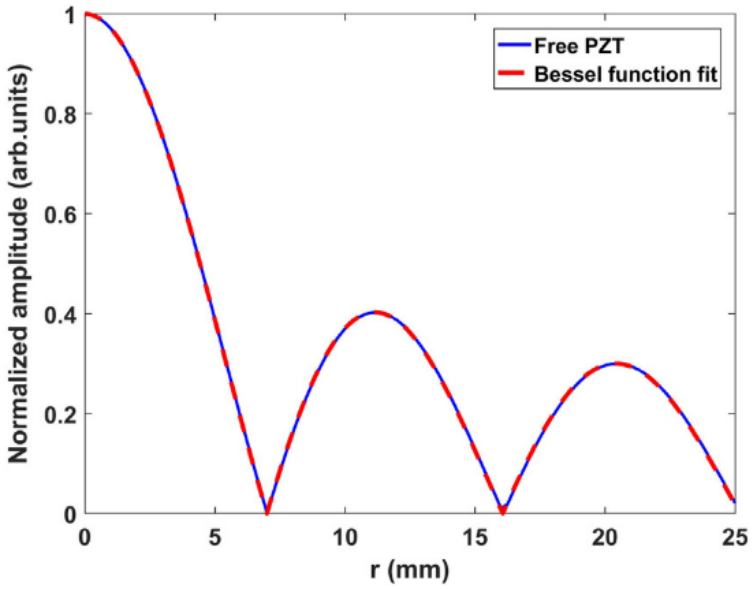

(b)

Figure 5.2: (a) FEMP Simulated z-component of the out-of-plane displacement pattern on the front surface of a free PZT-5A disk vibrating in air at the third radial mode, RM3 (161.8 kHz). (b) Same as in Fig. 5.2a, but the simulation result presented by Chilara et al. in [40].

Fig. 5.2 show that the simulated z-component of the out-of-plane displacement pattern on the front surface of a free PZT-5A using FEMP also agrees with the results presented in [40].

5.1.3 Sound pressure field

For the sound pressure field simulations the distance R_{inf} has been increased to 0.4 m, in order to obtain a higher resolution in the pressure phase information. The finite elements offer higher resolution compared to the infinite elements due to their increased node density. Because of the increase in computation time associated with such a large value for R_{inf}, the sound pressure field of the free PZT-5A disk has only been simulated at 161.8 kHz.

The sound pressure field simulations presented in [40] are all done using water as the fluid medium. This is convenient, since simulations of piezoelectric disks in water tend to be a lot less computationally expensive than in air. The acoustic wavelength in air is about one-quarter of the wavelength in water. As a result, more than four times as many elements are required to mesh the same fluid region with a certain number of elements per wavelength for the in-air case compared to the in-water case [14].

When the fluid medium is water, the fluid loading effect on the piezoelectric transducer is usually not negligible [14]. Although this is more important for heavier fluid loads, the water loading will lead to a downward frequency shift of the series resonant frequencies, and a widening of the resonance peaks [91]. This means that the sound pressure field simulation performed at 161.8 kHz in water is not located at the series resonance frequency of RM3 in water. The frequency shift is noticeable, but is only about 800 Hz, resulting in a new series resonance frequency, f_s = 161 kHz for RM3 in water.

The simulated sound pressure field of the free PZT-5A disk vibrating in water at 161.8 kHz using FEMP is shown in Fig. 5.3a. The results presented by Chilara et al. in [40] for the same frequency is shown in Fig. 5.3b

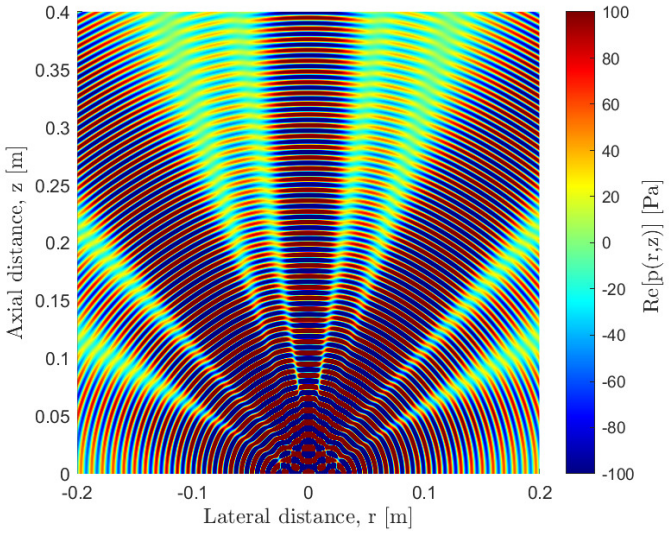

(a)

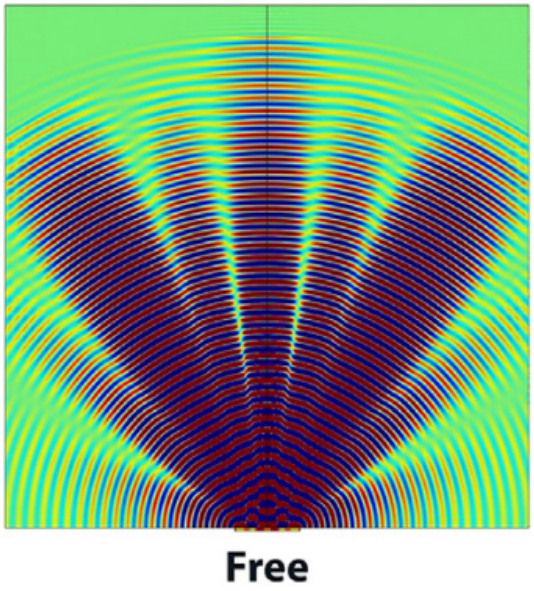

(b)

Figure 5.3: (a) FEMP Simulated sound pressure field for a free (50 mm x 2.1 mm) PZT-5A disk vibrating in water at 161.8 kHz. The real component of the sound pressure p is plotted as a function of the radial distance, r from -0.2 m to 0.2 m, and the axial distance, z from 0 to 0.4 m (b) Same as in Fig. 5.3a, but as simulated by Chilara et al. in [40]

The radiation patterns in Fig. 5.3a and 5.3b show clear similarities. The result shown in Fig. 5.3b is a snapshot from a time domain simulation. This might explain some of the difference between the two figures. In Fig. 5.3a a frequency domain simulation is shown. This should give the same result as a time domain simulation with an infinite pulse length; Therefore the wave fronts can not be seen. For the snapshot in Fig. 5.3b, the wave-fronts is propagating outwards as a function of time.

5.2 Clamped disk

A rigidly clamped PZT-5A disk with radius, r_p = 25 mm and thickness, t_p = 2.1 mm is simulated vibrating in both air and water using the FEMP structure **`Piezodisk_Clamped_Fluid`**. The outer radius of the clamp, $r_{c,o}$ = 50 mm. The material parameters used to simulate the disk, and air is the same as for the free disk in Sec. 5.1. Steel is used as a basis for the clamping material parameters, as listed in Tab. 3.4. In order to achieve a rigid clamping effect, the steel density ρ has been increased to $\rho = 1 \times 10^8 \frac{\text{kg}}{\text{m}^3}$. This value is based on a convergence test, where the density was gradually increased to the point where a change in the conductance could no longer be detected. The simulations are performed in the frequency range 20 to 200 kHz with a 100 Hz resolution.

5.2.1 Electrical admittance

Fig. 5.4 shows the simulated electrical conductance and susceptance for the clamped disk vibrating in air, as a function of frequency, from 20 to 200 kHz. The three peaks in the conductance, G_T represent the three first radial modes of the disk.

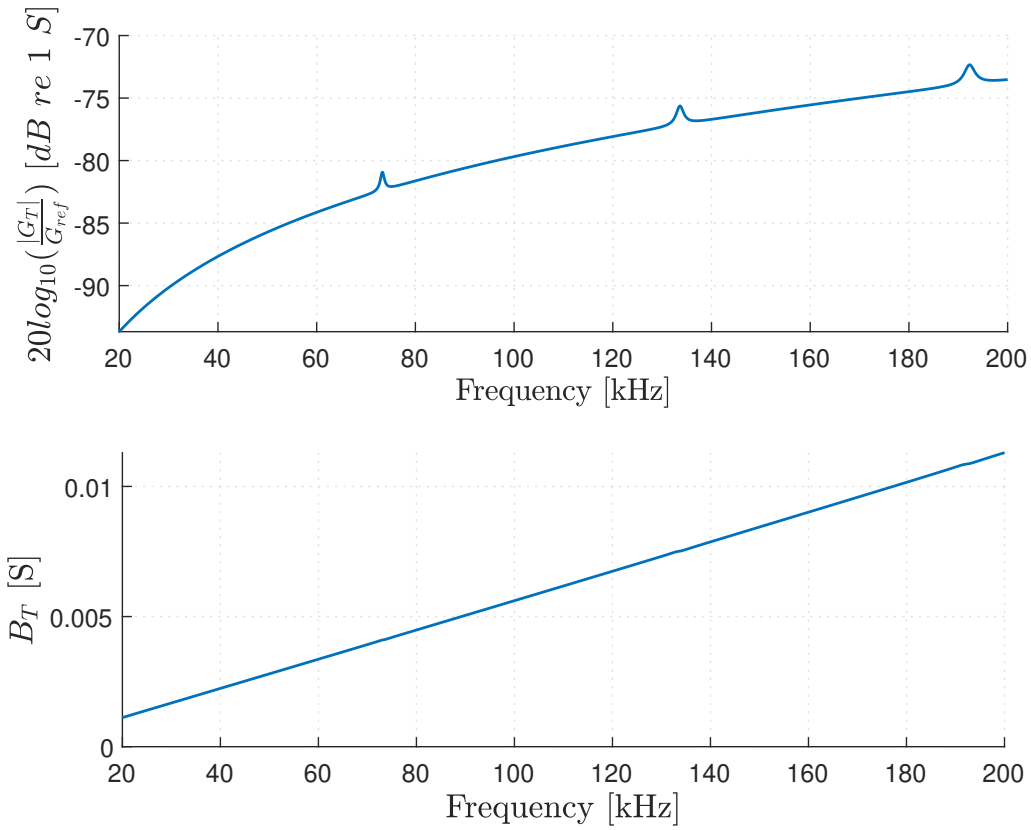

Figure 5.4: Simulated electrical conductance and susceptance of a clamped (25x2.1) mm PZT-5A disk vibrating in air, using FEMP.

In Fig. 5.4 the conductance peaks have decreased significantly compared to the free disk in Fig. 5.1. This might indicate that the radiated energy from the disk has been decreased because of the clamp. An upward shift in the resonating frequency for each mode can also be seen.

In Tab. 5.2, the series resonant frequencies of the three modes shown in Fig. 5.4, are compared to the clamped series resonant frequencies simulated by Chilara et al. in [40].

Table 5.2: Comparison of the simulated series resonant frequencies for a clamped (25x2.1) mm PZT 5A disk vibrating in air using FEMP, and the simulated series resonant frequencies presented in [40].

Mode	Clamped disk [kHz]	Clamped disk, FEMP [40] [kHz]
RM1	73.3	73.3
RM2	133.6	133.6
RM3	192.3	192.3

The series resonant frequencies for the three first radial modes in Tab. 5.2 all match. This indicates that the clamping method used in this work show similar results to that of the spring-loaded clamping method in [40]. A further investigation of the out-of-plane displacement pattern and radiated sound pressure field will be done in order to confirm this.

5.2.2 Front surface displacement

Fig. 5.5a shows shows the z-component of the simulated out-of-plane displacement pattern on the front surface of the clamped PZT-5A disk vibrating in air at the third radial mode, RM3. The blue line is the normalized displacement amplitude without any material damping. The orange dotted line has a dielectric and mechanical damping in the PZT material ($Q_m = 75$, $\tan(\delta) = 0.02$).

Fig. 5.5b shows the z-component of the simulated out-of-plane displacement pattern on the front surface of the clamped disk at third radial mode RM3 as presented in [40]. The red dotted line is a Bessel function fit $|J_0(\alpha r)|$ [40] and has nothing to do with dampening in Fig. 5.2b.

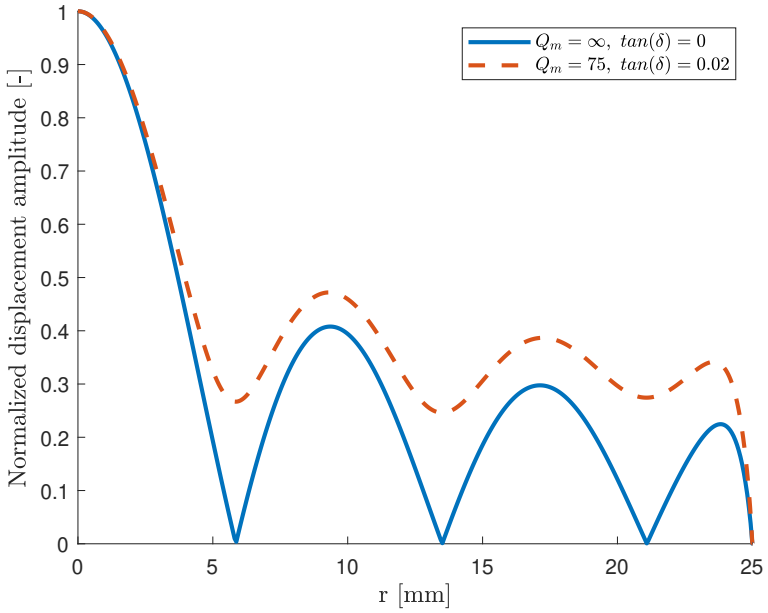

(a)

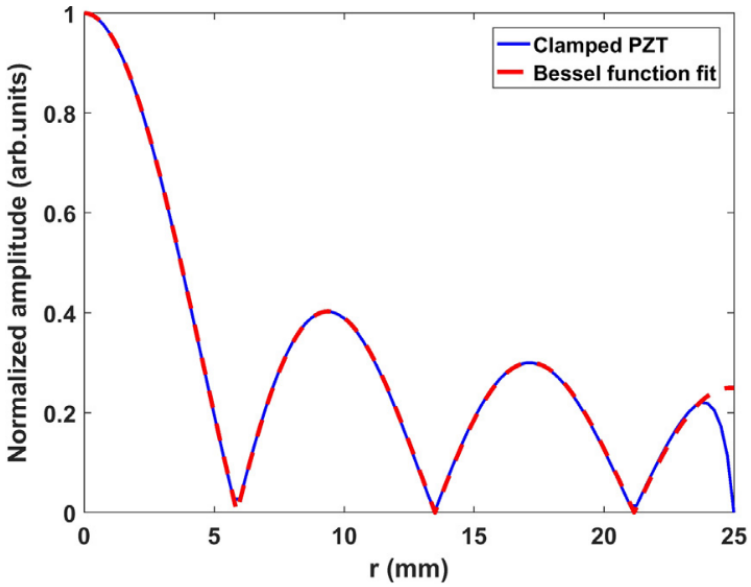

(b)

Figure 5.5: (a) FEMP Simulated z-component of the out-of-plane displacement pattern on the front surface of the clamped PZT-5A disk vibrating in air at the third radial mode, RM3 (192.3 kHz) (b) Same as in Fig. 5.5a, but the simulation result presented by Chilara et al. in [40].

The two lines in Fig. 5.5a show a significant deviation in the displacement pattern between the lossy and lossless simulation. There are no longer any displacement nodes with zero displacement on the disk surface, but the displacement pattern is still recognizable with the same locations for minimums and maximums.

The lossless simulation in Fig. 5.5a shows agreement with the simulation results in Fig. 5.5b. This is another indication that the clamping method used in FEMP gives corresponding results to the spring loaded clamping method used in [40]

5.2.3 Sound pressure field

For the same reasons as for the free disk in Sec. 5.1.3 the distance R_{inf} = 0.4 m for the sound pressure field simulations. The clamped disk sound pressure field in water has been simulated at 161.8 kHz. This is no longer the series resonance frequency of the disk after clamping, but this is the frequency at which the pressure field was presented in [40]. Why the sound pressure field was not shown at the series resonance frequency of RM3 at 192.3 kHz is unknown. The downward shift in the resonant frequency caused by the water fluid loading can not be seen in the clamped simulation. This means that the resonant frequency for the third radial mode is at 192.3 kHz when the disk vibrates in both air and water.

The simulated sound pressure field of the clamped PZT-5A disk vibrating in water at 161.8 kHz using FEMP is shown in Fig. 5.3a. The results presented by Chilara et al. in [40] for the same frequency is shown in Fig. 5.3b

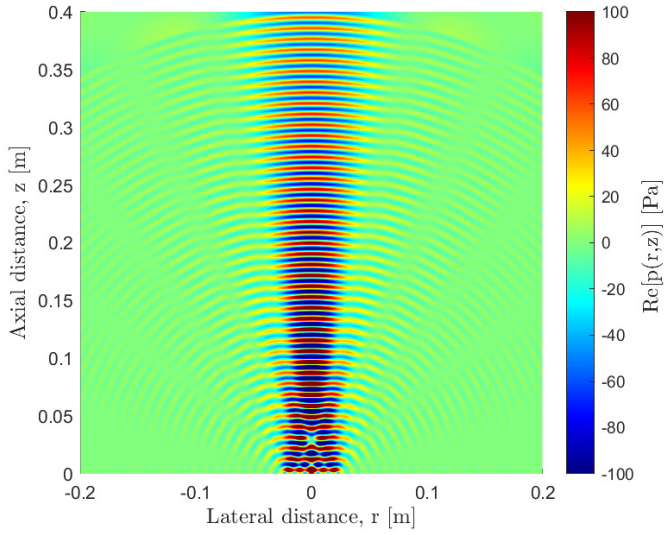

(a)

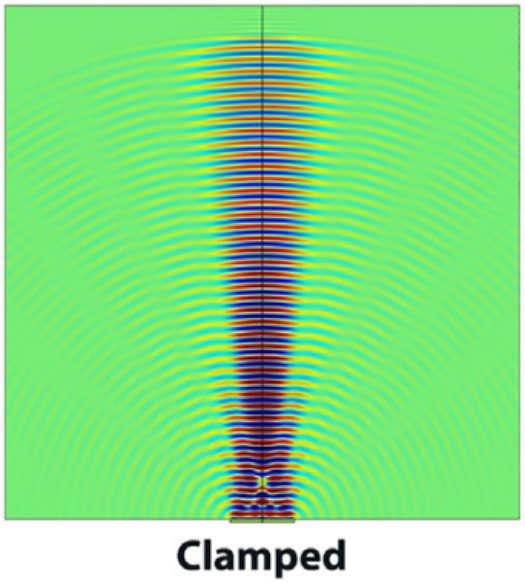

(b)

Figure 5.6: FEMP Simulated sound pressure field for a clamped (50 mm x 2.1 mm) PZT-5A disk vibrating in water at 161.8 kHz. The real component of the sound pressure p is plotted as a function of the radial distance, r from -0.2 m to 0.2 m, and the axial distance, z from 0 to 0.4 m (b) Same as in Fig. 5.6a, but as presented in [40] by Chilara et al.

The radiation patterns in Figs. 5.6a and 5.6b show clear similarities. This indicates that the results presented in [40] are reproducible using FEMP. When comparing the simulated sound pressure fields for the free and clamped disk, a clear decrease in side-lobes can be seen. A decrease in side lobe levels is presumed to be beneficial for a transducer in gas, and the results are therefore to be investigated further.

5.3 Further investigations

The results in Sec. 5.1 and 5.2 confirm that the FEMP structures **`Piezodisk_Clamped_Fluid`** and **`Piezodisk_Fluid`** can be used to create similar results to what was presented by Chi-

lara et al. in [40]. This allows for a further investigation of transducer characteristics of interest that was not presented in [40–42].

Fig. 5.7 shows the beam pattern for the sound pressure field simulation presented in Figs. 5.3a and 5.6a. The PZT-5A piezoelectric disk with nominal dimensions (50 mm x 2.1 mm) is simulated vibrating in water at 161.8 kHz.

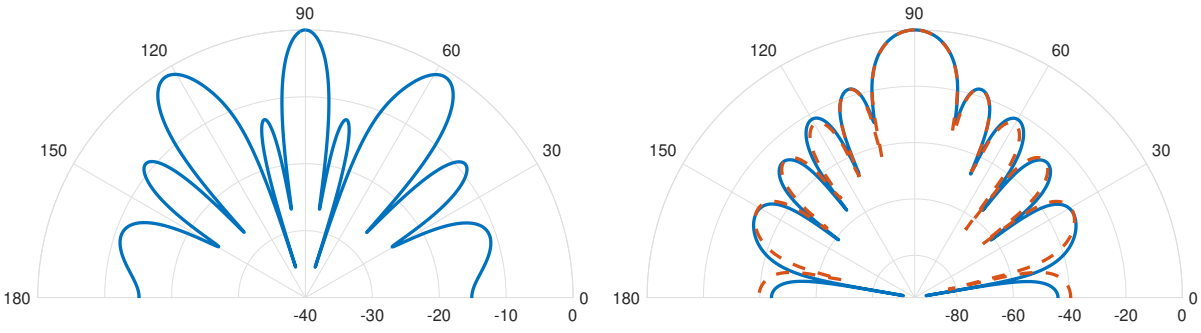

Figure 5.7: (a) Beam pattern of the radiated sound pressure field in Fig. 5.3a. (b) Beam pattern of the radiated sound pressure field in Fig. 5.6a in blue. The baffled piston model radiating in water at 161.8 kHz in orange.

Fig. 5.7a shows a beam pattern with two large side lobes that are almost equal in strength to that of the main lobe. A beam pattern with large side lobes is sub-optimal for the transducer applications that are considered during this work. The beam pattern in Fig. 5.7b shows a clear reduction in the side lobe levels. The orange dotted lines are the beam pattern generated by a piston source with the same dimensions at 161.8 kHz in water. The two results are closely aligned. The beam patterns in Fig. 5.7 give a more traditional description of the sound pressure fields in Figs. 5.3a and 5.6a. The sound pressure field in Fig. 5.6a can be misleading by not showing the side lobes that are present.

The voltage source sensitivity of the free and clamped disk radiating in air has also been simulated. The Simulated voltage source sensitivity from the FEMP structures **`Piezodisk_Fluid`** and **`Piezodisk_Clamped_Fluid`** are presented in Fig. 5.8. Fig ref shows that the radial clamping significantly decreases the voltage source sensitivity around the radial modes. A transducer with a high voltage source sensitivity is desired, and the simulation results are thus not very encouraging.

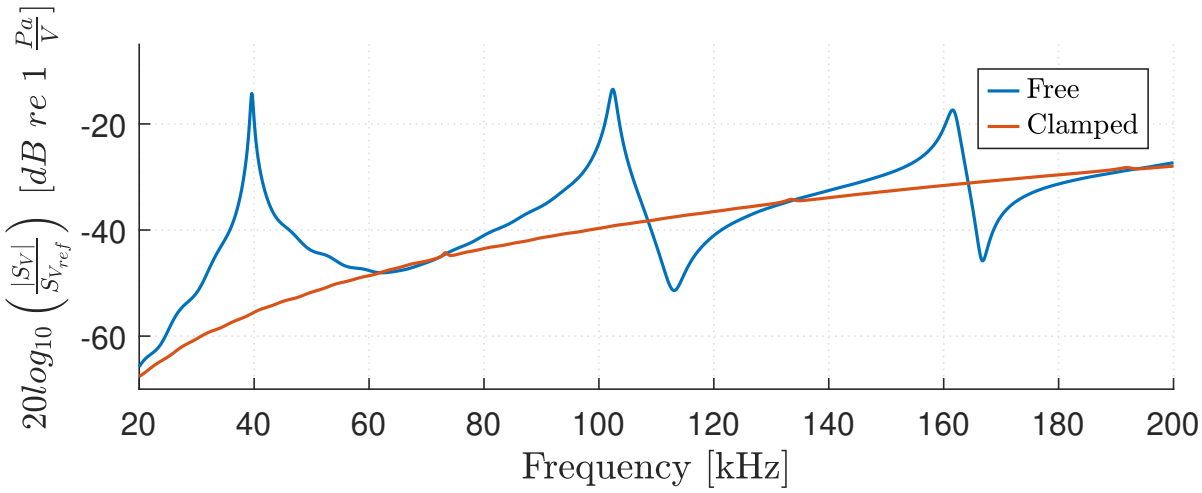

Figure 5.8: The simulated voltage source sensitivity S_V of the disk with and without a clamp.

Fig. 5.8 shows that the radial clamping significantly decreases the voltage source sensitivity around the radial modes. A transducer with a high voltage source sensitivity is desired, and the simulation results are thus not very encouraging for practical use. The Effects from radial clamping of piezoelectric disks will be studied further in the next Chapter.

Chapter 6

Results - Transducer Design Study

This chapter presents a transducer design study aimed at creating a transducer with favourable characteristics for measuring the speed of sound in gas. The characteristics include a high voltage source sensitivity, a large frequency bandwidth, and a beam pattern with a narrow main lobe, and small side lobe levels.

The design process uses the finite element software, FEMP, and the simulation structures presented in Sec. 3.4 to gradually build the transducer design. This gradual build-up allows for a deeper insight into each part's effect on the transducer characteristics. Some of the material parameters used in the simulations will be altered to study what transducer materials might benefit the characteristics.

The simulation results in Chapter 5 and [40] showed that rigid radial clamping of a piezoelectric disk can significantly decrease the side lobe levels. However, the beam pattern and sound pressure field simulations in Chapter 5 are mainly focused on the third radial mode, RM3, of a (50 mm x 2.1 mm) PZT-5A piezoelectric disk. This work will use the first radial mode, RM1, of a Pz27 piezoelectric disk with nominal dimensions (20mm x 2mm).

In Chapter 5 a unrealistically high density ($\rho_c = 1\times10^8 \frac{\text{kg}}{\text{m}^3}$) was used to simulate a rigid radial clamp. In Sec. 6.1, the FEMP structure **`Piezodisk_Clamped_Fluid`** will be used along with more realistic clamp densities to see if the effects shown in Chapter 5 can be seen when using lower-density materials and the Pz27 disks. In Sec. 6.2, the clamp length will be extended to resemble a transducer casing. In Sec. 6.3, a matching layer is applied to the piezoelectric disk and transducer casing to find the matching layer thickness that provides the best bandwidth and voltage source sensitivity, S_V. In Sec. 6.4, the thickness of the transducer backing layer will be decided. Sec. 6.5 summarizes the final transducer design. The final transducer design will be constructed in Chapter 7.

6.1 Clamped piezoelectric disk

In this section, the FEMP structure **`Piezodisk_Clamped_Fluid`** will be used to investigate if the same clamping effects shown in Chapter 5 are achievable with the Pz27 piezoelectric disks, and lower density clamp materials.

The FEMP structure **`Piezodisk_Clamped_Fluid`** simulates a partially clamped Pz27 piezoelectric ceramic disk, with radius, $r_p = 10.07$ mm, and thickness $T_p = 1.99$ mm vibrating in air. The clamp is ring-formed and has an inner radius, $r_i = r_p$, and outer radius, $r_o = 12.07$ mm. The thickness of the clamp, $T_c = T_p$.

The material parameters for steel in Tab. 3.4 are used as a basis for the clamp material. Multiple simulations where the density of the steel is altered are performed to see if a change

in density and the characteristic acoustic impedance of the clamp can lead to a reduction in the side lobes, or increase the transducer bandwidth. The longitudinal sound velocity c_l, the shear sound velocity c_s, and the mechanical quality factor Q_m are kept constant to reduce the simulation complexity. The clamp density, ρ_c, is varied between $1 \times 10^3 \frac{kg}{m^3}$ and $20 \times 10^3 \frac{kg}{m^3}$. The upper density is close to that of the densest know metal, osmium, which has a density $\rho = 22.61 \times 10^3 \frac{kg}{m^3}$ [92]. The material data for the piezoelectric material Pz27 can be found in Tab. 3.1.

In Sec. 6.1.1, the simulated electrical response functions are studied to see if the clamp density affects the series resonance frequency of the first and second radial modes. Sec 6.1.2 and 6.1.3 investigate how the change in ρ_c affects the voltage source sensitivity and beam pattern, respectively.

6.1.1 Electrical response functions

In Chapter 5, rigid clamping of a piezoelectric disk has been shown to strongly affect the disks series resonant frequencies, f_s. Fig. 6.1 shows the simulated conductance and susceptance of a clamped (20.14 mm $\times$ 1.99 mm) Pz27 piezoelectric disk with varying clamp density, as a function for frequency from 50 to 300 kHz. The conductance and susceptance of the free disk without a clamp can be seen in dark blue, marked as "Air". Fig. 6.2 shows the same plot as in Fig. 6.1, but only for the frequencies surrounding the first radial mode, RM1, from 80 to 105 kHz

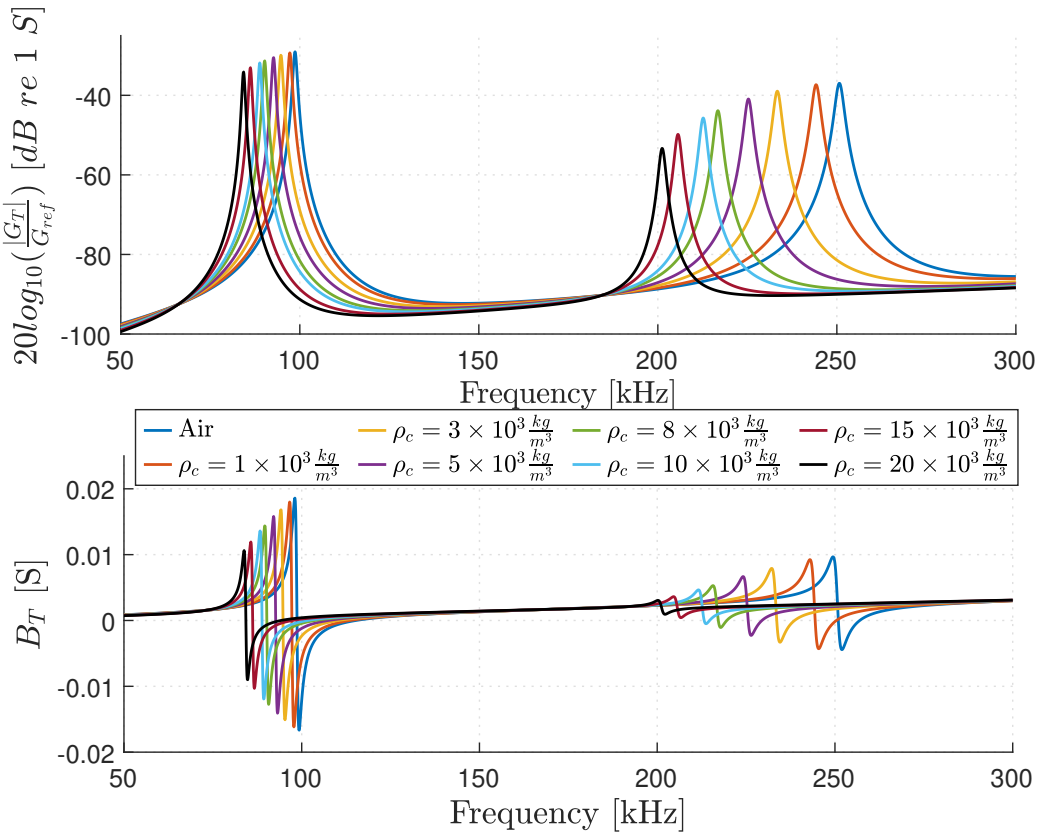

Figure 6.1: Comparison of the simulated electrical conductance and susceptance of a partially clamped (20.14 mm $\times$ 1.99 mm) Pz 27 piezoelectric disk vibrating in air, with varying clamp density ρ_c.

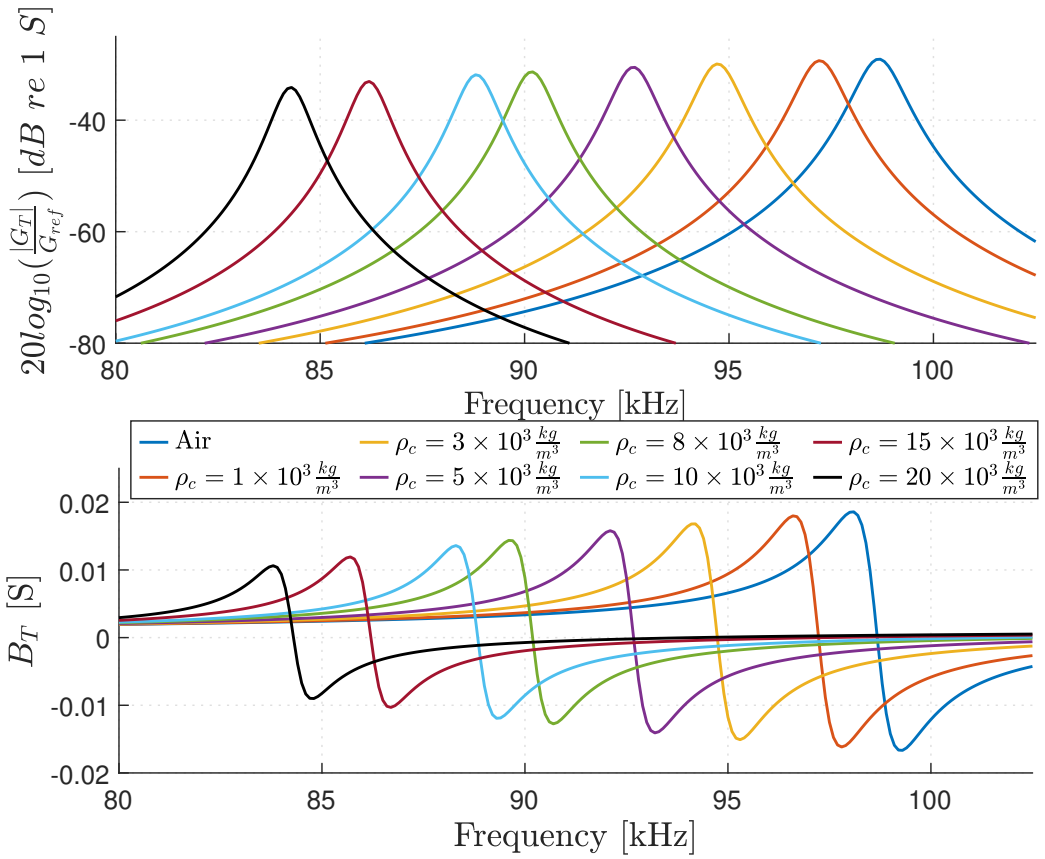

Figure 6.2: Same as Fig. 6.1, but from 80 to 105 kHz

Fig. 6.1 and 6.2 show a clear correlation between the clamp density and series resonant frequency. Additionally, it is worth noting that the conductance peaks show a slight decrease as the clamp density increases. The simulated series resonant frequencies at RM1 for the different clamp densities can be seen in Tab. 6.1.

Table 6.1: Simulated series resonant frequency, f_s with varying clamp density, ρ_c. The simulations are performed using the FEMP structure **`Piezodisk_Clamped_Fluid`**.

ρ_c [$\frac{kg}{m^3}$]	f_s RM1 [kHz]
Air	98.7
1×10^3	97.2
3×10^3	94.7
5×10^3	92.7
8×10^3	90.2
10×10^3	88.8
15×10^3	86.2
20×10^3	84.3

The frequency shift is quite significant for the denser clamping materials, with a shift of 14.4 kHz between the free, and the partially clamped disk with clamp density, $\rho_c = 20 \times 10^3 \frac{kg}{m^3}$. This downward frequency shift might have beneficial effects in some applications, but in this work, the transducer's operating frequency should be around 100 kHz. This indicates that a lighter material might be necessary for the transducer casing.

The observed downward frequency shift in this section is the opposite to what is observed in Figs. 5.1 and 5.4, where the clamp causes an increase in the series resonant frequency of the disk.

6.1.2 Voltage source sensitivity, S_V

The upper plot in Fig. 6.3 shows the voltage source sensitivity of a clamped (20.14 mm × 1.99 mm) Pz27 piezoelectric disk with varying clamp density, as a function of frequency from 50 to 300 kHz. The lower plot is identical to the upper plot but zoomed in around the first radial mode from 80 to 103 kHz. The voltage source sensitivity of the free disk without a clamp can be seen in dark blue, marked as "Air."

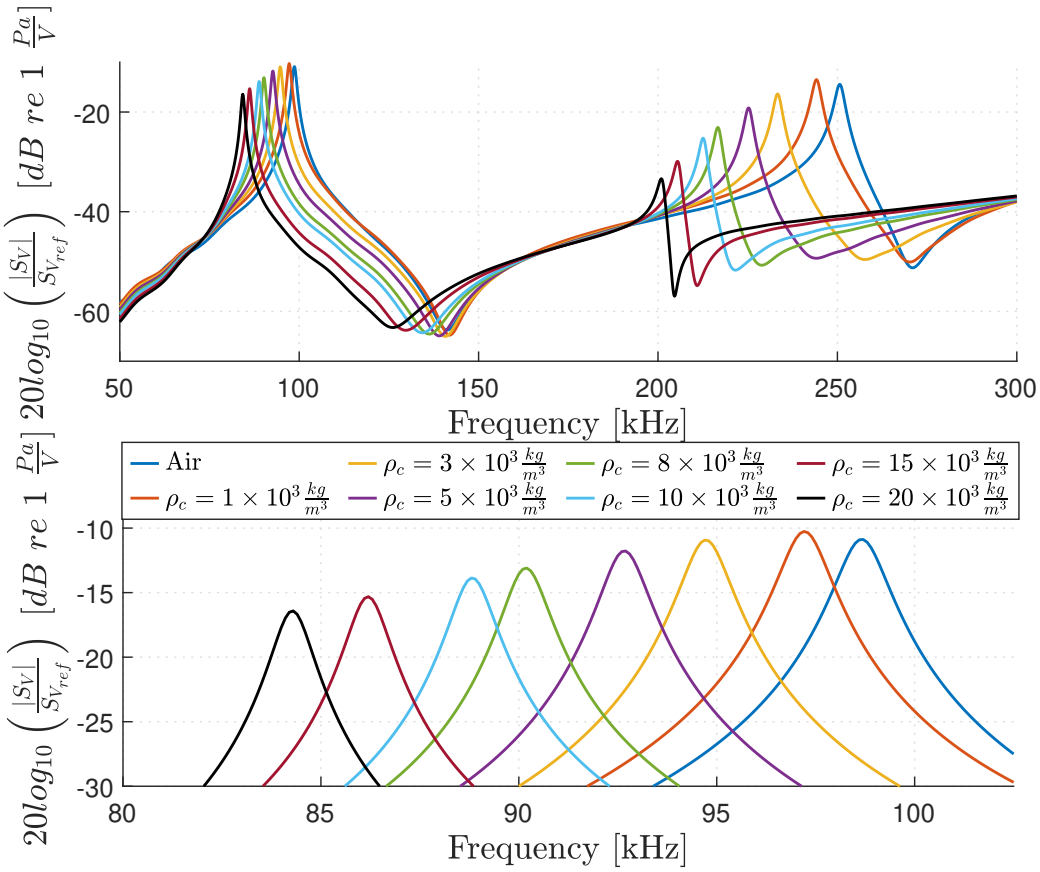

Figure 6.3: Comparison of the simulated voltage source sensitivity at 1 m, for a of a partially clamped (20.14 mm × 1.99 mm) Pz 27 piezoelectric disk vibrating in air, with varying clamp density, ρ_c.

Fig. 6.3 shows that the peaks in voltage source sensitivity follows the series resonance frequencies presented in Tab. 6.1. Similar to the peaks in conductance, the sensitivity is seen to decrease with an increasing clamp density, except for the clamp with $\rho_c = 1000\frac{kg}{m^3}$, where a 0.5 dB increase can be detected relative to the free disk in air.

6.1.3 Beam pattern

Fig. 6.4 shows a comparison of the beam pattern, $D(\theta)$ for a free and clamped disk, with three different clamp densities at their respective series resonance frequencies, f_s. The beam pattern is symmetrical around radial axis and is therefore only plotted for the angles [0 180°].

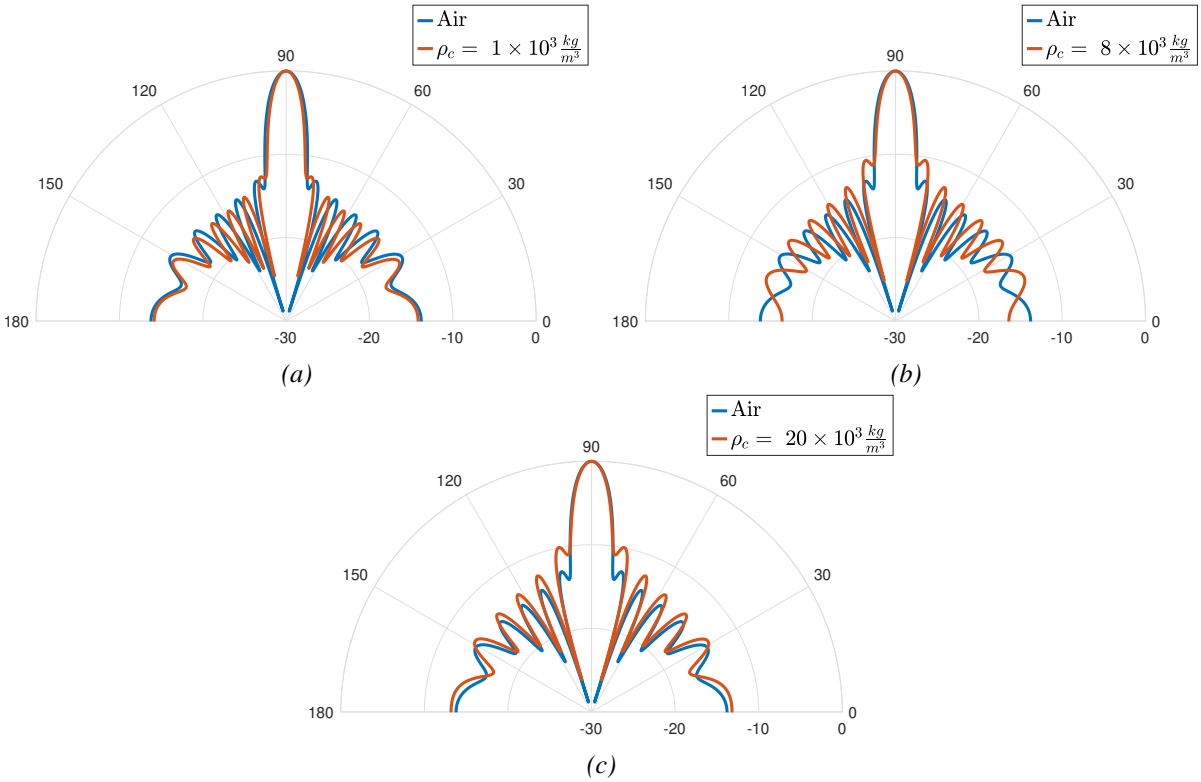

Figure 6.4: (a) Comparison of the simulated beam patterns for a free (20.14 mm × 1.99 mm) Pz 27 piezoelectric disk vibrating in air at f_s = 98.7 kHz, and a partially clamped disk with clamp density $\rho_c = 1 \times 10^3 \frac{kg}{m^3}$ vibrating in air at f_s = 97.2 kHz. (b) Same as in Fig. 6.4a, but with clamp density $\rho_c = 8 \times 10^3 \frac{kg}{m^3}$, and f_s = 90.2 kHz. (c) Same as in Fig. 6.4a, but with clamp density $\rho_c = 20 \times 10^3 \frac{kg}{m^3}$, and f_s = 84.3 kHz.

Fig. 6.4 shows that the lightest clamp, with density $\rho_c = 1 \times 10^3 \frac{\text{kg}}{\text{m}^3}$ causes a slight narrowing of the main lobe and a small increase of the first side lobe level. The clamp with density $\rho_c = 8 \times 10^3 \frac{\text{kg}}{\text{m}^3}$ causes less of a main lobe narrowing, and the side lobe levels have increased more than for the $\rho_c = 1 \times 10^3 \frac{\text{kg}}{\text{m}^3}$ case. The clamp with density $\rho_c = 20 \times 10^3 \frac{\text{kg}}{\text{m}^3}$ does not cause a main lobe a narrowing, and the side lobe levels have increased more than for the $\rho_c = 8 \times 10^3 \frac{\text{kg}}{\text{m}^3}$ case. Beam pattern simulations have been done for all seven clamp densities shown in the voltage source sensitivity and electrical plots, but all the beam patterns will not be shown here for practical reasons. Nevertheless, a trend can be seen, where the main lobe narrowing decreases and the first side lobe level increases with an increasing clamp density.

6.2 Piezoelectric disk with a transducer casing

In this section, the ring-formed clamp in Sec. 6.1 has been extended to a hollow cylinder using the FEMP structure **`Piezodisk_Casing_Fluid`**. This is done to see if the same effects shown in Sec. 6.1 can be seen for a piezoelectric disk with a transducer casing attached to the circumferential edge of the disk.

The FEMP structure **`Piezodisk_Casing_Fluid`** simulates a piezoelectric ceramic disk with a radius, $r_p = 10.07$ mm, and thickness $T_p = 1.99$ mm vibrating in air inside a transducer casing. The casing is a hollow cylinder with an inner radius, $r_i = r_p$, and outer radius, $r_o = 12.07$ mm. The length of the transducer casing, which extends behind the piezoelectric disk, $T_c = 8$ mm. In the final construction of the transducer, the casing needs to have a length exceeding 10 mm to accommodate both a front and backing layer. However, due to the extended computational time required to model the complete casing with an increased R_{inf} distance, only a small section of the casing is included in the current model. This is a simplification, but the results should indicate the effect a full-length casing has on the transducer characteristics.

Based on the results shown in Sec. 6.1, the casing material parameters have been replaced with that of nylon. Nylon has a density $\rho = 1.12 \times 10^3 \frac{\text{kg}}{\text{m}^3}$ [93], which is close to the clamp density $\rho_c = 1 \times 10^3 \frac{\text{kg}}{\text{m}^3}$ that led to an increase in voltage soruce sensitivity and narrowing of the main lobe in Sec. 6.1.

Three different casing densities are simulated. This is done to see if a change in density and characteristic acoustic impedance in the casing shows similar results to that of the clamp in Sec. 6.1. The three densities include the original density for nylon $\rho_c = 1.12 \times 10^3 \frac{\text{kg}}{\text{m}^3}$, a density close to steel $\rho_c = 8 \times 10^3 \frac{\text{kg}}{\text{m}^3}$ and a density close to osmium $\rho_c = 20 \times 10^3 \frac{\text{kg}}{\text{m}^3}$. The longitudinal sound velocity c_l, shear sound velocity c_s, and mechanical quality factor Q_m are kept constant as for nylon. The material data for nylon and Pz27 can be seen in Tab. 3.5 and 3.1, respectively.

6.2.1 Electrical response functions

Fig. 6.5 shows the simulated conductance and susceptance of a (20.14 mm $\times$ 1.99 mm) Pz27 piezoelectric disk inside a transducer casing. The density of the clamp material is altered, and the conductance and susceptance are plotted as a function of frequency from 50 to 300 kHz. The conductance and susceptance of the free disk without a casing can be seen in blue, marked as "Air."

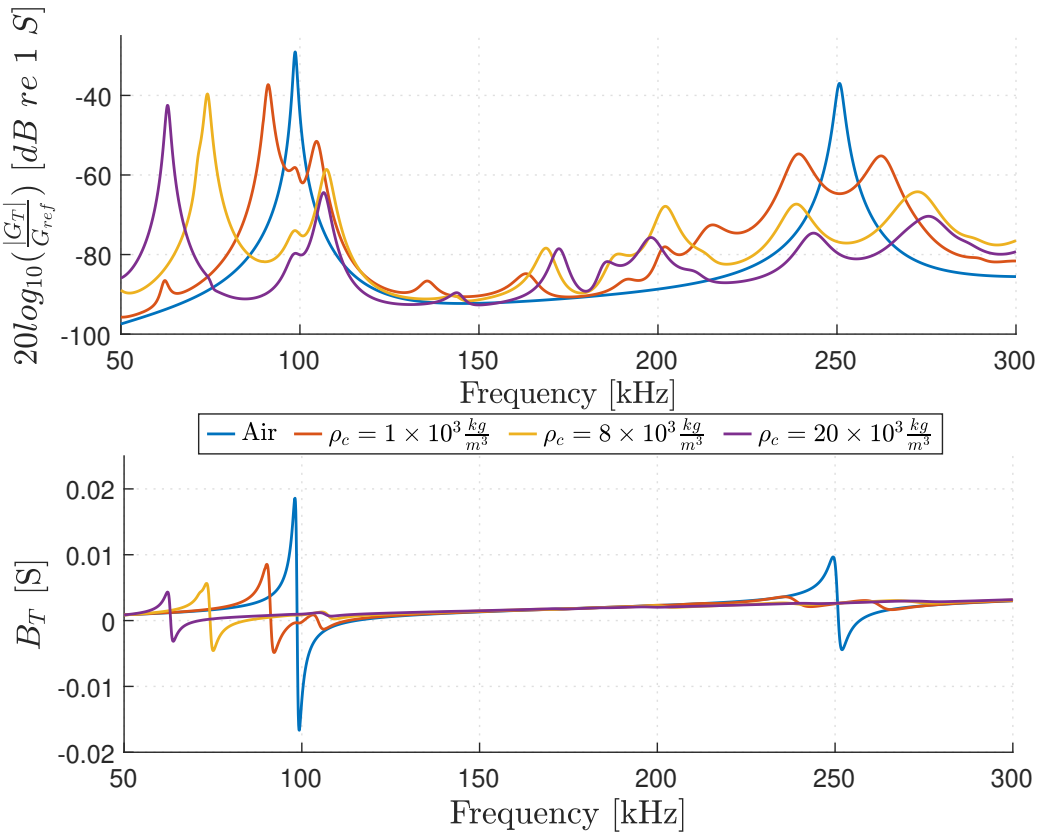

Figure 6.5: Comparison of the simulated electrical conductance and susceptance of a (20.14 mm × 1.99 mm) Pz 27 piezoelectric disk inside a transducer casing, vibrating in air, with varying casing density ρ_c.

Fig. 6.5 shows similar results to that of the partially clamped disk in Sec. 6.1. As the casing density increases, the series resonant frequency of the disk drops. The magnitude of the conductance peaks are also seen to decrease with increasing clamp density. In contrast to the conductance plot of the clamped disks in Fig. 6.1 several smaller modes can be seen for the disk inside the casing. These modes are possibly caused by standing waves in the transducer casing.

Tab. 6.2 shows the series resonant frequencies of the first radial mode, RM1 for the three different casing densities.

Table 6.2: Simulated series resonant frequency, f_s while varying the casing density, ρ_c. The simulations are performed using the FEMP structure ***`Piezodisk_Casing_Fluid`***.

ρ_c [$\frac{kg}{m^3}$]	f_s RM1 [kHz]
Air	98.7
1.12×10^3	91.1
8×10^3	74.2
20×10^3	63.0

When compared to the resonant frequencies, f_s of the clamped disk with similar densities in Tab. 6.1 the frequencies are seen to decrease even further for the disks with a casing. As mentioned previously this indicates that the Nylon with density $\rho_c = 1.12 \times 10^3 \frac{kg}{m^3}$ is a good choice when trying to construct a transducer with operating frequency around 100 kHz. The

simulation results show that higher density materials might cause a significant decrease in the series resonant frequency.

6.2.2 Voltage source sensitivity, S_V

Fig. 6.6 shows the simulated voltage source sensitivity of a (20.14 mm × 1.99 mm) Pz27 piezoelectric disk inside a transducer casing. The density of the clamp material is altered, and the voltage source sensitivity is plotted as a function of frequency from 50 to 300 kHz. The voltage source sensitivity of the free disk without a casing can be seen in blue, marked as "Air."

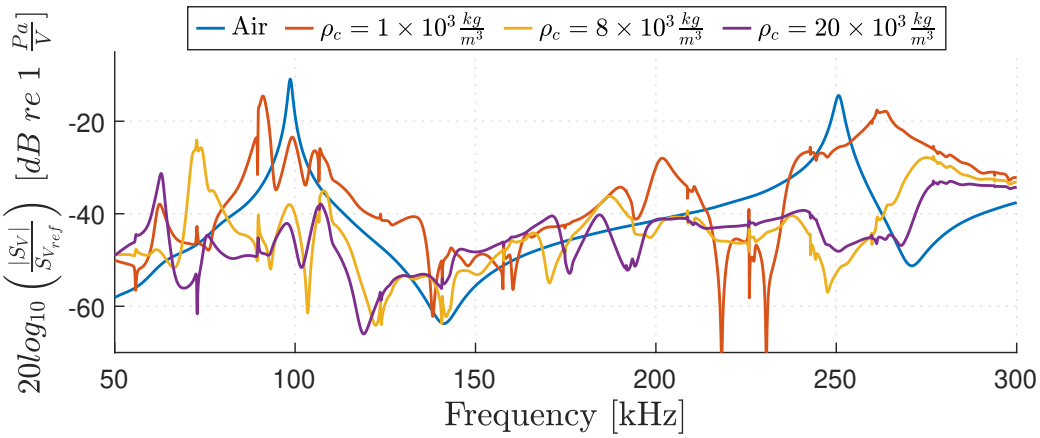

Figure 6.6: Comparison of the simulated voltage source sensitivity at 1 m, for a (20.14 mm × 1.99 mm) Pz 27 piezoelectric disk inside a transducer casing vibrating in air, with varying clamp density, ρ_c.

Fig. 6.6 shows that the largest peaks in voltage source sensitivity around the first radial mode of the disk follows the series resonance frequencies presented in Tab. 6.2. When compared to the voltage source sensitivity of the clamped disk in Fig. 6.3 the voltage source sensitivty of the disk with casing is seen to fluctuate a lot more. This fluctuation might be caused by acoustic contributions from the transducer casing vibrating in the air. The magnitude of the voltage source sensitivity is also seen to decrease with an increasing casing density, ρ_c, similar to what is seen for the clamped disk. The small increase in voltage source sensitivity that could be seen for the clamped disk with clamp density $\rho_c = 1 \times 10^3 \frac{\text{kg}}{\text{m}^3}$ in Sec. 6.1.2 is not seen for the casing with density, $\rho_c = 1.12 \times 10^3 \frac{\text{kg}}{\text{m}^3}$.

6.2.3 Beam pattern

Fig. 6.7 shows a comparison of the beam pattern, $D(\theta)$, for a free disk and a disk inside a casing, with three different casing densities at their respective series resonance frequencies f_s.

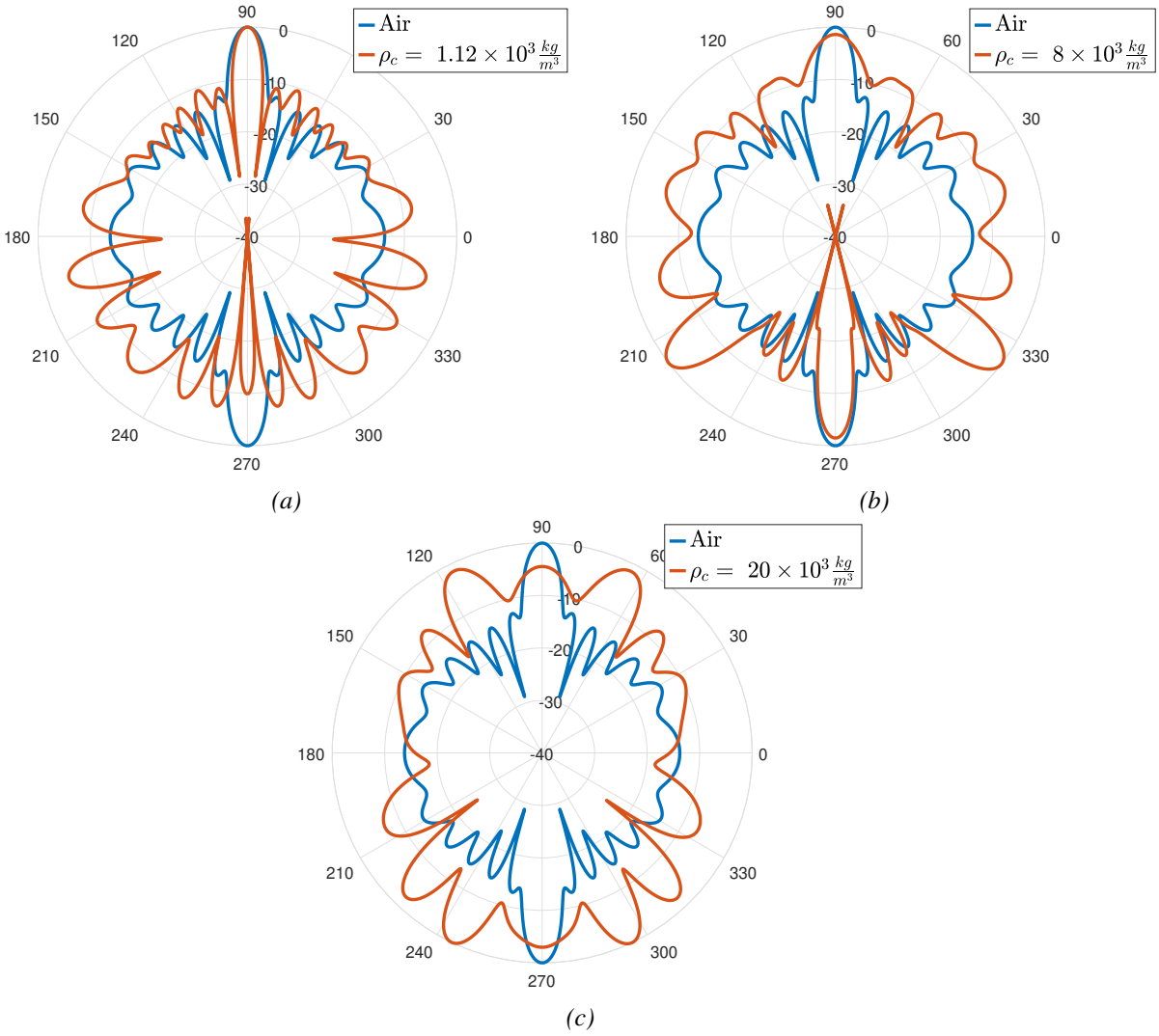

Figure 6.7: Comparison of the simulated beam patterns for a free (20.14 mm × 1.99 mm) Pz 27 piezoelectric disk vibrating in air at f_s = 98.7 kHz, and the same disk inside a casing with density $\rho_c = 1.12 \times 10^3 \frac{kg}{m^3}$ vibrating in air at f_s = 91.1 kHz. (b) Same as in Fig. 6.7a, but with casing density $\rho_c = 8 \times 10^3 \frac{kg}{m^3}$, and f_s = 74.2 kHz. (c) Same as in Fig. 6.7a, but with casing density $\rho_c = 20 \times 10^3 \frac{kg}{m^3}$, and f_s = 63.0 kHz.

Fig. 6.7 shows that the beam pattern of the higher density casings does no longer have a strong main lobe, as can bee seen for the free disk. The acoustic radiation is most powerful at the sides, which might indicate that a lot of the acoustic radiation comes from the transducer casing. The transducer with casing density $\rho_c = 1.12 \times 10^3 \frac{\text{kg}}{\text{m}^3}$ does maintain the main lobe, and a small narrowing can be seen. The narrowing is similar to what was seen for the clamped disk with clamp density $\rho_c = 1 \times 10^3 \frac{\text{kg}}{\text{m}^3}$ in Sec. 6.1.3. The acoustic radiation to the sides has also increased for the casing with density $\rho_c = 1.12 \times 10^3 \frac{\text{kg}}{\text{m}^3}$. Based on these results, the following simulations will utilize the nylon material data presented in Tab. 3.5 for the transducer casing.

6.3 Piezoelectric disk with a casing and matching layer

Because of an impedance mismatch between the Pz27 disks and air, a matching layer is required to transfer acoustic energy from the disk to the air more efficiently. The use of a quarter

wavelength matching layer of the correct material should, when using plane wave theory, lead to a total transmission of acoustic energy from the disk to air, as shown in Sec. 2.2. Using material data from Tab. 3.1 the Pz27 piezoelectric disk has a characteristic acoustic impedance

$$Z_p = \rho_p c_{l,p} = 29.4 \text{ MRayl.}$$

From Tab. 3.8 the characteristic acoustic impedance of air

$$Z_a = \rho_a c_a = 415 \text{ Rayl.}$$

By using Eq. 2.13, the ideal quarter wavelength matching layer characteristic acoustic impedance is

$$Z_m = \sqrt{Z_p Z_a} = 110 \text{ kRayl.}$$

No known solids that can be used in a transducer construction have this low of a characteristic acoustic impedance, and a compromise has therefore been made.

The matching layer material used in this work is Aplex R3, which is a non conductive synthetic foam with a low specific gravity, high hydrostatic compressive strength and chemical resistance [58]. The material is supplied in sheet form and can then be machined into detailed components [58].

By using the adjusted longitudinal sound velocity, c_l, from Tab. 3.3 and the series resonance frequency, f_s, for the piezoelectric disk inside a nylon casing with density ρ_c = 1.12 $\times 10^3$ $\frac{\text{kg}}{\text{m}^3}$ from Tab. 6.2, the quarter wavelength thickness, $t_{m,\frac{\lambda}{4}}$, of the matching layer can be calculated to

$$T_{m,\frac{\lambda}{4}} = \frac{c_l}{4 f_s} \approx 5.8 \text{ mm.} \tag{6.1}$$

To investigate if the quarter wavelength thickness is the ideal matching layer thickness, simulations are conducted using the FEMP structure **`PiezodiskCasingFront`** from Sec. 3.4. The Pz27 piezoelectric disk is simulated with dimensions of 20.14 mm $\times$1.99 mm. The total length of the nylon casing is varied for each simulation because of the change in the matching layer thickness, T_m. The total length of the casing T_c is equal to the thickness of the matching layer plus an additional 10 mm of casing extending from the front of the disk and backwards. If the matching layer thickness T_m = 4.9 mm, this gives a total casing thickness

$$T_c = T_m + 10 \text{ mm} = 14.9 \text{ mm}$$

The casing has an inner radius r_i = 10.07 mm and an outer radius r_o = 12.07 mm. Between each simulation the thickness of the matching layer was first changed in increments of 0.2 mm from 6.2 to 4.6 mm, in order to find the thickness, T_m that offers the best bandwidth and air coupling.

6.3.1 Voltage source sensitivity, S_V

Three simulations of the voltage source sensitivity magnitude, $|S_V|$ with the three different matching layer thicknesses, T_m = 5.8 mm, T_m = 5.4 mm and T_m = 4.8 mm in the frequency range 70-140 kHz are presented in Fig. 6.8.

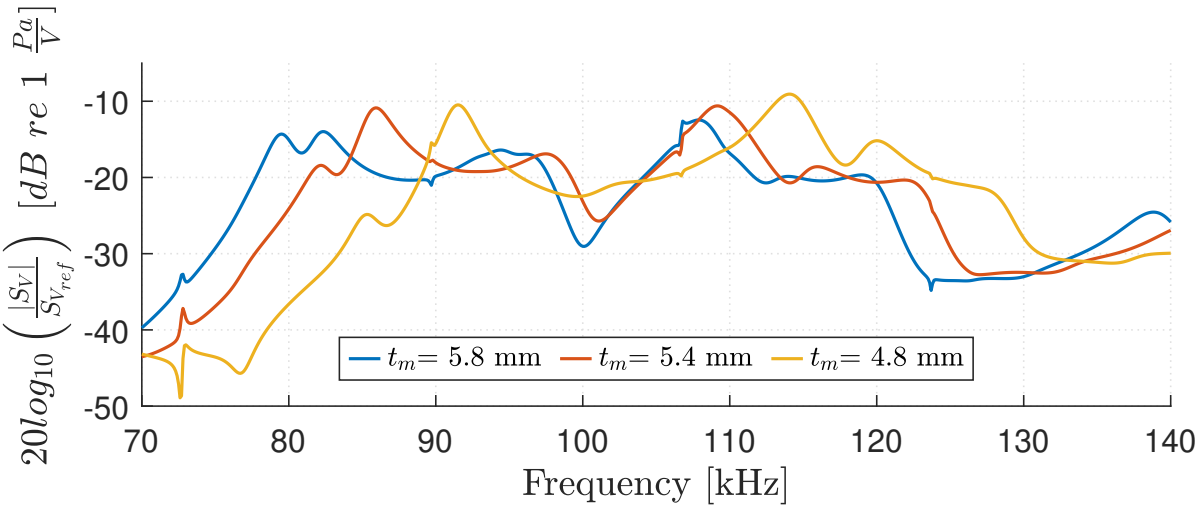

Figure 6.8: Comparison of the simulated voltage source sensitivity of a (20.14 mm ×1.99 mm) Pz27 piezoelectric disk vibrating in air inside a casing with a varying matching layer thickness, T_m

Fig. 6.8 shows that a matching layer thickness, T_m = 4.8 mm gives a better voltage source sensitivity, and a smoother frequency response than the quarter wavelength thickness $T_{m,\frac{\lambda}{4}}$ = 5.8 mm. The dip in $|S_V|$ around 100 kHz, that can be observed for T_m = 5.8 mm, is something that should be avoided.

A second round of simulations with thickness increments of 0.1 mm, from T_m = 5.1 mm to T_m = 4.7 mm, are conducted to see if any improvement can be made. Based on the results from these simulations, the best matching layer thickness is found to be, T_m = 4.9 mm. A comparison of the voltage source sensitivity for a disk and casing with matching layer thickness T_m = 4.9 mm, and a single (20.14 mm ×1.99 mm) piezoelectric disk, from 70-140 kHz can be seen in Fig. 6.9.

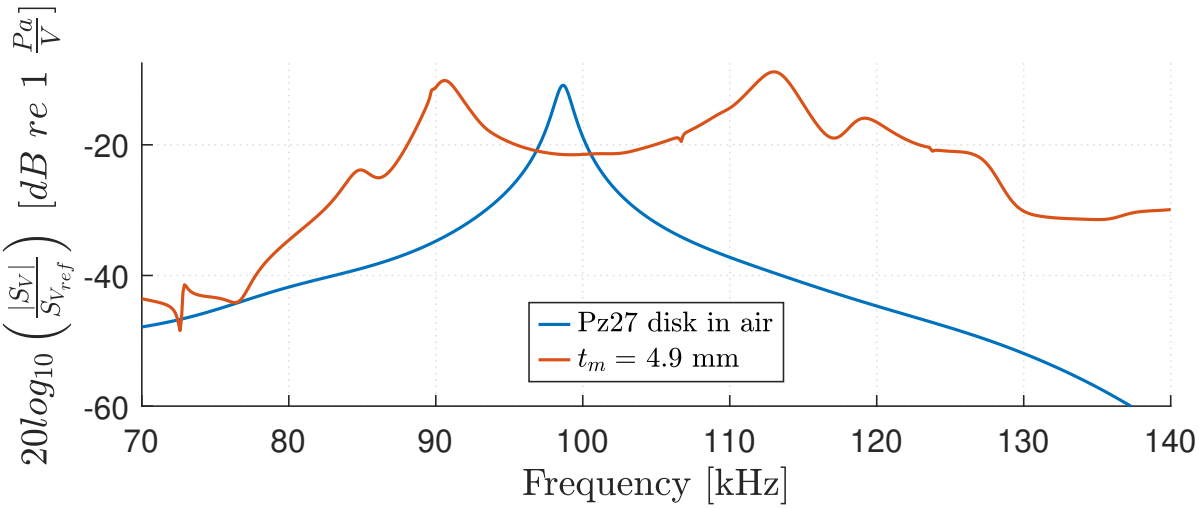

Figure 6.9: Comparison of the simulated voltage source sensitivity of a 20.14 mm ×1.99 mm Pz27 piezoelectric disk and the simulated voltage source sensitivity of the same piezoelectric disk with a 4.9 mm AplexR3 matching layer inside a 14.9 mm nylon casing

Fig. 6.9 shows that the matching layer provides a significant increase in bandwidth around the first radial mode. The magnitude of the voltage source sensitivity has not increased significantly, but the transducer now has two peaks with a magnitude of approximately -15 dB [re 1

Pa/V], compared to only one for the single disk.

The next part of the transducer construction to be added is a backing layer. A high density backing layer, might dampen the two peaks in voltage source sensitivity, giving a smooth response around 100 kHz. The matching layer thickness T_m = 4.9 mm will be used in the following finite element simulations.

6.4 Transducer construction with backing layer

A tungsten/epoxy mix is used as the transducer backing layer [61]. The material data from Tab. 3.6 will be used to model the backing layer for all the simulation results presented in this section. The purpose of the backing layer is to increase the transducer bandwidth, provide mechanical support for the transducer and avoid standing waves to form inside the transducer casing.

The backing material was originally designed so that it's characteristic acoustic impedance would be as close as possible to the piezoelectric materials Pz27 and Pz37 [61]. This is done so that the acoustic energy from the back of the piezoelectric disk will radiate into the backing layer.

The length of the backing layer is important to achieve sufficient damping of the acoustic waves. If the backing layer is to short the dampening will not be sufficient and standing waves will form inside the backing layer at specific frequencies. This problem is also known as ringing and can reduce the transducer ability to transmit short pulses.

Because of a limited access to the computational power needed to simulate transducer structures with lengths approaching 10 cm vibrating in air, the simulations preformed in this section are done using the FEMP structure **`TransducerVacuum`**. Simulations in vacuum unfortunately only allow for a study of the conductance, G_T, and suceptance, B_T. Simulations of the voltage source sensitivity, S_V, and beam pattern, $D(\theta)$, will therefore not be presented here.

Fig. 6.10 show the simulated conductance, G_T and suceptance, B_T, using the FEMP structure **`TransducerVacuum`**. The length of the backing layer, T_b is varied between 50mm and 100 mm with increments of 25 mm.

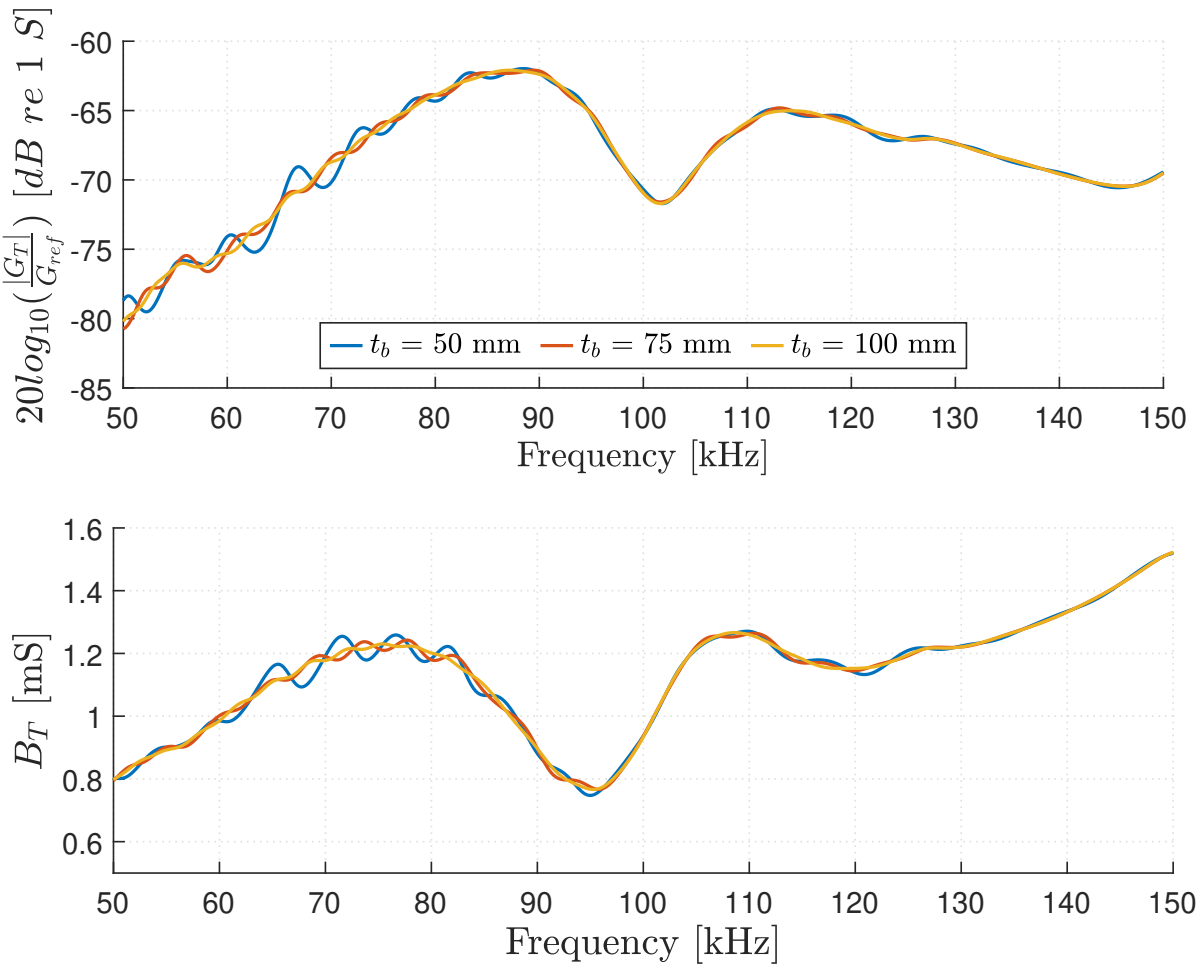

Figure 6.10: Comparison of the simulated conductance and susceptance of the transducer with a varying backing layer length, T_b. The simulations are performed using the FEMP structure ***`Transducer_Vacuum`***

Fig. 6.10 shows that an increase in the length T_b causes a reduction in the conductance and susceptance fluctuations that are observed for frequencies below 100 kHz. This is likely an sign of standing waves in the backing layer, indicating that the backing layer should be at least 75 mm long. A thickness t_b of approximately 80 mm will be used in the constructed transducers.

6.5 Final Transducer Design

The final transducer design that will be constructed in Chapter 7 is based on the simulation results of the previous four sections. Fig. 6.11 shows a sketch of the final transducer design.

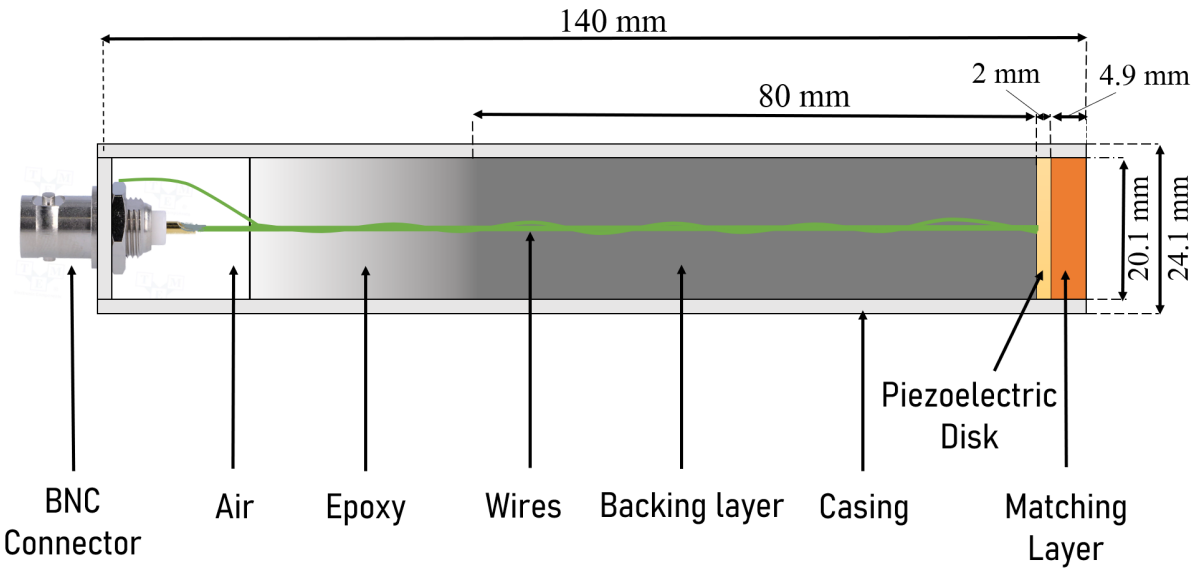

Figure 6.11: Sketch of the final transducer design. Showing the piezoelectric disk, matching layer, backing layer, transducer casing, wires and BNC Connector.

The transducer is made up of several components including a Pz 27 piezoelectric disk, an Aplex R3 Matching layer, an Epoxy/Tungsten backing layer, and a Nylon casing. Nylon was chosen as the casing material because simulations in Sec. 6.1 and 6.2 showed that a low-density material like Nylon could help reduce the beam pattern side lobes, and provide a narrowing og the main lobe. When the transducer casing is made out of a non conductive material like nylon the casing can not be used for grounding of the piezoelectric disk. An alternative method where the disk is grounded using a copper tape is presented in Chapter 7. The length of the matching and backing layers were determined in sec. 6.3 and 6.4, respectively.

A mixture of tungsten and epoxy is poured into the casing to create the backing layer. However, since the tungsten grains will settle towards the bottom near the piezoelectric element, determining the exact length of the backing layer can be challenging. As a result, the top portion of the backing layer may only contain epoxy without any tungsten, as illustrated in Fig. 6.11. It is important to note that while the dimensions shown in Fig. 6.11 are nominal, the actual construction dimensions may differ from these values. Measurements are conducted in Chapter 7 to determine the dimensions used in the individual transducers.

Chapter 7

Transducer Construction

This chapter will cover the construction of the final transducer design presented in Sec. 6.5. The chapter begins with a measurement of the diameter and radius of the piezoelectric disks as presented in Sec.7.1. Sec.7.2 covers the attachment of a wire to the electrode facing the backing layer, and Sec.7.3 covers the attachment of a copper strip to the electrode facing the matching layer. The copper strip is then connected to a wire that will be soldered onto the BNC connector. In Sec.7.4, the matching layer is attached to the piezoelectric disk, and Sec.7.5 covers the attachment of the transducer casing to the piezoelectric disk and matching layer. In Sec.7.6, the tungsten/epoxy backing layer is mixed and poured into the transducer casing. Finally, in Sec.7.7, the BNC connector is soldered onto the two wires connected to the disk electrodes.

7.1 Piezoelectric ceramics

The first component in the transducer structure is a Pz27 piezoelectric ceramic disk [55], produced by Ferroperm piezoceramics. A total of 10 disks are selected from a larger batch of around 50 disks. All of the disks have the nominal dimensions 20 mm $\times$ 2 mm, as stated by the manufacturer, with a tolerance of $\pm$ 3% [55]. The piezoelectric material Pz27 is a soft lead zirconate titanate, with a Curie temperature above 350 $^{\circ}$C .

The disks come with a screen-printed silver electrode on the top and bottom surface in order to set up an even electric field inside the disk. The 10 disks used during this work are selected to be as equal as possible based on a rough diameter measurement of every disk in the batch. A picture of a Pz27 disk with nominal dimensions 20 mm $\times$ 2 mm is shown in Fig.7.1.

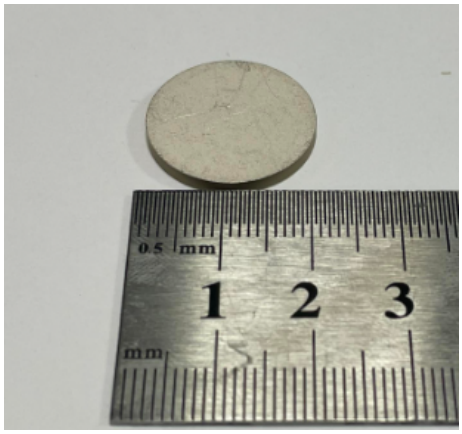

Figure 7.1: Pz27 piezoelectric ceramic disk with nominal dimensions 20 mm ×2 mm

Each disk's diameter, D_p, and thickness, T_p are measured using a Mitutoyo MDH-25 digimatic micrometer [89]. Details about the measurement setup can be found in Sec.4.5, and the measurement results are shown in Tab. 7.1. The 10 disks are numbered 20-29 to avoid using numbers previously used by other members of the acoustics group at UiB.

Table 7.1: Measured dimensions for Pz27 disk # 20-29

Disk #:	D_p [mm]	T_p [mm]
20	20.12 ±0.01	1.995 ±0.001
21	20.14 ±0.01	1.989 ±0.003
22	20.14 ±0.02	1.987±0.002
23	20.134 ±0.009	1.995 ±0.003
24	20.13 ±0.01	1.989 ±0.002
25	20.140 ±0.009	1.988 ±0.001
26	20.14 ±0.02	1.996 ±0.001
27	20.137 ±0.005	1.996 ±0.002
28	20.13 ±0.02	1.989±0.002
29	20.13 ±0.02	1.995 ±0.002

Before proceeding to the next step of the construction process, conductance and susceptance measurements are performed on all 10 disks. The electrical measurement setup is described in Sec. 4.2. The electrical measurement results for disks # 25 and # 29, which are used in the two completed transducers, can be found in Sec.8.1.1. Additionally, the section will include Tab.8.1, which presents the measured and simulated series resonant frequency f_s for all the 10 disks.

7.2 Soldering back electrode

In order to later connect the electrode facing the backing layer to a BNC connector, a 0.22 mm multi-stranded wire is attached to the center of the disk using a 0.8 mm solder wire containing 63 % tin and 37 % lead from Elsold [94]. The manufacturer marked the back side of the disks with a small black dot to differentiate the two sides.

Senior Engineer Bilal Hasan Qureshi performs the first soldering attempts on disks # 21 and # 24 at the University of Bergen. Element # 21 and # 24 are chosen first due to a relatively

poor agreement between simulated and measured series resonance frequency f_s, as shown in Tab.8.1. The soldering iron tip is set to 260 °C, and no preheating of the disk is used. Preheating of the disk is sometimes used so that the temperature of the soldering iron can be reduced to protect the polarization of the disk. However, findings presented by Prøytz in [95] demonstrate that preheating does not necessarily improve the soldering outcomes. The preheating step is therefore omitted.

The soldering of the disks numbered 20, 22, 23, and 25 through 29 is performed by fellow Ocean technology student Ola Wiik. The soldering iron tip is set to 280°C, and no preheating of the element is used. The following procedure is followed during the soldering process [96].

Procedure for soldering:

1. Clean the surface to be soldered with an abrasive (pencil eraser) and wipe with alcohol.
2. Apply a small amount of flux to the electrode area to be soldered. A liquid flux is used here, and a drop the size of a needle head is applied to the disk center.
3. Apply a small amount of solder to the iron tip and transfer the solder to the disk electrode by touching the iron tip to the flux drop.
4. Apply another small dot of liquid flux to the solder dot on the electrode.
5. Position a pre-tinned wire on the solder dot and the apply soldering iron to the wire until the solder melts on both the electrode and wire.
6. The remaining flux is removed with rubbing alcohol.

Electrical measurements are performed once the wire has been soldered to the disk. The electrical measurement setup is detailed in Sec.4.2, and the measurement results for disk # 25 and # 29 utilized in the final transducers are presented in Sec. 8.1.2. The measured series resonance frequency, f_s, before and after soldering for all disks except # 21, # 23, and # 24 can be seen in Tab. 8.1. The table does not include these specific disks due to the use of a different construction method, which requires connecting the front electrode before the back electrode. This alternative method will be further detailed in the next section.

7.3 Connecting the front electrode

To achieve physical contact between the disks circumferential edge and the transducer casing, a traditional wire can not be used when connecting the front electrode to the BNC connector. Physical contact between the disks circumferential edge and the casing is necessary when constructing the transducer design presented in Sec.6.5, and an alternative conductor is therefore used. Multiple solutions have been attempted, and a thin copper tape [97] proved to be the best solution of the ones investigated. The tape is approximately 60 μm thick and cut into 200 mm long and 4 mm wide strips as shown in Fig.7.4a. The thin copper strip will be applied to the electrode facing the matching layer and then drawn around the edge of the disk to the side facing the backing layer, as shown in Fig.7.5. This method is not perfect but considered to deviate less from the transducer design when compared to using, e.g., a wire.

Two methods for attaching the copper strip to the electrode are attempted. In the first method, the adhesive on the copper strip is used when attaching the copper strip to the disks front electrode. The adhesive is electrically insulating, and an additional conductive glue is therefore used to establish electrical contact between the copper strip and the electrode. The second method removes the copper strips adhesive before the strip is glued between the disk and the matching layer. The first and second methods are covered more closely in Sec.7.3.1 and 7.3.2, respectively.

7.3.1 Method 1

Method 1 is the method that was attempted first and was therefore applied to the disks with the largest deviation in measured and simulated series resonance frequency, f_s. These disks include numbers 21, 23, 24, and 26. Method 1 involves attaching copper strips to the electrode that will be facing the matching layer using the adhesive on the copper strip. However, since the adhesive is not electrically conductive, an electrically conductive epoxy glue [98] establishes a connection between the electrode and copper strip.

The copper strip is placed around 2 mm from the edge of the disk, as shown in Fig.7.2a. Then, a masking tape is applied around the edge of the copper, leaving a small gap to expose the disk where the conductive epoxy will be applied, as shown in Fig.7.2b. Next, a thin layer of conductive epoxy is applied to form a conductive bridge between the disk and the conductive side of the copper strip. Finally, the masking is removed, and the assembly is transferred to a heat chamber set to 80 °C. The assembly and epoxy are left in the heating chamber for 60 minutes, as this is the cure time and temperature specified by the epoxy manufacturer [98]. The cured epoxy and attached copper strip are shown in Fig.7.2c

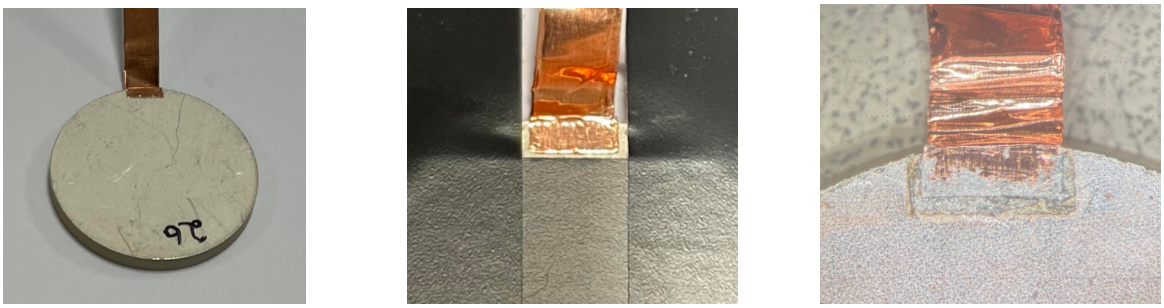

(a) *(b)* *(c)*

Figure 7.2: (a) Pz27 disk with a copper strip attached approximately 2 mm from the edge of the disk. (b) Masking put on the disk before applying the conductive epoxy. (c) The copper strip and cured epoxy after removing the masking

Method 1 seemed usable at first, but problems started to appear about one week after curing the conductive epoxy. Fig.7.3 shows the measured conductance, G_T, and susceptance, B_T, for disk # 24, two and seven days after curing. A decrease in the G_T of about 10 dB is measured at the first radial mode RM1. The reason for this might be that the silver particles in the epoxy start to oxidize when exposed to air, which in turn reduces the conductivity of the epoxy. A brown layer is seen to form at the surface, supporting this hypothesis.

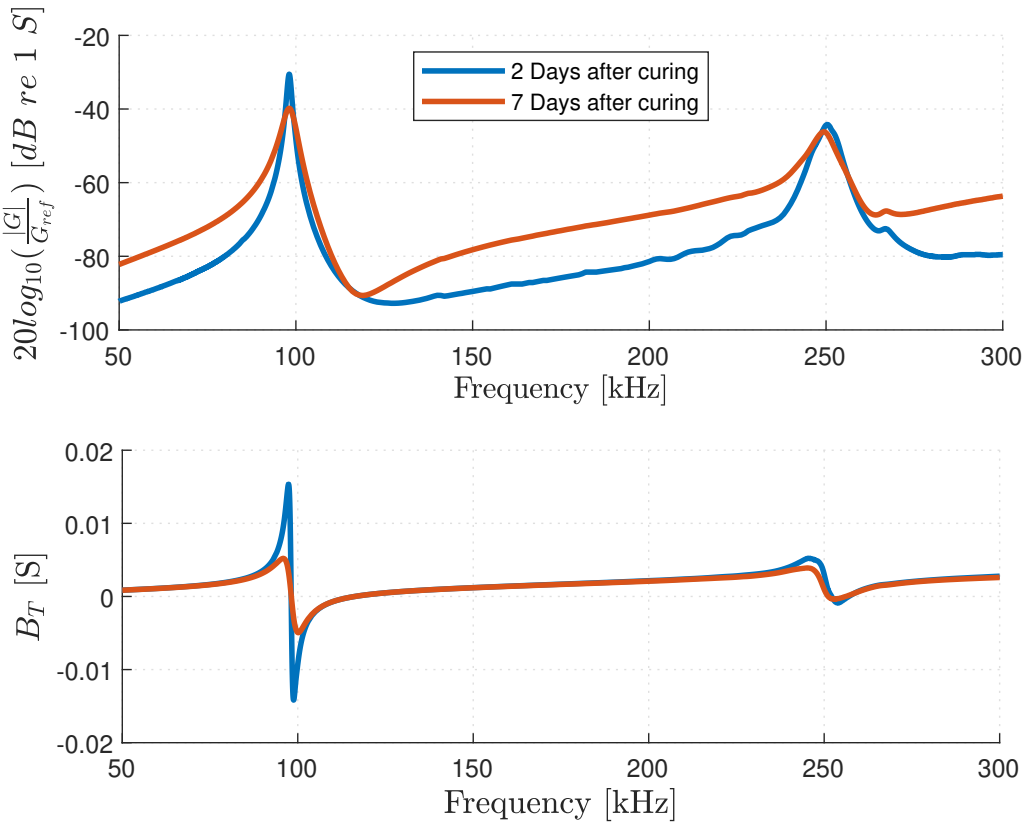

Figure 7.3: Measured conductance and susceptance of disk # 24 with a copper strip attached using method 1. Measurements are performed 2 and 7 days after curing the conductive epoxy glue

7.3.2 Method 2

In method 2, the electrically insulating adhesive on the copper strip is removed from the 2 mm section at the tip of the strip that will be in contact with the electrode facing the matching layer. The insulating adhesive will be used on the strip section that is in contact with the edge of the disk and the electrode facing the backing layer. Without the insulating adhesive, the copper strip will short-circuit the disk.

Before the adhesive can be removed from the tip of the strip, the rest of the adhesive is protected using a masking tape, as shown in Fig.7.4b. Isopropyl alcohol [99] is then applied to the un-masked area using a paper towel. The alcohol allows for the careful removal of the adhesive layer by rubbing the paper against the strip surface. A picture of the copper strip after removing the adhesive layer is shown in Fig.7.4c.

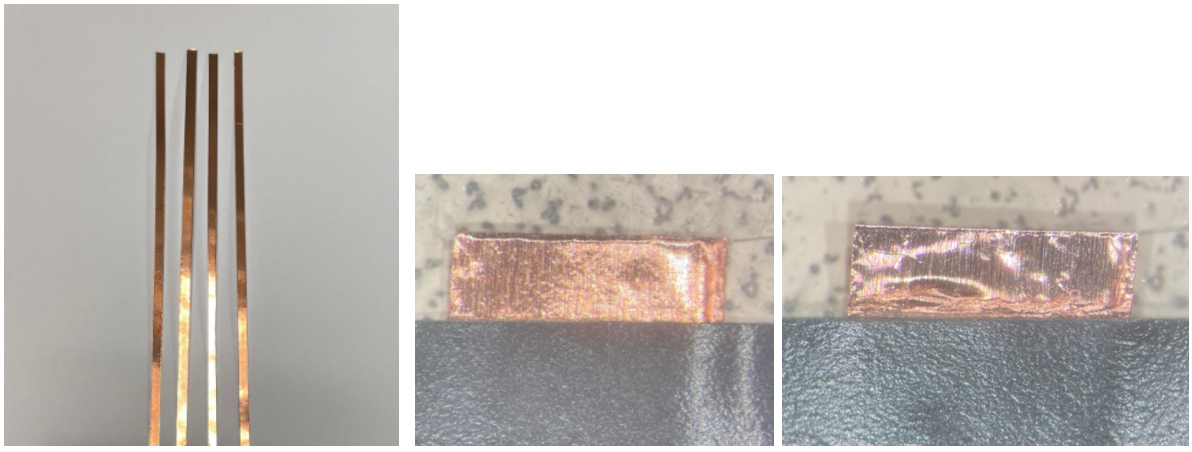

(a) *(b)* *(c)*

Figure 7.4: (a) 200 mm long and 4 mm wide strips of copper (b) The tip of a copper strip, after the masking tape is applied. (c) Same as Fig.7.4b, but after removal of the adhesive layer

After removing the adhesive on the tip of the strip, the copper strip is attached to the disk's edge using the remaining adhesive. The section without adhesive is then wrapped over the edge so that it makes contact with the electrode that will be facing the matching layer, as shown in Fig.7.5

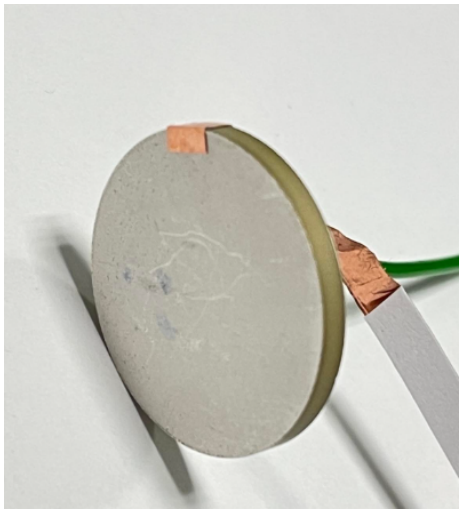

Figure 7.5: Pz27 disk with a copper strip attached to the front and edge

With the adhesive layer removed, the strip has a thickness of around 20μm. In Sec.7.4, a matching layer will secure the strip section without adhesive to the electrode. Method 2 was applied to disk numbers 20, 22, and 25-29 and is the technique used in the completed transducers. For disk # 26, both methods were attempted by removing the conductive epoxy from method 1.

When using method 2, no electrical measurements are conducted during this construction step, as the copper strip is not yet attached to the electrode. However, the electrical measurements performed after attaching the matching layer indicate that method 2 is the best method. Therefore, the disks where method 1 was applied (# 21,# 23,# 24) are not carried along for the following construction step.

7.4 Matching layer

A matching layer improves the acoustic coupling and energy transfer from the piezoelectric disk to the air. The material Aplex R3 [58] by Precision Acoustics is chosen as the matching layer due to readily available and measured material data found by Hauge and Mosland [29, 30]. Additionally, the matching layer secures the copper strip onto the electrode, thereby ensuring electrical contact between the disk and copper strip, as shown in Fig.7.6.

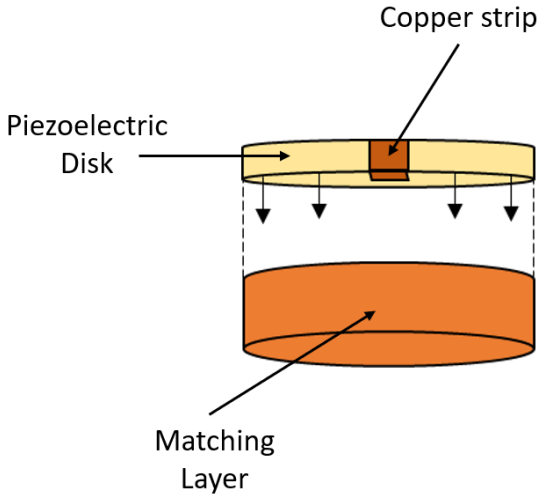

Figure 7.6: Sketch illustrating the attachment of a matching layer to a piezoelectric disk. The 2 mm tip of copper strip is placed between the two surfaces.

8 disks with nominal dimensions 20.14 mm x 4.9 mm of the matching layer are machined by Roald Langøen in the mechanical workshop at the Department of Physics and Technology, UiB. The measured diameter, D_m, and thickness, T_m, of the matching layers after machining are shown in Tab. 7.2. The measurement setup is presented in Sec.4.5.

Table 7.2: Measured dimensions for AplexR3 matching layer # 1-8

Matching layer #:	D_m [mm]	T_m [mm]
1	20.15 ±0.01	4.91 ±0.01
2	20.15 ±0.01	4.85 ±0.01
3	20.13 ±0.01	4.85 ±0.01
4	20.142 ±0.01	4.90 ±0.01
5	20.147 ±0.01	4.89 ±0.02
6	20.149 ±0.02	4.87 ±0.02
7	20.144 ±0.004	4.86 ±0.01
8	20.146 ±0.007	4.908 ±0.006

The matching layers are bonded to their respective piezoelectric disks using a fast-curing cyanoacrylate glue from Casco [62]. The glue is chosen due to its low viscosity, which allows it to form a thin layer [63]. A simple holder shown in Fig.7.7a ensures proper alignment between the disk and matching layer.

A small drop of glue, about 1 cm in diameter, is added to the matching layer, as shown in Fig. 7.7b. The piezoelectric disk with the copper strip attached as in Figs. 7.5 and 7.6 is then

added to the matching layer and compressed for about 30 seconds as shown in Fig.7.7c. It is important to avoid the glue from seeping in between the copper strip and electrode, as this can break the electrical contact. Once the disk has been placed on the matching layer, the curing time of the glue is only a couple of seconds [62].

The amount of glue applied between the disk and the matching layer is seen to have great importance for the compliance between simulation and measurement results. Experience shows that if too little glue is applied, the entirety of the two surfaces will not bind, and the results tend to deviate. In later attempts, a thin layer of glue is therefore brushed onto the matching layer surface to cover the entire surface properly. This leaves excess glue on the side of the disk and matching layer after attachment. The excess glue can be wiped off using tissue paper. It is unclear if the brushed on glue layer gave better results than a single drop, as both methods gave electrical measurements with small and large discrepancies relative to the simulation, as shown in Figs. 7.10 and 7.9 respectively.

(a) *(b)* *(c)*

Figure 7.7: (a) Alignment holder (b) Matching layer and alignment holder with glue applied to the matching layer. (c) Matching layer and piezoelectric disk glued together.

Before electrical measurements are performed on the disks and matching layer, a wire that will connect the copper strip to the BNC-connector is attached. The copper strip is first cut where it makes contact with the insulation on the soldered wire, as shown in Fig.7.8a. Next, a heat shrink tube is positioned onto the soldered wire to provide additional electrical insulation between it and the copper strip, as shown in Fig.7.8b. Finally, a wire similar to the one soldered on the electrode facing the backing layer is soldered to the copper strip, as shown in Fig.7.8c.

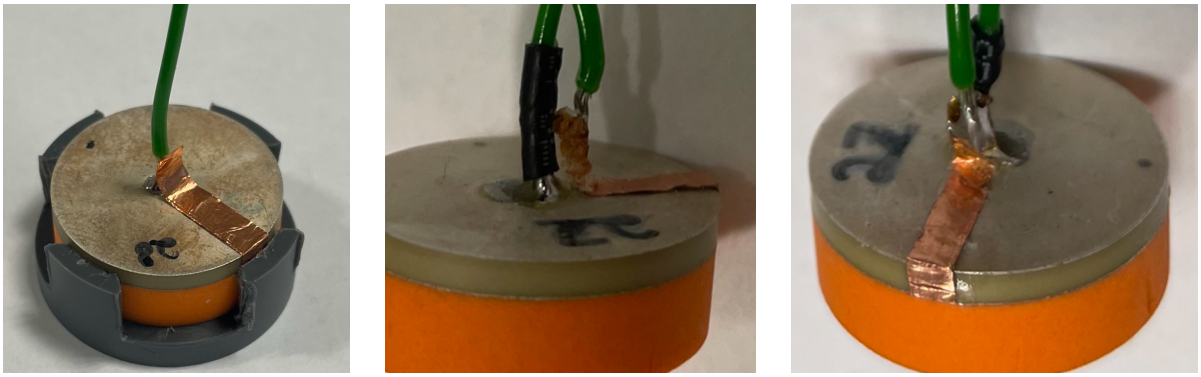

(a) *(b)* *(c)*

Figure 7.8: (a) Copper strip after cutting of excess length (b) Black shrink tube used to insulate the wire which is soldered to the electrode facing the backing layer (c) The copper strip after attachment of a wire using solder.

A total of 7 disks and matching layers are glued together. In Tab. 7.3, the measured thickness of the disk and matching layer before and after gluing them together is shown. The column $(T_p + T_m)$ is the sum of the measurements T_p and T_m as presented in Tab.7.1 and Tab.7.2, respectively, and the column $(T_p + T_m + T_g)$ is the measured thickness of the piezoelectric disk, matching layer and glue layer after assembly. The difference in the two columns is used to determine the thickness of the glue layer, T_g. For the remaining FEMP simulations where a matching layer is used, a glue layer with thickness T_g will be included.

Table 7.3: Measured thickness of the Pz27 disks, T_p, and the matching layer thickness, T_m, before and after applying a glue layer of thickness, T_g between them.

Disk #:	Matching layer #	$(T_p + T_m)$ [mm]	$(T_p + T_m + T_g)$ [mm]	T_g [mm]
20	8	6.903 $\pm$0.006	6.9448 $\pm$0.009	0.04 $\pm$0.01
22	3	6.84 $\pm$0.01	6.87 $\pm$0.01	0.03 $\pm$0.01
25	7	6.85 $\pm$0.01	6.88 $\pm$0.01	0.03 $\pm$0.01
26	5	6.89 $\pm$0.02	6.91 $\pm$0.05	0.03 $\pm$0.05
27	4	6.85 $\pm$0.01	6.94 $\pm$0.02	0.09 $\pm$0.02
28	1	6.90 $\pm$0.01	6.906 $\pm$0.006	0.01 $\pm$0.01
29	2	6.85 $\pm$0.01	6.87 $\pm$0.02	0.02 $\pm$0.03

The compliance between electrical measurements and simulations is observed to differ. For some disks and matching layers, the compliance between measurement and simulation is good, while for others, not so well. The simulated and measured conductance, G_T and susceptance, B_T for disk # 28 and matching layer # 1 is shown in Fig.7.9

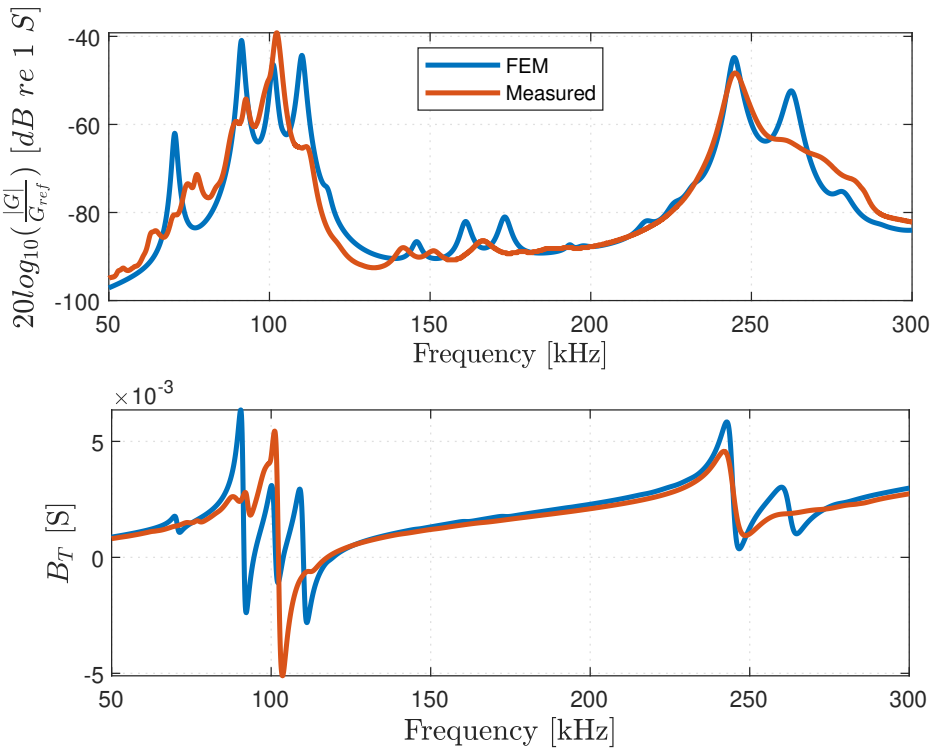

Figure 7.9: Conductance and susceptance of Disk # 28 and matching layer # 1 in the frequency range 50 kHz to 300 kHz. Measurements are compared with simulations of the disk, glue and matching layer vibrating in a vacuum using the FEMP structure ***`Piezodisk_Front_Vacuum`***.

Fig.7.9 shows a relatively poor agreement between measurement and simulation. The discrepancy is likely caused by insufficient glue between the disk and the matching layer.

Fig.7.10 shows the simulated and measured conductance, G_T and suceptance, B_T for disk # 29 and matching layer # 2.

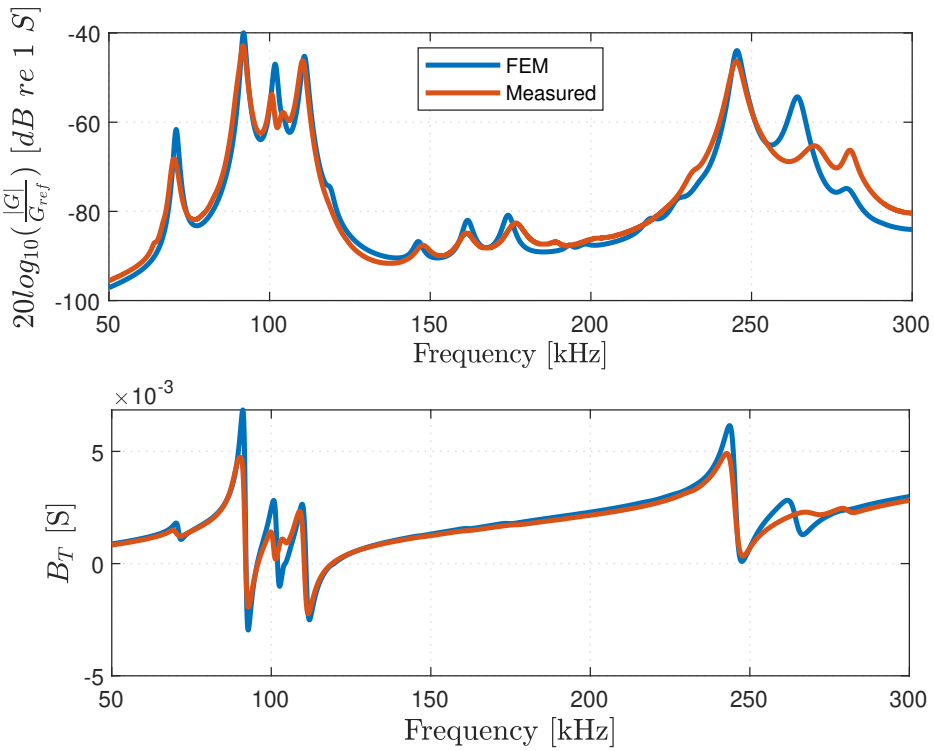

Figure 7.10: Same as in Fig.7.9 but for disk # 29 and matching layer # 2

The compliance between measurement and simulation in Fig.7.10 is much better than in Fig.7.9. For disk # 29 and matching layer # 2, the amount of glue was increased compared to what was used on disk # 28 and matching layer # 1. The results indicate it is better to use too much glue than too little.

Similar results to what is shown in Fig.7.10 were achieved for the three disks numbered 20, 25, and 27, with matching layers numbered 8, 7, and 4, respectively. Therefore, these disks and matching layers will be used in the next step of the construction process. Disks 22, 26, and 28, with matching layers 3, 5, and 1, will be discarded due to measurement and simulation discrepancies. The measured and simulated conductance G_T and susceptance B_T for the disks and matching layers used in the final two transducers will be presented in Sec.8.1.3. Fig.7.11 shows three fully assembled disks and matching layers with wires attached to the two electrodes.

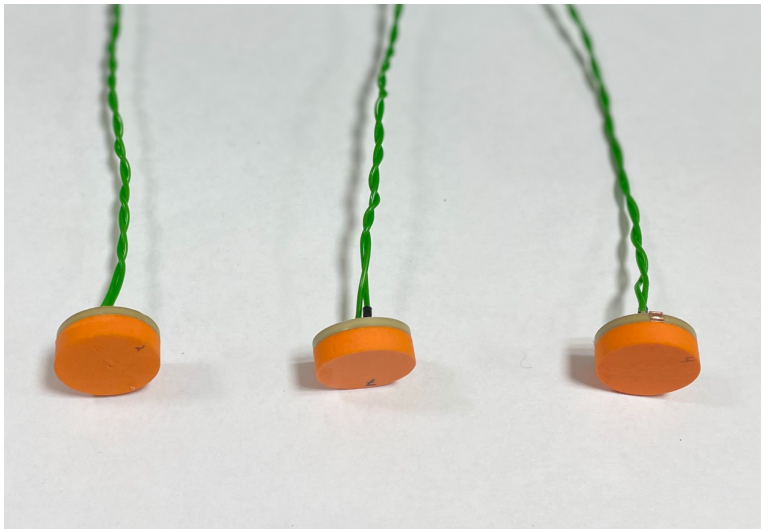

Figure 7.11: Fully assembled disks and matching layers with wires attached to the disk electrodes

7.5 Transducer Casing

In this step of the transducer construction, the piezoelectric disks and matching layers that were assembled in the previous section will be inserted into a transducer casing as illustrated in Fig.7.12.

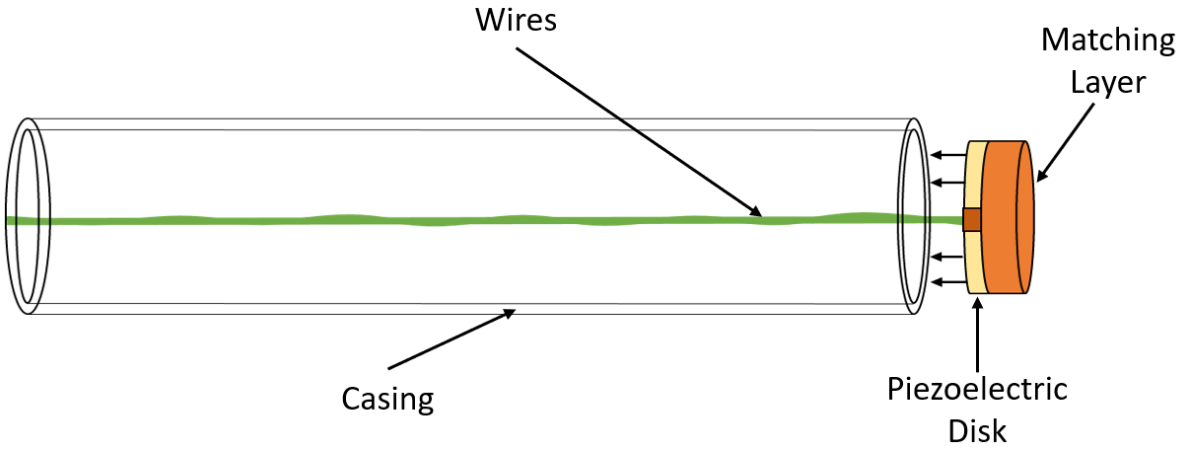

Figure 7.12: Sketch illustrating insertion of the piezoelectric disk and matching layer into the transducer casing.

From this section onward, the four remaining transducer assemblies will be referred to as transducer #x. The transducer number corresponds to the disk number used in the transducer, i.e., transducer # 27 is the transducer containing disk # 27.

Four transducer casings made out of Nylon are machined by Roald Langøen in the machine workshop at the Department of Physics and Technology, UiB. The four casings are specified to have an inner diameter, $D_{c,i}$ = 20.3 mm, an outer diameter $D_{c,o}$ = 24.3 mm, and a length L_c = 140 mm. Due to some inaccuracies in the machining process, the measured dimensions deviate slightly from the specified values. The measured values L_c, $D_{c,i}$, and $D_{c,o}$ for each of the casings are provided in Tab. 7.4.

Table 7.4: Measured dimensions of the Nylon transducer casings used in the transducer construction

Transducer #	Casing #	L_c [mm]	$D_{c,i}$ [mm]	$D_{c,o}$ [mm]
20	1	101.72 ±0.05	20.35 ±0.08	24.07 ±0.08
25	2	139.56 ±0.08	20.35 ±0.08	23.6 ±0.5
27	3	139.71±0.07	20.31 ±0.06	24.12 ±0.07
29	4	139.25 ±0.05	20.31 ±0.07	24.09 ±0.07

The deviation between specifications and measurement is largest for Transducer # 25, where the outer diameter of the casing is seen to vary along the length of the casing; hence the large uncertainty of measurement. The length of Transducer # 20 is shorter due to a short circuit of the disk occurring after attachment to the casing. Therefore, the top of the casing has been cut off so that the same casing can be reused with a different disk and matching layer. This short circuit is likely a result of a tear in the insulating adhesive on the copper strip. Therefore a thin layer of cyanoacrylate glue is applied to the copper strips on the remaining disks to enhance the insulation where the strip makes contact with the electrode facing the backing layer. The glue is allowed to dry before the strip is placed back into position, as shown in Fig.7.8c.

The piezoelectric disks and matching layers are glued inside the transducer casing using the same cyanoacrylate glue used previously between the disk and matching layer. However, the fast-curing nature of the glue can be slightly problematic because of the short amount of time left to adjust the disk and matching layer orientation. As a result, the matching layer is slightly angled inside the casing of transducer # 20 and # 25. Therefore, a different, slower curing type of glue is recommended if the process were to be re-attempted. A picture of the transducers numbered 25, 27, and 29 after attaching the casing is shown in Fig.7.13a. Fig.7.13b shows the disk and matching layer inside the casing as seen from the opening in the back of the casing.

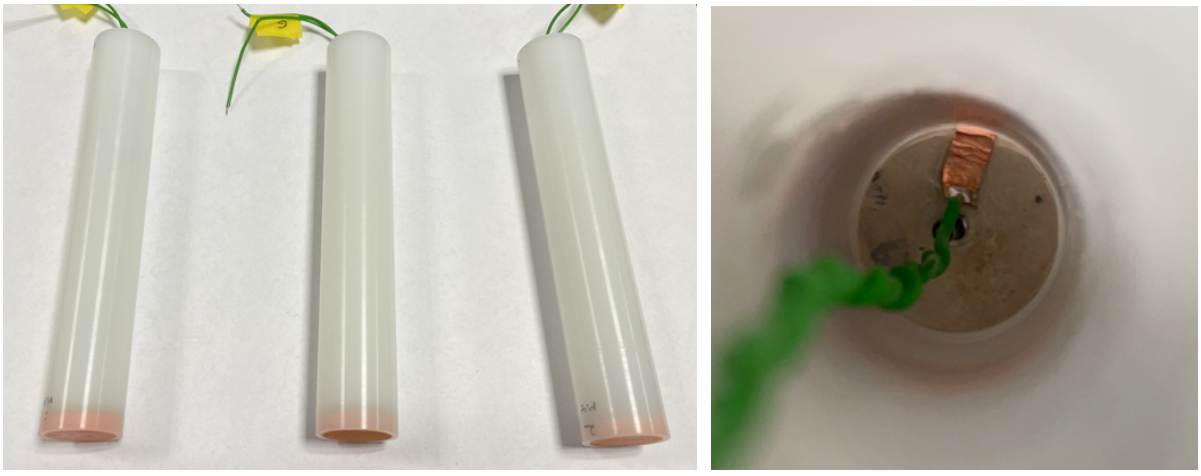

(a) *(b)*

Figure 7.13: (a) Three nylon transducer casings with disks and matching layers inserted (b) The piezoelectric disk inside the casing as seen from the opening in the back of the casing

After the casings have been attached to the disk and matching layer, the conductance, G_T, and susceptance B_T are measured as described in Sec.4.2. Fig.7.14 shows the measured and simulated conductance, G_T and suceptance B_T for transducer # 27.

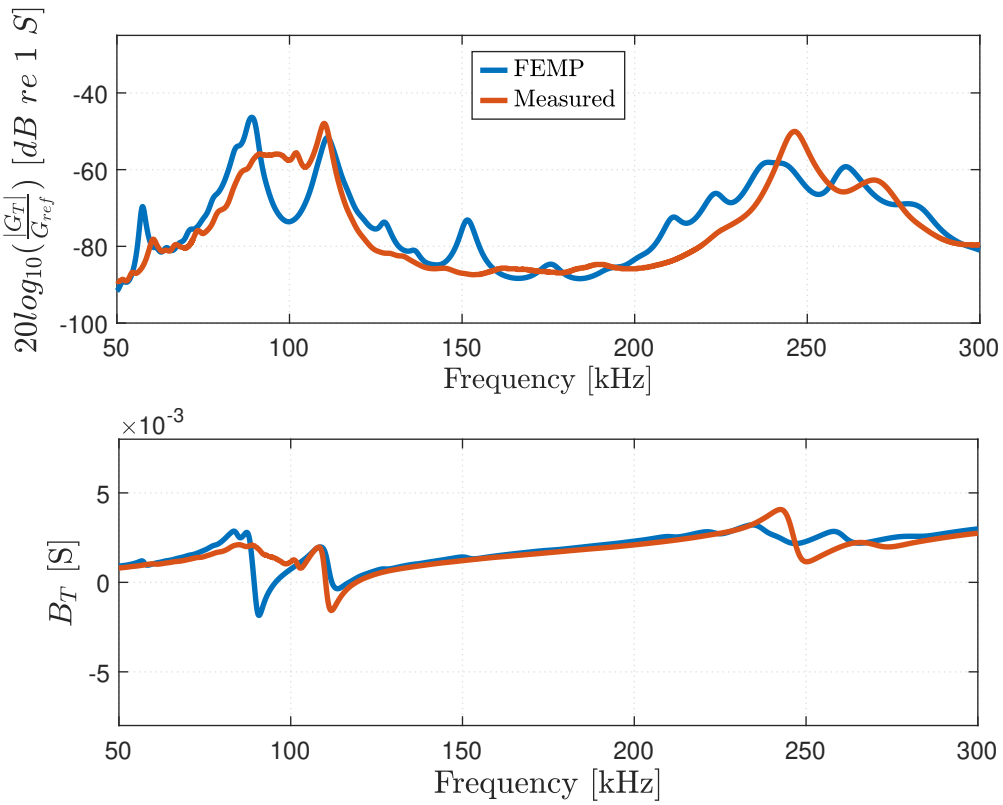

Figure 7.14: Conductance and susceptance of Transducer# 27 in the frequency range 50 kHz to 300 kHz. Measurements after attachment of the transducer casing compared with simulations of the transducer vibrating in a vacuum using the FEMP structure ***Piezodisk_Casing_Front_Vacuum.***

Fig.7.14 shows an increased discrepancy between measurement and simulation compared to the results presented in Fig.7.10. This might indicate that the attachment of the casing was not performed properly or that the material data used when simulating the transducer casing is inaccurate. The measurement and simulation results for transducer # 25 and # 29 will be presented in Sec.8.1.4.

Because of the decrease in casing length for transducer # 20 and limited access to the materials needed in the next step of the construction process, transducer # 20 is discarded. It will not be included in the next step of the construction.

7.6 Backing layer

A tungsten/epoxy mix is used as the transducer backing layer [61]. The backing consists of an SDS-Epofix epoxy from Struers [100], mixed with 50-250 μm diameter tungsten grains. The epoxy is a two-component mixture, where a hardener has to be added to the epoxy, using a 25:3 mass ratio [61]. After mixing the epoxy and hardener thoroughly, the tungsten grains are added using a 10:1, tungsten:epoxy mass ratio [61].

The backing for the three transducers is mixed in three separate batches; 250 g of Tungsten grains and 25 g of epoxy are used in all of them. After mixing the epoxy and tungsten until no dry spots of tungsten remain, the mix is left to pre-cure for 30 minutes. A picture of the epoxy tungsten mixture is shown in Fig.7.15a. After 30 minutes, the mix is stirred one final time before being poured into the transducer casing, as shown in Fig.7.15b.

After pouring the epoxy and tungsten, air bubbles start forming at the top of the epoxy surface. The air bubbles are popped manually using a needle approximately once an hour until the epoxy is no longer liquid. This has to be done so that the foam doesn't take up to much space in the casing. When the epoxy is cured after 48 hours, about 2 cm is left in the top of the casing, as shown in Fig.7.15c. This free space will be used to fit a BNC connector from Amphenol [101].

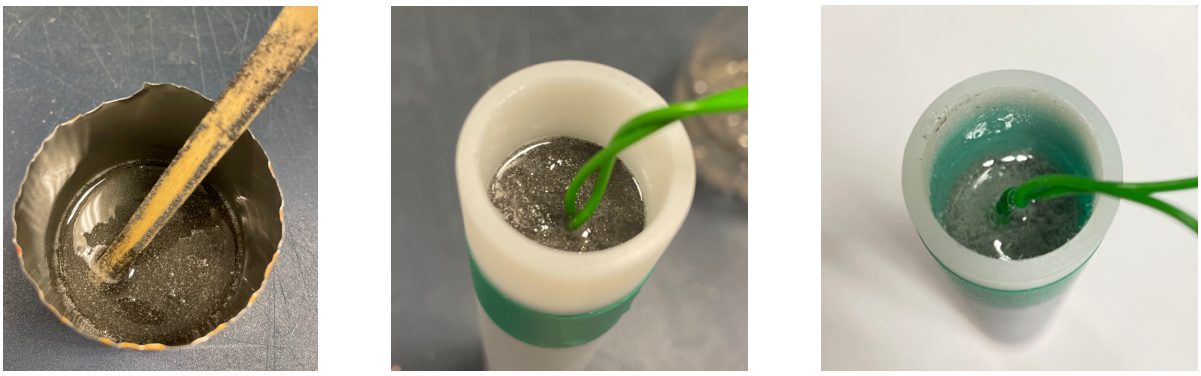

(a) (b) (c)

Figure 7.15: (a) Stirred tungsten/epoxy mixture (b) The tungsten/epoxy mixture after being poured into the transducer casing (c) Same as in Fig. 7.15b, 48 hours later

The final length of the backing layer is difficult to determine accurately. In previous work where a similar backing layer has been used [61, 95], settling of the tungsten grains towards the piezoelectric disk has been observed. This leaves a portion of epoxy without tungsten towards the top of the backing layer, as shown in Fig.6.11. This section of epoxy and the coaxial connector is not included in the FEMP simulations. The amount of tungsten grains is measured in an attempt to create a section of backing with tungsten with length, T_b = 80 mm. The actual length is unknown, but the backing length, T_b = 80 mm, will be used for the simulations. Fig.7.16 shows the three transducers numbered 25, 27, and 29 after attachment of the backing layer.

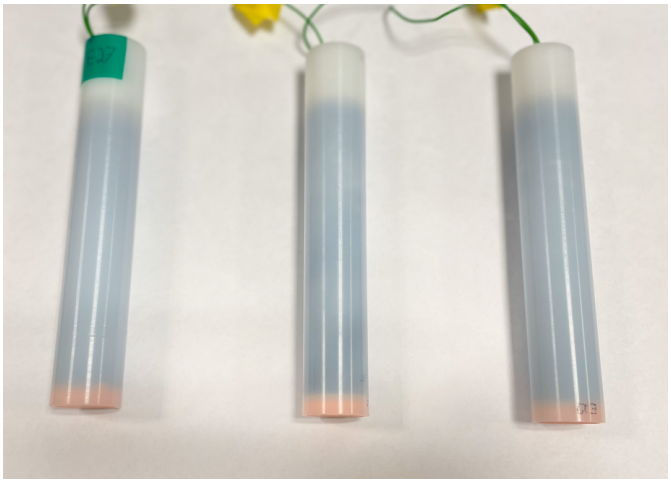

Figure 7.16: Transducer # 25, # 27 and # 29 after attachment of the tungsten/epoxy backing layer.

The tungsten/epoxy mix is left to cure in the transducer casings for 48 hours before electrical measurements are conducted as described in Sec.4.2. Fig.7.17 shows the measured and

simulated conductance, G_T and suceptance, B_T for transducer # 27 after the attachment of the backing layer.

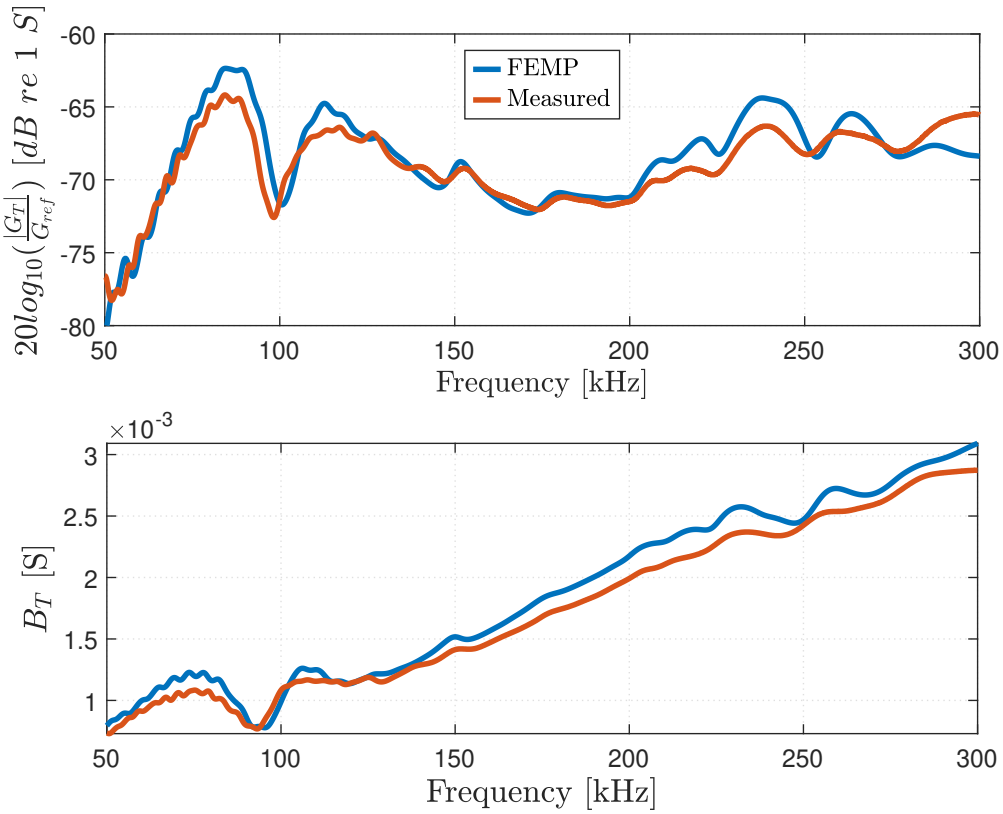

Figure 7.17: Conductance and susceptance of Transducer# 27 in the frequency range 50 kHz to 300 kHz. Measurements after attachment of the backing layer compared with simulations of the transducer vibrating in a vacuum using the FEMP structure **`Transducer_Vacuum`**.

Fig.7.17 shows an increased compliance between measurement and simulation when compared to the same transducer without a backing layer in Fig.7.14. The measured and simulated G_T, and B_T are similar to the simulation results presented in Sec.6.4 for the final transducer design.

7.7 BNC-Connector

The final step of the transducer construction is the installment of a BNC connector and a lid at the back end of the transducer. The lid is machined from the same nylon material which is used in the transducer casing and is designed to fit an Amphenol b6351b1-nd3g-50 BNC connector [101], as shown in figure 7.18.

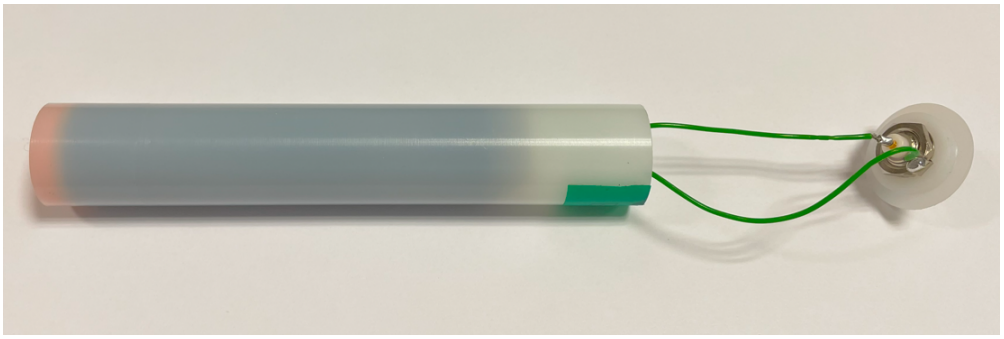

Figure 7.18: Transducer # 29 after the two wires have been soldered to the Amphenol BNC-connector.

The signal wire from the electrode facing the backing layer is soldered to the gold-plated tip on the connector, and the wire from the electrode facing the matching layer is soldered to a stainless steel soldering tab as shown in Fig.7.18. After soldering, the wires are placed inside the casing, and the lid is placed as shown in Fig. 7.19.

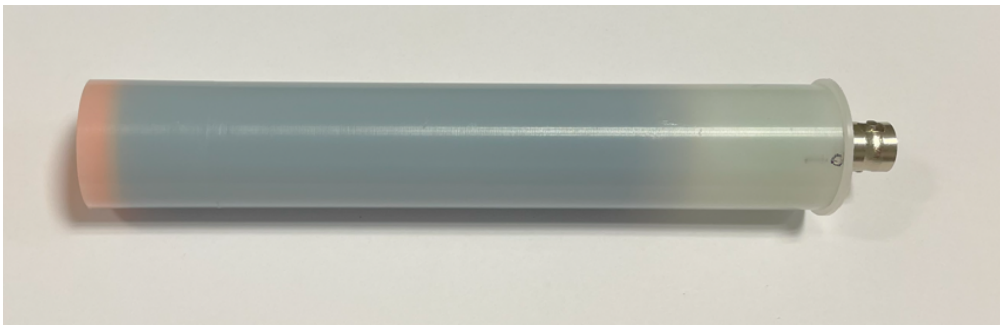

Figure 7.19: Transducer # 27 after completed construction.

Unfortunately, transducer # 27 experienced a short circuit a few days after completion. The exact reason for this short circuit is unknown, but a likely reason is that an unisolated part of the copper strip got in touch with the electrode facing the backing layer. Therefore, the copper strips electrical insulation must be enhanced using additional glue, as mentioned in Sec. 7.5. Because of this short circuit, acoustical measurements have only been performed on transducer # 25 and # 29.

Chapter 8

Results - Transducer characteristics

In this chapter, the experimental and simulated results for the two completed transducers numbered 25 and 29, are presented. The electrical measurements and simulations for each step in the construction process are presented in Sec. 8.1. The experimental measurements of the voltage source sensitivity, S_V, are compared to the simulated results in Sec. 8.2. Additionally, some of the recorded voltage signals V_{0m} and V_6 used in the S_V calculation are presented at selected frequencies of interest. In Sec. 8.4 the measured measurement system transfer function $H^{VV}_{0m6\alpha}$ is compared to $H^{VV}_{0m6\alpha}$ simulations performed using the FEMP structure **`Transducer_Fluid`**, and the system model theory presented in Sec. 2.3. Some of the recorded waveforms, V_{0m} and V_6 used in the $H^{VV}_{0m6\alpha}$ measurements are also be presented.

8.1 Electrical measurements and simulations

Electrical measurements are conducted for each step in the construction process from Chapter 7. The compliance between measurements and simulations of the conductance G_T, and susceptance B_T, lies the foundation for which assembly is carried along for the next step in the construction process. This section will present and compare the electrical measurements conducted during the construction of transducer # 25 and # 29. The measurements are compared to simulation results from the FEMP structures presented in Sec. 3.4. All electrical simulations are performed using the vacuum configuration of their respective simulation structure. The effects from the neglected fluid loading are expected to be negligible compared to other effects, such as, e.g., assembly inaccuracies and uncertainties related to material parameters. The electrical measurement setups are described in Sec. 4.2.

8.1.1 Piezoelectric ceramic disks

Figs. 8.1 and 8.2 shows the simulated conductance G_T, and suceptance, B_T for disk # 25 and # 29 respectively. The simulations are performed using the FEMP structure **`Piezodisk_Vacuum`**, and compared to the electrical measurements conducted before any wires are soldered to the disks. Material parameters and disk dimensions utilized in the simulations are provided in Tabs. 3.1 and 7.1 respectively.

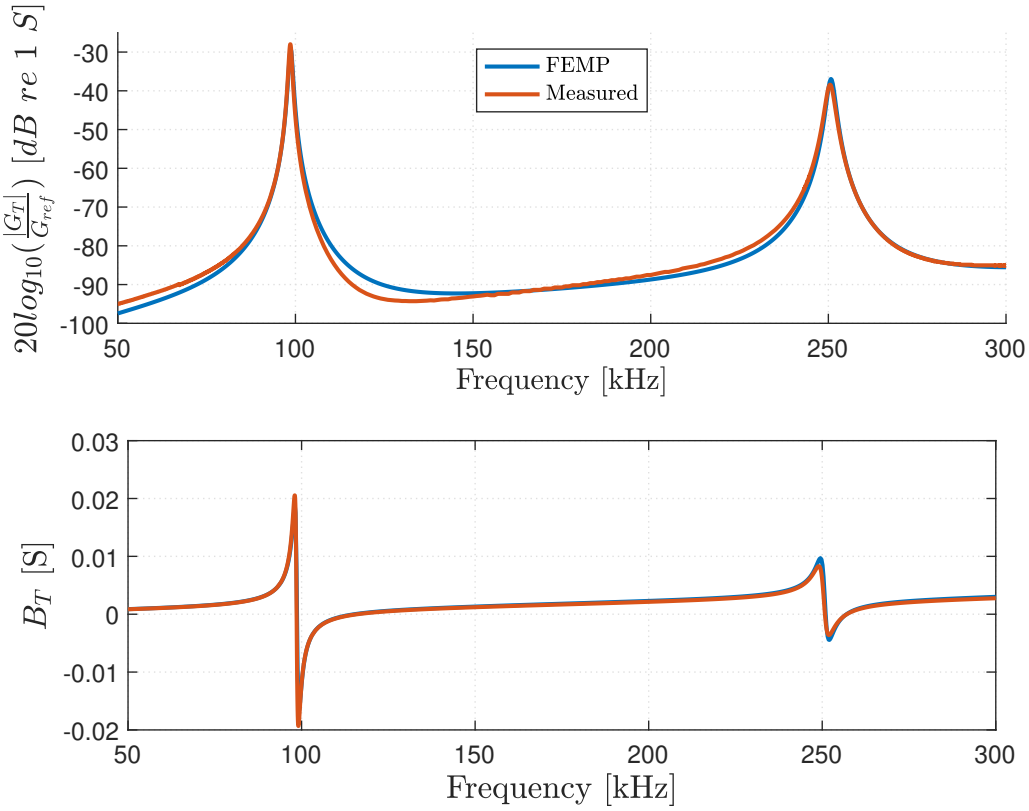

Figure 8.1: Conductance and susceptance of disk # 25 in the frequency range 50 to 300 kHz. Measurements in air before soldering wires to the elements are compared with simulations of the disk vibrating in a vacuum using the FEMP structure **`Piezodisk_Vacuum`**.

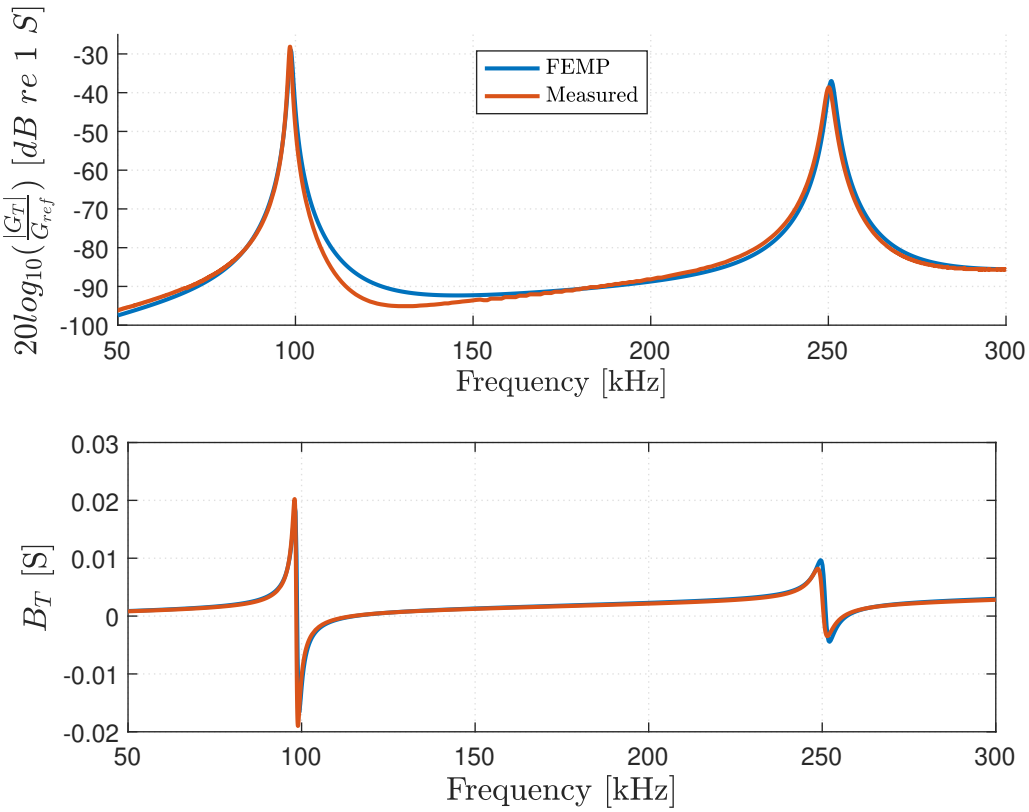

Figure 8.2: Same as Fig. 8.1, but for disk # 29

Figs. 8.1 and 8.2 show a good agreement between simulation and measurements. Of all the 10 disks that were measured and simulated, disk # 20 and # 21 were the two disks, respectively, where the best and worst agreement of the measured and simulated series resonance frequency, f_s at the first radial mode, is observed. Fig. 8.3 shows the measured and simulated conductance, G_T, and susceptance, B_T for disk # 20 and # 21 around the first radial mode, RM1.

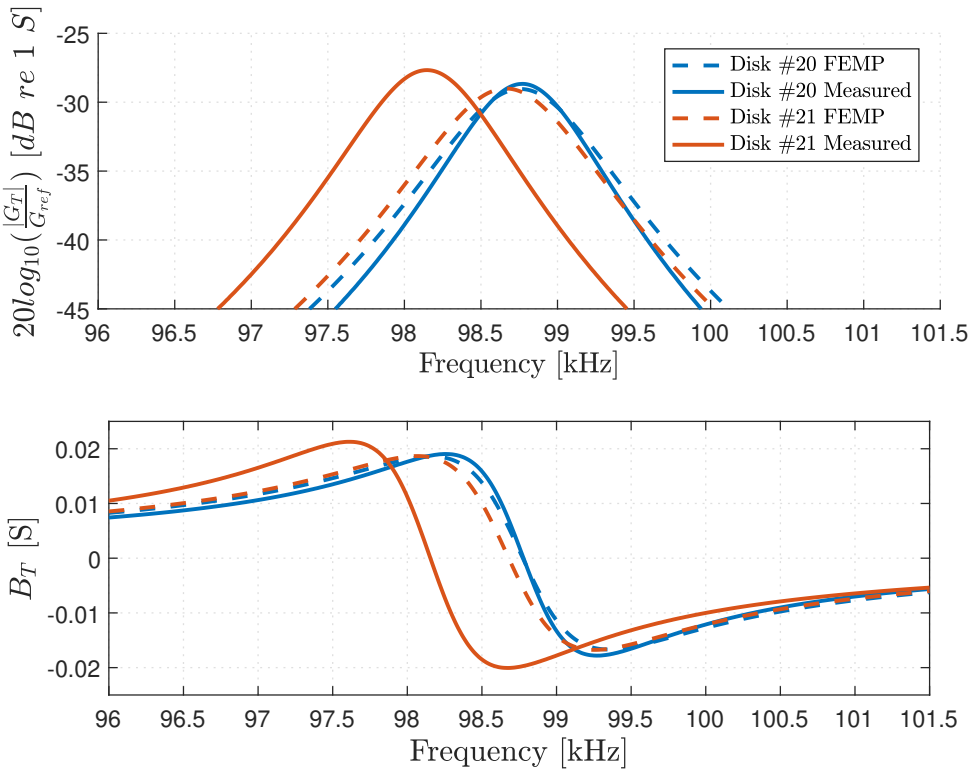

Figure 8.3: Same as in Fig. 8.1 but for disk # 20 and # 21 in the frequency range 96 to 101.5 kHz.

In Fig. 8.3, there is a difference of 10 Hz between the measured and simulated series resonance frequency, f_s for disk # 20. For disk # 21 the discrepancy is 620 Hz. For the other 8 disks, the difference in the measured and simulated f_s lies somewhere in between that of disk # 20 and # 21. The conductance and susceptance plots for the other disks will not be displayed here, but the measured and simulated series resonance frequency, f_s at RM1 for all the 10 disks are shown in Tab. 8.1.

8.1.2 Piezoelectric disk with soldered back electrode

The attachment of wires to the back electrode on the piezoelectric should ideally affect the conductance, G_T, and susceptance, B_T as little as possible. However, some effects are expected due to, e.g., an added mass load on the disks surface, and the electrical resistance inherent in the solder material [102]. The soldering procedure in Sec. 7.2 is performed to reduce these effects as much as possible. Figs. 8.4 - 8.7 shows the measured conductance G_T, and suceptance, B_T, before and after soldering disk # 25 and # 29.

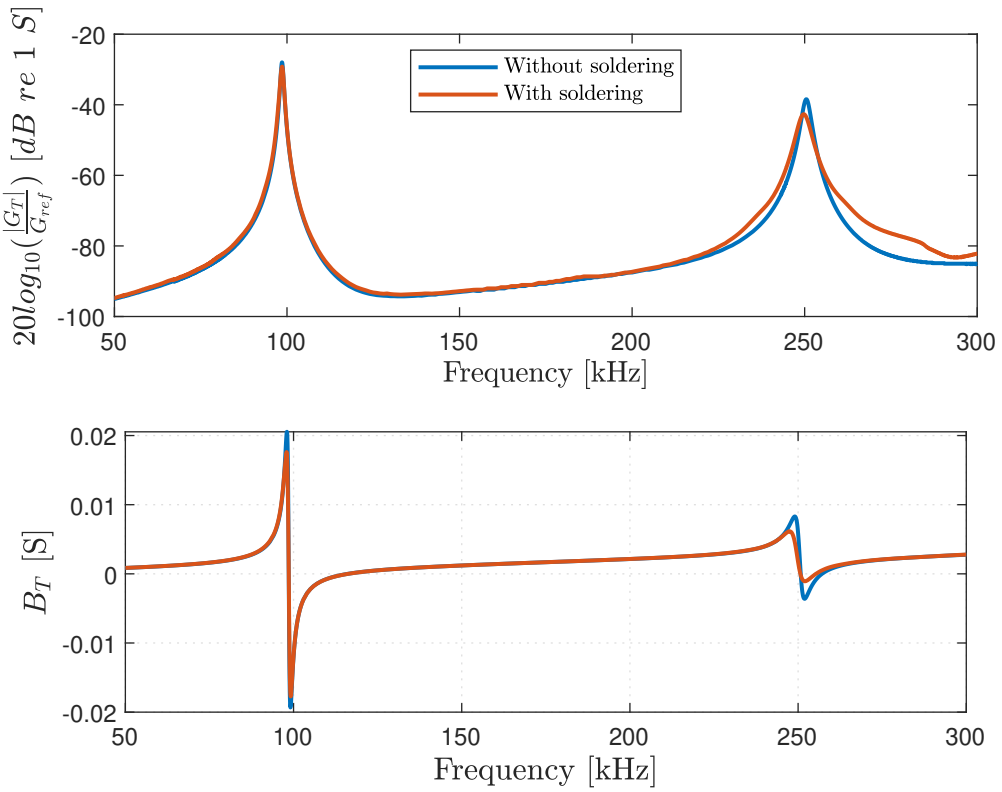

Figure 8.4: Conductance and susceptance of disk # 25 in the frequency range 50 to 300 kHz. Measurements are performed before and after the applying solder to the back electrode as described in Sec. 7.2

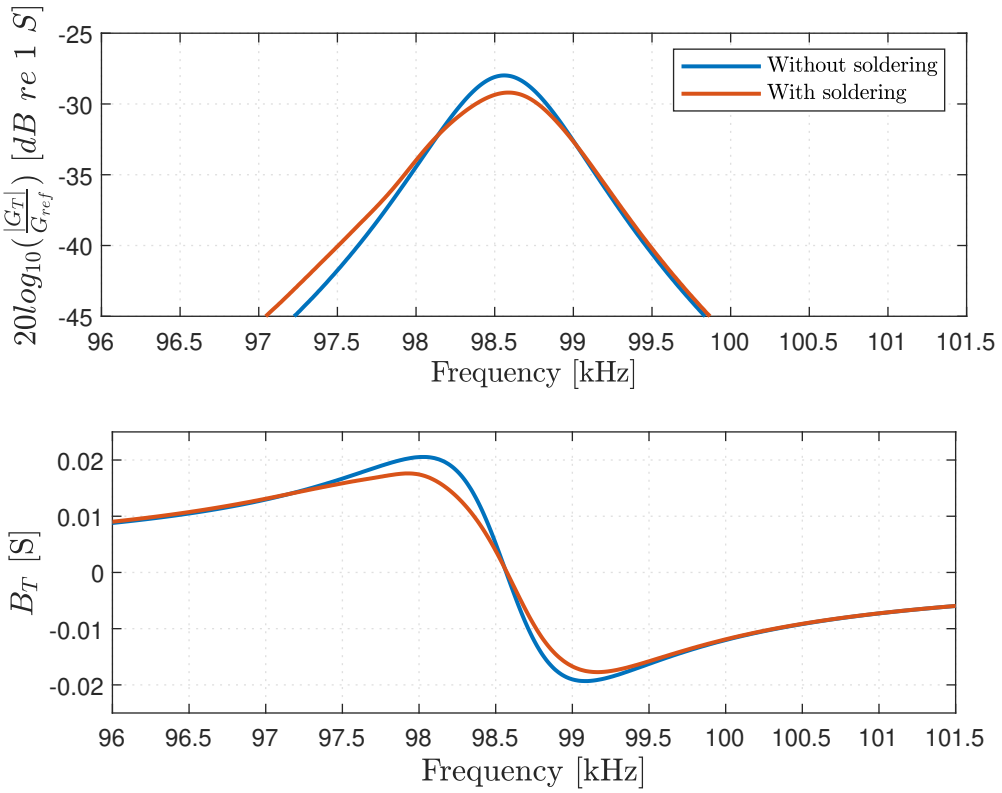

Figure 8.5: Same as in Fig. 8.4, but in the frequency range 96 to 101.5 kHz around the first radial mode RM1

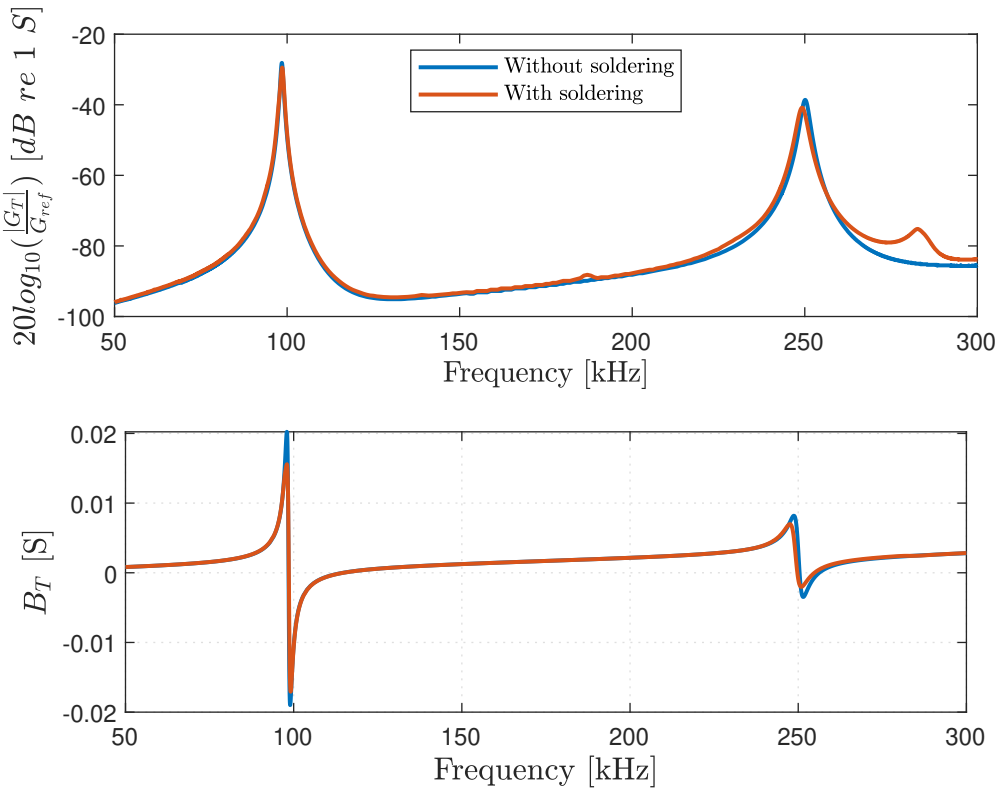

Figure 8.6: Conductance and susceptance of disk # 29 in the frequency range 50 to 300 kHz. Measurements are performed before and after the applying solder to the back electrode as described in Sec. 7.2

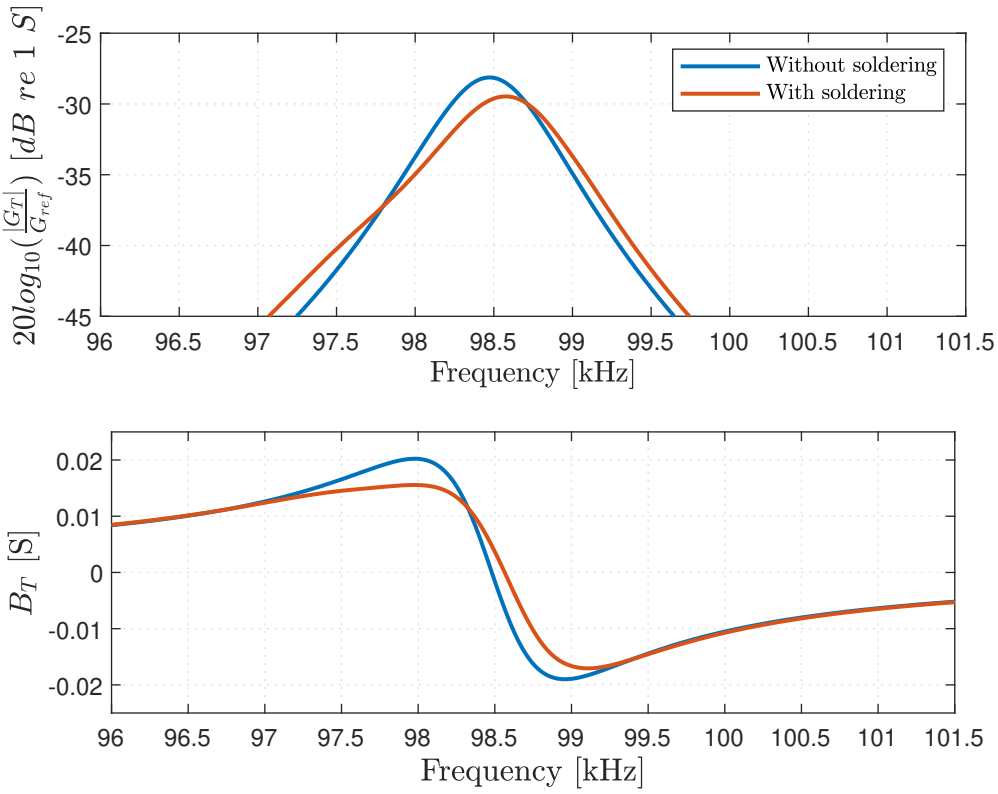

Figure 8.7: Same as in Fig. 8.6, but in the frequency range 96 to 101.5 kHz around the first radial mode RM1

For both disk # 25 and # 29, the soldering of the back electrode causes a slight drop in the peak conductance of around 2 dB, at the first radial mode, RM1. A similar drop in peak conductance can also be seen at the second radial mode, RM2. The largest deviations in the two measurements are observed at frequencies above 250 kHz, where the solder causes an increase in the conductance, G_T. The solder also causes a slight upward shift in the series resonance frequency at RM1. This effect is observed for all the soldered disks, except for disk # 26, where the solder causes a downward shift. Tab. 8.1 shows the measured series resonance frequency, f_s, before and after soldering the back electrode on all 7 disks. The simulated series resonance frequency, f_s, from the FEMP structure **`Piezodisk_Vacuum`** is also displayed in Tab. 8.1

Table 8.1: Measured and simulated series resonance frequency, f_s for the 10 Pz27 disks used during the work. A measurement has been performed before and after soldering.

Disk #:	Meas, f_s, w/o solder [kHz]	Meas, f_s w/ solder [kHz]	Sim, f_s FEMP [kHz]
20	98.77	98.98	98.76
21	98.15	N/A	98.67
22	98.63	98.66	98.67
23	98.33	N/A	98.70
24	98.30	N/A	98.72
25	98.56	98.59	98.67
26	98.69	98.67	98.66
27	98.60	98.79	98.68
28	98.48	98.53	98.72
29	98.47	98.58	98.71

8.1.3 Piezoelectric disk with matching layer

Figs. 8.8 and 8.9 shows the measured conductance, G_T, and susceptance, B_T for disk # 25 and # 29, respectively. The measurements are conducted after attachment of a matching layer as described in Sec. 7.4, and compared to simulations performed using the FEMP structure **`Piezodisk_Front_Vacuum`**. The matching layer material data, and the matching layer thickness, T_m used in the simulations are provided in Tabs. 3.3 and 7.2 respectively. The glue layer material data and thickness, T_g are provided in Tabs 3.7 and 7.3, respectively. A picture of the electrical measurement setup is shown in Fig. 4.2b.

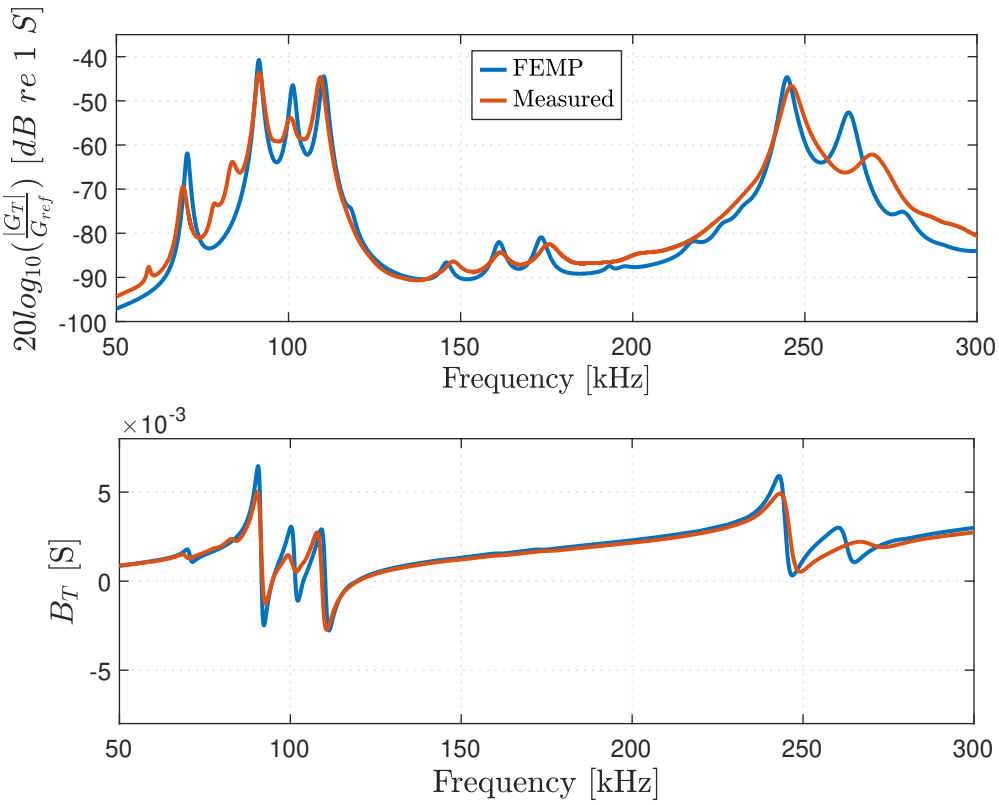

Figure 8.8: Conductance and susceptance of disk # 25 and matching layer # 7 in the frequency range 50 to 300 kHz. Measurements are compared with simulations of the disk, glue and matching layer vibrating in a vacuum using the FEMP structure **`Piezodisk_Front_Vacuum`**.

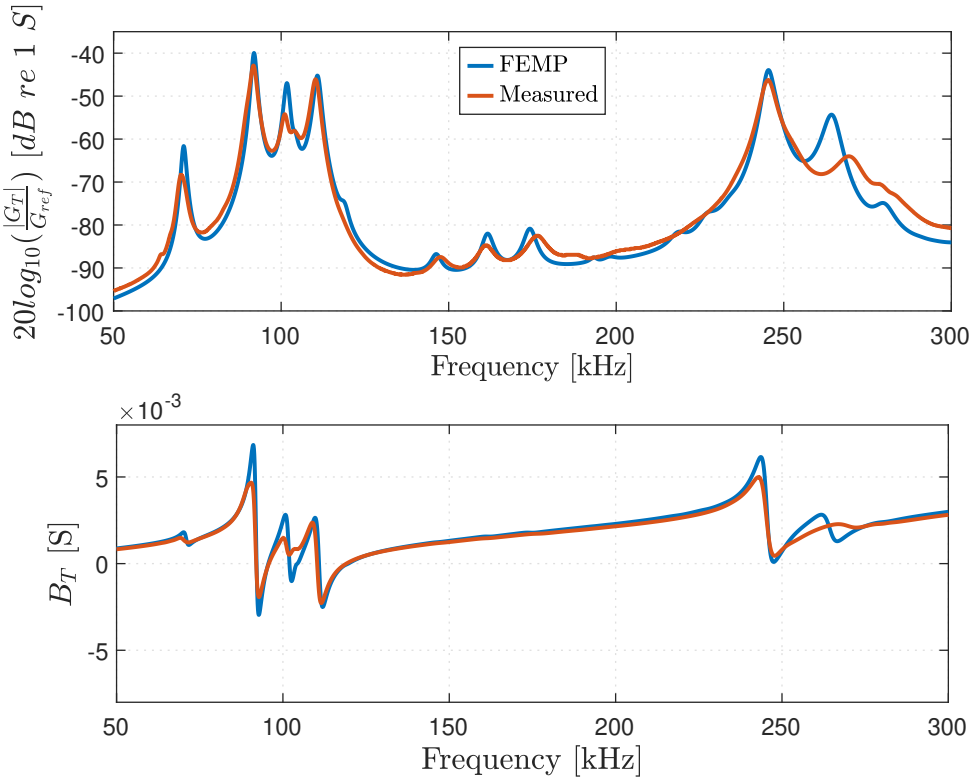

Figure 8.9: Same as Fig. 8.9 but for disk # 29 and matching layer # 2

Figs. 8.8 and 8.9 show that there is still a fair agreement between measurement and simulations with a matching layer attached to the disk. Similarly to what is observed for the soldered disks, the measured conductance, G_T, and susceptance, B_T are slightly lower around the peaks when compared to the simulations. The more considerable discrepancies between measurement and simulation at frequencies above 250 kHz, are likely a result of the soldering effects shown in Figs. 8.4 and 8.6. The measured conductance G_T for disk # 25, also shows some additional modes around 80 kHz. The cause of these modes is unknown, but imperfections in the gluing process are considered the most likely cause.

8.1.4 Matching layer and transducer casing

Figs. 8.10 and 8.11 shows the measured conductance, G_T, and susceptance, B_T for transducer # 25 and # 29, respectively. The measurements are conducted after the attachment of a transducer casing to the disk and matching layer, as described in Sec. 7.5, and compared to simulations performed using the FEMP structure **`Piezodisk_Casing_Front_Vacuum`**. The simulated casing material parameters and casing dimensions are provided in Tab. 3.5 and 7.4 respectively. A picture of the electrical measurement setup is shown in Fig. 4.2c,

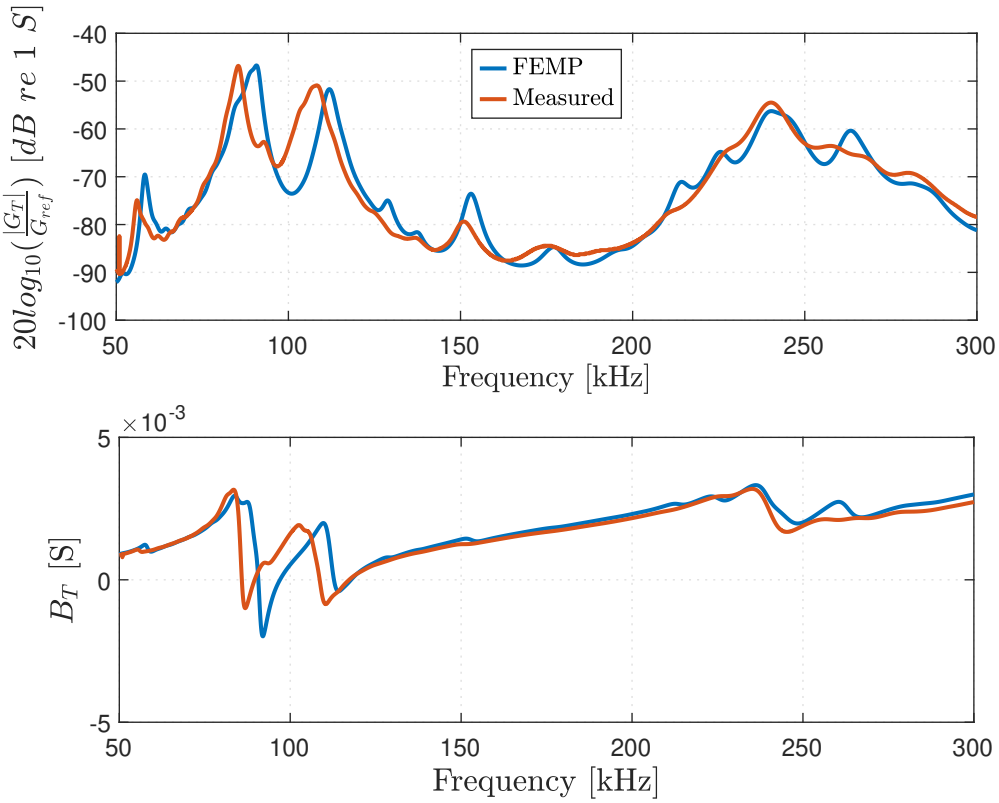

Figure 8.10: Conductance and susceptance of transducer # 25 with matching layer # 7, and casing # 2 in the frequency range 50 to 300 kHz. Measurements are compared with simulations of the disk, glue, matching layer and casing vibrating in a vacuum using the FEMP structure ***`Piezodisk_Casing_Front_Vacuum`***.

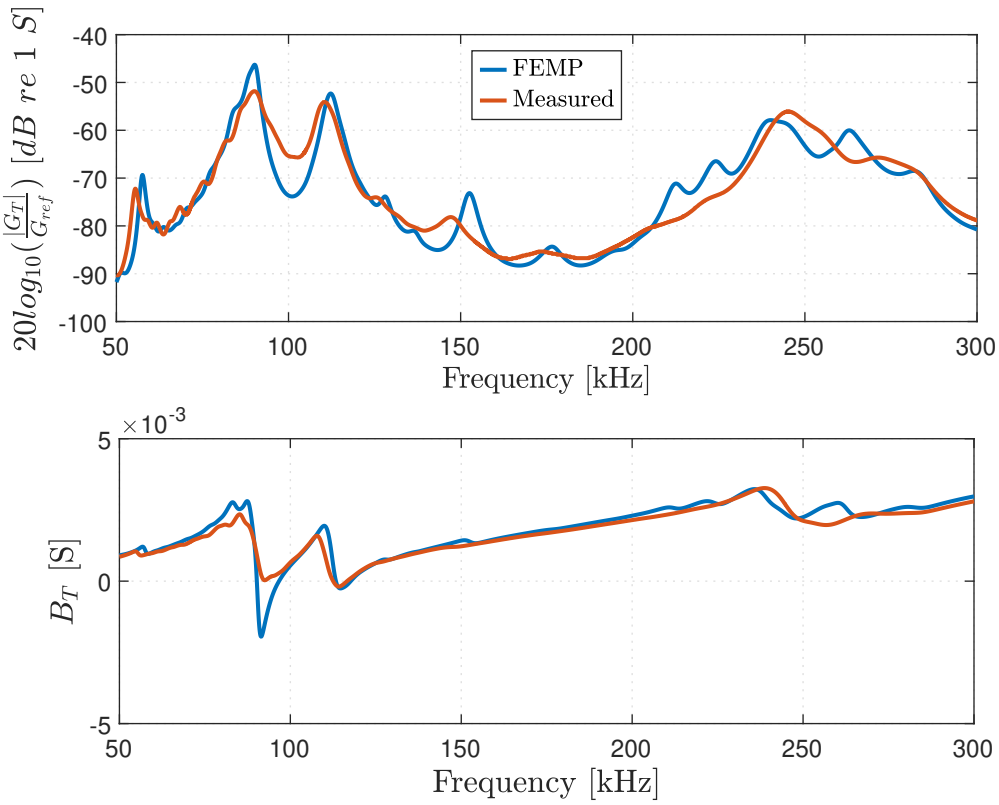

Figure 8.11: Same as Fig. 8.10, but for transducer # 29, with matching layer # 2 and casing # 4.

Figs. 8.10 and 8.11 show that there is still a reasonable agreement between simulation and measurement after attachment of the transducer casing. The two distinct peaks in the conductance, G_T are visible in both measurements and simulations at approximately 90 and 110 kHz. However, for transducer # 25, there is a quite considerable downward shift in frequency for the measured peaks relative to the simulation. This downward shift is also apparent in Fig. 8.8, before the casing is attached, but the effect increases after the attachment of the casing. For transducer # 29, the match in the frequency of the measured and simulated peaks is better. However, there is a more significant discrepancy in the conductance magnitude of the two peaks, relative to the simulated and measured result for transducer # 25 in Fig. 8.10.

The most significant contributor to the discrepancies between measurement and simulation in Figs. 8.10 and 8.11 is likely to be inaccuracies in the transducer construction. As mentioned in Sec. 7.5, the disk and matching layer in transducer # 25 is placed slightly angled inside the transducer casing. Other factors contributing to the discrepancies, include errors in the material parameters, and the measured dimensions used in the simulations.

8.1.5 Transducer

Figs. 8.12 and 8.13 shows the measured conductance, G_T, and susceptance, B_T for transducer # 25 and # 29, respectively. The measurements are conducted after the attachment of the backing layer, as described in Sec. 7.6, and compared to simulations performed using the FEMP structure **`Transducer_Vacuum`**. The electrical measurement setup is shown in Fig. 4.2d, and the backing layer material parameters are provided in Tab. 3.6. The simulated backing layer thickness T_b = 80 mm, for both transducers.

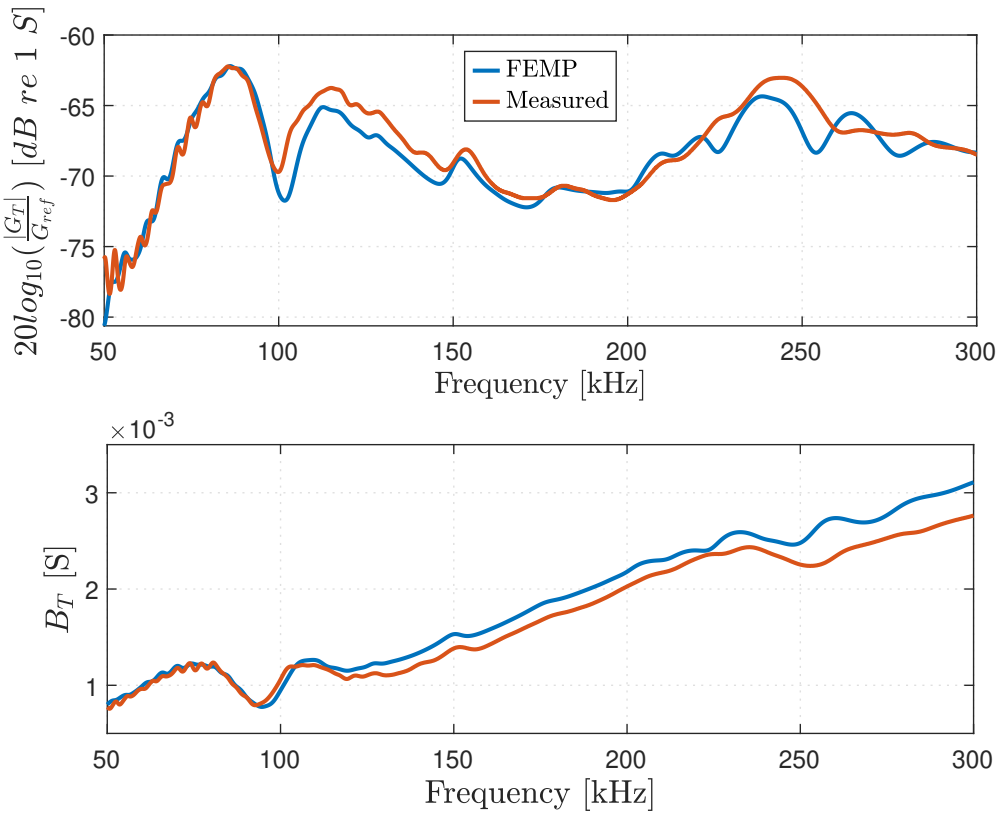

Figure 8.12: Conductance and susceptance of transducer # 25 in the frequency range 50 to 300 kHz. Measurements are compared with simulations of the transducer vibrating in a vacuum using the FEMP structure ***`Transducer_Vacuum`***.

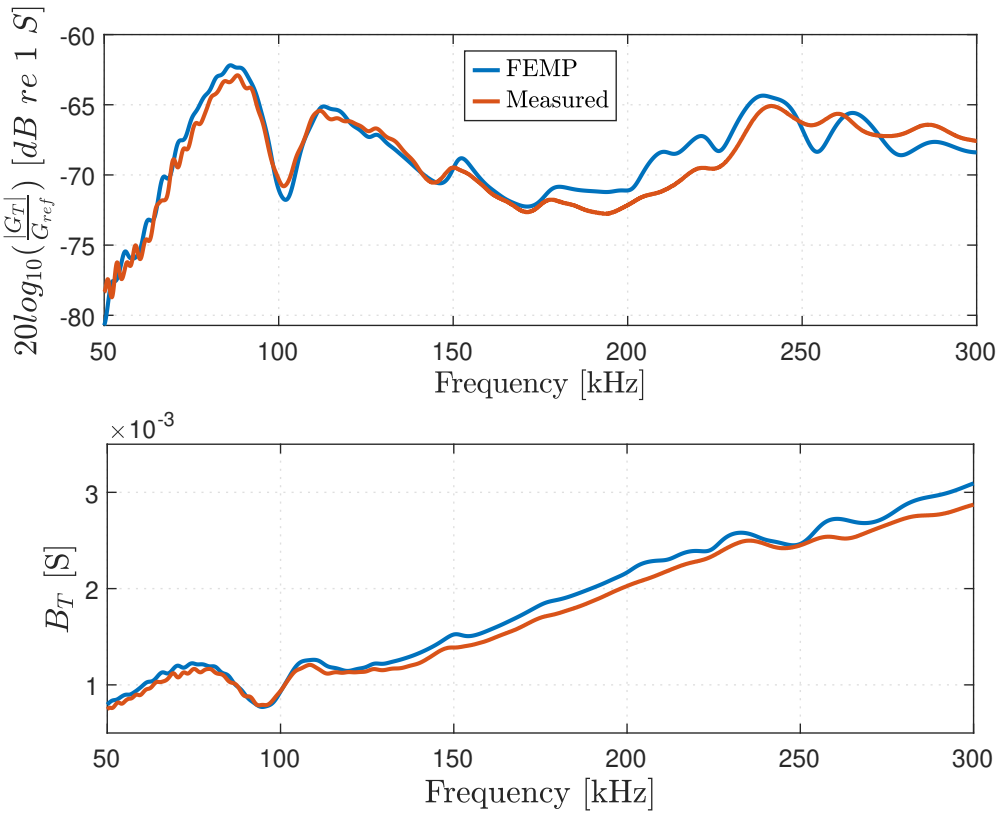

Figure 8.13: Same as Fig. 8.12, but for transducer # 29.

Figs. 8.12 and 8.13 show a fair agreement between measurement and simulation for both transducers. In Fig. 8.12, the simulated and measured conductance, G_T, and susceptance, B_T for transducer # 25 closely align at frequencies below 100 kHz. For transducer # 29 in Fig. 8.13, the measured conductance and susceptance are slightly lower than the simulated values in the same frequency range. Between 100 kHz and 150 kHz, the match between measurement and simulation is better for transducer # 29, when compared to transducer # 25, which shows elevated conductance measurements across the same frequency range. At higher frequencies above 200 kHz, there is less compliance between measured and simulated conductance, G_T. The measured susceptance, B_T is lower than the simulated result for both transducers at frequencies above 125 kHz. However, a close to a linear increase in B_T with the frequency, f is observed in both measurement and simulation.

8.2 Acoustical measurements and simulations: Transducer to microphone

This section presents the results from the acoustical measurements conducted using the two completed transducers as the transmitter, and the Brüel & Kjær type 4138 condenser microphone as the receiver. A picture of the measurement setup is shown in Fig. 4.3b. The transducer and microphone are coaxially aligned on the z-axis and separated by a distance, d = 0.5 m. During the voltage source sensitivity measurements, the signal generator is configured to provide a nominal output voltage of V_{pp} = 20 V, with a 1.2 ms burst length.

The measured transducer voltage source sensitivity magnitude, $|S_V|$ is compared to simulation results obtained using the FEMP structure **`Transducer_Fluid`**. A distance R_{inf} = 0.2 m, and the measured transducer dimensions presented in Chapter 7 have been used in the FEMP simulations.

Based on the $|S_V|$ measurements of the two transducers, the quality factor, Q_{3dB} will be calculated in order to quantify the bandwidth of each transducer. In the end of the section, some of the recorded voltage waveforms, V_{0m} and V_6, will be presented at the frequency of maximum voltage source sensitivity magnitude, f_0.

8.2.1 Voltage source sensitivity, S_V

Figs. 8.14 shows the magnitude of the measured voltage source sensitivity, $|S_V|$, for transducer # 25. The measurement is performed at a distance d = 0.5m, and extrapolated to d = 1 m using Eq. 2.135 [29]. The measurements are compared to simulations performed using the FEMP structure **`Transducer_Fluid`** from 50 to 200 kHz.

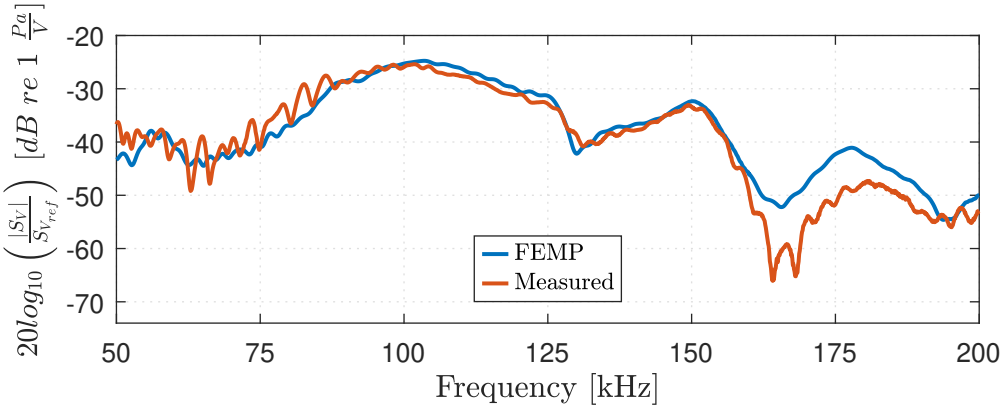

Figure 8.14: Magnitude of the voltage source sensitivity, $|S_V|$ at 1 m for transducer # 25 in the frequency range 50 to 200 kHz. Measurements are compared with simulations of the transducer vibrating in air using the FEMP structure ***Transducer_Fluid****.*

In Fig. 8.14, the measurement and simulation shows similar results, with $|S_V|$ peaks at 101.8 and 103.6 kHz, respectively. At frequencies below 90 kHz, some significant peaks in the measured $|S_V|$ are not present in the simulation. The cause of these peaks has not been investigated further, but one hypothesis is that they originate from standing waves or reflections in the backing layer. The presence of large air bubbles within the backing layer could potentially contribute to these effects. At around 165 kHz, the measured $|S_V|$exhibits a notably deeper dip compared to the simulation. Additionally, while both the measured and simulated $|S_V|$ show an upward trend towards 175 kHz, a persistent discrepancy is observed between the two curves, up to approximately 195 kHz.

Fig. 8.15 shows the same as in Fig. 8.14, but only for the frequencies around the peak in measured voltage source sensitivity magnitude, $|S_V|$.

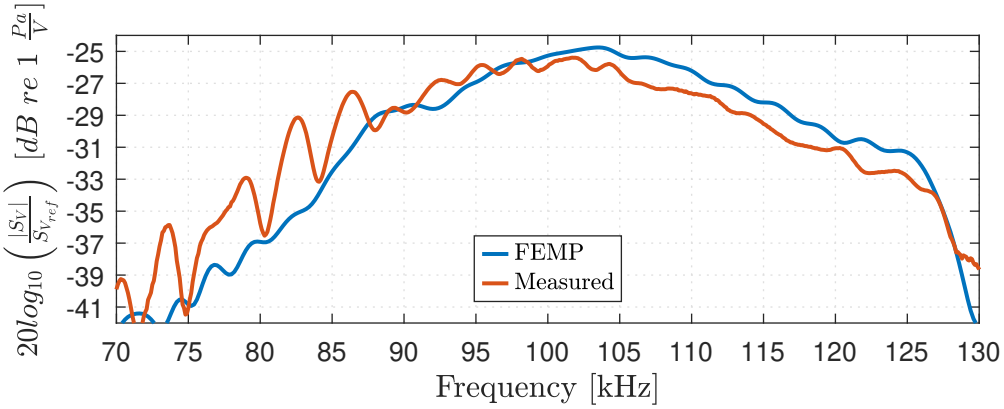

Figure 8.15: Same as in Fig. 8.15, but in the frequency range 70 to 130 kHz.

Fig. 8.15 shows that the measured $|S_V|$ is generally higher than the simulation at the frequencies below 96 kHz. However, above 96 kHz, the simulated $|S_V|$ is higher, with a discrepancy of approximately 2 dB between measurement and simulation.

Fig. 8.16 shows the magnitude of the measured voltage source sensitivity, $|S_V|$, for transducer # 29. The measurements are compared to simulations performed using the FEMP structure **`Transducer_Fluid`**, from 50 to 200 kHz.

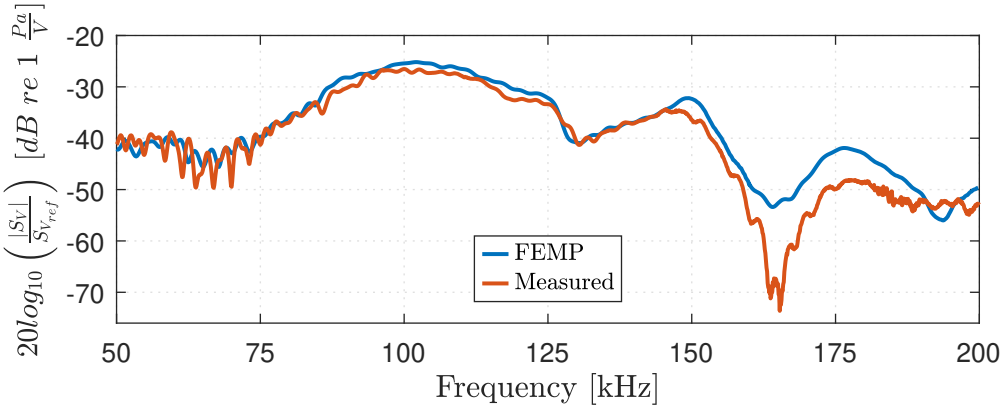

Figure 8.16: Magnitude of the voltage source sensitivity, $|S_V|$ at 1 m for transducer # 29 in the frequency range 50 to 200 kHz. Measurements are compared with simulations of the transducer vibrating in air using the FEMP structure ***Transducer_Fluid****.*

Fig. 8.16 also shows a reasonable agreement between measurement and simulation for transducer # 29. The measured and simulated $|S_V|$ peaks at 100 and 102 kHz, respectively.

The resonance peaks at frequencies below 90 kHz observed in the measured $|S_V|$ for transducer # 25 in Fig. 8.14, are not as prominent in transducer # 29. This supports the hypothesis that the peaks are caused by air bubbles and imperfections in the backing layer of transducer # 25. At frequencies below 75 kHz, there are still some peaks in the measured $|S_V|$, but they are also visible in the simulation. For transducer # 29, there is also a significant dip in the measured $|S_V|$ around 165 kHz. This dip causes a relatively large discrepancy between the measurement and simulation up to around 190 kHz.

Fig. 8.17 shows the same as in Fig. 8.16, but only for the frequencies around the peak in measured voltage source sensitivity magnitude, $|S_V|$.

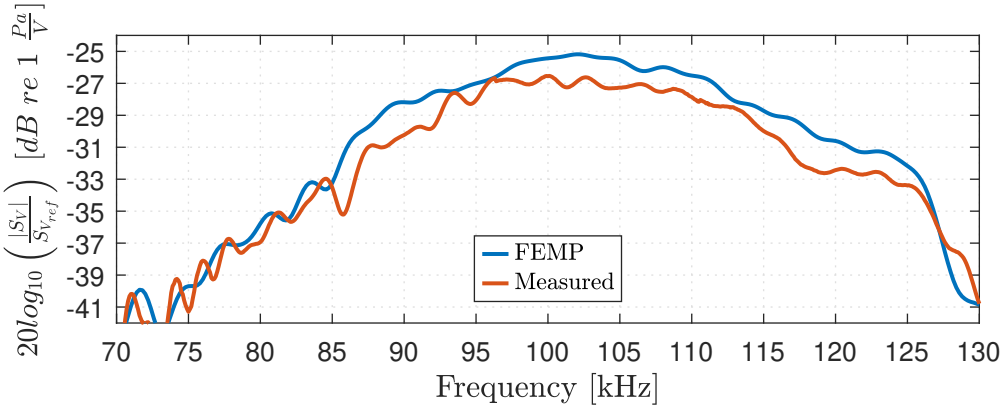

Figure 8.17: Same as in Fig. 8.16, but in the frequency range 70 to 130 kHz.

Fig. 8.17 shows that the measured $|S_V|$ is generally lower than the simulation. At the frequencies below 85 kHz the agreement is good, but above this frequency the discrepancy increases to between 1 and 2 dB.

Fig. 8.18 shows a comparison of the measured voltage source sensitivity magnitude, $|S_V|$ for transducer # 25 and # 29.

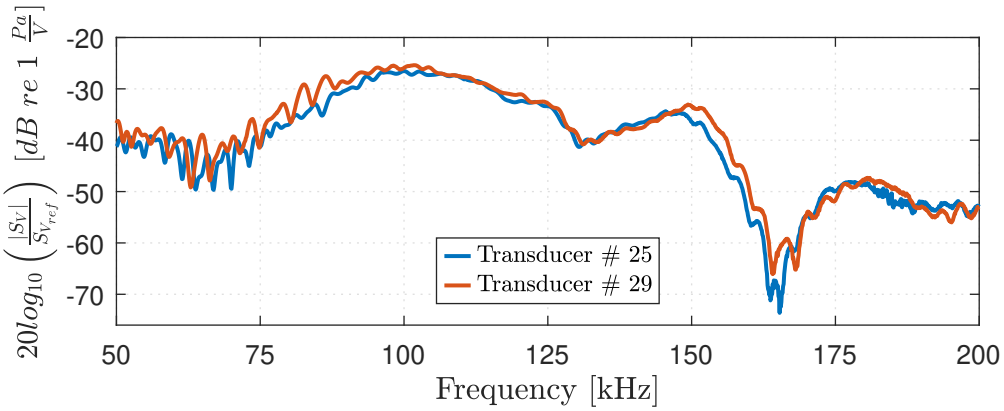

Figure 8.18: Measured voltage source sensitivity magnitude, $|S_V|$ at 1 m for transducer # 25 and # 29 in the frequency range 50 to 200 kHz.

Fig. 8.18 shows that the two constructed transducers have a similar voltage source sensitivity magnitude, $|S_V|$. As mentioned previously, the largest discrepancy in the two measurements is seen between 70 and 90 kHz, where transducer # 25 has some peaks in the voltage source sensitivity that are not present in transducer # 29. Additionally, the drop in $|S_V|$ observed around 165 kHz initiates at a lower frequency for transducer # 25 compared to transducer # 29. Despite these differences, the overall agreement between the two measurements is reasonably good, suggesting a certain level of reproducibility has been achieved in the transducer construction process.

8.2.2 Nonlinearity check

To investigate if any of the discrepancies between the measured and simulated voltage source sensitivity magnitude $|S_V|$, in Figs. 8.14 - 8.17 can be related to nonlinearities in the transmitting transducer or the fluid medium, an additional measurement is performed on transducer # 25 with a decreased output voltage from the signal generator. The two measurements are performed to be as equal as possible, but the nominal output voltage from the signal generator is decreased from, $V_{pp} = 20$ V to $V_{pp} = 1$ V.

Fig. 8.19 shows the measured voltage source sensitivity magnitude, $|S_V|$ for transducer # 25, with the nominal signal generator output voltage set to both $V_{pp} = 1$ V, and $V_{pp} = 20$ V. The measurements are conducted in a limited frequency range around the peak of the measured $|S_V|$, as this is the frequency range where the largest effect from nonlinearities are expected.

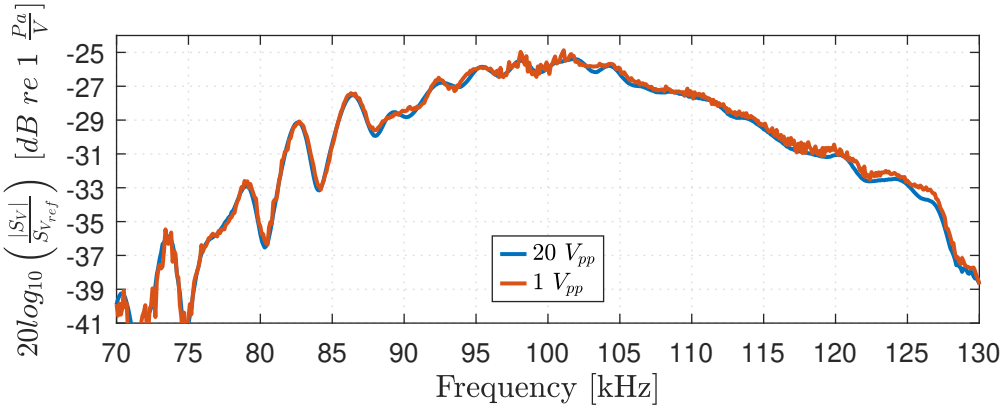

Figure 8.19: Comparison of the measured voltage source sensitivity magnitude, $|S_V|$ for transducer # 25 with the signal generator nominal output set to 20 V_{pp} and 1 V_{pp}.

Fig. 8.19 shows that there is a small increase in the measured $|S_V|$ when the output voltage from the signal generator is decreased. The increase is larger at the highest frequencies of the measurement, but is not large enough to fully explain the discrepancies seen between the measurement and simulation in Figs. 8.14 - 8.17. In Fig. 8.18 transducer # 25 and # 29 are shown to be relatively similar during transmission. A measurement with reduced output voltage from the signal generator is therefore not performed on transducer # 29.

8.2.3 Transducer Bandwidth

Figs. 8.20 and 8.21 displays the measured magnitude of $|S_V|$ for transducer # 25 and # 29 respectively. The graphs include vertical lines indicating the -3 dB frequencies, f_{3dB}^- and f_{3dB}^+, at which the voltage source sensitivity magnitude, $|S_V|$ drops by 3 dB from its maximum at the frequency, f_0.

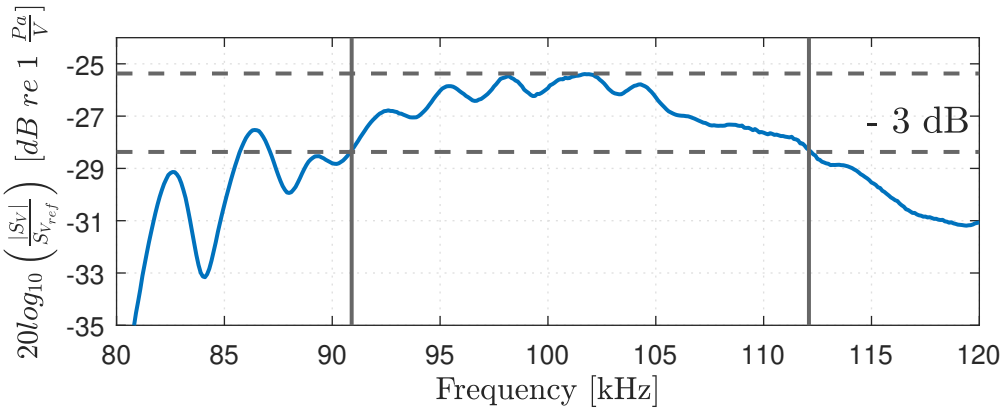

Figure 8.20: Measured $|S_V|$ for transducer # 25

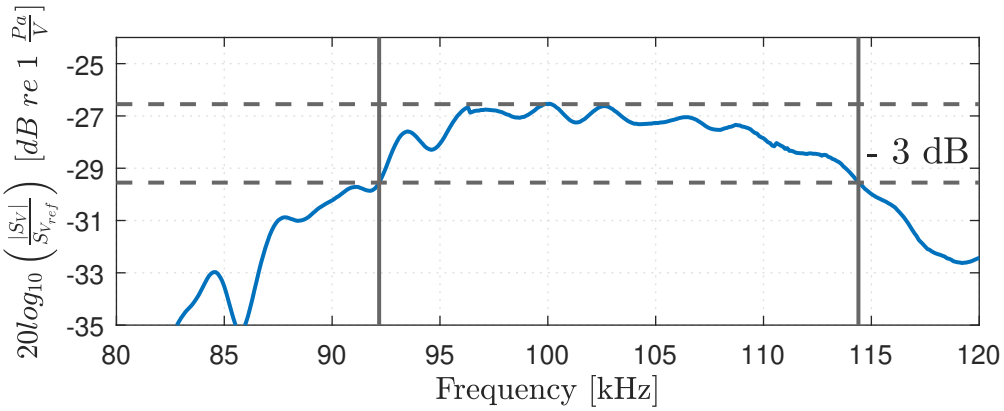

Figure 8.21: Measured $|S_V|$ for transducer # 29

Tab. 8.2 shows the measured frequencies, f_0, f^-_{-3dB}, f^+_{-3dB}, and the calculated quality factor Q_{3dB} for transducer # 25 and # 29. Q_{3dB} is calculated using Eq. 2.10.

Table 8.2: Measured frequencies, f_0, f^-_{-3dB}, f^+_{-3dB}, and the calculated quality factor Q_{3dB} for transducer # 25 and # 29.

Transducer #	f_{res} [kHz]	f^-_{-3dB} [kHz]	f^+_{-3dB} [kHz]	Q_{3dB}
25	101.8	90.9	112.1	4.8
29	100.0	92.18	114.4	4.5

Tab. 8.2 shows that transducer # 29 has a slightly better bandwidth when compared to transducer # 25. The difference in bandwidth is likely a result of inaccuracies during the constrcution process.

8.3 Beam pattern simulations

Because of hardware limitations in the acoustical measurement setup, the beam pattern, $D(\theta)$ of the two constructed transducers, has not been characterized experimentally. However, the reasonable agreement in the measured and simulated voltage source sensitivity S_V and admittance Y_T might indicate that the simulated beam pattern can provide helpful information about the constructed transducers. Fig. 8.22 displays the simulated beam pattern of transducer # 29 at 90, 100, and 110 kHz. Due to some issues with the plotting software, the first side lobe on the left side of the beam pattern is slightly flattened. The beam pattern from $\theta = 90°$ to $\theta = 270°$ has not been altered and is correct.

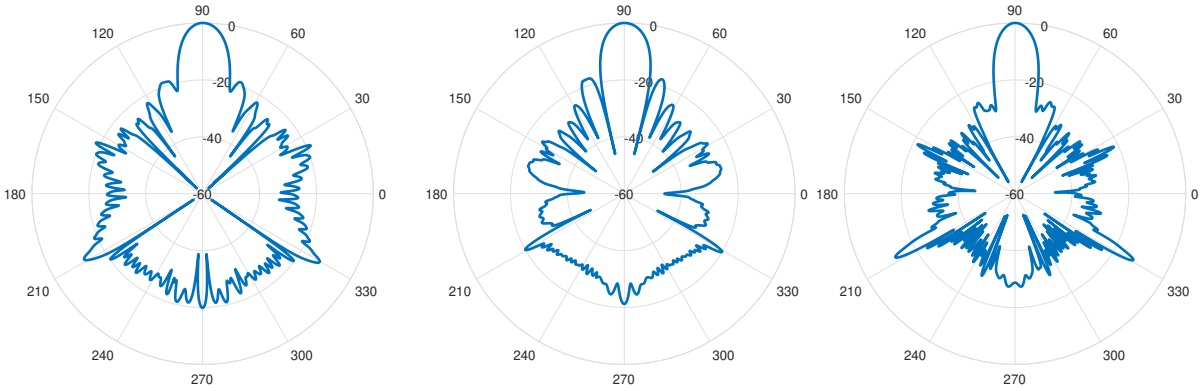

(a) *(b)* *(c)*

Figure 8.22: (a) Simulated Beam pattern for transducer # 29 at 90 kHz (b) Same as in Fig. 8.22a, but at 100 kHz (c) Same as in Fig. 8.22a, but at 110 kHz

In Fig.8.22, the beam pattern at 90 kHz shows a side lobe level of - 18.5 dB for the first side lobe. At the frequency of maximum measured $|S_V|$, 100 kHz, the first side lobe level is - 18 dB. At 110 kHz, the first side lobe level decreases to - 26 dB. The simulation results indicate that the constructed transducers have a solid main lobe with relatively small side lobes at frequencies near the peak in voltage source sensitivity, S_V.

8.3.1 Recorded waveforms, V_{0m} and V_6

Some of the recorded waveforms, V_{0m} and V_6 used in the measurement of the voltage source sensitivity, $|S_V|$ will be displayed here. Due to similar results for the two transducers, only waveforms recorded using transducer # 29 as the transmitter and the microphone as the receiver will be shown. No signal processing is performed on the waveforms, i.e., the 60 dB amplification on the output voltage from the receiving electronics, V_6 has not been subtracted from the measurement.

Fig. 8.23 shows the waveforms, V_{0m} and V_6, recorded at 100 kHz when using transducer # 29 as the transmitter and the Brüel & Kjær microphone as the receiver. The burst length is 1.2 ms, as used in the $|S_V|$ measurements, and 100 kHz is the frequency of the maximum recorded $|S_V|$ for transducer # 29. The separation distance between transducer and microphone is 0.5 m.

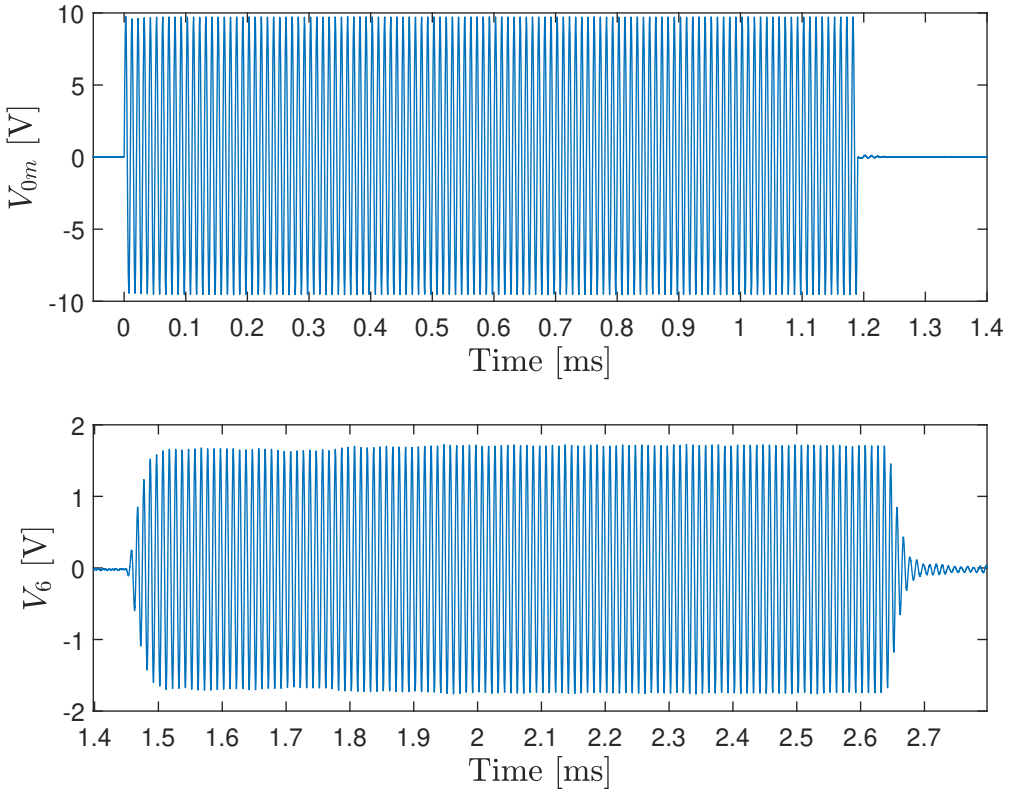

Figure 8.23: Recorded voltage signals, V_{0m} and V_6 at 100 kHz. Transducer # 29 is the transmitter, and the Brüel & Kjær condenser microphone is the receiver, with a separation distance d = 0.5 m.

In Fig. 8.23, the recorded output voltage from the signal generator, V_{0m} is shown to have minimal distortion and reaches a steady state without any transients at the start or end of the signal. However, the recorded signal, V_6 from the receiving electronics shows a transient of approximately 7 periods at the start of the signal. After 7 periods, a portion of the signal maintains a nearly constant amplitude until approximately 1.7 ms, where there is a slight increase in voltage amplitude. After this increase, the amplitude remains constant until the transient at the end of the signal.

Fig. 8.24 shows the same as in Fig. 8.23, but the burst length is decreased to 0.1 ms. This is done to study how the transducer behaves when transmitting shorter burst. The shorter bursts are not used in any of the voltage source sensitivity calculations.

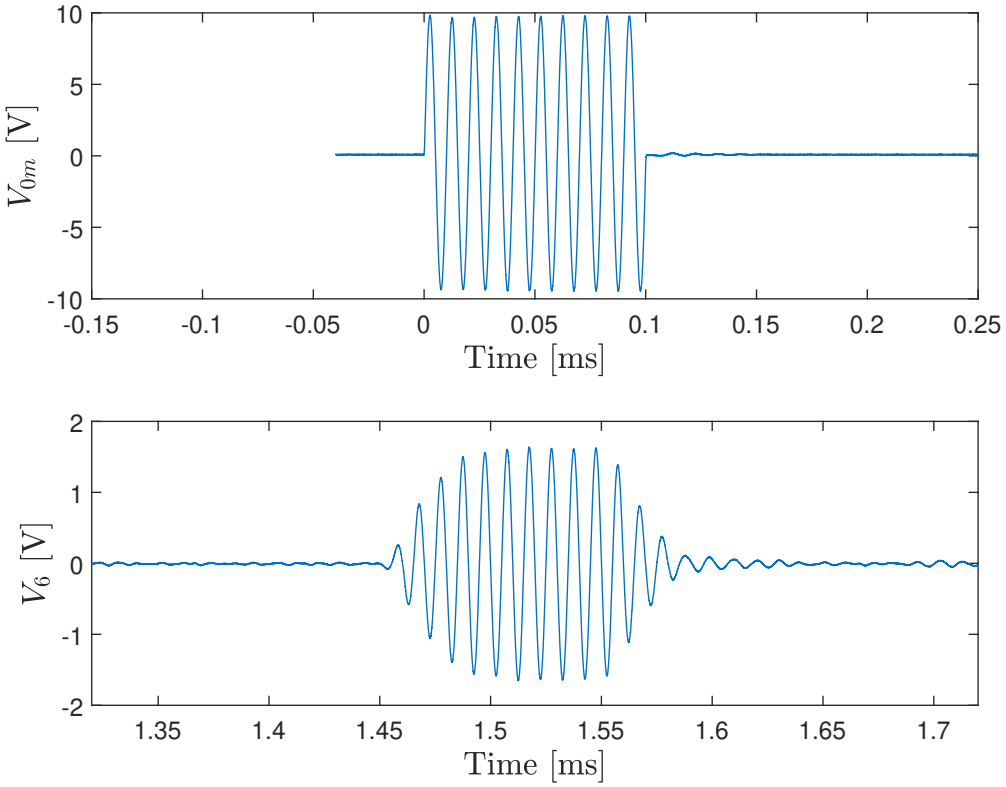

Figure 8.24: Same as in Fig. 8.23, but with a 0.1 ms burst length.

Similar to the recorded output voltage from the signal generator, V_{0m} in Fig. 8.23, the signal with a 0.1 ms burst length also shows little to no signs of transients or distortion. The recorded output voltage from the receiving electronics, V_6, reaches comparable amplitude levels as those recorded with the long burst in Fig. 8.23. The last four peaks before the transient at the end of the signal also show almost identical amplitudes, indicating that the signal is close to steady state.

Fig. 8.25 shows the same as in Figs. 8.23 and 8.24, but the burst length is decreased further, to 0.05 ms.

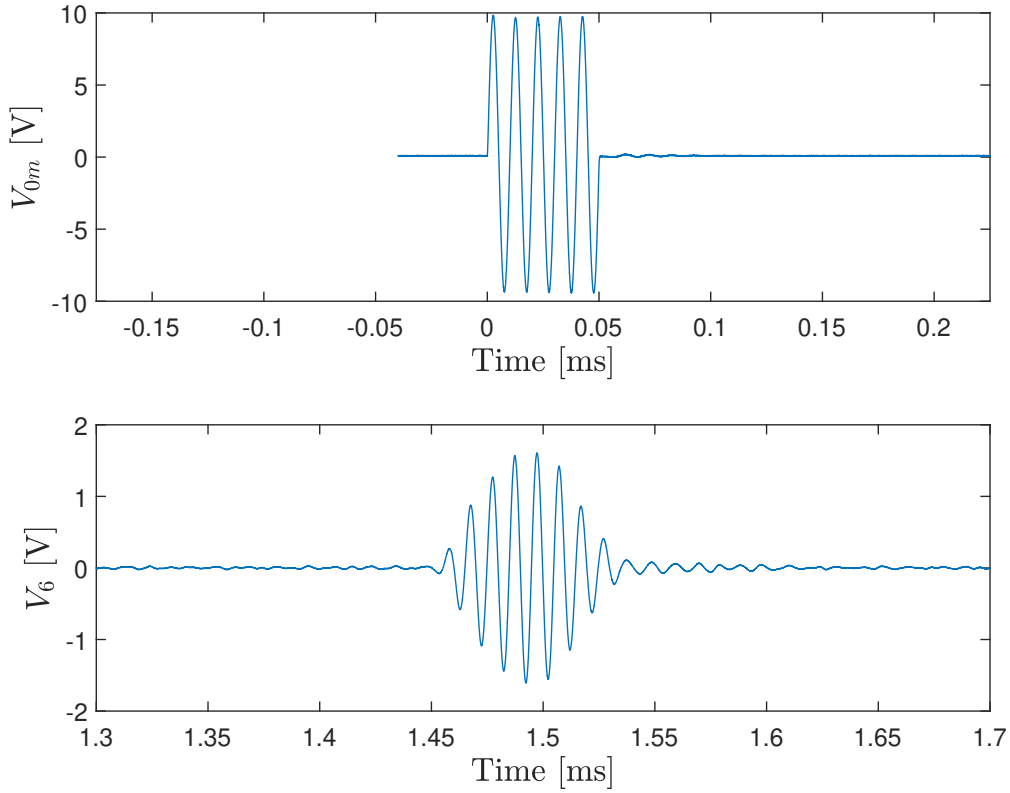

Figure 8.25: Same as in Fig. 8.23, but with a 0.05 ms burst length.

In Fig. 8.25 the recorded output signal from the signal generator V_{0m} still shows little to no sign of transients or distortion. The recorded voltage from the receiver electronics, V_6 does not reach a steady state, but the amplitude levels are close to those achieved when transmitting the long burst in Fig. 8.23.

The results in Figs. 8.23 - 8.25 demonstrate the constructed transducers ability to transmit bursts with relatively short transient periods at the start and end of the signal. Results presented by Hauge in [29] display a transient period of approximately 0.2 ms in the start of the recorded V_6 signal when utilizing a single Pz27 piezoelectric disk as the transmitter. By using the transducers constructed during this project, the start transient period is reduced to approximately 0.05 ms.

8.4 Acoustical measurements and simulations: Transducer to transducer

This section presents the results from the acoustical measurements conducted using transducer # 29 as the transmitter and transducer # 25 as the receiver. A picture of the measurement setup is shown in Fig. 4.3c. The transducers are coaxially aligned on the z-axis and separated by a distance, $d = 0.5$ m. The nominal output voltage from the signal generator is set to $V_{pp} = 20$ V.

The measured magnitude of the measurement system transfer function, $|H^{VV}_{0m6,\alpha}|$ is compared to simulations from the FEMP structure **`Transducer_Fluid`**, and the system model theory presented in Sec. 2.3. Based on the $|H^{VV}_{0m6,\alpha}|$ measurements the measurement systems bandwidth and quality factor, Q_{3dB} is calculated. At the end of the section, some of the recorded waveforms, V_{0m} and V_6 will be presented at the peak frequency of the measured transfer function $|H^{VV}_{0m6,\alpha}|$.

8.4.1 Measurement system transfer function, $H^{VV}_{0m6,\alpha}$

The measurement system transfer function magnitude $|H^{VV}_{0m6,\alpha}|$ is measured by inserting the recorded amplitudes, V_{0m} and V_6 into Eq. 2.28. When calculating the simulated $|H^{VV}_{0m6,\alpha}|$ using the system model presented in Sec. 2.3, some simplifications are used to save computing time and simplify the system model calculations. This simplification implies that only the simulated transducer characteristics for transducer # 29 have been used as input in the system model. That means that the transmitting and receiving transducers respective input and output impedance are equal, i.e., $Z^{Tx}_T = Z^{Rx}_T$. Furthermore, the receivers voltage source sensitivity, S^{Rx}_V also equals the simulated voltage source sensitivity of the transmitter, S^{Tx}_V, i.e., $S^{Tx}_V = S^{Rx}_V$. These simplifications are also used when calculating the receiving transducers free field open-circuit receiving sensitivity, M^{Rx}_V, using spherical wave reciprocity. The simplifications might induce some errors in the simulations, but Fig. 8.18 shows that the voltage source sensitivities of the two constructed transducers are relatively similar.

Fig. 8.26 shows the measured magnitude of the measurement system transfer function, $|H^{VV}_{0m6,\alpha}|$ at 0.5 m. Transducer # 29 is used as transmitter and transducer # 25 is the receiver. Measurements are compared with simulations of transducer # 29 acting as both transmitter and receiver, using the FEMP structure **`Transducer_Fluid`**.

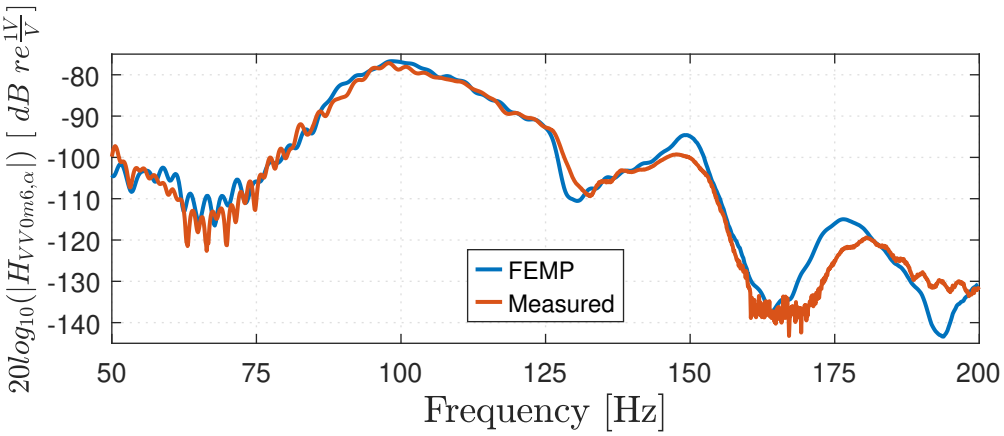

Figure 8.26: Comparison of measured and simulated $|H^{VV}_{0m6,\alpha}|$, at 0.5 m in the frequency range 50 to 200 kHz.

Fig. 8.26 demonstrates a reasonable agreement between the simulation and measurement. The measured and simulated $|H^{VV}_{0m6,\alpha}|$ peaks at frequencies of 98 and 98.4 kHz, respectively. However, some discrepancies are observed at frequencies below 75 kHz, where the simulation displays peaks that are absent in the measurement. Between 75 and 125 kHz, the measurement and simulation closely align, with a maximum discrepancy of approximately 2 dB. At around 125 kHz, the simulation exhibits a sharper dip compared to the measurement, while at 150 kHz, the simulation displays a higher peak than observed in the measurement. It should be noted that around 160 kHz, the signal-to-noise ratio in the measurement is insufficient to obtain accurate amplitude measurements for the recorded signal V_6. Consequently, the actual dip may extend further than what can be measured, similar to the observations in the measured voltage source sensitivity presented in Figs. 8.14 and 8.16. Towards 175 kHz, both the measurement and simulation show an increase in $|H^{VV}_{0m6,\alpha}|$. However, an increased deviation is also evident here, corresponding to the discrepancy observed earlier for the measured and simulated voltage source sensitivity, S_V at the same frequencies.

Fig. 8.27 displays the same measurement and simulation results presented in Fig. 8.26, but focused around the measured peak of $|H^{VV}_{0m6,\alpha}|$ at 98 kHz.

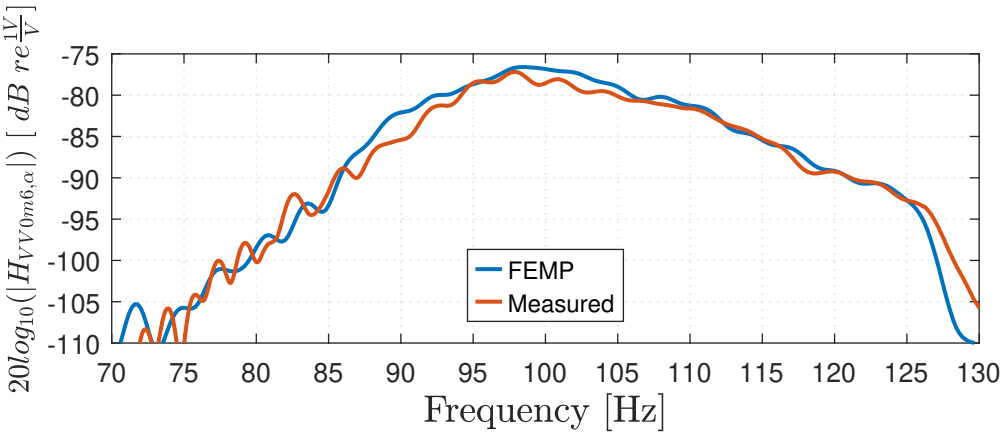

Figure 8.27: Same as in Fig. 8.26 but in the frequency range 70 to 130 kHz.

As in Fig. 8.26 the measurement and simulation in Fig. 8.27 show close alignment, and a maximum discrepancy of approximately 3 dB.

8.4.2 Free field open-circuit receiving sensitivity, M_V

By the use of spherical wave reciprocity as described in [31], the simulated transducer free field open-circuit receiving sensitivity, M_V can be calculated. Fig. 8.28 shows the simulated $|M_V|$ for transducer # 29.

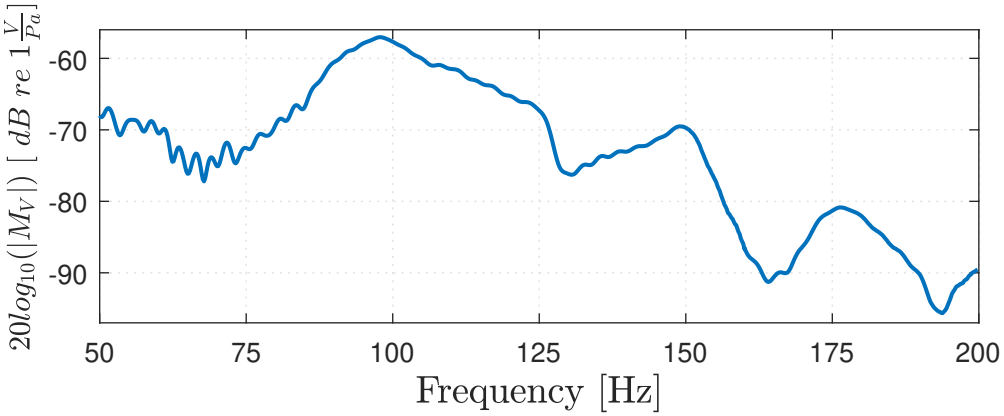

Figure 8.28: Simulated $|M_V|$ for transducer # 29.

Fig. 8.28 shows that the simulated free field open-circuit receiving sensitivity magnitude, $|M_V|$ for transducer # 29, peaks at 97.8 kHz. This is slightly lower than the measured and simulated peak in voltage source sensitivity, $|S_V|$ for the same transducer at 100 and 102 kHz, respectively. This result is in contrast to the observations in [29, 31], where the peak in simulated $|M_V|$ for a single Pz 27 disk is located approximately 16.5 kHz above the peak in simulated, $|S_V|$.

8.4.3 Measurement system bandwidth

Fig. 8.29 shows the measured magnitude of the measurement system transfer function, $|H^{VV}_{0m6,\alpha}|$ at 0.5 m. Transducer # 29 is used as transmitter and transducer # 25 is the receiver. The figure includes vertical lines indicating the frequencies at which the transfer function magnitude, $|H^{VV}_{0m6,\alpha}|$ drops by 3 dB from the peak value observed at the peak frequency f_0. The measurement system quality factor, Q_{3dB} is calculated using Eq. 2.10, but the frequencies, f^{+}_{3dB} and f^{-}_{3dB} are now the upper and lower frequency, where a -3 dB drop from the peak value of $|H^{VV}_{0m6,\alpha}|$ is achieved.

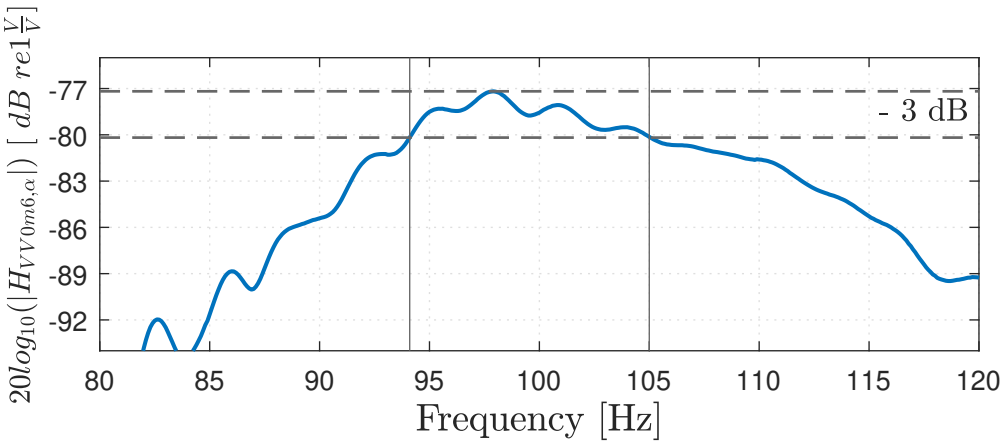

Figure 8.29: Measured $|H^{VV}_{0m6,\alpha}|$, at 0.5 m

From fig 8.29 the frequencies f_0 = 98.0 kHz, f^{-}_{3dB} = 94.1 kHz , and f^{+}_{3dB} = 105.0 kHz. By the use of Eq. 2.10 the measurement system quality factor Q_{3dB} = 9.0. The measurement system bandwidth is thus lower than the bandwidth for the individual transducers, which had a quality factor of Q_{3dB} = 4.5 and Q_{3dB} = 4.8. This result is in contrast with the findings in [29, 31], where the use of a piezoelectric disk as both transmitter and receiver contributed to an increase in the overall system bandwidth.

8.4.4 Recorded waveforms, V_{0m} and V_6

Some of the recorded waveforms, V_{0m} and V_6 used in the measurement of $|H^{VV}_{0m6,\alpha}|$ will be displayed here. Transducer # 29 is used as the transmitter and transducer # 25 is the receiver. No signal processing is performed on the waveforms, i.e., the 60 dB amplification on the output voltage signal from the receiving electronics, V_6 has not been subtracted from the measurement.

Fig. 8.23 shows the waveforms, V_{0m} and V_6, recorded at 98 kHz, which is the peak frequency of the measured $|H^{VV}_{0m6,\alpha}|$. The burst length is 1.3 ms, as used in the $|H^{VV}_{0m6,\alpha}|$ measurements, and the separation distance between the transducers is 0.5 m.

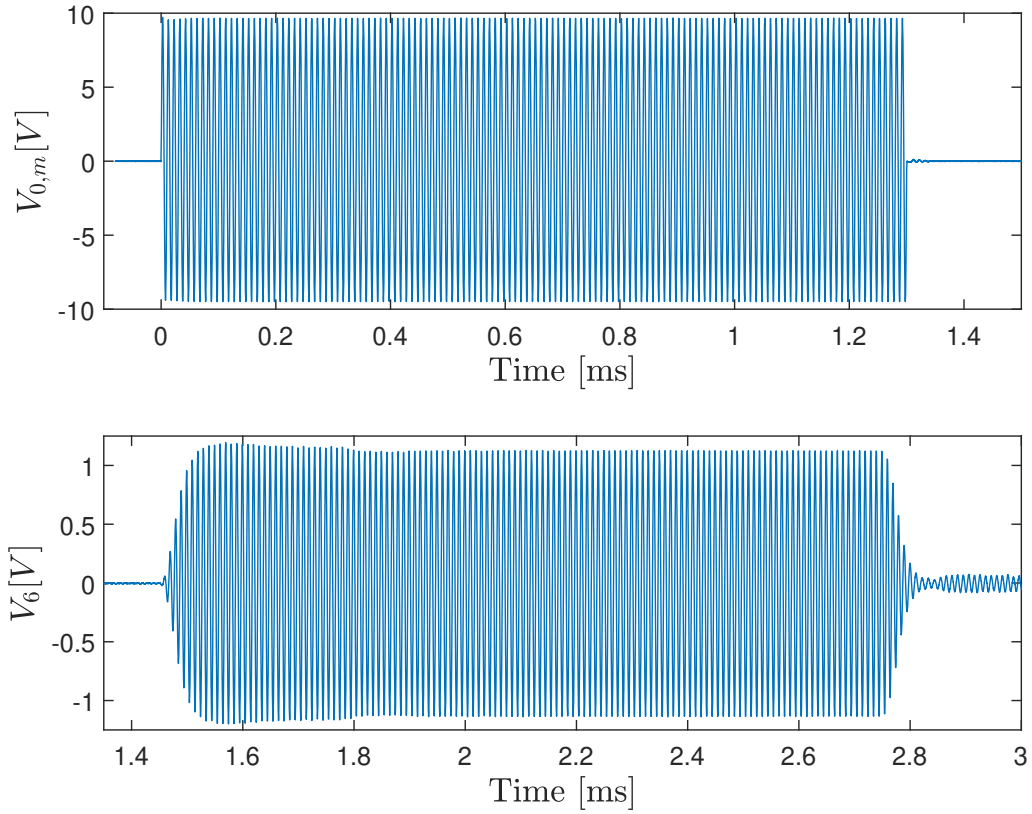

Figure 8.30: Recorded waveforms of the voltage signals, V_{0m} and V_6 at 98 kHz. Transducer # 29 is the transmitter, and Transducer # 25 is the receiver, with a separation distance d = 0.5 m. The burst length is 1.3 ms.

As expected the signal generators recorded output voltage, V_{0m} in Fig. 8.30 is similar to the waveform V_{0m} recorded using the transducer to microphone setup in Fig. 8.23. The recorded output signal from the receiving electronics, V_6 uses about 11 periods before it peaks and has a small overshoot, which settles at approximately, 1.85 ms. For comparison the transducer to microphone measurement in Fig. 8.23 took about 7 periods to reach the peak amplitude. This increase in the transient period can be related to the reduction in system bandwidth for, $|H^{VV}_{0m6,\alpha}|$, relative to $|S_V|$, as shown in Figs. 8.29 and 8.21, respectively.

Fig. 8.31 shows the same as in Fig. 8.30, but the burst length is decreased to 0.102 ms, to study how the system behaves when transmitting a short burst. The displayed signals have not been used in any of the $|H^{VV}_{0m6,\alpha}|$ measurements.

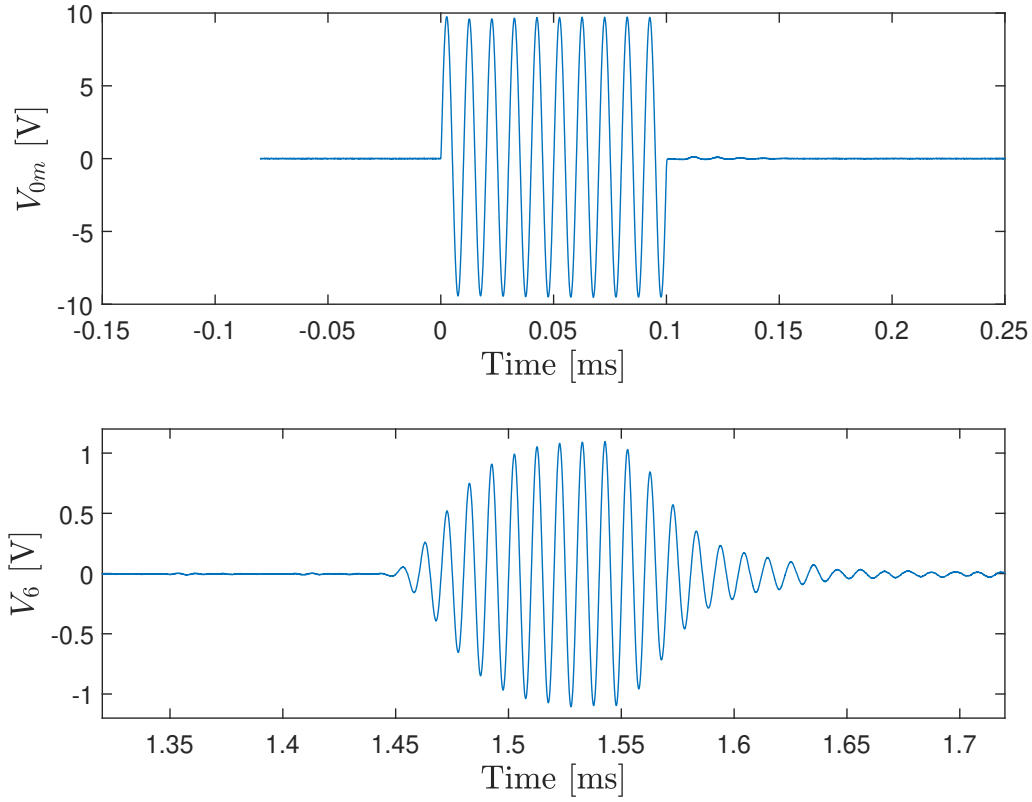

Figure 8.31: Same as in Fig. 8.30, but with a 0.102 ms burst length

Similar to the recorded output voltage from the signal generator, V_{0m} in Fig. 8.30, the signal with a 0.102 ms burst length shows little to no signs of transients or distortion. The recorded output voltage from the receiving electronics, V_6, has an increased transient period at the start of the signal relative to the transducer to microphone measurement in Fig.8.24. The voltage signal, V_6 does not reach a steady state, and an increased amount of ringing is also seen in the transient at the end of the signal. These effects are likely related to the reduction in bandwidth for the $|H^{VV}_{0m6,\alpha}|$ measurements relative to the bandwidth in the measured $|S_V|$.

Fig. 8.32 shows the same as in Figs. 8.30 and 8.31, but the burst length is decreased to 0.051 ms.

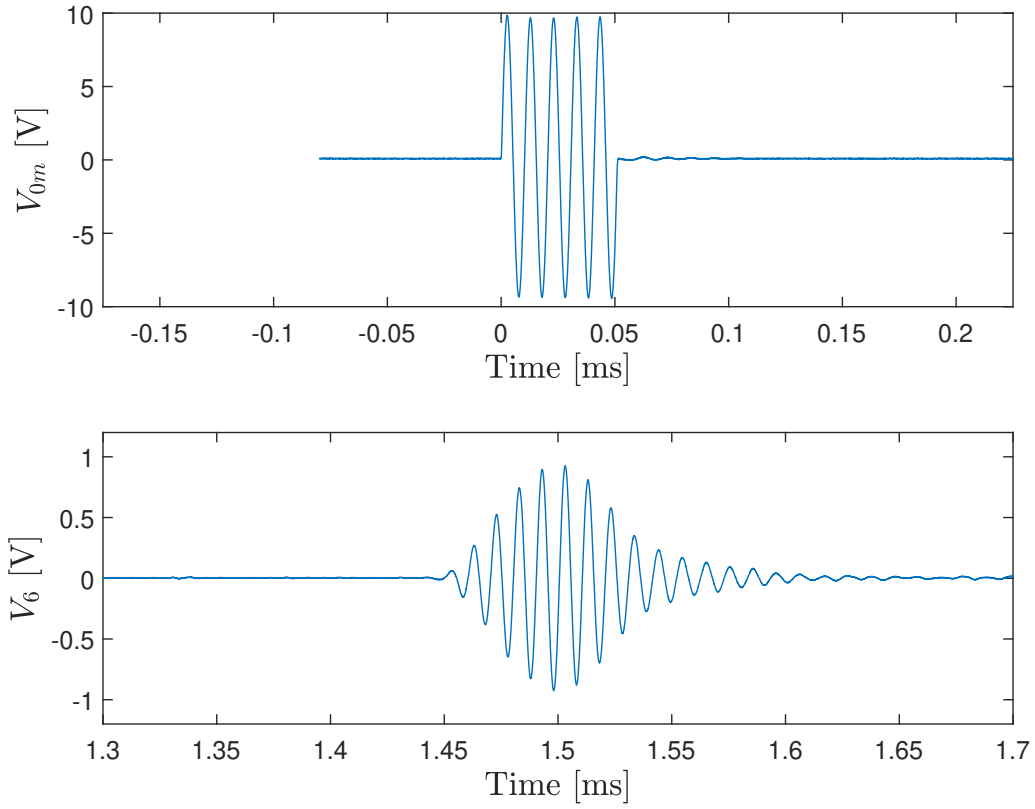

Figure 8.32: Same as in Fig. 8.30, but with a 0.051 ms burst length

In fig. 8.32 the recorded output signal from the signal generator, V_{0m} still shows little to no sign of transients or distortion. The recorded voltage from the receiver electronics, V_6 does not reach a steady state, and the maximum amplitude is slightly decreased, from the steady state amplitude in Fig. 8.30.

Chapter 9

Conclusions and further work

9.1 Conclusions

In this project, two piezoelectric transducers have been designed, constructed, and experimentally characterized. In addition, experimental measurements of the transducer characteristics were compared to finite element simulations during and after the transducer construction.

Initially, a finite element simulation study was conducted to investigate and reproduce results presented in [40–42], related to the clamping of radial modes in piezoelectric disks. Based on the results from the initial simulation study, an additional transducer design study was conducted to create a transducer design with the desired transducer characteristics. The desired characteristics include a high voltage source sensitivity, a beam pattern with low side lobe levels, and a large bandwidth around the transducer's operating frequency at approximately 100 kHz.

The final transducer design utilizes the first radial vibration mode, RM1, of a piezoelectric disk with nominal dimensions 20 mm x 2 mm. The transducer design was constructed and characterized experimentally using an acoustic and electric measurement setup. The acoustical measurements of the transducer voltage source sensitivity magnitude, $|S_V|$, have been compared with $|S_V|$ simulations from the FE modeling tool FEMP 6.1. Comparisons of the measured and simulated Conductance, G_T, and susceptance, B_T have also been performed during each step of the transducer construction process.

The two constructed transducers have also been implemented in a transmit-receive measurement system developed in [29, 30, 81, 83–86], where the transducers are utilized as both transmitter and receiver. Furthermore, the measurement system is modeled using a linear ultrasonic transmit-receive system model developed in [29, 31, 48]. The system model has been compared with experimental measurements of the systems voltage to voltage transfer function magnitude, $|H^{VV}_{0m6,\alpha}|$.

The comparison between the electrical measurements of Conductance, G_T, and susceptance B_T and their corresponding simulations demonstrate a fair level of agreement throughout all stages of the construction process. Measurements and simulations of the Conductance, G_T, in the frequency range 50 to 150 kHz, yield an agreement within 2 dB for the two completed transducers.

The two constructed transducers show an increase in bandwidth compared to measurements in [29] of a single piezoelectric disk with nominal dimensions, 20 mm x 2 mm radiating air. A reasonable agreement between measurements and simulations of the voltage source sensitivity magnitude $|S_V|$ is observed for both the constructed transducers. In the frequency range 70 to 130 kHz, an agreement within 3 dB is observed for transducer # 29, which pro-

vided slightly better agreement than transducer # 25.

The simulated and measured measurement system voltage to voltage transfer function, $|H^{VV}_{0m6,\alpha}|$ also yield a reasonable agreement between measurement and simulation. In the frequency range 70 to 130 kHz, a maximum discrepancy of 3 dB is observed. The measured and simulated $|H^{VV}_{0m6,\alpha}|$ both show a decrease in the measurement system bandwidth when compared to the voltage source sensitivity, $|S_V|$ of the individual transducers. The decrease in bandwidth is also evident in the measured waveforms, V_6, where an increase in the number of transient periods is observed when transmitting from one transducer to another.

The discrepancy between measurements and simulations are presumably caused by a number of contributors. In the simulations of the complete transducer, a simplification is made when opting not to include the BNC connector and the casing which extends further back than the estimated length of the backing layer, T_b. Additionally, uncertainties associated with the material parameters contribute to the observed discrepancy. Notably, the material parameters for the transducer casing and the glue layers exhibit a significant degree of uncertainty. These values are based on measurements conducted on materials similar to those employed in the constructed transducers; however, no direct measurements have been performed on the exact materials utilized in the transducer construction.

In the system model used to simulate the transfer function $|H^{VV}_{0m6,\alpha}|$ an assumption of spherical wave reciprocity is adopted. Additionally, it is presumed that the transmitting and receiving transducers are identical, and their characteristics are thus based on the same finite element simulation. However, a better match between simulation and measurement could potentially be obtained by performing a new simulation where the differences in the two transducers are accounted for.

9.2 Further Work

Further work is needed to fully characterise the constructed transducers. The beam pattern and the radiated pressure field of the constructed transducers has yet to be characterized experimentally due to hardware limitations in the acoustical measurement setup. However, the beam pattern and pressure field characterization can be achieved by adding a new and shorter transducer holder to the transmitting side of the measurement setup. By doing this the face of the transmitting transducer will be aligned with the axis of the rotation stage in the measurement setup.

The decrease in system bandwidth for the voltage to voltage transfer function $|H^{VV}_{0m6}|$, compared to the transducer voltage source sensitivity S_V, emphasizes the need to focus on the bandwidth of the entire measurement system during the transducer design. In [29, 31], an increase in the measurement system bandwidth was observed when using single piezoelectric disks as both transmitter and receiver due to the difference in peak frequency for the voltage source sensitivity S_V and the free field open-circuit receiving sensitivity, M_V. However, for the transducers constructed during this work, the peak frequency of S_V and M_V are much closer aligned, thus not increasing the system bandwidth.

Additional work should also be conducted to more accurately determine the length of the tungsten/epoxy backing layer. During this work a rough estimate was made when deciding the length of the backing layer, T_b. This estimation is a source of discrepancy between the FE simulations and the experimental measurements. Work can also be performed to optimize the characteristic acoustic impedance of the backing layer to more closely match the characteristic acoustic impedance of the Pz27 piezoelectric disks.

For a transducer to operate inside a VOS cell for natural gas, it has to withstand high pressure and temperature levels. During this project, no special considerations are made concerning construction and material choices needed to withstand such an environment. In addition, the project has not given sufficient attention to the limitations associated with the dimensions of the transducers within the VOS cell. The two mentioned challenges must be solved for a transducer to operate in an industrial application.

Bibliography

[1] ISO Standard 17089-1:2019. *Measurement of Fluid Flow in Closed Conduits Ultrasonic Meters for Gas- Part 1: Meters for Custody Transfer and Allocation Measurement* (International Organization for Standardization, Geneva, Switzerland, 2019).

[2] Norsk forskningsråd. Subsea gas energy and quality measurement using ultrasonic flow meters: https://bit.ly/3INCPFs, last accessed: 29.05.2023.

[3] K. E. Frøysa, P. Lunde, A. Paulsen, and E. Jacobsen. "Density and calorific value measurement in natural gas using ultrasonic flow meters. Results from testing on various north sea gas field data". In *Proceedings of the 24th International North Sea Flow Measurement Workshop* (St. Andrews, Scotland 24-27 October, 2006).

[4] E. Storheim. "Diffraction effects in the ultrasonic field of transmitting and receiving circular piezoceramic disks in radial mode vibration FE modelling and comparison with measurements in air". Ph.D. thesis, Departement of Physics and Technology, Univesity of Bergen, Norway (2015).

[5] P. Lunde and M. Vestrheim. *Precision sound velocity cell for natural gas at high pressures. Phase 1 - feasibility study.* Technical Report CMR-98-A10039 (1998).

[6] P. Norli. "High-precision sound velocity cell for gas characterization". Ph.D. thesis, Departement of Physics and Technology, University of Bergen, Norway (2007).

[7] K.-E. Frøysa and P. Lunde. "Density And Calorific Value Measurement In Natural Gas Using Ultrasonic Flow Meters-quality flowmeter". volume 24, (2006), 27.

[8] B. Mirshab. *Analog Electronics Design to Improve Performance of Ultrasonic Gas Flow Meter*. Technical Report SNAA284A, Texas Instruments, Dallas, TX (2016).

[9] L. Estevez and C. Hao. "Ultrasonic sensing of gas flow". Texas Instruments (2019).

[10] ANSI Standard 1.26-1995 (R2014). *Methods for Calculation of the Absorption of Sound by the Atmosphere* (American National Standards Institute, New York, 1995).

[11] H. Blend. "Free-Field technique for measuring ultrasonic dispersion and absorption in gases". J. Acoust. Soc. Am. **47,** 757–761 (1970).

[12] M. R. Moldover, J. P. Trusler, T. J. Edwards, J. B. Mehl, and R. S. Davis. "Measurement of the Universal Gas Constant R Using a Spherical Acoustic Resonator". J. Res. Natl. Bur. Stand. (U. S.) **93,** 85–144 (1988).

[13] M. R. Moldover. "Measurement of the Universal Gas Constant R Using a Spherical Acoustic Resonator". Physical Review Letters **60,** 249–252 (1988).

[14] J. Kocbach. "Finite Element Modeling of Ultrasonic Piezoelectric Transducers". Phd thesis, Departement of Physics, University of Bergen, Norway (2000).

[15] F. Duck. "Paul Langevin, U-boats, and ultrasonics". Physics Today **75,** 42–48 (2022).

[16] W. Mason. *Electromechanical Transducers and Wave Filters*, (D. Van Nostrand Company, New York,1942).

[17] A. Meitzler, H. O'Bryan, and H. Tiersten. "Definition and Measurement of Radial Mode Coupling Factors in Piezoelectric Ceramic Materials with Large Variations in Poisson's Ratio". IEEE Transactions on Sonics and Ultrasonics **20,** 233–239 (1973).

[18] P. Lunde and M. Vestrheim. "Comparison of models for radial and thickness modes in piezoceramic disks". In *Proceedings of IEEE Ultrasonics Symposium* (Cannes, France 31-03 November, 1994).

[19] IEEE Standard on Piezoelectricity - std 176 1987 (The institute of Electrical and Electronics Engineers, Inc., New York, 1988).

[20] A. Lygre, M. Vestrheim, P. Lunde, and V. Berge. "Numerical simulation of ultrasonic flowmeters". In *Proceedings of Ultrasonics International 1987* (London, UK 06-09 July, 1987).

[21] P. Lunde and M. Vestrheim. *Piezoelectric transducer modelling. Thickness mode vibration*. Technical Report CMI-91-A10003 (1991).

[22] L. E. Kinsler, A. R. Frey, A. B. Coppens, and J. V. Sanders. *Fundamentals of Acoustics (4th Edition)* (John Wiley Sons, New York, 1999).

[23] J. Kocbach, Norce. Private communication (2022).

[24] M. Van Crombrugge. "Optimization of the transmitting characteristics of a Tonpilztype transducer by proper choice of impedance matching layers". J. Acoust. Soc. Am. **77,** 747–752 (1984).

[25] H. Allik and T. J. R. Hughes. "Finite element method for piezoelectric vibration". International Journal for Numerical Methods in Engineering **14,** 151–157 (1970).

[26] E. P. EerNisse. "Variational method for electroelastic vibration analysis". IEEE Transactions on Sonics and Ultrasonics **14,** 153–160 (1967).

[27] R. R. Smith, J. T. Hunt, and D. Barach. "Finite element analysis ofacoustically radiating structures with applications to sonar transducers". J. Acoust. Soc. Am. **54,** 1277–1288 (1973).

[28] J. Kocbach, P. Lunde, M. Vestrheim, and R. Kippersund. *Finite element modeling of ultrasonic piezoelectric transducers. Extension of FEMP to 3D analysis*. Technical Report CMR-06-A10046-RA-01 (2006).

[29] R. Hauge. "Finite element modeling of ultrasound measurement systems for gas. Comparison with experiments in air". Master thesis, Department of Physics and Technology, University of Bergen, Norway (2013).

[30] E. Mosland. "Acoustic Reciprocity calibration method for ultrasonic piezoelectric transducers in air". Master thesis, Department of Physics and Technology, University of Bergen, Norway (2013).

[31] R. Øyerhamn, E. N. Mosland, E. Storheim, P. Lunde, and M. Vestrheim. "Finite element modeling of ultrasound measurement systems for gas. Comparison with experiments in air". J. Acoust. Soc. Am. **144,** 2613–2625 (2018).

[32] A. Khimunin. "Numerical calculation of the diffraction corrections for the precise measurement of ultrasound absorption". Acustica **27,** 173–181 (1972).

[33] A. Khimunin. "Numerical calculation of the diffraction corrections for the precise measurement of ultrasound absorption". Ultrasonics **11,** 94 (1973).

[34] P. Lunde, UiB. Private communication (2023).

[35] C. M. Kang, Y. joo Baek, J. Y. Jeong, J. Sim, E. J. Gwak, T. J. Je, D. S. Choi, G. M. Kim, and J. S. Han. "Acoustic and rheological characterization of hollow glass microsphere composite for development of optimized air-coupled ultrasonic matching layer". Ceramics International **48,** 32036–32048 (2022).

[36] A. Khimunin. "Numerical calculation of the diffraction dorrections for the precise Measurement of ultrasound phase velocity". Acustica **32,** 192–200 (1975).

[37] R. Kippersund, P. Lunde, and M. Vestrheim. "Finite element modelling of piezoelectric ultra- sonic transducer properties in natural gas". In *Proceedings of the 27th Scandinavian Symposium on Physical Acoustics* (Ustaoset, Norway, 25-28 January 2004).

[38] E. Mosland, E. Storheim, P. Lunde, M. Vestrheim, and J. Kocbach. "Diffraction correction for precision measurements of sound velocity in gas. Is full receiver modelling needed?". In *Proceedings of the 44th Scandinavian Symposium on Physical Acoustics* (Online, 1-2 February 2021).

[39] E. N. Mosland, J. Kocbach, and P. Lunde. "Errors using the spatially averaged free-field pressure approximation for description of the receiving properties of piezoelectric transducers". J. Acoust. Soc. Am. **152,** (2022) A227 (2022).

[40] V. K. Chillara, C. Pantea, and D. N. Sinha. Radial modes of laterally stiffened piezoelectric disc transducers for ultrasonic collimated beam generation. Wave Motion **76,** 19–27 (2018).

[41] V. K. Chillara, C. Pantea, and D. N. Sinha. "Low-frequency ultrasonic Bessel-like collimated beam generation from radial modes of piezoelectric transducers". Applied Physics Letters **110,** (2017).

[42] V. K. Chillara, E. S. Davis, C. Pantea, and D. N. Sinha. "Ultrasonic Bessel beam generation from radial modes of piezoelectric discs". Ultrasonics **96,** 140–148 (2019).

[43] M. Vestrheim. Forelesningsnotater i kurset PHYS272 Akustiske Transdusere. Department of Physics and Technology, University of Bergen, Norway (2013).

[44] X. Lurton. *An introduction to underwater acoustics: principles and applications* (Springer-Verlag, Berlin, Germany 2002).

[45] K. T. Rich and T. Douglas Mast. "Methods to calibrate the absolute receive sensitivity of single-element, focused transducers". J. Acoust. Soc. Am. **138,** 193–198 (2015).

[46] Y. B. Kim and Y. Roh. "New design of matching layers for high power and wide band ultrasonic transducers". Sensors and Actuators, A: Physical **71,** 116–122 (1998).

[47] R. W. King. *Transmission lines antennas and wave guides*. 1st edition edition, (McGraw-Hill Book Company, New York 1945).

[48] P. Lunde. "Modellar for beskrivelse av elektroakustisk sender-mottakar målesystem, inkl. diffraksjonseffektar/diffraksjonskorreksjon", Unpublished note. Department of Physics and Technology, University of Bergen, Norway (2013).

[49] Brüel & Kjær. *Product Data: 1/8-inch pressure-field microphone - Type 4138*. DK-2850 Nærum, Denmark (2008).

[50] S. Garrett. *Understanding Acoustics*. Second edition, (Springer, Pine Grove Mills, PA, USA 2020).

[51] K. Riley, M. P. Hobson, and S. J. Bence. *Mathematical methods for physics and engineering*. Third edition, (Cambridge University Press, Cambridge, UK 2006).

[52] R. E. White. *An Introduction to the Finite Element Method with Applications to Nonlinear Problems.* (John Wiley Sons, New York, 1985).

[53] J. Kocbach. Endelig Element Modellering av Piezoelektriske Skiver. Master thesis, Department of Physics and Technology, University of Bergen, Norway (1996).

[54] M. Aanes. "A guide to FEMP 5". Department of Physics and Technology, University of Bergen, Norway (2011).

[55] Ferroperm Piezoceramics A/S. "High quality components and materials for the electronic industry". DK-3490 Kvistgård, Denmark (2003).

[56] Kjetil Lohne. Undersøkelse og Utnyttelse av Svingemoder i Ultralyd Transduserkonstruksjoner. Master thesis, Department of Physics and Technology, University of Bergen, Norway (2005).

[57] V. Knappskog. Radiellmode Svingninger i Piezoelektriske Ultralydtransdusere for Luft. Målinger og Endelig Element Analyser. Masters thesis, Department of Physics and Technology, University of Bergen, Norway (2007).

[58] Precision Acoustics Ltd. *Technical datasheet: Aplex R3*. Dorchester, UK (2022).

[59] K. D. Lohne, M. Vestrheim, and P. Lunde. "Study of a steel plate immersed in water". In *Proceedings of the 31th Scandinavian Symposium on Physical Acoustics*, January 2008 (Geilo, Norway 27-30 January 2008).

[60] B. Hartmann and J. Jarzynski. "Immersion apparatus for ultrasonic measurements in polymers". J. Acoust. Soc. Am. **56,** 1469–1477 (1974).

[61] M. M. Saether. "Elastic wave velocities and attenuation under methane hydrate growth in Bentheim sandstone-Measurements and modelling". Phd thesis, Department of Physics and Technology, University of Bergen, Norway (2018).

[62] Casco. *Technical data sheet: Casco Express glue*. Skjetten, Norway (2020).

[63] R. Hevroni, N. Karaev, E. Gudinetsky, V. Paris, and A. Yosef-Hai. "Studying the dynamic properties of ethyl-cyanoacrylate adhesive up to 6.5 GPa". In *Proceedings of the Conference of the American Physical Society Topical Group on Shock Compression of Condensed Matter* (Portland, Oregon 16-21 June 2019).

[64] Hewlett-Packard Company. *Operating and service manual: 4192A LF Impedance analyzer* (1982).

[65] Agilent. *User guide: Type 33220A signal generator*. Santa Clara, CA (2007).

[66] Tektronix Inc. *Users manual: Type DPO3012 digital oscilloscope*. Beaverton, OR (2010).

[67] Brüel & Kjær. *Data handbook: Condenser microphones and microphone preamplifiers*. DK-2850 Nærum, Denmark (1982).

[68] Brüel & Kjær. *Product Data: Wide Range Measuring Amplifiers - Types 2610 and 2636*. DK-2850 Nærum, Denmark (1996).

[69] Brüel & Kjær. *Product Data: Pistonphone - Type 4228"*. DK-2850 Nærum, Denmark (1996).

[70] Krohn-Hite. *Operating manual: Type 3940A bandpass filter*. Brockton, MA (2012).

[71] Vaisala. *User guide: HMT310 Humidity and Temperature Transmitter*. Helsinki, Finland (2014).

[72] Isotech North America. *Operating manual: F250 Mk II Precision Thermometer*. Colchester, VT (1997).

[73] Paroscientific Inc. *Programming and operation manual: Digiquartz precision pressure instruments Model 740* . Redmond, NE (2002).

[74] Keyence. *User manual: High-speed, High-accuracy LK-G Series CCD Laser Displacement Sensor*. Itasca, IL (2013).

[75] Physik Instrumente GmbH. *User manual: Hydra Handbook*. Karlsruhe, Germany (2016).

[76] Physik Instrumente GmbH. *User manual: C-843 Motor Controller Card*. Karlsruhe, Germany (2009).

[77] Physik Instrumente GmbH. *Operating manual: MS44 E C-852 Signal Processor For Incremental Encoders*. Waldbronn, Germany (1995).

[78] Physik Instrumente GmbH. *Operating manual: MP 30 E M-500 Linear Positioning Stages.* Waldbronn, Germany (1998).

[79] Physik Instrumente GmbH. *Operating manual: MP 33E M-501 Series Linear Positioning Stages.* Waldbronn, Germany (1998).

[80] Physik Instrumente GmbH. *User manual: Linear Stage for Very High Loads, LS-270*. Karlsruhe, Germany (2018).

[81] Ø. Amundsen. Material constants determination for piezoelectric disks, and influence on source sensitivity. Measurements and simulations. Master's thesis, Department of Physics and Technology, University of Bergen, Norway (2011).

[82] K. K. Andersen. Reciprocity calibration of ultrasonic piezoelectric disks in air. Master's thesis, Department of Physics and Technology, University of Bergen, Norway (2015).

[83] A. A. Søvik. Ultrasonic measurement systems for gas. Finite element modelling compared with measurements in air. Master's thesis, Department of Physics and Technology, University of Bergen, Norway (2015).

[84] R. Grindheim. Ultrasonic measurement system for gas. Experimental and theoretical characterization using piezoelectric elements at radial mode vibration in air. Master's thesis, Department of Physics and Technology, University of Bergen, Norway (2019).

[85] S. K. Finstad. "Characterization and finite element modelling of piezoelectric ceramic discs vibrating in air, for a frequency range including the first two radial modes". Master's thesis, Department of Physics and Technology, University of Bergen, Norway (2021).

[86] E. Fosse. Finite element modeling and experimental characterization of piezoelectric ceramic disk in air. Master's thesis, Department of Physics and Technology, University of Bergen, Norway (2022).

[87] R. Ankit. WebPlotDigitizer : Version 4.5. https://automeris.io/WebPlotDigitizer, last accessed: 29.04.2023.

[88] Brüel & Kjær. *Calibration data: Type 4228 pistonphone, Serial no: 1918465*. DK-2850 Nærum, Denmark (1996).

[89] Mitutoyo. *User manual: Mitutoyo High Accuracy Digital Micrometer 0-25mm*. Kawasaki, Japan (2021).

[90] Mitutoyo. *User manual: Vernier Caliper Series 530 - Standard model*. Kawasaki, Japan (2016).

[91] P. Lanceleur, J. F. D. Belleval, and N. Mercier. "Modeling of Transient Deformation of Piezoelectric Ceramics". IEEE Transactions on Ultrasonics, Ferroelectrics, and Frequency Control **39,** (1992) 293–301.

[92] I. N. Stepanenko, G. E. Büchel, B. K. Keppler, and V. B. Arion. *Osmium Complexes with Azole Heterocycles as Potential Antitumor Drugs*, (Springer, New York, 2013), 1596–1614.

[93] A. R. Selfridge. "Approximate Material Properties in Isotropic Materials". IEEE Transactions on Sonics and Ultrasonics **32,** 381–394 (1985).

[94] Elsold GmbH. "Product Catalog". Goslar, Germany (2012).

[95] C. Prøytz. Underwater Ultrasonic Transducer Technology. Construction, Characterization and Finite-Element Modelling. Master thesis, Department of Physics and Technology, University of Bergen, Norway (2022).

[96] R. Carter and R. Kensley. Introduction to Piezoelectric Transducers: https://piezo.com/pages/intro-to-piezoelectricity, last accessed: 04.05.2023.

[97] Biltema. Kobbertape. https://www.biltema.no/fritid/hage/skadedyr/kobbertape-2000039666, last accessed: 21.02.2023 .

[98] MG Chemicals. *Technical data sheet: Silver conductive epoxy adhesive 8331*. Ontario, Canada (2018).

[99] KiiltoClean AS. *Technical data sheet: Isopropanol prima 1 liter, Teknisk sprit* . Asker, Norway (2022).

[100] Struers ApS. "Cold mounting systems for all materialographic applications". DK-2750 Ballerup, Denmark (2018).

[101] Amphenol. *Technical data sheet: BNC Bulkhead receptor jack, B6351B1-ND3G-50* .

[102] M. G. Cain and M. Stewart. *Characterisation of Ferroelectric Bulk Materials and Thin Films*, (Springer Netherlands, Dordrecht 2014).

Appendix A

FEMP-structures

A.1 Piezodisk_clamped_vacuum

```
function [read]=read_inn_project(read,commands);
%Piezoceramic disk with radial clamp vibrating in a vacuum
%
% Håvard Råheim Økland 2023

% Based on FEMP models presented in Norli(2007), Hauge/Mosland (2013) and Storheim(2015)

%%%%%%%%%%%%%%%%%%%%%%%%%%%%%%%%%%%%%%%%%%%%%%%%%%%%%%%%%%%%%%%%%%%
% Read .inn-file. Note that this function calls a project specific
% read_inn_project.m which should be in the working directory
%
% Part of FEMP (Finite Element Modeling of Piezoelectric structures)
% Programmed by Jan Kocbach (jan@kocbach.net)
% (C) 2000 Jan Kocbach. This file is free software;  you can redistribute
% it and/or modify it only under the the terms of the GNU GENERAL PUBLIC
% LICENSE which should be included along with this file.
% (C) 2000-2010 Christian Michelsen Research AS
%%%%%%%%%%%%%%%%%%%%%%%%%%%%%%%%%%%%%%%%%%%%%%%%%%%%%%%%%%%%%%%%%%%

% Put a file read_inn_project.m in your project directory to define local
% FEMP input commands. Also include init_const_project.m in this directory
% and define the commands there.
global glob;
read=read;

```

```
26
27 %% Piezodisk_Clamped_Vacuum
28 if ~isempty(read.piezodisk_clamped_vacuum)
29     r_p = read.piezodisk_clamped_vacuum(1,1,:);  %Radius
          piezoelectric disk
30     t_p = read.piezodisk_clamped_vacuum(1,2,:);  %Thickness
          piezoelectric disk
31     el_p = read.piezodisk_clamped_vacuum(1,3,:); %Elem/Lambda
          piezoelectric disk
32     mat_p = read.piezodisk_clamped_vacuum(1,4,:);%Material
          piezoelectric disk
33     r_c = read.piezodisk_clamped_vacuum(1,5,:);  %Radius Clamp
34     el_c = read.piezodisk_clamped_vacuum(1,6,:); %Elem/Lambda
          Clamp
35     mat_c = read.piezodisk_clamped_vacuum(1,7,:);%Material
          Casing
36
37
38
39
40     for s=1:size(mat_c,3)
41         read.points(:,:,s)= ...
42         [1 0 t_p(s)/2;
43         2 0 -t_p(s)/2;
44         3 r_p(s) -t_p(s)/2;
45         4 r_p(s) t_p(s)/2;
46         5 r_c(s) -t_p(s)/2;
47         6 r_c(s) t_p(s)/2];
48
49         %Set up the different areas in the model
50         read.areas(:,:,s)=[
51         %Piezoelectric disk
52          1 1 2 3 4 el_p(s) el_p(s) 0 0;
53         %Clamp
54          2 3 5 6 4 el_c(s) el_c(s) 0 0];
55
56        %Defining the various materials
57         read.materials(:,:,s)=...
58         [1 glob.globvariables.piezo mat_p(s);
59          2 glob.globvariables.mechanic mat_c(s)];
60
61       %Ground at the front electrode of the piezoelectric disk
62        read.restraints(:,:,s)=[-1 1 -t_p(s)/2-1e-9 -t_p(s)/2+1e
            -9 glob.free.ep 1];
63
64       %Imposing a 1 V electrical potential at the rear surface
           of the piezoelectri disk
65        read.dof(:,:,s) = [-1 1 t_p(s)/2-1e-9 t_p(s)/2+1e-9 glob
```

```
          .free.ep];
66
67
68      end
69  end
```

A.2 Piezodisk_Clamped_Fluid

```
1  function [read]=read_inn_project(read,commands);
2   %Piezoceramic disk with radial clamp vibrating in a fluid
3   %
4   % Håvard Råheim Økland 2023
5
6  % Based on FEMP models presented in  Norli(2007), Hauge/
       Mosland(2013) and Storheim(2015)
7
8
9  %%%%%%%%%%%%%%%%%%%%%%%%%%%%%%%%%%%%%%%%%%%%%%%%%%%%%%%%%%%%%%%%
10 % Read .inn-file. Note that this function calls a project
       specific
11 % read_inn_project.m which should be in the working directory
12 %
13 % Part of FEMP (Finite Element Modeling of Piezoelectric
       structures)
14 % Programmed by Jan Kocbach (jan@kocbach.net)
15 % (C) 2000 Jan Kocbach. This file is free software;  you can
       redistribute
16 % it and/or modify it only under the the terms of the GNU
       GENERAL PUBLIC
17 % LICENSE which should be included along with this file.
18 % (C) 2000-2010 Christian Michelsen Research AS
19 %%%%%%%%%%%%%%%%%%%%%%%%%%%%%%%%%%%%%%%%%%%%%%%%%%%%%%%%%%%%%%%%
20
21 % Put a file read_inn_project.m in your project directory to
       define local
22 % FEMP input commands. Also include init_const_project.m in
       this directory
23 % and define the commands there.
24
25 global glob;
26 read=read;
27
28 %% Piezodisk_clamped_fluid
29
30
31 % Read parameters from the .inn file
32 if ~isempty(read.piezodisk_clamped_fluid)
```

```
33      read.points=[]; read.areas=[]; read.materials=[]; read.dof
           =[]; read.restraints=[];
34      r_p=read.piezodisk_clamped_fluid(1,1,:); %Radius
           Piezoelectric disk
35      t_p=read.piezodisk_clamped_fluid(1,2,:); %Thickness
           Piezoelectric disk
36      elr_p=read.piezodisk_clamped_fluid(1,3,:);%Elem/lambda r
           dir piezo
37      elt_p=read.piezodisk_clamped_fluid(1,4,:);%Elem/lambda t
           dir piezo
38      mat_p=read.piezodisk_clamped_fluid(1,5,:);%Material number
            piezo
39      rfluid=read.piezodisk_clamped_fluid(1,6,:);%Radius finite
           fluid elem
40      elfluid=read.piezodisk_clamped_fluid(1,7,:);%Elem/lamda
           fluid
41      mat_fluid=read.piezodisk_clamped_fluid(1,8,:);%Material
           number fluid
42      theta1=read.piezodisk_clamped_fluid(1,9,:);%Mesh angle 1,
           from disk
43      r_c=read.piezodisk_clamped_fluid(1,10,:); %Radius Clamp
44      elr_c=read.piezodisk_clamped_fluid(1,11,:);%Elem/lambda
           r_dir Clamp
45      elt_c=read.piezodisk_clamped_fluid(1,12,:);%Elem/lambda
           t_dir Clamp
46      mat_c=read.piezodisk_clamped_fluid(1,13,:);%Material
           number clamp
47      theta2=read.piezodisk_clamped_fluid(1,14,:); %Mesh angle
           1, from clamp
48
49  %Specify the points in the model.
50      for s=1:size(r_p,3)
51          rfluidtemp=0+rfluid(s);
52          rinffluid=rfluidtemp*2;
53          read.points(:,:,s)=[1 0 t_p(s)/2;
54          2 r_p(s) t_p(s)/2;
55          3 0 0;
56          4 r_p(s) 0;
57          5 0 -t_p(s)/2;
58          6 r_p(s) -t_p(s)/2;
59          7 r_c(s) t_p(s)/2;
60          8 r_c(s) 0;
61          9 r_c(s) -t_p(s)/2;
62          10 0  rfluid(s);
63          11 rfluid(s)*sin(theta2(s))  rfluid(s)*cos(theta2(s));
64          12 rfluid(s)*sin(theta1(s)) rfluid(s)*cos(theta1(s));
65          13 rfluid(s) 0;
66          14 rfluid(s)*sin(theta1(s)) -rfluid(s)*cos(theta1(s));
```

```
67          15 rfluid(s)*sin(theta2(s))  -rfluid(s)*cos(theta2(s))
               ;
68          16 0 -rfluid(s);
69          17 0 rinffluid;
70          18 rinffluid(s)*sin(theta2(s))  rinffluid(s)*cos(
               theta2(s));
71          19 rinffluid(s)*sin(theta1(s)) rinffluid(s)*cos(theta1
               (s));
72          20 rinffluid 0;
73          21 rinffluid(s)*sin(theta1(s)) -rinffluid(s)*cos(
               theta1(s));
74          22 rinffluid(s)*sin(theta2(s))  -rinffluid(s)*cos(
               theta2(s));
75          23 0 -rinffluid(s)];
76
77          %Set up the different areas in the model
78          read.areas(:,:,s)=[
79          %Piezoelectric element
80          1,3,4,2,1,elr_p(s),elt_p(s),0,0;
81          1,5,6,4,3,elr_p(s),elt_p(s),0,0;
82          %Clamp
83          2,4,8,7,2,elr_c(s),elt_c(s),0,0;
84          2,6,9,8,4,elr_c(s),elt_c(s),0,0;
85          %Finite fluid elements
86          3,1,2,11,10,elfluid(s),elfluid(s),0,3;
87          3,2,7,12,11,elfluid(s),elfluid(s),0,3;
88          3,7,8,13,12,elfluid(s),elfluid(s),0,3;
89          3,8,9,14,13,elfluid(s),elfluid(s),0,3;
90          3,9,6,15,14,elfluid(s),elfluid(s),0,3;
91          3,6,5,16,15,elfluid(s),elfluid(s),0,3;
92          %Infinite fluid elements
93          4,10,11,18,17,1,1,3,3;
94          4,11,12,19,18,1,1,3,3;
95          4,12,13,20,19,1,1,3,3;
96          4,13,14,21,20,1,1,3,3;
97          4,14,15,22,21,1,1,3,3;
98          4,15,16,23,22,1,1,3,3];
99
100         %Defining the various materials
101         read.materials(:,:,s)=[
102         1 glob.globvariables.piezo mat_p(s);
103         2 glob.globvariables.mechanic mat_c(s);
104         3 glob.globvariables.fluid mat_fluid(s);
105         4 glob.globvariables.infinitefluid mat_fluid(s)];
106
107     %Ground at the front electrode of the piezoelectric disk
108         read.dof(:,:,s)=[-1 1 t_p(s)/2-1e-9 t_p(s)/2+1e-9 glob
               .free.ep];
```

```
109     %Imposing a 1 V electrical potential at the rear surface
           of the piezoelctric disk
110         read.restraints(:,:,s)=[-1 1 -t_p(s)/2-1e-9 -t_p(s)
               /2+1e-9 glob.free.ep 1];
111     end
112 end
```

A.3 Piezodisk_Casing_Vacuum

```
1     function [read]=read_inn_project(read,commands);
2  %Piezoceramic disk with casing vibrating in a vacuum
3  %
4  % Håvard Råheim Økland 2023
5
6 % Based on FEMP models presented in  Norli(2007), Hauge/
      Mosland(2013) and
7 % Storheim(2015)
8
9
10 %%%%%%%%%%%%%%%%%%%%%%%%%%%%%%%%%%%%%%%%%%%%%%%%%%%%%%%%%%%%
11 % Read .inn-file. Note that this function calls a project
      specific
12 % read_inn_project.m which should be in the working directory
13 %
14 % Part of FEMP (Finite Element Modeling of Piezoelectric
      structures)
15 % Programmed by Jan Kocbach (jan@kocbach.net)
16 % (C) 2000 Jan Kocbach. This file is free software;  you can
      redistribute
17 % it and/or modify it only under the the terms of the GNU
      GENERAL PUBLIC
18 % LICENSE which should be included along with this file.
19 % (C) 2000-2010 Christian Michelsen Research AS
20 %%%%%%%%%%%%%%%%%%%%%%%%%%%%%%%%%%%%%%%%%%%%%%%%%%%%%%%%%%%%
21
22 % Put a file read_inn_project.m in your project directory to
      define local
23 % FEMP input commands. Also include init_const_project.m in
      this directory
24 % and define the commands there.
25
26 global glob;
27 read=read;
28
29 %% Piezodisk_Casing_Vacuum
30 if ~isempty(read.piezodisk_casing_vacuum)
```

```
31      read.points=[]; read.areas=[]; read.materials=[]; read.dof
          =[]; read.restraints=[];
32      r_p=read.piezodisk_casing_vacuum(1,1,:); %Radius
          Piezoelectric disk
33      t_p=read.piezodisk_casing_vacuum(1,2,:); %Thickness
          Piezoelectric disk
34      elr_p=read.piezodisk_casing_vacuum(1,3,:); %Elem/lambda r
          dir piezo
35      elt_p=read.piezodisk_casing_vacuum(1,4,:); %Elem/lambda t
          dir piezo
36      mat_p=read.piezodisk_casing_vacuum(1,5,:); %Material
          number piezo
37      r_c=read.piezodisk_casing_vacuum(1,6,:); %Radius Casing
38      t_c = read.piezodisk_casing_vacuum(1,7,:); %Thickness
          casing extending behind the disk
39      elr_c=read.piezodisk_casing_vacuum(1,8,:); %%Elem/lambda
          r_dir Casing
40      elt_c=read.piezodisk_casing_vacuum(1,9,:); %Elem/lambda
          t_dir Casing
41      mat_c=read.piezodisk_casing_vacuum(1,10,:); %Material
          number Casing
42      elt_c2=read.piezodisk_casing_vacuum(1,11,:);%Elem/lambda
          t_dir Casing extending behind disk
43
44
45      r1 = r_p;
46      r2 = r_c;
47      T = t_p + t_c;
48      t1 = T/2;
49      t2 = T/2 - t_p;
50      t3 = -T/2;
51  %Specify the points in the model.
52        for s=1:size(t_c,3)
53          read.points(:,:,s)=[1 0 t1(s);
54          2 r1(s) t1(s);
55          3 r2(s) t1(s);
56          4 0 t2(s);
57          5 r1(s) t2(s);
58          6 r2(s) t2(s);
59          7 0 t3(s);
60          8 r1(s) t3(s);
61          9 r2(s) t3(s)];
62         %Set up the different areas in the model
63          read.areas(:,:,s)=[
64          %Piezoelectric element
65          1,4,5,2,1,elr_p(s),elt_p(s),0,0;
66          %Casing on the side of the disk
67          2,5,6,3,2,elr_c(s),elt_c(s),0,0;
```

```
68          %Casing extending behind the disk
69          2,6,5,8,9,elr_c(s),elt_c2(s),0,0];
70
71
72
73          %Defining the various materials
74          read.materials(:,:,s)=[
75          1 glob.globvariables.piezo mat_p(s);
76          2 glob.globvariables.mechanic mat_c(s)];
77
78       %Ground at the front electrode of the piezoelectric disk
79          read.dof(:,:,s)=[-1 1 t1(s)-1e-9 t1(s)+1e-9 glob.free.
               ep];
80       %Imposing a 1 V electrical potential at the rear surface
            of the transmitter
81          read.restraints(:,:,s)=[-1 1 t2(s)-1e-9 t2(s)+1e-9
               glob.free.ep 1];
82      end
83  end
```

A.4 Piezodisk_Casing_Fluid

```
1       function [read]=read_inn_project(read,commands);
2    %Piezoceramic disk with radial clamp vibrating in a fluid
3    %
4    % Håvard Råheim Økland 2023
5
6   % Based on FEMP models presented in  Norli(2007), Hauge/
       Mosland(2013) and
7   % Storheim(2015)
8
9
10  %%%%%%%%%%%%%%%%%%%%%%%%%%%%%%%%%%%%%%%%%%%%%%%%%%%%%%%%%%%%
11  % Read .inn-file. Note that this function calls a project
       specific
12  % read_inn_project.m which should be in the working directory
13  %
14  % Part of FEMP (Finite Element Modeling of Piezoelectric
       structures)
15  % Programmed by Jan Kocbach (jan@kocbach.net)
16  % (C) 2000 Jan Kocbach. This file is free software;  you can
       redistribute
17  % it and/or modify it only under the the terms of the GNU
       GENERAL PUBLIC
18  % LICENSE which should be included along with this file.
19  % (C) 2000-2010 Christian Michelsen Research AS
20  %%%%%%%%%%%%%%%%%%%%%%%%%%%%%%%%%%%%%%%%%%%%%%%%%%%%%%%%%%%%
```

```
21
22 % Put a file read_inn_project.m in your project directory to
      define local
23 % FEMP input commands. Also include init_const_project.m in
      this directory
24 % and define the commands there.
25
26 global glob;
27 read=read;
28
29 %% Piezodisk_Casing_Fluid
30
31
32 % Read parameters from the .inn file
33 if ~isempty(read.piezodisk_clamped_fluid)
34     read.points=[]; read.areas=[]; read.materials=[]; read.dof
         =[]; read.restraints=[];
35     r_p=read.piezodisk_clamped_fluid(1,1,:); %Radius
         Piezoelectric disk
36     t_p=read.piezodisk_clamped_fluid(1,2,:); %Thickness
         Piezoelectric disk
37     elr_p=read.piezodisk_clamped_fluid(1,3,:);%Elem/lambda r
         dir piezo
38     elt_p=read.piezodisk_clamped_fluid(1,4,:);%Elem/lambda t
         dir piezo
39     mat_p=read.piezodisk_clamped_fluid(1,5,:);%Material number
          piezo
40     rfluid=read.piezodisk_clamped_fluid(1,6,:);%Radius finite
         fluid elem
41     elfluid=read.piezodisk_clamped_fluid(1,7,:);%Elem/lamda
         fluid
42     mat_fluid=read.piezodisk_clamped_fluid(1,8,:);%Material
         number fluid
43     theta1=read.piezodisk_clamped_fluid(1,9,:);%Mesh angle 1,
         from disk
44     r_c=read.piezodisk_clamped_fluid(1,10,:); %Radius Clamp
45     elr_c=read.piezodisk_clamped_fluid(1,11,:);%Elem/lambda
         r_dir Clamp
46     elt_c=read.piezodisk_clamped_fluid(1,12,:);%Elem/lambda
         t_dir Clamp
47     mat_c=read.piezodisk_clamped_fluid(1,13,:);%Material
         number clamp
48     theta2=read.piezodisk_clamped_fluid(1,14,:); %Mesh angle
         1, from clamp
49
50 %Specify the points in the model.
51     for s=1:size(r_p,3)
52         rfluidtemp=0+rfluid(s);
```

```
53          rinffluid=rfluidtemp*2;
54          read.points(:,:,s)=[1 0 t_p(s)/2;
55          2 r_p(s) t_p(s)/2;
56          3 0 0;
57          4 r_p(s) 0;
58          5 0 -t_p(s)/2;
59          6 r_p(s) -t_p(s)/2;
60          7 r_c(s) t_p(s)/2;
61          8 r_c(s) 0;
62          9 r_c(s) -t_p(s)/2;
63          10 0  rfluid(s);
64          11 rfluid(s)*sin(theta2(s))  rfluid(s)*cos(theta2(s));
65          12 rfluid(s)*sin(theta1(s)) rfluid(s)*cos(theta1(s));
66          13 rfluid(s) 0;
67          14 rfluid(s)*sin(theta1(s)) -rfluid(s)*cos(theta1(s));
68          15 rfluid(s)*sin(theta2(s))  -rfluid(s)*cos(theta2(s))
               ;
69          16 0 -rfluid(s);
70          17 0 rinffluid;
71          18 rinffluid(s)*sin(theta2(s))  rinffluid(s)*cos(
               theta2(s));
72          19 rinffluid(s)*sin(theta1(s)) rinffluid(s)*cos(theta1
               (s));
73          20 rinffluid 0;
74          21 rinffluid(s)*sin(theta1(s)) -rinffluid(s)*cos(
               theta1(s));
75          22 rinffluid(s)*sin(theta2(s))  -rinffluid(s)*cos(
               theta2(s));
76          23 0 -rinffluid(s)];
77
78          %Set up the different areas in the model
79          read.areas(:,:,s)=[
80          %Piezoelectric element
81          1,3,4,2,1,elr_p(s),elt_p(s),0,0;
82          1,5,6,4,3,elr_p(s),elt_p(s),0,0;
83          %Clamp
84          2,4,8,7,2,elr_c(s),elt_c(s),0,0;
85          2,6,9,8,4,elr_c(s),elt_c(s),0,0;
86          %Finite fluid elements
87          3,1,2,11,10,elfluid(s),elfluid(s),0,3;
88          3,2,7,12,11,elfluid(s),elfluid(s),0,3;
89          3,7,8,13,12,elfluid(s),elfluid(s),0,3;
90          3,8,9,14,13,elfluid(s),elfluid(s),0,3;
91          3,9,6,15,14,elfluid(s),elfluid(s),0,3;
92          3,6,5,16,15,elfluid(s),elfluid(s),0,3;
93          %Infinite fluid elements
94          4,10,11,18,17,1,1,3,3;
95          4,11,12,19,18,1,1,3,3;
```

```
        4,12,13,20,19,1,1,3,3;
        4,13,14,21,20,1,1,3,3;
        4,14,15,22,21,1,1,3,3;
        4,15,16,23,22,1,1,3,3];

        %Defining the various materials
        read.materials(:,:,s)=[
        1 glob.globvariables.piezo mat_p(s);
        2 glob.globvariables.mechanic mat_c(s);
        3 glob.globvariables.fluid mat_fluid(s);
        4 glob.globvariables.infinitefluid mat_fluid(s)];

    %Ground at the front electrode of the piezoelectric disk
        read.dof(:,:,s)=[-1 1 t_p(s)/2-1e-9 t_p(s)/2+1e-9 glob.free.ep];
    %Imposing a 1 V electrical potential at the rear surface of the transmitter
        read.restraints(:,:,s)=[-1 1 -t_p(s)/2-1e-9 -t_p(s)/2+1e-9 glob.free.ep 1];
    end
end
```

A.5 Piezodisk_Front_Vacuum

```
    function [read]=read_inn_project(read,commands);
%Piezoelectric disk with matching layer and glue layer vibrating in vacuum

 % Håvard Råheim Økland 2023

% Based on FEMP models presented in  Norli(2007), Hauge/Mosland(2013) and Storheim(2015)




% %%%%%%%%%%%%%%%%%%%%%%%%%%%%%%%%%%%%%%%%%%%%%%%%%%%%%%%%%%%%%%%%%%%%%
% Read .inn-file. Note that this function calls a project specific
% read_inn_project.m which should be in the working directory
%
% Part of FEMP (Finite Element Modeling of Piezoelectric structures)
% Programmed by Jan Kocbach (jan@kocbach.net)
```

```
% (C) 2000 Jan Kocbach. This file is free software;  you can redistribute
% it and/or modify it only under the the terms of the GNU GENERAL PUBLIC
% LICENSE which should be included along with this file.
% (C) 2000-2010 Christian Michelsen Research AS
% %%%%%%%%%%%%%%%%%%%%%%%%%%%%%%%%%%%%%%%%%%%%%%%%%%%%%%%%%%%%%%%%%%%%

% Put a file read_inn_project.m in your project directory to define local
% FEMP input commands. Also include init_const_project.m in this directory
% and define the commands there.

global glob;
read=read;

%% Piezodiskfront_Vacuum
if ~isempty(read.piezodiskfrontgluevacuum)
    read.points=[]; read.areas=[]; read.materials=[]; read.dof=[]; read.restraints=[];
    r_p = read.piezodiskfrontgluevacuum(1,1,:); %Radius Piezoelectric disk
    t_p = read.piezodiskfrontgluevacuum(1,2,:); %Thickness Piezoelectric disk
    elr_p = read.piezodiskfrontgluevacuum(1,3,:); %Elem/lambda r_dir piezo
    elt_p = read.piezodiskfrontgluevacuum(1,4,:); %Elem/lambda t dir piezo
    mat_p = read.piezodiskfrontgluevacuum(1,5,:); %Material number piezo
    t_m = read.piezodiskfrontgluevacuum(1,6,:);  %Thickness matching layer
    elr_m = read.piezodiskfrontgluevacuum(1,7,:); %Elem/lambda r_dir Matching layer
    elt_m = read.piezodiskfrontgluevacuum(1,8,:); %Elem/lambda t_dir Matching layer
    mat_m = read.piezodiskfrontgluevacuum(1,9,:); %Material number matching layer
    t_g = read.piezodiskfrontgluevacuum(1,10,:); %Thickness Glue layer
    elr_g = read.piezodiskfrontgluevacuum(1,11,:); %Elem/lambda r_dir Glue layer
    elt_g = read.piezodiskfrontgluevacuum(1,12,:);  %Elem/lambda t_dir Glue layer
    mat_g = read.piezodiskfrontgluevacuum(1,13,:);  % Material
```

```
        number Glue layer
46
47
48      r1 = r_p;
49      T = t_p + t_m + t_g;
50      t1 = T/2;
51      t2 = T/2 - t_m;
52      t3 = T/2 -t_m - t_g ;
53      t4 = -T/2;
54
55     for s=1:size(r_p,3)
56      %Specify the points in the model.
57         read.points(:,:,s)=[1 0 t1;
58         2 r1 t1;
59         3 0 t2;
60         4 r1 t2;
61         5 0 t3;
62         6 r1 t3;
63         7 0 -T/2;
64         8 r1 -T/2];
65
66         read.areas(:,:,s)=[
67         %Piezoelctric disk
68         1,7,8,6,5,elr_p(s),elt_p(s),0,0;
69         %Glue layer
70         2,5,6,4,3,elr_g,elt_g,0,0;
71         %Matching layer
72         3,3,4,2,1,elr_m(s),elt_m(s),0,0];
73        %Defining the various materials
74         read.materials(:,:,s)=[1 glob.globvariables.piezo
              mat_p(s);
75         2 glob.globvariables.mechanic mat_m(s);
76         3 glob.globvariables.mechanic mat_m];
77       %Ground at the front electrode of the piezoelectric disk
78         read.dof(:,:,s)=[-1 1 t3-1e-9 t3+1e-9 glob.free.ep];
79       %Imposing a 1 V electrical potential at the rear surface
             of thepiezoelectric disk
80         read.restraints(:,:,s)=[-1 1 t4-1e-9 t4+1e-9 glob.free
              .ep 1];
81     end
82 end
```

A.6 Piezodisk_Casing_Front_Vacuum(Glue)

A.7 `Piezodisk_Casing_Front_Fluid` (No Glue)

```
1     function [read]=read_inn_project(read,commands);
2  %Piezoceramic disk with matching layer and casing vibrating
      in a fluid
3  %
4  % Håvard Råheim Økland 2023
5
6  % Based on FEMP models presented in  Norli(2007), Hauge/
      Mosland(2013) and
7  % Storheim(2015)
8
9
10 %%%%%%%%%%%%%%%%%%%%%%%%%%%%%%%%%%%%%%%%%%%%%%%%%%%%%%%%%%%%
11 % Read .inn-file. Note that this function calls a project
      specific
12 % read_inn_project.m which should be in the working directory
13 %
14 % Part of FEMP (Finite Element Modeling of Piezoelectric
      structures)
15 % Programmed by Jan Kocbach (jan@kocbach.net)
16 % (C) 2000 Jan Kocbach. This file is free software;  you can
      redistribute
17 % it and/or modify it only under the the terms of the GNU
      GENERAL PUBLIC
18 % LICENSE which should be included along with this file.
19 % (C) 2000-2010 Christian Michelsen Research AS
20 %%%%%%%%%%%%%%%%%%%%%%%%%%%%%%%%%%%%%%%%%%%%%%%%%%%%%%%%%%%%
21
22 % Put a file read_inn_project.m in your project directory to
      define local
23 % FEMP input commands. Also include init_const_project.m in
      this directory
24 % and define the commands there.
25
26 global glob;
27 read=read;
28
29 %% Piezodisk_Casing_Front_Fluid
30
31 % Read parameters from the .inn file
32 if ~isempty(read.piezodisk_casing_front_fluid )
33     read.points=[]; read.areas=[]; read.materials=[]; read.dof
         =[]; read.restraints=[];
34     r_p=read.piezodisk_casing_front_fluid (1,1,:); %Radius
         Piezoelectric disk
35     t_p=read.piezodisk_casing_front_fluid (1,2,:); %Thickness
         Piezoelectric disk
```

```
36      elr_p=read.piezodisk_casing_front_fluid (1,3,:); %Elem/
           lambda r dir piezo
37      elt_p=read.piezodisk_casing_front_fluid (1,4,:); %Elem/
           lambda t dir piezo
38      mat_p=read.piezodisk_casing_front_fluid (1,5,:); %Material
            number piezo
39      r_c=read.piezodisk_casing_front_fluid (1,6,:); % Radius
           casing
40      mat_c=read.piezodisk_casing_front_fluid (1,8,:); %Material
            number Casing
41      elr_c=read.piezodisk_casing_front_fluid (1,9,:); %Elem/
           lambda r dir Casing
42      elt_c1=read.piezodisk_casing_front_fluid (1,10,:); %Elem/
           lambda t dir casing side of matching layer
43      elt_c2=read.piezodisk_casing_front_fluid (1,11,:); %Elem/
           lambda t dir casing side of Piezo
44      elt_c3=read.piezodisk_casing_front_fluid (1,12,:); %Elem/
           lambda t dir casing extending behind disk
45      t_m =read.piezodisk_casing_front_fluid (1,14,:); %
           Thickness Matching layer
46      mat_m =read.piezodisk_casing_front_fluid (1,15,:); %
           Material number matching layer
47      elr_m =read.piezodisk_casing_front_fluid (1,16,:); %Elem/
           lambda r dir Matching layer
48      elt_m =read.piezodisk_casing_front_fluid (1,17,:); %Elem/
           lambda t dir Matching layer
49      t_b=read.piezodisk_casing_front_fluid (1,19,:); %
           Thickness casing extending behind disk
50
51      rfluid=read.piezodisk_casing_front_fluid (1,23,:); %Radius
            finite fluid elem
52      elfluid=read.piezodisk_casing_front_fluid (1,24,:); %Elem/
           lamda fluid
53      mat_fluid=read.piezodisk_casing_front_fluid (1,25,:); %
           Material number fluid
54
55
56
57        for s=1:size(t_m,3)
58
59          rinff(s) = 2* rfluid(s);
60          r1(s) = r_p(s);
61          r2(s) = r_c(s);
62          T(s) = t_p(s) + t_m(s) + t_b(s);
63          t1(s) = T(s)/2;
64          t2(s) = T(s)/2 - t_m(s);
65          t3(s) = T(s)/2 - (t_m(s) + t_p(s));
66          t4(s) = -T(s)/2;
```

```
67
68
69          rfluidtemp=0+rfluid(s);
70          rinffluid=rfluidtemp*2;
71          theta1(s) = atan(t1(s)/r1(s));
72          theta2(s) = atan(t1(s)/r2(s));
73          theta3(s) = atan(t2(s)/r2(s));
74          theta4(s) = atan(t3(s)/r2(s));
75          theta5(s) = atan(t4(s)/r2(s));
76          theta6(s) = atan(t4(s)/r1(s));
77
78
79         %Specify the points in the model.
80          read.points(:,:,s)=[1 0 t1(s);
81          2 r1(s) t1(s);
82          3 r2(s) t1(s);
83          4 0 t2(s);
84          5 r1(s) t2(s);
85          6 r2(s) t2(s);
86          7 0 t3(s);
87          8 r1(s) t3(s);
88          9 r2(s) t3(s);
89          10 0 t4(s);
90          11 r1(s) t4(s);
91          12 r2(s) t4(s);
92          13 0 rfluid(s);
93          14 rfluid(s)*cos(theta1(s)) rfluid(s)*sin(theta1(s));
94          15 rfluid(s)*cos(theta2(s)) rfluid(s)*sin(theta2(s));
95          16 rfluid(s)*cos(theta3(s)) rfluid(s)*sin(theta3(s));
96          17 rfluid(s)*cos(theta4(s)) rfluid(s)*sin(theta4(s));
97          18 rfluid(s)*cos(theta5(s)) rfluid(s)*sin(theta5(s));
98          19 rfluid(s)*cos(theta6(s)) rfluid(s)*sin(theta6(s));
99          20 0 -rfluid(s);
100         21 0 0;
101         22 0 rinff(s);
102         23 rinff(s)*cos(theta1(s)) rinff(s)*sin(theta1(s));
103         24 rinff(s)*cos(theta2(s)) rinff(s)*sin(theta2(s));
104         25 rinff(s)*cos(theta3(s)) rinff(s)*sin(theta3(s));
105         26 rinff(s)*cos(theta4(s)) rinff(s)*sin(theta4(s));
106         27 rinff(s)*cos(theta5(s)) rinff(s)*sin(theta5(s));
107         28 rinff(s)*cos(theta6(s)) rinff(s)*sin(theta6(s));
108         29 0 -rinff(s)];
109
110        %Set up the different areas in the model
111         read.areas(:,:,s)=[
112         %Matching layer
113         1,4,5,2,1,elr_m(s),elt_m(s),0,0;
114         %Casing
```

```
115         2,5,6,3,2,elr_c(s),elt_c1(s),0,0;
116         2,8,9,6,5,elr_c(s),elt_c2(s),0,0;
117         2,11,12,9,8,elr_c(s),elt_c3(s),0,0;
118         %Piezoelectric element
119         3,7,8,5,4,elr_p(s),elt_p(s),0,0;
120         %Backing layer
121         4,10,11,8,7,elfluid(s),elfluid(s),0,0;
122         %Finite fluid reginon
123         4,1,2,14,13,elfluid(s),elfluid(s),0,21;
124         4,2,3,15,14,elfluid(s),elfluid(s),0,21;
125         4,3,6,16,15,elfluid(s),elfluid(s),0,21;
126         4,6,9,17,16,elfluid(s),elfluid(s),0,21;
127         4,9,12,18,17,elfluid(s),elfluid(s),0,21;
128         4,12,11,19,18,elfluid(s),elfluid(s),0,21;
129         4,11,10,20,19,elfluid(s),elfluid(s),0,21;
130         %Infinite fluid regions
131         5,13,14,23,22,1,1,21,21;
132         5,14,15,24,23,1,1,21,21;
133         5,15,16,25,24,1,1,21,21;
134         5,16,17,26,25,1,1,21,21;
135         5,17,18,27,26,1,1,21,21;
136         5,18,19,28,27,1,1,21,21;
137         5,19,20,29,28,1,1,21,21];
138
139
140
141        %Defining the various materials
142         read.materials(:,:,s)=[1 glob.globvariables.mechanic
              mat_m(s);
143         2 glob.globvariables.mechanic mat_c(s);
144         3 glob.globvariables.piezo mat_p(s);
145         4 glob.globvariables.fluid mat_fluid(s)
146         5 glob.globvariables.infinitefluid mat_fluid(s)];
147
148       %Ground at the front electrode of the piezoelectric disk
149         read.dof(:,:,s)=[-1 1 t2(s)-1e-9 t2(s)+1e-9 glob.free.
              ep];
150       %Imposing a 1 V electrical potential at the rear surface
            of the piezoelectric disk
151         read.restraints(:,:,s)=[-1 1 t3(s)-1e-9 t3(s)+1e-9
              glob.free.ep 1];
152     end
153 end
```

A.8 Transducer_Fluid (Glue)

```
1     function [read]=read_inn_project(read,commands);
```

```
%Complete transducer vibrating in a fluid.

 % Håvard Råheim Økland 2023

% Based on FEMP models presented in  Norli(2007), Hauge/Mosland(2013) and
% Storheim(2015)




% %%%%%%%%%%%%%%%%%%%%%%%%%%%%%%%%%%%%%%%%%%%%%%%%%%%%%%%%%%%%%%%%%%%%
% Read .inn-file. Note that this function calls a project specific
% read_inn_project.m which should be in the working directory
%
% Part of FEMP (Finite Element Modeling of Piezoelectric structures)
% Programmed by Jan Kocbach (jan@kocbach.net)
% (C) 2000 Jan Kocbach. This file is free software;  you can redistribute
% it and/or modify it only under the the terms of the GNU GENERAL PUBLIC
% LICENSE which should be included along with this file.
% (C) 2000-2010 Christian Michelsen Research AS
% %%%%%%%%%%%%%%%%%%%%%%%%%%%%%%%%%%%%%%%%%%%%%%%%%%%%%%%%%%%%%%%%%%%%

% Put a file read_inn_project.m in your project directory to define local
% FEMP input commands. Also include init_const_project.m in this directory
% and define the commands there.

global glob;
read=read;

%% Transducer_Fluid
if ~isempty(read.transducer_fluid)
    read.points=[]; read.areas=[]; read.materials=[]; read.dof=[]; read.restraints=[];
    r_p=read.transducer_fluid(1,1,:); %Radius Piezoelectric disk
    t_p=read.transducer_fluid(1,2,:); %Thickness Piezoelectric disk
```

```
36      mat_p=read.transducer_fluid(1,3,:); %Material number piezo
37      elr_p=read.transducer_fluid(1,4,:); %Elem/lambda r_dir
           piezo
38      elt_p=read.transducer_fluid(1,5,:); %Elem/lambda t dir
           piezo
39      r_c=read.transducer_fluid(1,6,:); % Radius Casing
40      mat_c=read.transducer_fluid(1,7,:); %Material number
           casing
41      elr_c=read.transducer_fluid(1,8,:); %Elem/lambda r_dir
           casing
42      elt_c1=read.transducer_fluid(1,9,:); %Elem/lambda t_dir
           casing upper part
43      elt_c2=read.transducer_fluid(1,10,:);  %Elem/lambda t_dir
           casing t middle part
44      elt_c3=read.transducer_fluid(1,11,:); %Elem/lambda t_dir
           casing lower part
45      t_m =read.transducer_fluid(1,12,:);   %Thickness matching
           layer
46      mat_m =read.transducer_fluid(1,13,:); %Material number
           matching layer
47      elr_m =read.transducer_fluid(1,14,:); %Elem/lambda r_dir
           Matching layer
48      elt_m =read.transducer_fluid(1,15,:); %Elem/lambda t_dir
           Matching layer
49      t_b=read.transducer_fluid(1,16,:);  %Thickness Backing
           layer
50      mat_b=read.transducer_fluid(1,17,:); %Material number
           backing layer
51      elr_b=read.transducer_fluid(1,18,:);  %Elem/lambda r_dir
           Backing layer
52      elt_b=read.transducer_fluid(1,19,:); %Elem/lambda t_dir
           Backing layer
53      t_g=read.transducer_fluid(1,20,:); %Thickness Glue layer
54      w_g=read.transducer_fluid(1,21,:); %Width Glue layer
55      mat_g=read.transducer_fluid(1,22,:); % Material number
           Glue layer
56      elr_g=read.transducer_fluid(1,23,:); %Elem/lambda r_dir
           Glue layer
57      elt_g=read.transducer_fluid(1,24,:); %Elem/lambda t_dir
           Glue layer
58      mat_fluid=read.transducer_fluid(1,25,:); %Material number
           fluid
59      r_fluid=read.transducer_fluid(1,26,:); %Radius finite
           fluid elements
60      el_fluid=read.transducer_fluid(1,27,:); %Elem/lambda Fluid
61
62
63
```

```
64
65      r1 = r_p;
66      r2 = r_p + w_g
67      r3 = r_c;
68      T = t_p + t_m + t_b + t_g;
69      t1 = T/2;
70      t2 = T/2 - t_m;
71      t3 = T/2 - (t_m + t_g)
72      t4 = T/2 - (t_m + t_g + t_p);
73      t5 = -T/2;
74
75      theta1 = atan(t1/r1);
76      theta2 = atan(t1/r2);
77      theta3 = atan(t1/r3);
78      theta4 = atan(t2/r3);
79      theta5 = atan(t3/r3);
80      theta6 = atan(t4/r3);
81      theta7 = atan(t5/r3);
82      theta8 = atan(t5/r2);
83      theta9 = atan(t5/r1);
84
85      r_inf = 2*r_fluid;
86        for s=1:size(r_p,3)
87
88  %Specify the points in the model.
89          read.points(:,:,s)=[1 0 t1;
90          2 r1 t1;
91          3 r2 t1;
92          4 r3 t1
93          5 0 t2;
94          6 r1 t2;
95          7 r2 t2
96          8 r3 t2;
97          9 0 t3;
98          10 r1 t3;
99          11 r2 t3;
100         12 r3 t3;
101         13 0 t4;
102         14 r1 t4;
103         15 r2 t4
104         16 r3 t4
105         17 0 t5;
106         18 r1 t5;
107         19 r2 t5;
108         20 r3 t5;
109         21 0 0;
110         22 0 r_fluid;
111         23 r_fluid*cos(theta1) r_fluid*sin(theta1);
```

```
112         24 r_fluid*cos(theta2) r_fluid*sin(theta2);
113         25 r_fluid*cos(theta3) r_fluid*sin(theta3);
114         26 r_fluid*cos(theta4) r_fluid*sin(theta4);
115         27 r_fluid*cos(theta5) r_fluid*sin(theta5);
116         28 r_fluid*cos(theta6) r_fluid*sin(theta6);
117         29 r_fluid*cos(theta7) r_fluid*sin(theta7);
118         30 r_fluid*cos(theta8) r_fluid*sin(theta8);
119         31 r_fluid*cos(theta9) r_fluid*sin(theta9);
120         32 0 -r_fluid
121         33 0 r_inf;
122         34 r_inf*cos(theta1) r_inf*sin(theta1);
123         35 r_inf*cos(theta2) r_inf*sin(theta2);
124         36 r_inf*cos(theta3) r_inf*sin(theta3);
125         37 r_inf*cos(theta4) r_inf*sin(theta4);
126         38 r_inf*cos(theta5) r_inf*sin(theta5);
127         39 r_inf*cos(theta6) r_inf*sin(theta6);
128         40 r_inf*cos(theta7) r_inf*sin(theta7);
129         41 r_inf*cos(theta8) r_inf*sin(theta8);
130         42 r_inf*cos(theta9) r_inf*sin(theta9);
131         43 0 -r_inf];
132
133         read.areas(:,:,s)=[
134         %Matching layer
135         1,5,6,2,1,elr_m(s),elt_m(s),0,0;
136         %Glue
137         2,6,7,3,2,elr_g(s),elt_g(s),0,0;
138         2,9,10,6,5,elr_g(s),elt_g(s),0,0;
139         2,10,11,7,6,elr_g(s),elt_g(s),0,0;
140         2,14,15,11,10,elr_g(s),elt_g(s),0,0;
141         %Casing
142         3,7,8,4,3,elr_c(s),elt_c1(s),0,0;
143         3,11,12,8,7,elr_c(s),elt_c2(s),0,0;
144         3,15,16,12,11,elr_c(s),elt_c3(s),0,0;
145         3,19,20,16,15,elr_c(s),elt_c3(s),0,0;
146         %Piezoelectric element
147         4,13,14,10,9,elr_p(s),elt_p(s),0,0;
148         %Backing layer
149         5,17,18,14,13,elr_b(s),elt_b(s),0,0
150         5,18,19,15,14,elr_b(s),elt_b(s),0,0
151         %Finite fluid elements
152         6,1,2,23,22,el_fluid,el_fluid,0,21
153         6,2,3,24,23,el_fluid,el_fluid,0,21
154         6,3,4,25,24,el_fluid,el_fluid,0,21
155         6,4,8,26,25,el_fluid,el_fluid,0,21
156         6,8,12,27,26,el_fluid,el_fluid,0,21
157         6,12,16,28,27,el_fluid,el_fluid,0,21
158         6,16,20,29,28,el_fluid,el_fluid,0,21
159         6,20,19,30,29,el_fluid,el_fluid,0,21
```

```
160         6,19,18,31,30,el_fluid,el_fluid,0,21
161         6,18,17,32,31,el_fluid,el_fluid,0,21
162         %Infinite fluid elements
163         7,22,23,34,33,1,1,21,21
164         7,23,24,35,34,1,1,21,21
165         7,24,25,36,35,1,1,21,21
166         7,25,26,37,36,1,1,21,21
167         7,26,27,38,37,1,1,21,21
168         7,27,28,39,38,1,1,21,21
169         7,28,29,40,39,1,1,21,21
170         7,29,30,41,40,1,1,21,21
171         7,30,31,42,41,1,1,21,21
172         7,31,32,43,42,1,1,21,21
173         ];
174
175
176
177       %Defining the various materials
178         read.materials(:,:,s)=[1 glob.globvariables.mechanic
              mat_m(s);
179          2 glob.globvariables.mechanic mat_g(s);
180          3 glob.globvariables.mechanic mat_c(s);
181          4 glob.globvariables.piezo mat_p(s);
182          5 glob.globvariables.mechanic mat_b(s);
183          6 glob.globvariables.fluid mat_fluid;
184          7 glob.globvariables.infinitefluid mat_fluid];
185
186      %Ground at the front electrode of the piezoelectric disk
187         read.dof(:,:,s)=[-1 1 t3-1e-9 t3+1e-9 glob.free.ep];
188      %Imposing a 1 V electrical potential at the rear surface
           of thepiezoelectric disk
189         read.restraints(:,:,s)=[-1 1 t4-1e-9 t4+1e-9 glob.free
              .ep 1];
190     end
191 end
```

Appendix B

MATLAB-Scripts

B.1 impanal.m

```
clear all
clc
close all
instrreset
vinfo = instrhwinfo('visa','agilent');
vinfo.ObjectConstructorName

obj1 = visa('agilent','GPIB0::17::INSTR');

% Connect to instrument object, obj1.
fopen(obj1);
fprintf(obj1, 'V1');

%%%%%%%%%%%%%%%%%%%%%%%%%%%%%%%%%%%%%%%%%%%%%%%%%%%%%%%

% Osc. level [V]
amplitude = 0.3;
   f = [50e3:100:300e3]/1e3
admittans = 1; % 1 = admittans målinger, 0 = impedans målinger


%%%%%%%%%%%%%%%%%%%%%%%%%%%%%%%%%%%%%%%%%%%%%%%%%%%%%%%
ol = sprintf('%3.3f',amplitude);

if admittans
    % Sett analysator i mode for admittans-måling
    fprintf(obj1, ['A2C3F1OL',ol,'EN']);
else
    % MS
    % Sett analysator i mode for impedans måling
    fprintf(obj1, ['A2C2F1OL',ol,'EN']);
end
```

```
33
34 % Tids-streng på format yyyymmddHHMMSS
35 time = datestr(now, 'yyyymmddHHMMSS');
36 % Tittelen som målingen blir lagra under
37
38 dnow = datetime('now');
39 et = milliseconds(dnow - datetime(1970,1,1));
40
41 et = et + (4240.9 / 3393) * length(f) * 1000;
42 dend = datetime(et,'ConvertFrom','epochtime','TicksPerSecond'
      ,1000);
43
44 tic
45
46 i = 1;
47 ii = 1;
48 antal = length(f);
49 g = ones(1,antal);
50 b = ones(1,antal);
51 fr = ones(1,antal);
52 disp([num2str(antal),' frekvensar.'])
53 disp('Starter måling...')
54 disp(['Slutt tid: ',datestr(dend)])
55 for freq = f
56     percent = i/antal*100;
57     if percent >= ii*10
58         disp([num2str(ii*10),' %'])
59         ii = ii + 1;
60     end
61
62     %disp(['Frekvens (',num2str(i),' av ',num2str(antal),'):
          ', num2str(freq), ' kHz'])
63     s = sprintf('%3.3f',freq);
64     fprintf(obj1, ['FR',s,'ENEX']);
65     pause(0.1)
66     data1 = fscanf(obj1);
67     d=sscanf(data1,'%4c%f,%4c%f,%2c%f');
68     g(i)=d(5);
69     b(i)=d(10);
70     fr(i)=d(13);
71     i = i + 1;
72 end
73 disp('Måling ferdig.')
74 disp('Lagrer data...')
75 stoptime = datestr(now, 'yyyymmddHHMMSS');
76 save(stoptime,'g','b','fr', 'admittans')
77 disp('Ferdig!')
78 toc
```

B.2 add_to_job_list.m

B.3 absorpsjonluft.m

```
1
2  function [korr_trykk,alfa] = absorbsjonluft( frekvens ,trykk ,
       fukt , temp )
3
4   %Vidar Knappskog 2007
5   %Programmet regner ut absorbsjonskoeffisienten for hver
       frekvens
6   f= frekvens ;
7   p= trykk ;
8   h_rel =fukt;
9   T= temp;
10
11  %f=10000; %Frekvens
12  %p=101.325; % Atmosfaeretrykket
13  %h_rel =50; %Relativ luftfuktighet
14  %T=253.15; % Temperatur i Kelvin
15
16
17  T_01 =273.16; % Trippelpunkts isotermisk temperatur (0.01 C)
18
19  p_ref =101.325; % Referansetrykket i kPa ( 1atm )
20  T_ref =293.15; % Referanse temperatur Kelvin .(20 deg C)
21
22  %Finner foerst den molare konsentrasjonen av vann i luften
23  V=10.79586*(1 -( T_01/T )) -5.02808.* log10 (T/T_01 )
       +1.50474*(10^ -4)*(1 -10^( -8.29692*( T/T_01 -1)))+0.42873
       e-3 * (-1 + (10^(4.76955 * (1 - (T_01/T))))) - 2.2195983;
24  h=h_rel *(10^ V)*( p/ p_ref )^ -1; %Molare luftfuktighet
25
26  % Relaksasjons frekvens for Oksygen
27  f_rO =(p/p_ref )*(24 + ((4.04*(10^4)*h )*(0.02+ h )/(0.391+ h
       )));
28
29  % Relaksasjonsfrekvensen for Nitrogen
30  f_rN =(p/p_ref )*( T/ T_ref )^( -0.5)*(9+280* h*exp (
       -4.170*(( T/ T_ref )^( -1/3) -1)));
31
32  disp("f_0 = "+ f_rO)
33
34  disp("f_N = " + f_rN)
35  % Dempningskoeffisient db/m
```

```
36  alfa = 8.686* f.^2.*( (1.84e-11*( p/ p_ref )^-1 * ( T/ T_ref
       )^(0.5)) + (T/ T_ref )^( -5/2) *(0.01275*( exp(-2239.1/T))
       .*(f_rO./(f_rO^2+f.^2)))+ 0.1068*exp(-3352/T).*(f_rN./(
       f_rN^2+f.^2)))
37
38  % Absorbsjon i dB/km
39  korr_trykk =alfa *1000;
```

B.4 CalibratePositionAndAlignment.m

```
1
2  % Script to calibrate position and alignment using the Keyence
       lasers, and
3  % to redefine the z-axis in accordance with this.
4
5  % Eivind Nag Mosland, UiB, March 2023
6
7  % % % Stop current move
8  % % %writeline(instr.controller.HydraTT,'1 nabort')
9  % %
10 % % % Motor restart
11 % % %writeline(instr.controller.HydraTT,'1 init')
12 % %
13 % % % Check if the output of np is nominal (0) or measured (1)
14 % % %writeread(instr.controller.HydraTT,'1 getselpos')
15 % %
16 % % % kabellengde: 260 cm, eller 266 om ein tar med der den
       splittar i to minipluggar
17 % % % Leidningsstubben på den andre er kanskje 85 cm.
18
19 % Initiate range measure move, i.e., move to upper limit
       switch
20 writeline(instr.controller.HydraTT,'1 nrm')
21
22 % Get hardware limits used at initialization (0 1016) mm
23 writeread(instr.controller.HydraTT,'1 getinilimit')
24
25 % Set current position (at limit switch) to 1016 mm
26 org_max_pos = 1016;
27 writeline(instr.controller.HydraTT,[num2str(org_max_pos) ' 1
       setnpos'])
28
29 % Wind up the Keyence laser equipment and start LK-navigator
30
31 % Move to laser position, at 458 mm, if maximum is 1016!
32 writeline(instr.controller.HydraTT,'458 1 nm')
33
```

```
34 % Align transducers and measure distance using the laser
35 d_Tx_at_calibration = 458; % Position of Tx at calibration (if
       maximum is 1016)
36 dx = 182.5692;  % Length of laser
37
38 % Håvard-transduser til mikrofon 13.04.2023
39 d_Tx_at_calibration = 458; % Position of Tx at calibration (if
       maximum is 1016)
40
41
42 dx = 182.5692;  % Length of laser
43 dx_Tx = 30 - (2.2990); % Distance between laser and Tx Øverste
       linje
44 dx_Rx  = 30 - (-2.4799); % Distance between laser and Rx
     Nederste linje
45 d = dx + dx_Tx + dx_Rx % Distance between Rx and Tx
46 d_Rx_at_calibration = d_Tx_at_calibration - d; % Position of
     Rx at calibration
47
48 % Position of limit switch relative to Rx is thus
49 new_max_pos = org_max_pos - d_Rx_at_calibration
50
51 % Initiate range measure move, i.e., move to upper limit
     switch
52 writeline(instr.controller.HydraTT,'1 nrm')
53
54 % Get current position (at limit switch) to account for
     possible offset
55 % from nominal position (org_max_pos)
56 tmp = writeread(instr.controller.HydraTT,'1 np');
57 current_pos = str2double(tmp)
58
59 % Set distance to new maximum, i.e., with Rx at 0
60 writeline(instr.controller.HydraTT,[num2str(current_pos-
     org_max_pos+new_max_pos) ' 1 setnpos'])
61
62 % Get current position (at limit switch) in new coordinate
     system
63 writeread(instr.controller.HydraTT,'1 np')
64
65 % Set allowed distances
66 min_pos = 10; % Minimum allowed distance [mm]
67 % min_pos = 850; % Minimum allowed distance [mm]
68 writeline(instr.controller.HydraTT,[num2str(min_pos) ' '
     num2str(current_pos-org_max_pos+new_max_pos) ' 1 setnlimit'
     ])
69
70 % Check if the limits are set as they should
```

```
71 writeread(instr.controller.HydraTT,'1 getnlimit')
72
73 % Write position to zero-file
74 zero.x = instr.controller.C863_xaxis.qPOS;
75 zero.y = instr.controller.C863_yaxis.qPOS;
76 zero.rotation = instr.controller.C863_rotation.qPOS;
77 zero.z_in_original_coord = d_Rx_at_calibration;
78 zero.z_at_limit_switch_in_original_coord = org_max_pos;
79 zero.z_at_limit_switch_in_new_coord = current_pos-org_max_pos+
     new_max_pos;
80 zero.z = 0;
81
82 zero.alignment.Rx_top = -0.39;
83 zero.alignment.Rx_bottom = -0.257;
84 zero.alignment.Rx_side_close_to_wall = -0.175;
85 zero.alignment.Rx_side_far_from_wall = -0.447;
86 zero.alignment.Rx_midpoint = -0.304;
87
88 zero.alignment.Tx_top = -1.512;
89 zero.alignment.Tx_bottom = -1.417;
90 zero.alignment.Tx_side_close_to_wall = -1.490;
91 zero.alignment.Tx_side_far_from_wall = -1.448;
92 zero.alignment.Tx_midpoint = -1.461;
93
94 tmp_str = datestr(now());
95 s = regexp(tmp_str, '\s+', 'split');
96 save(['zero_' s{1} '.mat'],'zero')
```